Characterisation and Calibration of the Compact High Energy Camera for the Cherenkov Telescope Array

Connor Duffy

Department of Physics and Astronomy

University of Leicester

December 2021

A thesis presented for the degree of

Doctor of Philosophy

Characterisation and Calibration of the Compact High Energy Camera for the Cherenkov Telescope Array. Connor Duffy.

Abstract

The interaction of very-high energy gamma rays and charged particles, produced in the Universe's most energetic environments, with the Earth's atmosphere produces a cascade of high energy particles. Particles within this cascading shower travel at speeds faster than the speed of light in the atmosphere. As such, the particles emit Cherenkov radiation. Ground-based imaging atmospheric Cherenkov telescopes use this phenomenon to observe the particle shower. In doing so, it is possible to determine the direction of the shower and thus the direction of the shower progenitor. This source determination can be used to provide an observation of the environments giving rise to such high-energy photons.

The Cherenkov Telescope Array represents the latest telescope array of this kind and will provide highly sensitive observations of gamma-rays ranging in energy from 20GeV to 300TeV with the use of three telescope sizes. CHEC-S is one of the Cherenkov imaging cameras proposed for the Small Sized Telescope. It is a compact imaging camera that is designed to be used with a dual-mirror Schwarzschild-Couder design telescope. In addition to this novel telescope design, CHEC-S will utilise silicon photomultipliers for the detection of Cherenkov light in conjunction with an updated iteration of front end electronics based on the TARGET ASIC.

In this thesis, relevant tasks completed for the comissioning of CHEC-S is presented. In addition, the calibration of the TARGET-C digitising ASIC is outlined with a discussion on performance. A proposed changed to the calibration method and enhanced performance is given. Finally, the results of the on-telescope campaign of CHEC-S is presented, highlighting the requirement for the method outlined in this thesis for the correction of TARGET-C saturation.

Acknowledgements

Firstly, I would like to thank my supervisor, Prof. Jon Lapington, for the support and guidance you have given throughout my PhD. I am incredibly thankful for the knowledge you have shared and hope that one day, I may retain as much as you.

I would also like to thank Dr. Steve Leach, for the huge amount of help you have given over the last four years. Without this help, I would not have been able to develop and progress my skills in the lab. I am also thankful for the various discussions over the years ranging from instrumentation, future career prospects, and the latest Netflix series.

A huge amount of thanks goes to Dr. Richard White, for continually pushing me to work harder and instigating the discussions that help improve my critical thinking and potential as a research scientist. I must also thank you for the time I spent at MPIK, specifically for your help in the lab and the at the climbing gym.

To Jason, I am incredibly grateful for your support over the past four years. Thank you for believing in my ability and helping with the numerous data analysis and programming queries I have bugged you with over the years.

Finally, to Charlotte, thank you for your continual reassurance, enthusiasm and patience with my work. Your support and motivation during the past year has been an invaluable source of encouragement needed to finish this thesis.

Contents

List of Figures

Chapter 1

Introduction

Contents

1.1 Gamma-ray Astrophysics

Gamma radiation was first discovered by Paul Villard in 1900 during observations of the radioactive emissions of Radium, following the discovery of α and β radiation by Ernest Rutherford one year prior. Villard was attempting to measure the deflection of β-rays, emitted by Radium, in the presence of a magnetic field [1]. He observed that, in addition to the expected β radiation, there was a second higher penetrating radiation that was unaffected by the magnetic field. This second source of radiation was assigned the gamma-ray (γ-ray) name by Rutherford in keeping with the naming convention describing the penetrating power of the three forms of ionising radiation [2].

The study of ionisation became the focus of many scientists at the end of the 19th century with the development of the *electroscope*: an instrument for the detection of electric charges in accordance to Coulomb's Law. During this early period, the use of electroscopes was for the study of ionisation produced in the presence of radioactive material and the expected ionisation due to Earth's radioactivity. At the start of the 20th century, scientists would begin to investigate the variation of ionisation at increasing amplitudes. Theodor Wulf, a German physicist, led the study of atmospheric radiation by measuring the rate of ionisation at the top of the Eiffel Tower (Paris) with a much improved electroscope. The use of the Eiffel Tower provided the opportunity to measure ionisation at different times of day and across multiple days. Wulf's observations would suggest a decrease in ionisation at the top of the Eiffel Tower when compared to measurements taken at ground level. He concluded that the source of ionising radiation must therefore be the Earth's crust. This conclusion was corroborated by many others following similar experiments. However, one Domenico Pacini conducted numerous experiments that would suggest a conflicting conclusion to that of Wulf's terrestrial source of ionising radiation. Pacini first determined the rate of ionisation measured at sea, in the Gulf of Genova (now Genoa), was the same as that measured on land. He later discovered that by submerging

the electroscope only a few metres in water would greatly reduce the rate of ionisation. He, therefore, concluded that the ionising radiation must be present within the atmosphere since it can be measured at great distances from land and was shown to be absorbed (and not produced) by the sea [3]. It was clear at this time that the use of weather balloons for high altitude experiments was necessary to confirm the source of such ionising radiation.

Although many scientists were conducting ionisation studies utilising weather balloons, it would be Victor F. Hess who would provide the greatest insight into atmospheric ionisation. Hess would do so with seven balloon flights conducted in 1912 using three instruments: one β radiation detector and two γ radiation detectors, reaching an altitude of $\sim 5200m$ [4].

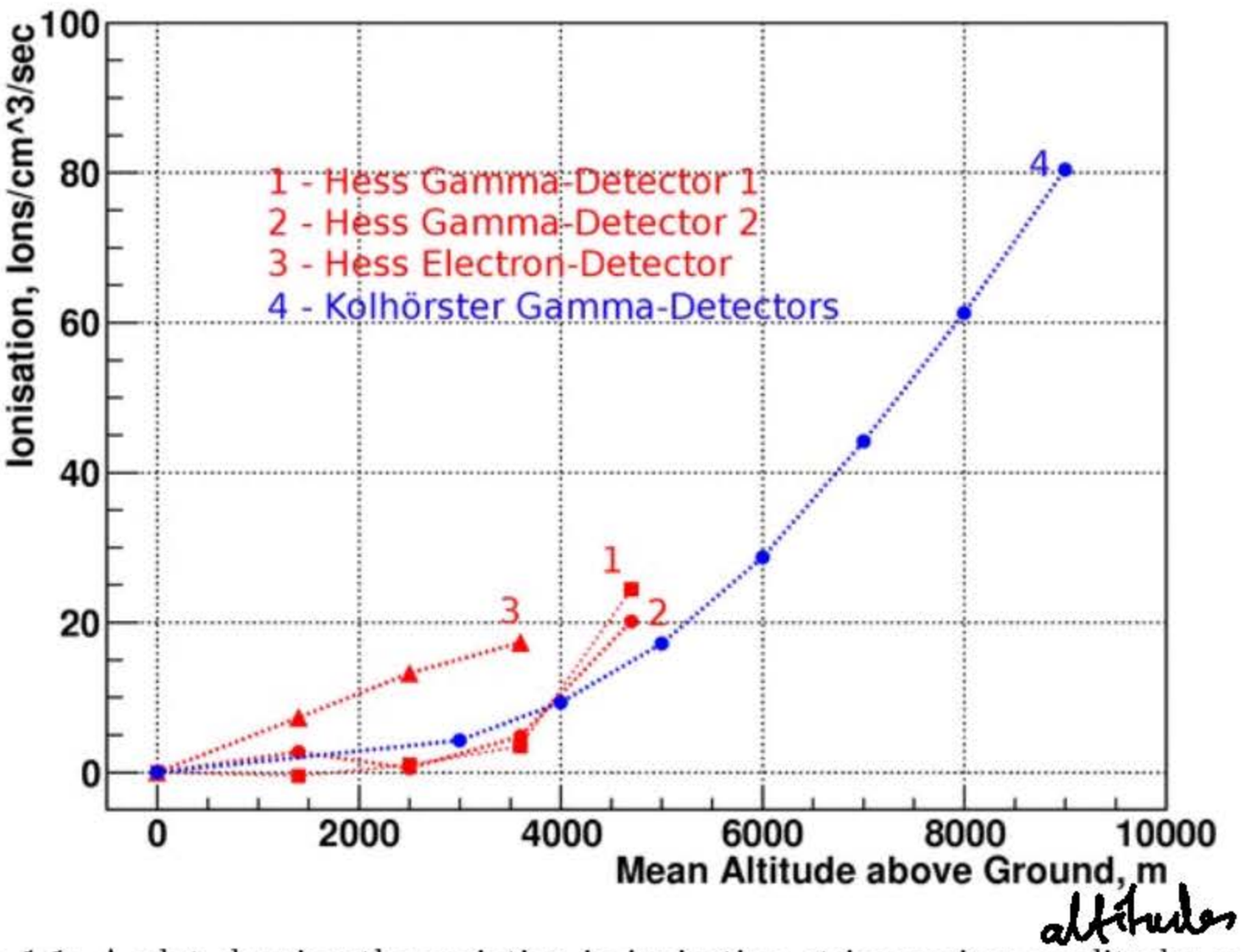

Figure 1.1: A plot showing the variation in ionisation at increasing amplitudes measured by Victor Hess during his seventh balloon flight in 1912. Hess' observations (red) show the ionisation rate increases with altitude, these findings were later confirmed by balloon flight observations at much higher altitudes conducted by Werner Kölhorster in 1914 (blue) [5].

Figure 1.1 shows the results obtained during these balloon flights, with the rate of ionisation at ground level subtracted from measurements made at increasing altitude.

In addition to this, the results obtained by Werner Kölhorster during a later balloon flight confirming Hess' findings is included. It can be seen that the ionisation rate, and hence presence, of γ radiation increases with altitude. Hess, therefore, concluded that the observed radiation must be emanating from above and deemed the source to be extra-terrestrial. With observations both during the day and night showing little variation in ionisation rate, Hess would finally conclude that the source of ionising radiation was not the Sun, as many believed, and must therefore arrive from outside our solar system. This ionising radiation would come be named *Cosmic Rays*, for which Hess would receive a Nobel Prize in physics for their discovery. The study of cosmic rays (CR) and ionising radiation would subsequently initiate the research fields of particle and astroparticle physics.

1.1.1 Cosmic Ray Spectrum

Cosmic Rays (CRs) are high energy, ionised particles that can be categorised as either primary or secondary CRs. Primary CRs consist of protons, high-energy nuclei (HZE) ions, electrons and positrons, and are extra-Solar (both galactic and extra-galactic) in origin. Since these particles are ionised it is not possible to determine the origin of CRs through observations and source extraction as their path becomes deflected by magnetic fields. Secondary CRs represent the charged particles produced during the interaction of primary CRs with the interstellar medium [6] and the atomic nuclei of Earth's atmosphere (described further in 1.3.1). These interactions can result in the production of lighter, ionised nuclei in addition to more exotic pions, kaons and muons. High energy neutrinos and γ-rays are produced following the decay of these exotic particles, but are not included as constituents of the secondary CRs. In addition, further electrons and positrons are produced through the pair production of γ-rays.

Figure 1.2 shows the all-particle energy spectrum of CRs in the range of $10^{13}eV$ to $\sim 10^{20}eV$, scaled with $E^{2.6}$ as observed by the many indicated instruments on Earth.

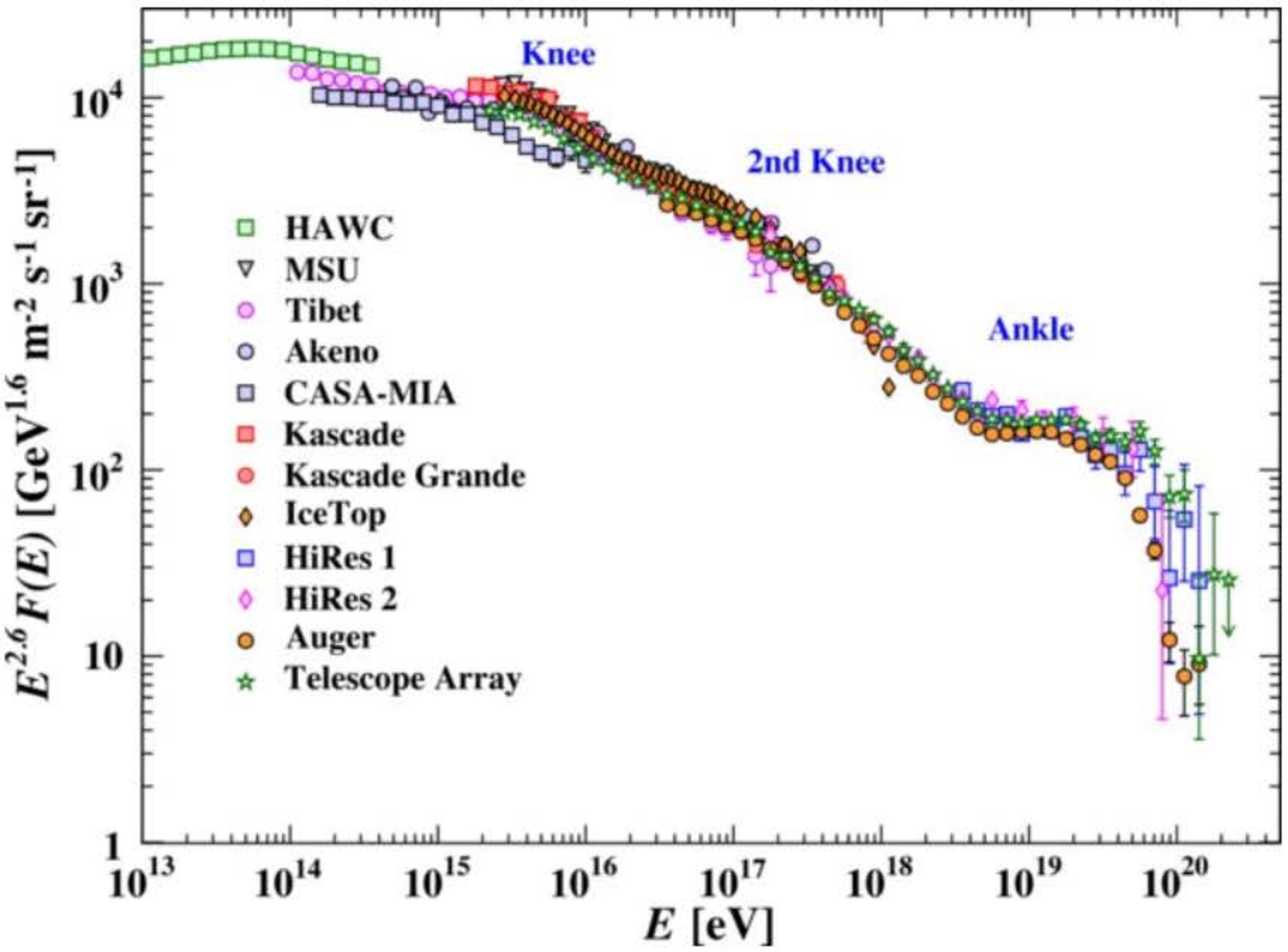

Figure 1.2: All-particle cosmic ray energy spectrum as measured by the experiments in the legend. The plot indicates breaks in the spectrum known as the *knee*, *2nd Knee* and *Ankle*. These features indicate a break in the power law of the spectrum [7].

The morphology of the CR spectrum can be used to indicate the suspected source and mechanism for the production of CRs as shown by the spectral breaks indicated by the annotations: *Knee, 2nd Knee* and *Ankle*. For CRs observed up to the *Knee* ($\sim 3*10^{15}eV$), it is generally accepted that such CRs are produced by diffuse shock acceleration in the shock fronts of supernova remnants. The region between the *Knee* and *Ankle* represents a transition between galactic CRs in origin at lower energies and extra-galactic sources at higher energies. The argument for this transition can be reinforced by considering the gyroradii of CRs within this region. The gyroradius (or Larmor radius) describes the radius of a charged particle in circular motion in the presence of a magnetic field. For relativistic particles, the gyroradius (r_g) in parsecs can be determined as follows [8]:

$$r_g(pc) = 1.08 * \frac{E_{15}}{ZB_{\mu G}} \tag{1.1}$$

where E_{15} is the particles energy in units of $10^{15}eV$, Z the atomic (proton) number of the particle, and $B_{\mu G}$ is the magnetic field strength in units of microgauss.

For a proton observed at the *Ankle* with an energy of $\sim 1*10^{19}eV$ and assuming a uniform galactic magnetic field strength of $3\mu G$, the subsequent gyroradius would be $> 1kpc$. The Hillas criterion states that, for a source to be considered a particle accelerator, the gyroradius of the particle cannot exceed the size of the object producing the acceleration [9][8]. This would suggest that even if protons could be accelerated to energies greater than $10^{19}eV$, they would not be confined to the Milky Way. It is therefore possible to argue that protons observed above the *Ankle* are extra-galactic in origin.

Since γ-rays are produced in the secondary processes of CR interactions, and are not affected by the magnetic fields within the interstellar medium, they become vital sources for the observations of the accelerating mechanisms producing both galactic and extra-galactic CRs. Research and observations of both CRs and γ-rays will add to an already complex CR spectrum. In doing so, the features of the spectrum may become more pronounced and provide further insight into the environments giving rise to such particles. In the following Section I will describe the mechanisms for the production of γ-rays and CRs.

1.2 Production of Cosmic and Gamma Rays

The morphology of the CR spectrum suggests that there must be a number of mechanisms for the acceleration and production of both CRs and γ-rays. In this section I will describe the most promising theories for the production of CRs and the environments that give rise to the particle acceleration.

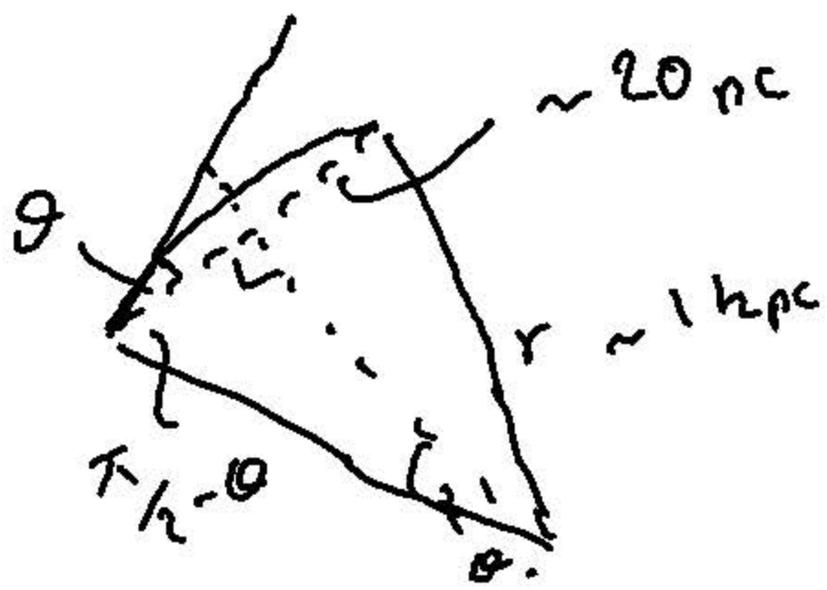

1.2.1 Acceleration of Cosmic Rays

The leading theory for the acceleration of CRs follows the statistical acceleration of charged particles through the interactions of such particles with irregularities in existing magnetic fields. The initial theory for statistical acceleration was developed by Enrico Fermi. Fermi suggested that when a charged particle collides with an irregularity of the magnetic field within a moving Galactic cloud, the particle is reflected and continues on its trajectory until it encounters another irregularity and is again reflected by this *"magnetic mirror"* [10]. The energy gained by the charge particle is on the order $\frac{\Delta E}{E} \sim (\frac{v}{c})^2$, where v is the speed of the Galactic cloud containing the *magnetic mirror*. This theory gives rise to the acceleration of charged particles and is known as second-order Fermi acceleration. However the resulting spectral index does not match that of observed CRs.

A modified version of the second-order Fermi acceleration was suggested as a mechanism for CR production in strong shock waves travelling through the interstellar medium. This theory is referred to as *diffusive shock acceleration* (or first-order Fermi acceleration). Since magnetic fields are present on both the upstream and downstream side of the shock front, a high energy charged particle will traverse the shock and again be reflected by the upstream or downstream magnetic field [11]. Neglecting the damping of charged particles by turbulent Alfven waves in the upstream side of the shock front, the energy of a charged particle [12] after crossing the shock front n times is given by:

$$E_n = E_0(1 + \frac{v}{c})^n \tag{1.2}$$

where E_0 is the initial energy of the charged particle, v the velocity of the particle and c the speed of light in a vacuum.

Since the probability of a charged particle to remain within shock is given by $(1 - P_{esc})^n$, where P_{esc} is the probability of a particle escaping the shock per crossing, it

is possible to determine the differential spectrum as follows:

$$\frac{dN(>N)}{dE} \propto \frac{1}{P_{esc}}(\frac{E}{E_0})^{-\gamma} \tag{1.3}$$

The result of this equation for supersonic shocks is a power law with a spectral index (γ) of 2, which closely resembles the spectral index observed in CRs and shown in Figure 1.2.

By modelling the shock produced by young supernova remnants (SNR) with the inclusion of magnetic field amplification by the accelerated CRs [13], it has been shown by Schure & Bell [14] that the diffusive shock acceleration mechanism is able to accelerate CRs to energies of $\sim 10^{15} eV$ (PeV). This again correlates with the CR spectrum shown in Figure 1.2. Since diffusive shock acceleration follows the observed spectrum and is applicable to a large number of astrophysical environments with fast moving shock fronts, this mechanism is well established as a process for the acceleration of CRs.

1.2.2 Production of Gamma Rays

Since γ-rays are not influenced by the magnetic environments within the interstellar medium, it is possible to determine the direction and location of the source of γ-rays through observations. As γ-rays are produced by the interactions of CRs, the detection of γ-rays can be used to directly investigate these interactions and gain further insight into the acceleration mechanisms and the production of the progenitor charged particles. The interactions of CRs that produce γ-rays are either Leptonic or Hadronic in nature, the following is a description of these production mechanisms.

1.2.2.1 Leptonic Production of Gamma Rays

As the name suggests, the leptonic production of γ-rays occurs following the interactions of leptons: mainly electrons and positrons, with matter through a number of processes including: bremsstrahlung radiation, synchrotron radiation, and inverse Compton scattering. What follows is a description of these processes.

Bremsstrahlung Radiation When an incident charged particle passes through the Coulomb field of another particle, it is deflected and emits electromagnetic radiation. The amplitude of the emitted radiation is proportional to the deceleration of the initial particle. For an electron of charge e and mass m deflected by an atomic nucleus of charge Ze, this deceleration, and hence photon energy, is proportional to Ze^2/m [15]. The deceleration of the charged particle gives this process its name Bremsstrahlung ("braking radiation" in German).

Cosmic γ-rays are produced when relativistic CR leptons interact with nuclei found in gaseous regions. The resulting γ-rays have energies of the same order as the incident electron, the spectral index (Γ_γ) of such photons also correlates directly to that of the progenitor leptons ($\Gamma_L \approx \Gamma_\gamma$ [16]). Observations of such γ-rays are therefore important for investigating CR leptons and interactions within gaseous regions of the galaxy.

Synchrotron Radiation When a charged particle moves through a region with a magnetic field, the particle is accelerated and deflected by the magnetic field so that the initial particle follows a curved path about the magnetic field. As the charged particle is accelerated, it loses energy by the emission of polarised electromagnetic radiation, this emission is synchrotron radiation. For relativistic CR leptons moving in a homogeneous magnetic field, in the absence of an electric field, an acceleration is induced by the purely magnetic Lorentz force perpendicular to the direction of travel of the CR lepton. In a

constant magnetic field, the electron/positron describes a circular orbit with constant radius along the magnetic field lines with cyclic frequency equal to the Larmor frequency [17]. The power of the polarised radiation emitted during the acceleration of an electron of mass m_e, with energy E_e and velocity β is givent by:

$$P_{sync} = \frac{4}{3} c \sigma_T (\frac{E_e}{m_e c^2})^2 \beta^2 u_B \tag{1.4}$$

where σ_T is the Thomson cross-section such that, $\sigma_T = \frac{8\pi}{3}(\frac{q^2}{m_e c^2})^2$, the magnetic energy density, $u_B = \frac{B^2}{2\mu_0}$, for a magnetic field with field strength B, and μ_0 the magnetic permeability in a vacuum.

Since the power of synchrotron radiation, and hence energy loss of the initial CR, follows $P_{sync} \propto \frac{1}{m_{CR}^4}$, the energy of the emitted radiation is higher for lighter CRs. It is therefore expected that CR leptons (electrons and positrons) are the dominating progenitor for γ-rays produced via synchrotron radiation [17].

Inverse Compton Scattering Compton scattering describes the interaction of an incident photon with a charged particle (usually electron) resulting in a scattered photon with reduced energy compared to the initial photon. Through the conservation of momentum, the charged particle recoils producing a transfer of energy from the photon to the charged particle. It is possible for reverse process to occur, whereby the charged particle up-scatters the photon, resulting in a photon with higher energy. This process is known as inverse Compton scattering and describes the process of CRs up-scattering the photons of ambient photon fields, such as the cosmic microwave background (CMB) radiation, to much higher energies. Inverse Compton scattering is categorised as one of two regimes,

depending on the energies of the photon field and the initial CR energy [16], since:

$$\varepsilon = \frac{E_{ph} E_{CR}}{m_{CR}^2 c^4} \,, \tag{1.5}$$

For $\varepsilon \ll 1$, the inverse Compton scattering follows the Thomson regime with a cross section of:

$$\sigma_{IC,T} \simeq \sigma_T (1 - 2\varepsilon) \simeq \sigma_T \,, \tag{1.6}$$

where σ_T is the Thomson cross section as mentioned before. For $\varepsilon \gg 1$, the scattering follows the Klein-Nishina regime with a cross section of:

$$\sigma_{IC,KN} \simeq \frac{3\sigma_T ln(4\varepsilon)}{8\varepsilon} \,. \tag{1.7}$$

For highly relativistic electrons, there is an apparent suppression of inverse Compton scattering caused by the cross section of the Klein-Nishina regime [18]. The energy loss of CR electrons, and energy of resulting up-scattered photons, can be approximated by the Thomson regime formula:

$$P_{IC,T} = \frac{4}{3} c \sigma_T (\frac{E_e}{m_e c^2})^2 \beta^2 u_R \,, \tag{1.8}$$

where u_R is the energy density of the ambient photon field. Similarly to 1.4, the energy loss of the CR follows $P_{sync} \propto \frac{1}{m_{CR}^4}$ and again suggests that CR leptons are the prevailing progenitor for the production of γ-rays via inverse Compton scattering.

A secondary emission process occurs whereby the photons produced by synchrotron radiation act as the initial photon for inverse Compton scattering, again resulting

in up-scattered high energy (γ-ray) photons, this process is synchrotron self-Compton scattering. In this manner, low energy synchrotron radiation can be up-scattered, producing γ-rays depending on the source environment.

1.2.2.2 Hadronic Production of Gamma Rays

High energy CR protons interact directly with the protons and nuclei of the interstellar medium through inelastic collisions producing charged and neutral pions in equal quantities via the following mechanism:

$$p + p \longrightarrow p + p + \pi^+ + \pi^- + \pi^0 . \tag{1.9}$$

The minimum energy of the CR proton required for *pion production* to occur can be determined by applying the conservation of momentum to 1.9 and is found to be $280 MeV$. The charged pions then decay via weak interactions producing muons and neutrinos which in turn decay into electrons/positrons and more neutrinos. Following is the decay process for both π^+ and π^-:

$$\begin{aligned} \pi^+ &\longrightarrow \mu^+ + \nu_\mu \longrightarrow e^+ + \overline{\nu_\mu} + \nu_\mu + \nu_e , \\ \pi^- &\longrightarrow \mu^- + \overline{\nu_\mu} \longrightarrow e^- + \nu_\mu + \overline{\nu_\mu} + \overline{\nu_e} . \end{aligned} \tag{1.10}$$

The neutral pion (π^0) decays via the electromagnetic force:

$$\pi^0 \longrightarrow \gamma + \gamma \tag{1.11}$$

Again, following the conservation of momentum, the energy from the two daughter photons is related to the kinetic energy of the neutral pion, and therefore

the kinetic energy of the progenitor CR. For interactions of relativistic CRs in a region with a large abundance of matter, it is possible to produce very-high energy γ-rays.

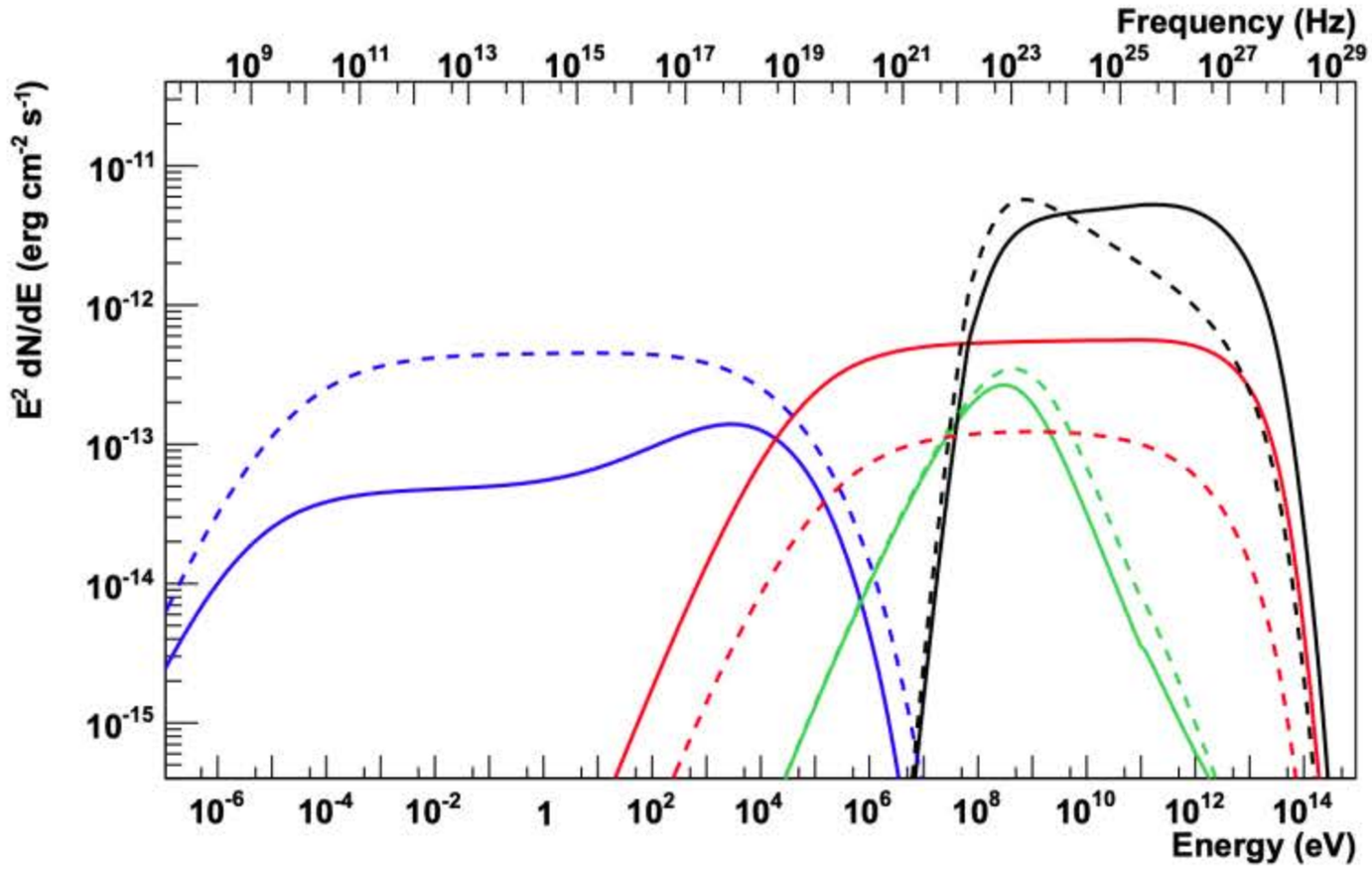

Figure 1.3: The modelled spectral energy distribution for a starburst region at a distance of $3.5Mpc$. The contribution of each γ-ray production process is indicated: synchrotron emission (blue), inverse Compton scattering (red), bremsstrahlung radiation (green) and π^0 decay (black). The solid (model 1) and dashed (model 2) lines represent the two models used with varying CR spectral index, radiation field energy density and magnetic field strength [19].

Figure 1.3 shows an example of the spectral energy distribution (SED) for a starburst region at a distance of $3.5Mpc$ modelled by Ohm & Hinton [19]. The SED shows the contribution of each of the aforementioned mechanisms for the production of γ-rays in the modelled source region.

Understanding the mechanisms that give rise to the production of γ-rays is a necessity to gain further insight into the regions that give rise to the highest form of radiation. In addition, observations of such radiation can help further the understanding of CRs and the varying environments found across our universe. The following section will describe the interactions of γ-rays and CRs with the Earth's atmosphere and the use of such interactions for the ground-based observations of very high energy (VHE) γ-rays.

1.3 Atmospheric Interactions

Throughout the history of astronomy, it has only been possible to observe the Universe through radiation that can be detected, at each given era of our astronomical evolution. As the Earth's atmosphere is only transparent for a small portion of the electromagnetic spectrum, observations of cosmic *gamma*-rays wouldn't occur until the *gamma*-ray space telescope on-board *Explorer 11* launched in 1962. Although it is impossible to directly observe γ-rays and CRs at the Earth's surface, they can be observed indirectly via the interactions of each with the atmosphere. The following describes these interactions and their use in ground based γ-ray astronomy.

1.3.1 Extensive Air Shower

VHE Cosmic and Gamma rays entering the Earth's atmosphere are absorbed through the interactions of such radiation with the atomic nuclei within the atmosphere (mainly oxygen and hydrogen). The collision of a CR or γ-ray with a single atmospheric nuclei produces secondary particles. These secondary particles propagate through the atmosphere and again interact with the atmospheric nuclei, resulting in more daughter particles. This process continues in a cascading shower of particles until the energy of particles within the cascade is no longer sufficient to produce further particles. This process describes the *Extensive Air Shower* (EAS). The structure of the particle shower depends on its progenitor and can be categorised as either an electromagnetic or hadronic shower for γ-ray or CR initiated cascades.

1.3.1.1 Electromagnetic Showers

An electromagnetic shower occurs when a VHE γ-ray hits the Earth's atmosphere resulting in a cascade of high-energy particles. As the shower name would suggest, the resulting

particles interact exclusively via the electromagnetic force [20]. Upon entering the atmosphere, a sufficiently energetic γ-ray photon converts into a electron-positron pair within the Coulomb field of a atmospheric nucleus by way of *pair production* [21] providing the energy of the photon is higher than twice the rest mass energy of an electron. The lepton pair share the remaining energy of the initial photon and continue on a downward path towards the Earth's surface at relativistic speeds. The emitted electron positron pair continue their trajectory until they interact with another atmospheric nucleus by way of bremsstrahlung emission, resulting in the emission of a γ-ray. This γ-ray again follows a similar path until it subsequently undergoes pair production, emitting another electron-positron pair. The subsequent cascade continues, increasing particle population, until the energy of the remaining particles is no longer sufficient enough to interact via pair production and bremsstrahlung. At this point ionisation becomes the dominant process for interactions.

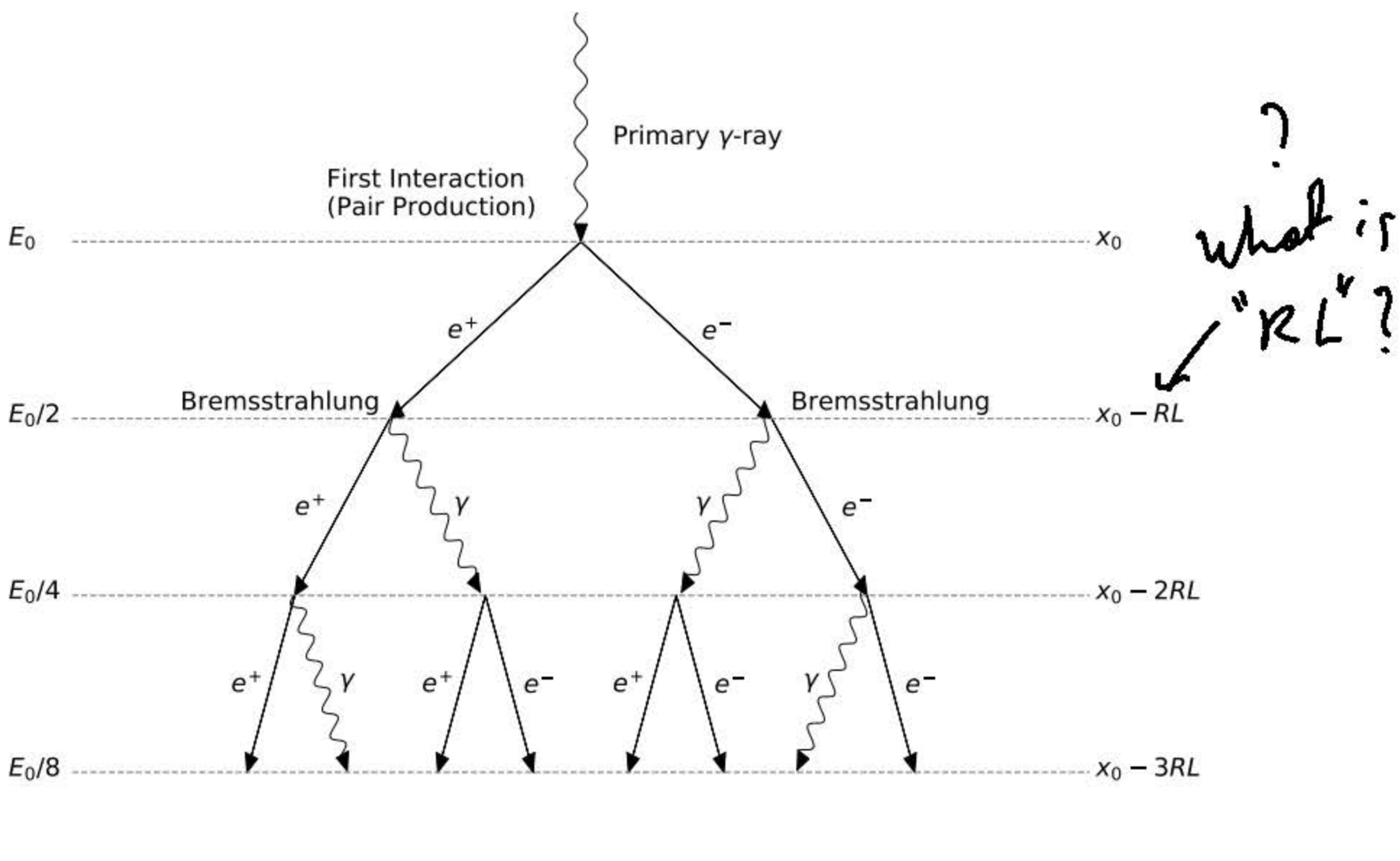

Figure 1.4: An illustration of an electromagnetic EAS initiated by the interaction of a γ-ray with atmospheric nuclei as described by Beth & Heitler [20]. Adapted from [22].

Figure 1.4 shows the progression of the electromagnetic shower. This mechanism can be initiated by a VHE γ-ray or a CR lepton, since the lepton would interact via bremsstrahlung producing the cascade as shown. It is possible to determine the number of particles and energy emitted in the cascading shower by adopting the simple model produced by Bethe & Heitler [20]. Heitler's model assumes the interactions in this cascade are only via bremsstrahlung and pair production and the radiation length X_0 (distance over which a lepton loses $\frac{1}{e}$ of it's original energy) of both processes are identical. Using this model, it is possible to determine the number of particles N_n, each with an energy E_n, at a shower depth of X_n following n cascade steps:

$$\begin{aligned} N_n &= 2^n \\ E_n &= E_0/2^n \\ X_n &= nX_0 \end{aligned} \tag{1.12}$$

As stated before, the cascade stops at the critical energy E_c where interactions no longer lose energy via bremsstrahlung emission. The maximum number of particles N_{nmax} can therefore be calculated as:

$$N_{max} = \frac{E_0}{E_c} \, . \tag{1.13}$$

By rearranging these equations, the maximum shower depth can also be given by:

$$X_{max} = X_0 ln(\frac{E_0}{E_c}) \tag{1.14}$$

Assuming a radiation length of $X_0 = 37 g/cm^2$, the height of the shower maximum is $\sim 10 km$ with an initial interaction at $\sim 25 km$.

The mechanism for electromagnetic particle showers result in a somewhat sym-

metrical and uniform shower. The particle shower that results from a hadronic CR interacting with the atmosphere are much more complex in shape and morphology.

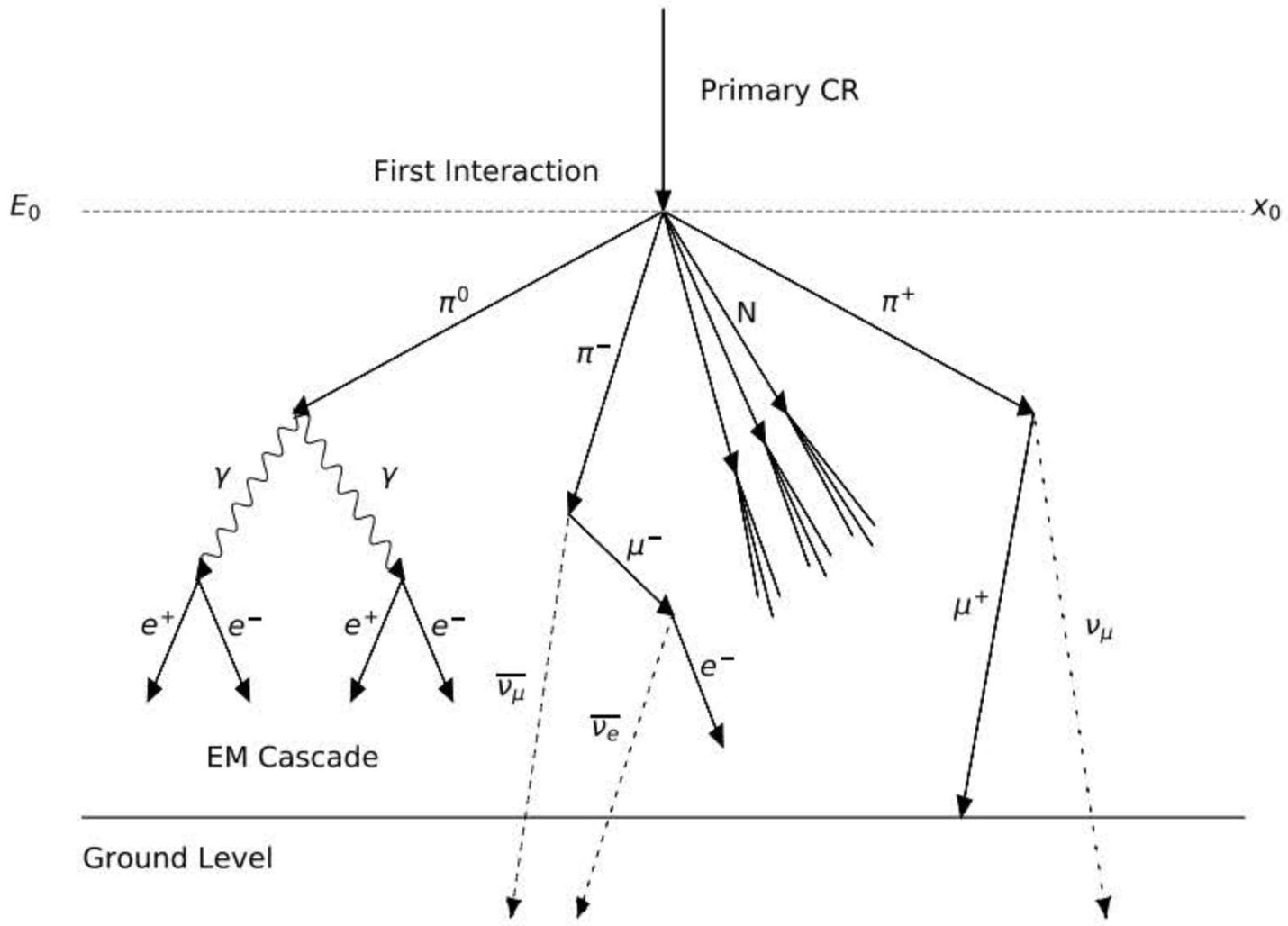

Figure 1.5: An illustration of a hadronic particle cascade produced by the interaction of a CR proton with atmospheric nuclei [23].

1.3.1.2 Hadronic Showers

The EAS initiated when hadronic CRs (largely protons) interact with nuclei in the atmosphere is categorised as a hadronic shower and is produced by a number of processes. When high energy protons collide with atmospheric nuclei, the collision products are largely pions (charged and neutral) in addition to more exotic particles in much smaller quantities (such as kaons). These interactions are mediated by the nuclear weak force, an example of the pion production is given in Equation 1.9.

Figure 1.5 shows a visualisation of the propagation of and mechanisms within a hadronic shower. Equations 1.10 and 1.11 describe the decay of the charged and neutral pions. The charged pions decay into muons and muon neutrinos which further decay into

leptons and more neutrinos, the flavour of lepton/muon/neutrinos depend on the charge of the initial pion. As described previously, the leptons (electrons and positrons) will initiate an electromagnetic particle shower which greatly adds to the number of particles within the hadronic shower. Muons and neutrinos, however, do not interact with atmospheric particles and instead continue towards the ground. Muons can provide a source of calibration for γ-ray astronomy and indeed neutrinos are the particle of concern for neutrino detectors such as SuperKamiokande [24] and IceCube [25]. The neutral pion decays into a pair of γ-rays, these γ-rays then undergo pair production resulting in another free pair of leptons which again produce further electromagnetic particle showers.

Since the majority of proton-proton reactions in a hadronic particle shower result in pion production, it is possible to model the cascade by assuming all interactions result in pions and their subsequent reaction products. This approach was adopted by J. Matthews (2005) [23] and follows a similar approach to the Heitler model. Using this model it is again possible to determine the energy of the progenitor of the EAS.

Whilst Figures 1.4 and 1.5 might suggest a similar profile in the particle cascade produced by γ-ray and CR interactions, there is a vast difference in the morphology of subsequent cascades. The variety of the particles and their energies produced in a hadronic particle shower result in an irregular and nonuniform shower when compared to the uniform and homogeneous cascade produced by an electromagnetic shower [23]. Figure 1.6 shows the disparity in shape between a γ-ray and CR induced EAS modelled using the CORSIKA simulation package [27]. The disparity in particle shower shape can be used to distinguish between the EAS progenitors through the observation of the Cherenkov radiation emitted by such relativistic cascades.

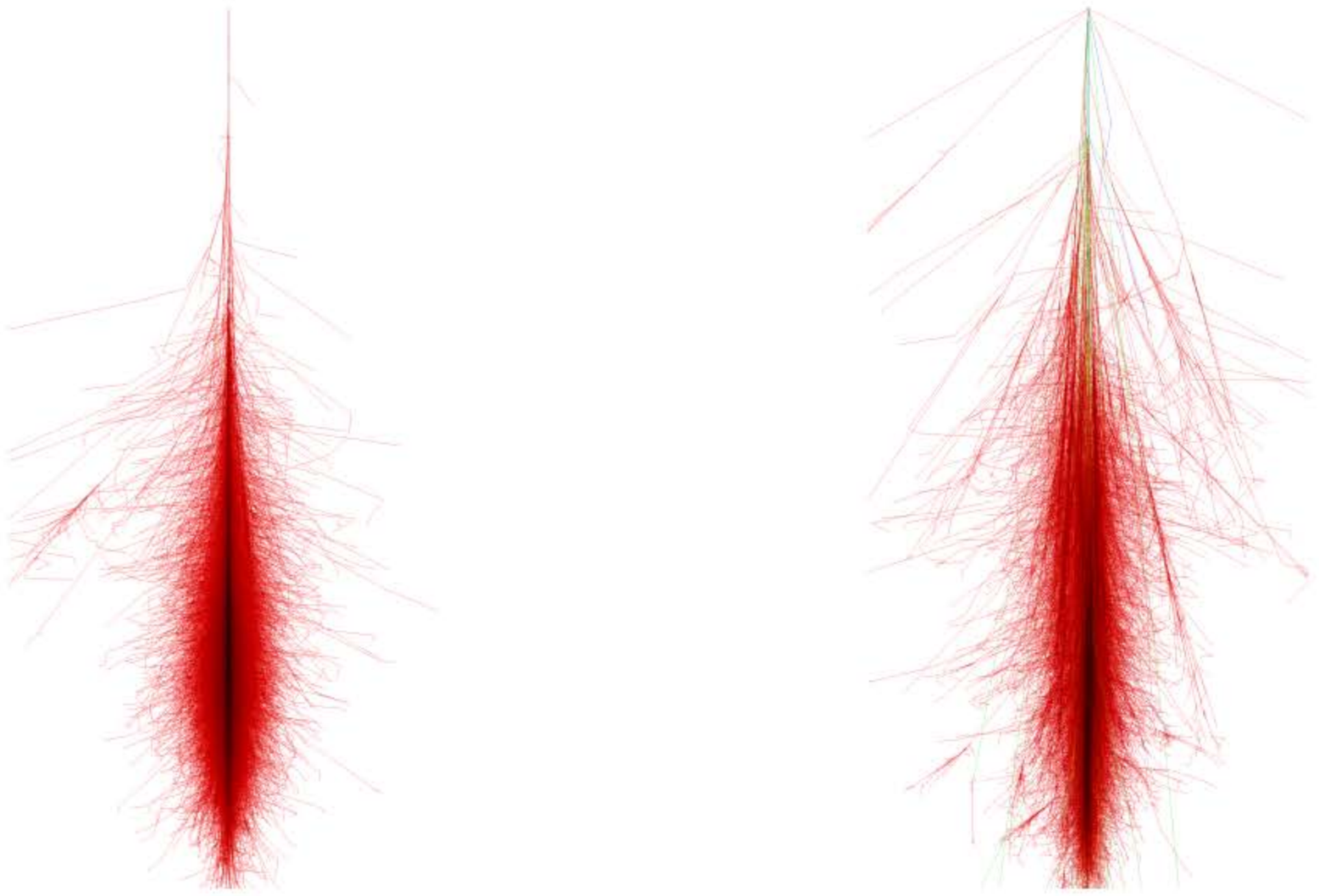

Figure 1.6: CORSIKA simulations for a EAS initiated by a $1TeV$ γ-ray photon (left) and a $1TeV$ CR (right). The shape of each particle cascade highlights the differences observed in Cherenkov shower images: hadronic particle showers are much less uniform than EM cascades and produce particles with greater transverse momentum [26].

1.3.2 Cherenkov Radiation

When a charged particle travels through a dielectric medium, the surrounding atoms and molecules become distorted due the electric field of the charged particle. The distorted atoms behave much like elementary dipoles with the electrons displaced to one side of the positive nucleus, opposing the charge of the moving particle. A polarisation field therefore forms momentarily around the charged particle as shown by Figure 1.7(a) with the charged particle at position P along the trajectory. Providing the velocity of the charged particle $v = \beta c$ (where $\beta = v/c$ and c the speed of light) is less than the phase velocity of light within the medium ($v_p = c/n$, where n is the refractive index of the medium) the polarisation field is symmetric, resulting in no net dipole within the medium. Therefore, when the polarised atoms return to their nominal polarisation state, the emitted

electromagnetic radiation from each dipole interferes destructively and no radiation is observed [28].

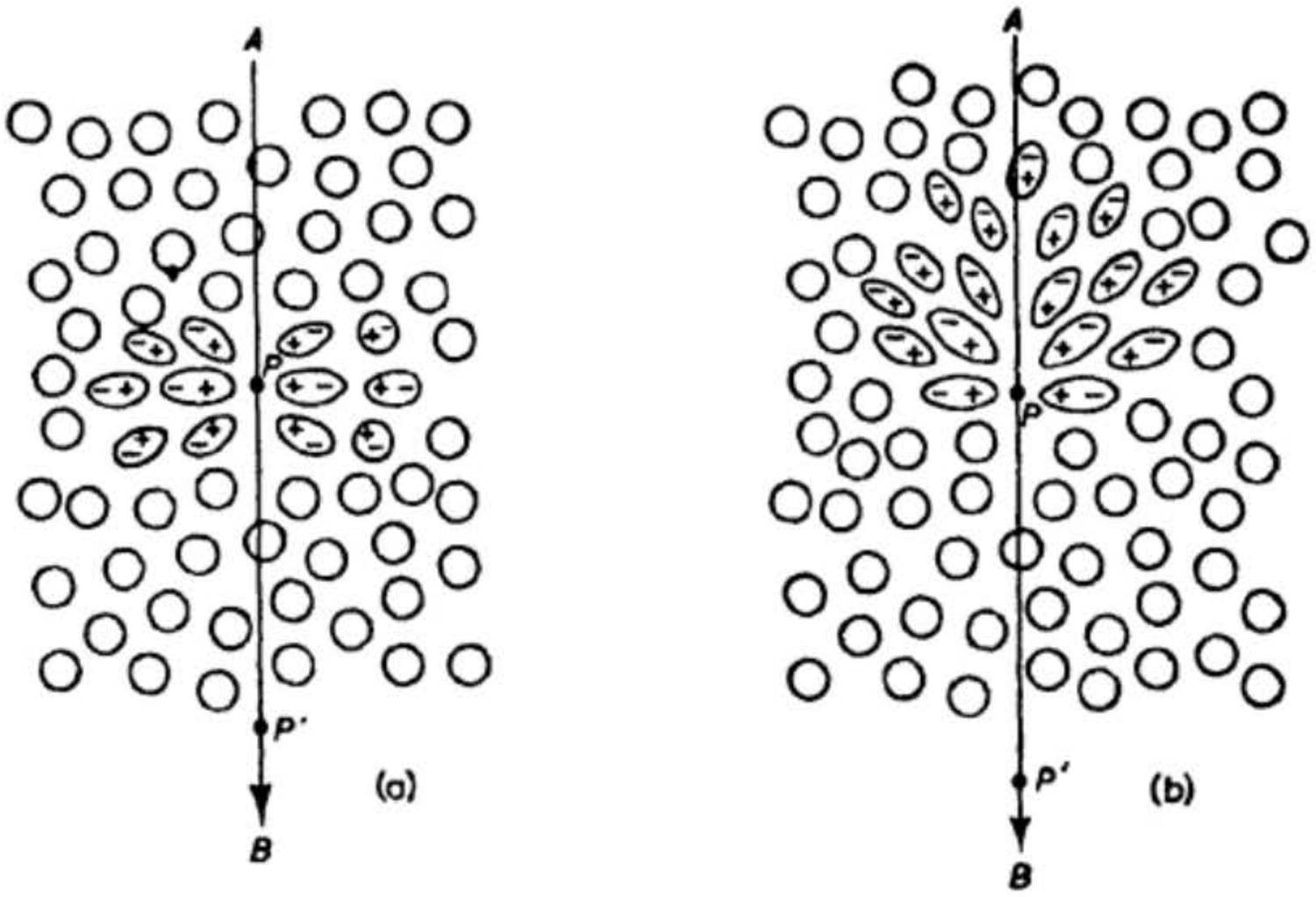

Figure 1.7: An illustration showing the polarisation induced in a dielectric medium when a charged particle moves through the medium with a velocity of $v < \frac{c}{n}$ (left) and $v \geq \frac{c}{n}$ (right) [28].

If the velocity of the charged particle is greater than the phase velocity of light within ~~such~~ the medium ($v = \beta c \geq c/n$) the polarisation induced in the surrounding atoms will be asymmetric, resulting in a net dipole field as shown by Figure 1.7(b). In this case, when the polarised atoms return to their nominal state, the emitted electromagnetic radiation will interfere constructively in the forward direction along the trajectory of the charged particle with ~~corresponding~~ opening angle ~~θ~~ θ. The opening angle describes the angle at which the wavefront is emitted from the direction of ~~a~~ relativistic charged particle, this can be seen by ~~θ~~ in Figure 1.8(a) and ~~θ in~~ 1.8(b). The radiation emitted along this plane wavefront is known as Cherenkov radiation.

It is possible to determine the opening angle of Cherenkov radiation by evaluating the geometry of the travelling charged particle as shown by Figure 1.8(a). In a time Δt, the charged particle moves a distance of $\beta c \Delta t$ along ~~it's~~ its trajectory whilst the

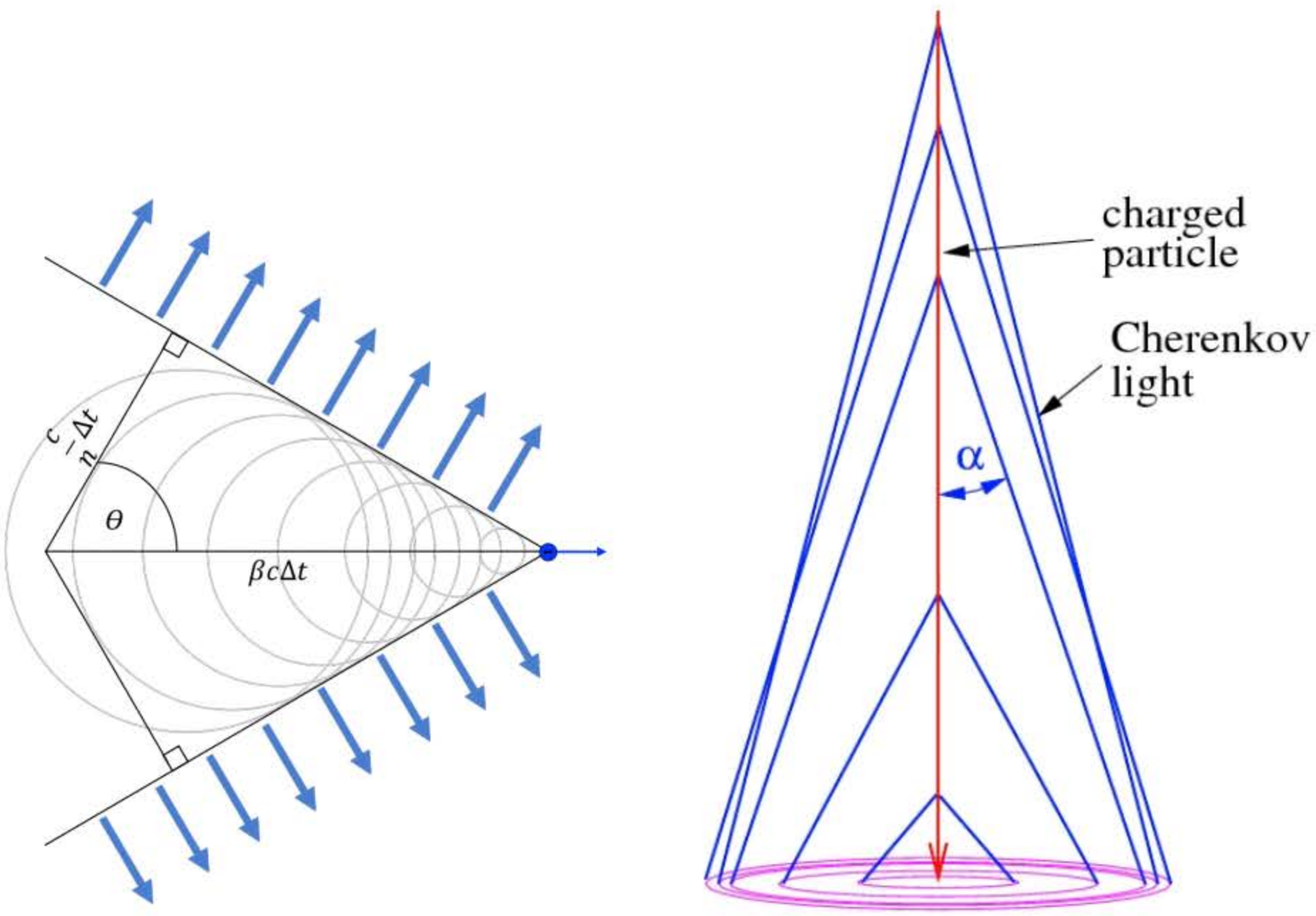

(a) (b)

Figure 1.8: Illustrations showing (a) the wave front of Cherenkov light produced as a relativistic charged particle moves through a dielectric medium [29] and (b) the cone of Cherenkov light produced by a relativistic charged particle with an increasing emission angle (α) [30].

Cherenkov radiation travels a distance in accordance to the phase velocity of light within the medium $\frac{c}{n}\Delta t$. The opening angle of the Cherenkov radiation [28] is therefore given by:

$$cos\theta = \frac{c}{vn} \quad . \tag{1.15}$$

Since the density of the atmosphere is non-uniform, the refractive index, and hence opening angle of Cherenkov radiation, varies as the charged particle travels towards ground level. The superposition of Cherenkov light produced by the relativistic charged particles in an EAS result in a cone of Cherenkov light which reaches the ground as a

Cherenkov light pool as shown by Figure 1.8(b). The radius of the Cherenkov light pool for a γ-ray initiated EAS is $\sim 125m$ and dependent on the energy of the original γ-ray. The non-uniformity of the hadronic EAS result in a much more irregular shape to the Cherenkov light pool, however, Cherenkov radiation is still observed by ground-based telescopes within this light pool.

The intensity of Cherenkov radiation (N) emitted per particle track length (x) and per wavelength (λ) can be determined by applying the Frank-Tamm formula [31]:

$$\frac{d^2N}{dxd\lambda} = \frac{2\pi\alpha Z^2}{\lambda^2}(1 - \frac{1}{\beta^2 n^2(\lambda)}). \tag{1.16}$$

where α is the fine structure constant, Z the charge of the charged particle and $n(\lambda)$ the frequency dependent refractive index. Since the intensity of Chernekov light is inversely proportional to the square of the wavelength, Cherenkov radiation tends towards shorter wavelengths. However, as the Earth's atmosphere absorbs high energy photons, the observable Cherenkov light has a wavelength of $\sim 300nm$ [32] resulting in a *blue-ish* light.

The absolute intensity of Cherenkov light produced in an EAS is determined by the summation of radiation emitted by each relativistic charged particle within the EAS. Since the number of charged particles within an EAS is dependent on the energy of the progenitor to the particle cascade, it is possible to determine the energy of the original γ-ray or CR by measuring the intensity of the Cherenkov radiation within a light pool on the ground. This forms the operational principal for the Imaging Atmospheric Cherenkov Telescope.

1.4 Imaging Atmospheric Cherenkov Telescope

Space-based γ-ray telescopes, such as the Fermi space telescope, are able to directly observe such radiation by utilising a calorimeter instrument. The large area telescope (LAT) of Fermi [33] comprises two integral components: firstly, a particle tracker which measures the path of electrons/positrons produced when a γ-ray interacts with a metal plate (via pair production); and secondly, a calorimeter consisting of stacks of Caesium-Iodide crystals. When the particles enter the calorimeter a particle shower is initiated, resulting in the energy of the initial particle being deposited within the calorimeter. As with EASs, the length of the particle shower depends on the energy of the progenitor of the cascade. It is therefore possible that the particle shower induced by a VHE γ-ray is not entirely contained within the calorimeter. This places a limit on the energy range of space-based *gamma*-ray telescopes.

As previously described, when a VHE γ-ray/CR enters Earth's atmosphere, the energy of such radiation is deposited into the atmosphere via an EAS. The atmosphere is therefore acting as a calorimeter, much like that of Fermi-LAT, but with a much higher upper energy threshold. Ground based telescopes are able to determine the energy of the initial γ-ray/CR by observing and measuring the intensity of Cherenkov radiation emitted by the relativistic particle shower. These telescopes are known as Imaging Atmospheric Cherenkov Telescopes (IACTs). An example of this imaging technique with two IACTs in the cone of a Cherenkov light pool is shown in Figure 1.9.

The first significant source detection using the IACT technique came from observations of γ-rays emitted by the Crab Nebula in 1989, by the $10m$ reflecting telescope at the Fred Lawrence Whipple Observatory [35]. This detection would give rise to the use of IACTs for the study of VHE γ-rays. Currently, the most notable observatories using

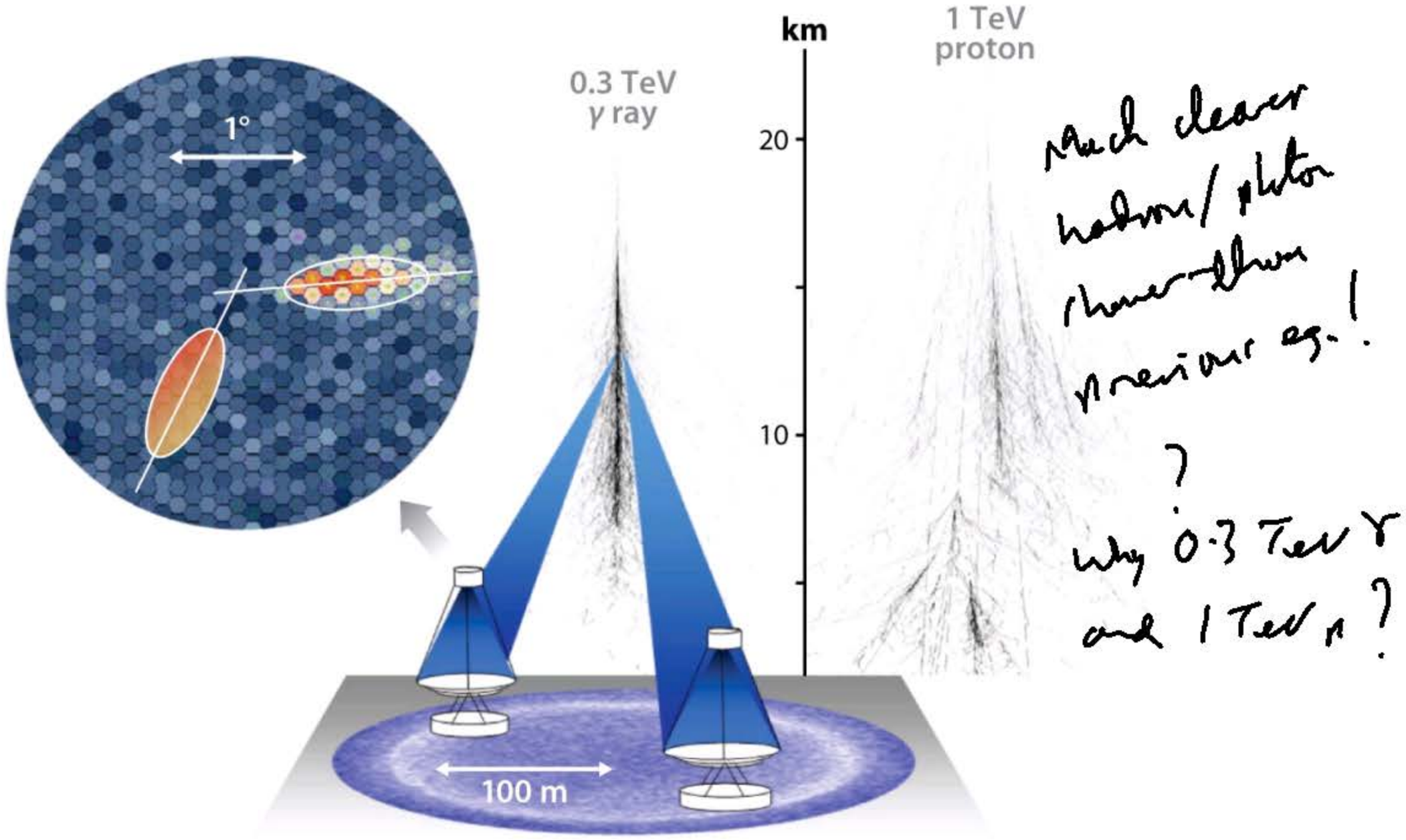

much clearer hadron/photon shower than previous eg.!

why 0.3 TeV γ and 1 TeV π?

Figure 1.9: Illustration of the IACT technique showing the Cherenkov light pool produced by the EAS initiated by a $300GeV$ γ-ray photon. The camera image observed by both IACTs is shown in addition to hadronic particle shower [34].

the IACT technique are the arrays: H.E.S.S. [36], VERITAS [37], and MAGIC [38].

The working principle of the IACT technique is simply a focusing telescope (or mirrors, see Section 2.3.1) and a camera sensitive to low intensity light in the blue and near ultraviolet electromagnetic energies. The Cherenkov light produced by an EAS has a very small timescale and relatively low intensity, comparable to the night sky background (NSB). As such, the Cherenkov imaging camera must be sensitive to very low intensities and possess high-speed readout electronics in order to capture the entirety of the Cherenkov event. The intensity of Cherenkov light within a light pool produced by an EAS is proportional to the energy of the progenitor of the particle shower. As such, the size of an IACT's primary mirror infers the targeted energy range of such telescopes; low intensity Cherenkov events initiated by low energy γ-rays require a larger collection

?
what is timescale?

(a)

(b)

(c)

Figure 1.10: The modern IACT arrays of H.E.S.S (a) MAGIC (b) and VERITAS (c).

area than higher intensity, high energy, events. The pixelated Cherenkov imaging camera placed at the focal plane of the mirror must also scale with mirror size to maintain resolution. In addition, the collection area, and number of telescopes, of an IACT array must increase for observations at higher energies since the flux of γ-rays decreases with increasing photon energy. More telescopes spread over a larger footprint increases the probability of observing high energy events.

The Cherenkov imaging camera utilises a high gain photomultipliers and high speed digitising electronics to directly image the Cherenkov light produced by an EAS.

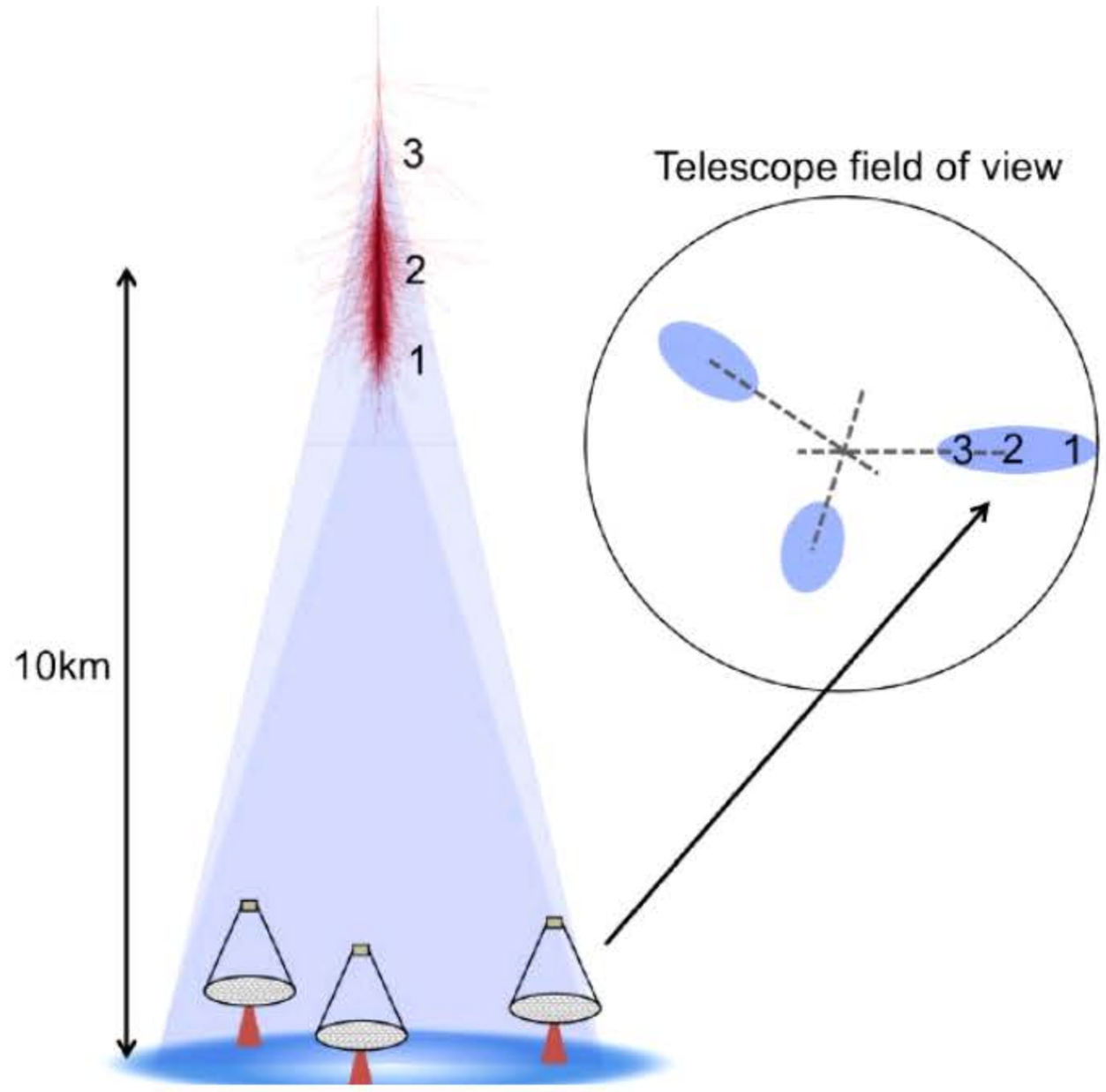

Figure 1.11: An illustration of stereoscopic observations for IACTs. The shower images observed by each of the telescopes in the Cherenkov light pool is shown by the inset diagram. The major axis of each Cherenkov ellipse is used to determine the arrival direction of the particle shower [39].

The emission angle of Cherenkov photons from the particle shower depends on the position (height) at which the photons were produced. This variation in emission angle produces varying incident angles with the telescope mirror, which results in Cherenkov photons interacting with the Cherenkov camera focal plane at different pixel positions. The uniform shape of the γ-ray induced EAS, and Cherenkov light pool, produces a shower image on the camera surface. The shape of this Cherenkov image corresponds directly to the characteristics of the EAS as shown by Figure 1.11. The ellipticity of the camera image describes the direction of the EAS in relation to the telescope pointing position: circular images are produced by on-axis Cherenkov events and elliptical images by off-axis events. The use of event timing can be used to portray the evolution of the particle shower as the Cherenkov light traverses the camera focal plane (see Figure 4.28). The intensity and

source direction of the EAS can then be determined by analysing the shape of the ellipses. This analysis technique was first proposed by A. M. Hillas [40] and is described further in Section 5.4.

Each of the IACT arrays shown in Figure 1.10 operate under stereoscopic observations, meaning they are comprised of multiple telescopes (5, 2, and 4 telescopes respectively) with each telescope observing the same γ-ray source. Stereoscopic observations greatly improve the performance of an IACT array by improving the shower reconstruction and background rejection when compared to that of a single telescope. Figure 1.11 shows three IACTs within the Cherenkov light pool of a γ-ray induced EAS. Each of the three telescopes produce an elliptical shower image, the shape of this ellipse depends on the direction and angle of the EAS with respect to the individual telescope. By overlaying the shower images and extending the major axes of each ellipse (as shown by the inset diagram), it is possible to find the arrival direction of the EAS and, hence, the arrival direction of the primary γ-ray [41]. In addition to the direction of the shower, the energy reconstruction from each telescope is averaged to provide a more accurate value for the shower and progenitor energy.

As the intensity of Cherenkov light produced by an EAS is relatively low, each Cherenkov camera in an IACT array must self-trigger at low intensities. It is therefore possible for a camera trigger to be produced by the NSB. Section 2.4.3 describes the trigger logic utilised to prevent such triggers. With stereoscopic observations, one can adopt an array-level trigger logic to further reduce background triggers. Coincident events must be observed across all cameras for such triggers to occur [43]. With NSB triggers minimised, the largest source of background light is the Cherenkov light produced in CR initiated EASs. It is possible to discriminate between CR and γ-ray induced showers through the parameterisation of the shower image as the image of a CR shower is much less symmetrical and broad in shape. However, muons produced in a hadronic EAS represent a further source of background Cherenkov light. Relativistic muons produced in such

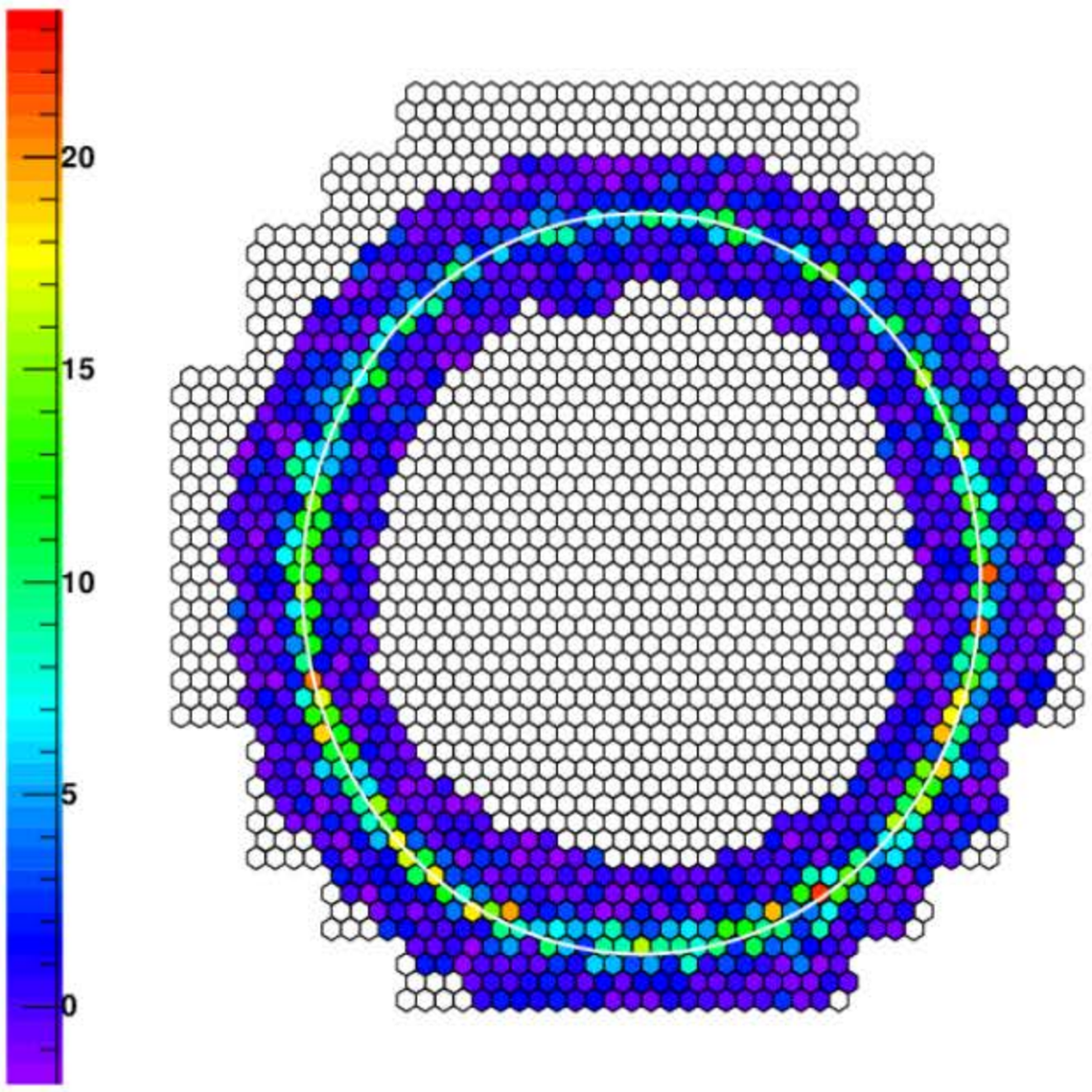

Figure 1.12: An example of a muon ring observed by the CT5 camera of the H.E.S.S. array. The colour scale indicates the photoelectron charge per pixel following calibration [42].

Muon rings due to interaction in atmosphere.

showers can reach the surface and interact with the structure of an IACT, the Cherenkov light cone produced in such interactions is focused by the telescope mirrors and imaged by the Cherenkov camera [44]. The shower image produced by a muon takes the shape of a ring as shown by Figure 1.12 whereby the radius of the ring is proportional to the energy of the muon. Such muon rings are indeed background events, but they do provide an opportunity for the calibration of the optical efficiency of a camera and telescope mirrors [45] as variations in pixel intensities across the ring would suggest less efficient pixels.

! Direct muon calibration ?

1.5 Thesis Outline

The focus of this thesis is on the silicon photomultiplier (SiPM) based Compact High Energy Camera (CHEC-S), the prototype Cherenkov imaging camera designed for the small-sized telescope of the Cherenkov Telescope Array (CTA). I begin by providing an

overview of CTA with a discussion of the scientific goals, array requirements and array composition of both northern and southern hemisphere sites in Chapter 2. I then give a detailed description of CHEC-S with a focus on the design and utilisation of the front end electronic (FEE) chain, including the SiPM, shaping electronics, and the trigger and digitising application specific integrated circuits (ASICs).

The various tasks that I had conducted upon first joining the CHEC team are described in Chapter 3. I start by discussing the build and assembly of CHEC-S, including the initial verification of electronic components with simple power and communication testing, before CHEC-S was shipped to the Max-Planck Institute for Nuclear Physics for further verification. I then discuss the full camera verification tasks undertaken at MPIK during a number of visits to the institute in collaboration with other members of the CHEC team. Finally, I describe a number of investigations completed at the University of Leicester with the use of a single FEE chain.

Chapter 4 outlines the improvements that I have made to the calibration procedure of the CHEC-S digitising ASIC (TARGET-C). I begin by describing the composition and structure of the ASIC before providing a discussion of the pedestal calibration required for digitised data. I then discuss the calibration of the TARGET-C analogue-to-digital converter (ADC) resulting in a transfer function (TF) lookup table containing the conversion of ADC counts to voltage. I present a new method for the generation of a TF calibration dataset which I have developed to further improve the accuracy of the such calibration. I then describe the effect of temperature on the TF calibration and outline a method for correcting the temperature dependence. Finally, I detail an investigation of the saturation regime of the digitising ASIC before describing the method I have developed for the correction of saturated waveforms and the performance gained by adopting this method.

In Chapter 5, I provide a description of the on-telescope campaigns performed

with CHEC-S installed on the ASTRI-Horn telescope on Mt. Etna, Sicily. I begin by outlining the operation of CHEC-S during on-telescope observations before describing the Hillas analysis technique utilised in the observations of Cherenkov showers. I then describe the occurrence of triggered events that seemingly do not contain Cherenkov shower images and propose a method for their production determined by analysing the digitised data from such events. Finally, I show the application of the saturation correction procedure I developed on high intensity Cherenkov shower events containing saturated waveforms.

Chapter 2

Cherenkov Telescope Array

Contents

2.1 Introduction

The Cherenkov Telescope Array (CTA) [46] is the next generation ground based γ-ray observatory designed to build upon the knowledge and experience gained throughout the operation of current IACT arrays (see Figure 1.10). The CTA consortium consists of $\sim$ 1500 members from more than 150 institutes in 25 countries (at the time of writing) with many members associated with the existing IACT arrays.

The design of CTA consists of $\sim$ 100 Cherenkov telescopes covering a few square kilometres at two array sites; one at the Roque de los Muchachos Observatory on La Palma, Spain, and the other $10km$ southeast of the Paranal Observatory in the Atacama Desert, Chile. In addition to this, CTA comprises three telescope sizes: a large sized telescope (LST), medium sized telescope (MST) and small sized telescope (SST). The advancements adopted in telescope design, camera technologies, and the shear number of telescopes proposed will improve the sensitivity of γ-ray observations by an order of magnitude when compared to current IACTs and extend the energy range at which γ-rays are observed. In this chapter, I will first discuss the aims of CTA and the requirements imposed on each telescope to ensure these aims are achieved, before covering the array and telescope composition. I will then discuss the Compact High Energy Camera (CHEC), giving a description of the various electronic components with further detail on the front-end electronics (FEE) as theses components represent a great focus of my research.

2.2 Science and Performance Goals

CTA will expand upon the current generation of IACTs by operating two arrays in both the northern and southern hemispheres. It will improve the sensitivity of observations by an order of magnitude at $1TeV$ when compared to MAGIC, HESS and Veritas, as shown by Figure 2.1 [47]. In addition to this, the large collection area and array size will significantly

increase the rate at which Cherenkov photons are observed. More advanced telescope and Cherenkov camera technologies will produce greater angular resolution and field of view (FoV) in an extended energy range of $20GeV$ to at least $300TeV$, providing the ability to observe extended and high redshift sources with greater accuracy than previously possible.

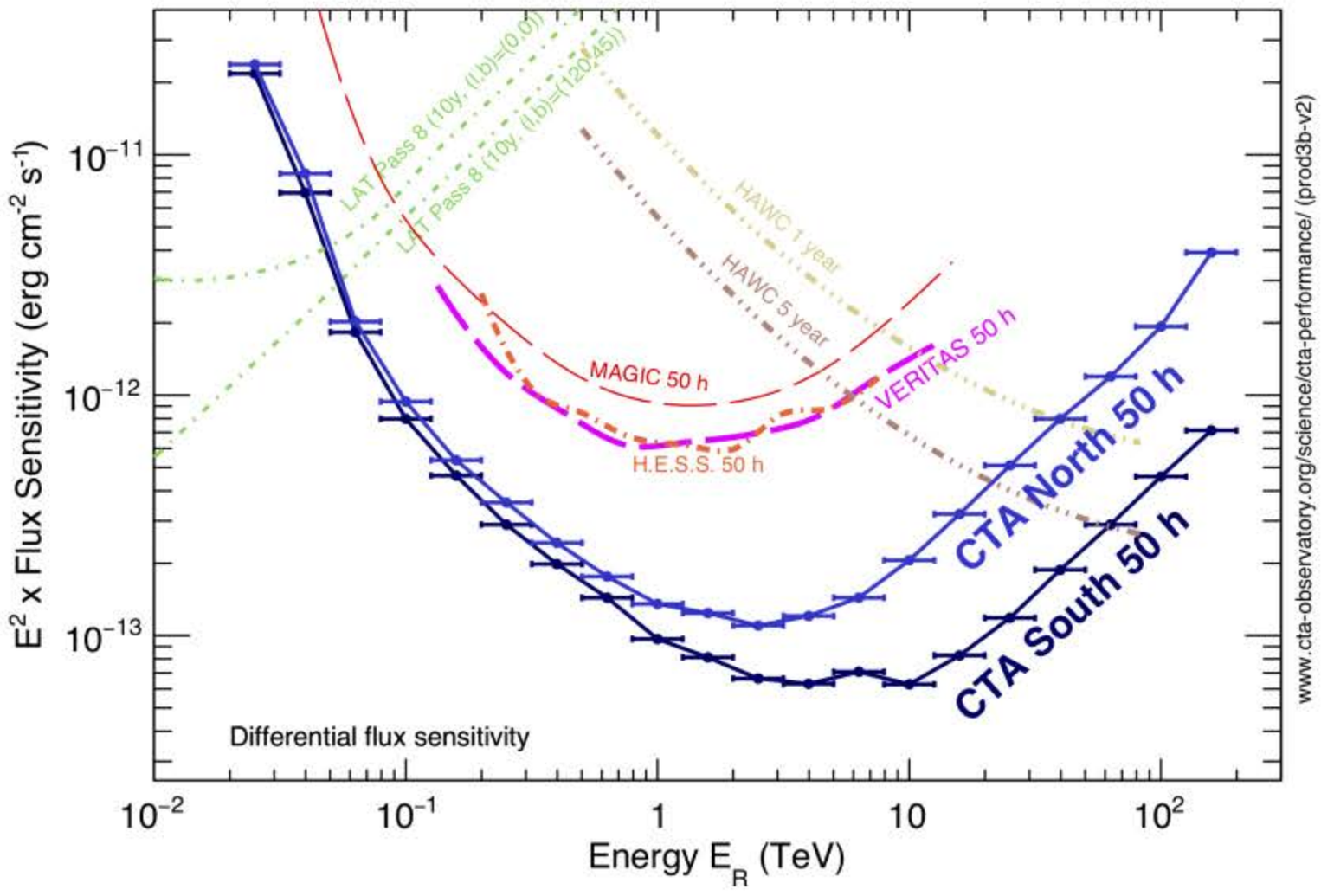

Figure 2.1: The simulated performance of CTA compared with existing gamma-ray experiments. The plot shows the differential energy flux sensitivity of the North and South arrays after 50 hours of observations. The overlapping sensitivity of multiple instruments allows for further validation and cross checking when observing gamma-ray sources.

CTA will be the first observatory of it's kind to operate as an *open observatory*, meaning observations will be on a proposal basis which should produce higher scientific output by the wider γ-ray astronomy field. Finally, the large number of telescopes will greatly enhance the surveying and monitoring capability of CTA whilst allowing for the observation of multiple sources with a subset of telescopes. Both HESS [48] and MAGIC [49] have proven the use of IACTs in multi-messenger astrophysics with observations of gamma-ray bursts (GRBs) after an initial detection by the FERMI and SWIFT space telescopes. By operating in both the northern and southern hemispheres, CTA will observe the entire sky and provide greater opportunities for the study of multi-messenger

astrophysics. In addition to this, CTA will be operate simultaneously with many new and next generation instruments such as: gravitational wave observatories LIGO and Virgo; Neutrino telescopes IceCube-Gen2 and KM3NeT; and many more. The synergy between these next generation instruments will significantly impact multi-messenger and transient astrophysics [50].

With an improved performance, collection area and all-sky capabilities, CTA aims to address many of the current questions find in very-high energy astrophysics. These questions have been categorised into three themes [47]:

1. Understanding the Origin and Role of Relativistic Cosmic Particles.
2. Probing Extreme Environments.
3. Exploring Frontiers in Physics.

As described earlier, the observation of γ-rays is primarily to gain further understanding of the mechanisms and environments giving rise to such photons ultimately so that one may understand the production and acceleration of cosmic rays (CRs) within these environments. CTA also aims to further explore the role of CRs in the formation of stars and galaxy evolution.

Observations of the most extreme environments, such as those ~~in proximity~~ around of neutron stars and black holes, will improve our understanding of physical processes present in such environments. CTA aims to achieve this by observing γ-rays produced by relativistic jets emanating from active galactic nuclei (AGN) [51]; pulsed emission from fast rotating pulsars; and those produced in the shock around supernova remnants (SNRs) and colliding wind binary systems. By observing the spectra of extragalactic sources, it is possible to probe the cosmic voids and subsequent radiation and magnetic fields giving rise to the intergalactic magnetic field (IGMF). Observations of this kind will help determine the interaction processes within cosmic voids [52].

Finally, with the extended energy range and increased sensitivity of CTA, it will probe the frontiers of astrophysics with the aim of observing unexplained phenomenon which may provide answers to the many open questions of fundamental physics. Dark matter (DM) constitutes $\sim 27\%$ [47] of the total energy in our Universe and represents a key target for CTA. The relative abundance of DM shapes the evolution of galaxies and cosmic structures through gravitational effects. The most promising particle candidate for DM is the weakly interacting massive particle (WIMP) with a rest mass between a few tens of GeV to a few TeV [53]. CTA aims to determine the abundance of WIMPs through the observation of γ-rays produced when DM particles annihilate, an abundance of WIMPs correlating with DM observations would confirm this theory [47]. Axions, or Axion-like particles (ALPS), represent another candidate for DM particles predicted by extensions to the standard model (SM) [54]. As extragalactic γ-rays traverse the intergalactic medium, they may interact and couple with ALPs under the influence of the IGMF [55]. Since γ-rays are attenuated via the scattering of photons within the extragalactic background light (EBL), ALP-photon coupling would reduce the effect of EBL absorption resulting in a detectable enhancement to the extragalactic γ-ray spectrum [56]. The observation of WIMPs or ALPs through their interactions with γ-rays would indicate the detection of dark matter and provide a remarkable breakthrough in our understanding of the physical universe.

Theme		Question	Dark Matter Programme	Galactic Centre Survey	Galactic Plane Survey	LMC Survey	Extra-galactic Survey	Transients	Cosmic Ray PeVatrons	Star-forming Systems	Active Galactic Nuclei	Galaxy Clusters
Understanding the Origin and Role of Relativistic Cosmic Particles	1.1	What are the sites of high-energy particle acceleration in the universe?		✔	✔✔	✔✔	✔✔	✔✔	✔	✔	✔	✔✔
	1.2	What are the mechanisms for cosmic particle acceleration?		✔	✔	✔		✔✔	✔✔	✔	✔✔	✔
	1.3	What role do accelerated particles play in feedback on star formation and galaxy evolution?		✔		✔				✔✔	✔	✔
Probing Extreme Environments	2.1	What physical processes are at work close to neutron stars and black holes?		✔	✔	✔			✔✔		✔✔	
	2.2	What are the characteristics of relativistic jets, winds and explosions?		✔	✔	✔	✔	✔✔	✔✔		✔✔	
	2.3	How intense are radiation fields and magnetic fields in cosmic voids, and how do these evolve over cosmic time?					✔	✔			✔✔	
Exploring Frontiers in Physics	3.1	What is the nature of Dark Matter? How is it distributed?	✔✔	✔✔		✔						✔
	3.2	Are there quantum gravitational effects on photon propagation?						✔✔	✔		✔✔	
	3.3	Do Axion-like particles exist?					✔	✔			✔✔	

Figure 2.2: Matrix of CTA science questions and proposed Key Science Projects (KSPs). The KSPs are sets of observations addressing multiple science questions within the CTA themes.

As stated previously, CTA observations will either be conducted as open observations via guest proposals or in accordance with the consortium's *Core Programme*. CTA's core programme will account for 40% of the overall observation time over the first year and consists of nine *Key Science Projects* (KSPs) [47]. Each of the KSPs corresponds to an observation source category or survey with the aim of addressing the science questions connected to the three themes of CTA described before. Figure 2.2 shows the KSPs representing the core programme of CTA in addition to the science questions and themes each KSP will contribute towards. The data obtained during the CTA core programme will be available to non-CTA members following a predefined period (∼1 year). Detailed information concerning each of the CTA KSPs can be found in *Science with the Cherenkov Telescope Array* (CTA consortium, 2018) [47].

2.2.1 Requirements

The performance of CTA is pivotal in ensuring that each of the science goals and questions are addressed, CTA has imposed a large number of requirements that each telescope must adhere to in order to ensure the performance and capability of exploring the KSPs. The requirements cover various aspects including: the performance of the telescope array under varying environmental conditions (temperature, humidity, high winds and earthquakes); the performance of the telescope structure in terms of pointing accuracy and target acquisition time; the response of the Cherenkov imaging camera under high night sky background (NSB) conditions, including operation under moonlight; and finally, there are requirements concerning the format and usability of the digitised and calibrated data following a Cherenkov light event. For a telescope to be accepted as an in-kind contribution, the structure and camera subsystems must surpass each requirement and be able to prove the reliability of the instrument for the duration of the array lifetime. The CTA requirements are currently accessed via the CTA Jama website [57], however, this is set

to change Q1 2022.

The focus of my research presented in the following Chapters largely concerns the performance of the silicon photomultiplier (SiPM) Cherenkov camera prototype (CHEC-S) designed for the small sized telescope (SST). The primary goal in characterising CHEC-S is to assess the performance of the camera electronics; analysis and calibration pipeline; and structural design with respect to the corresponding requirements imposed by CTA. The assessment of CTA requirements in regards to CHEC-S performance was conducted by many members of the SST Camera team through the analysis of data taken with a fully populated CHEC-S or a subset of camera electronics.

Whilst the research presented in this thesis contributes to the overall characterisation of CHEC-S, the only direct comparison to a CTA requirement is with that of requirement **B-TEL-1010**. This requirement is further described in Section 4.6 and relates to the fractional charge resolution of CHEC-S front-end electronics (FEEs); a measure of the performance of the SiPM, digitising electronics, calibration, and event reconstruction by comparing the expected photoelectron (p.e.) level to that of the extracted p.e. level. In Section 4.6 **B-TEL-1010** is used to compare the charge resolution performance of CHEC-S before and after the application of a saturation recovery algorithm. In addition to this, **B-SST-1680** provides the justification for the investigation into the performance of the FEE chain under varying night sky background (NSB) conditions outlined in ??. **B-SST-1680** describes the NSB conditions under which each telescope must be able to observe γ-ray induced Cherenkov radiation.

2.3 Array Composition

CTA will cover a more extensive energy range of $20GeV$ to $300TeV$ when compared with current IACTs, as shown by Figure 2.1, this vast energy range necessitates the use of three

sizes of telescopes. The telescope composition of CTA is as follows:

- The Large Sized Telescope (LST), consisting of a single parabolic reflecting surface with a diameter of $23m$, an on-axis point spread function (PSF) of $0.05°$ and a field of view (FoV) of $4.3°$ [58]. The LST will utilise a large camera comprising 1855 photomultiplier tube (PMT) pixels to observe low energy Cherenkov light events between $20GeV$ and $200GeV$ [59].

- The Medium Sized Telescope (MST) represents the second largest of the three telescope sizes, of which two designs currently exist. Firstly, the further advanced, modified Davies-Cotton layout with a $12m$ diameter reflecting surface [60] and two proposed Cherenkov cameras: FlashCam [61] and NectarCam [62]. The two Cherenkov cameras contain 1764 and 1855 PMT pixels with a FoV of $7.5°$ and $7.7°$, respectively. The second, and less developed, MST design is that of the dual-mirror Schwarzschild-Couder Telescope (SCT) [63]. The SCT consists of a $9.7m$ diameter primary reflecting surface and a $5.4m$ diameter secondary mirror. This design allows for the use of a smaller Cherenkov camera comprising $11,328$ SiPM pixels with a FoV of $7.6°$: similar to that of the MST despite the variation in mirror diameter and camera size. Both variations of the MST will observe showers in the core energy range of CTA between $150GeV$ to $5TeV$

- The Small Sized Telescope (SST) utilises a Schwarzschild-Couder, dual-mirror design housing a $4.3m$ primary mirror and $1.8m$ secondary mirror [64]. As with the SCT MST, the dual-mirror design of the SST structure allows for a smaller Cherenkov camera. The SST Camera will consist of 2048 SiPM pixels thermally coupled to a liquid cooled focal plane, producing a $\sim 9°$ FoV and $\sim 0.1°$ PSF [65]. The SST will observe the highest energy Cherenkov showers between $\sim 1TeV$ and $300TeV$.

The PSF and FoV are both commonly used parameters which describe the optical performance of each telescope. In the absence of atmospheric turbulence, the response of any

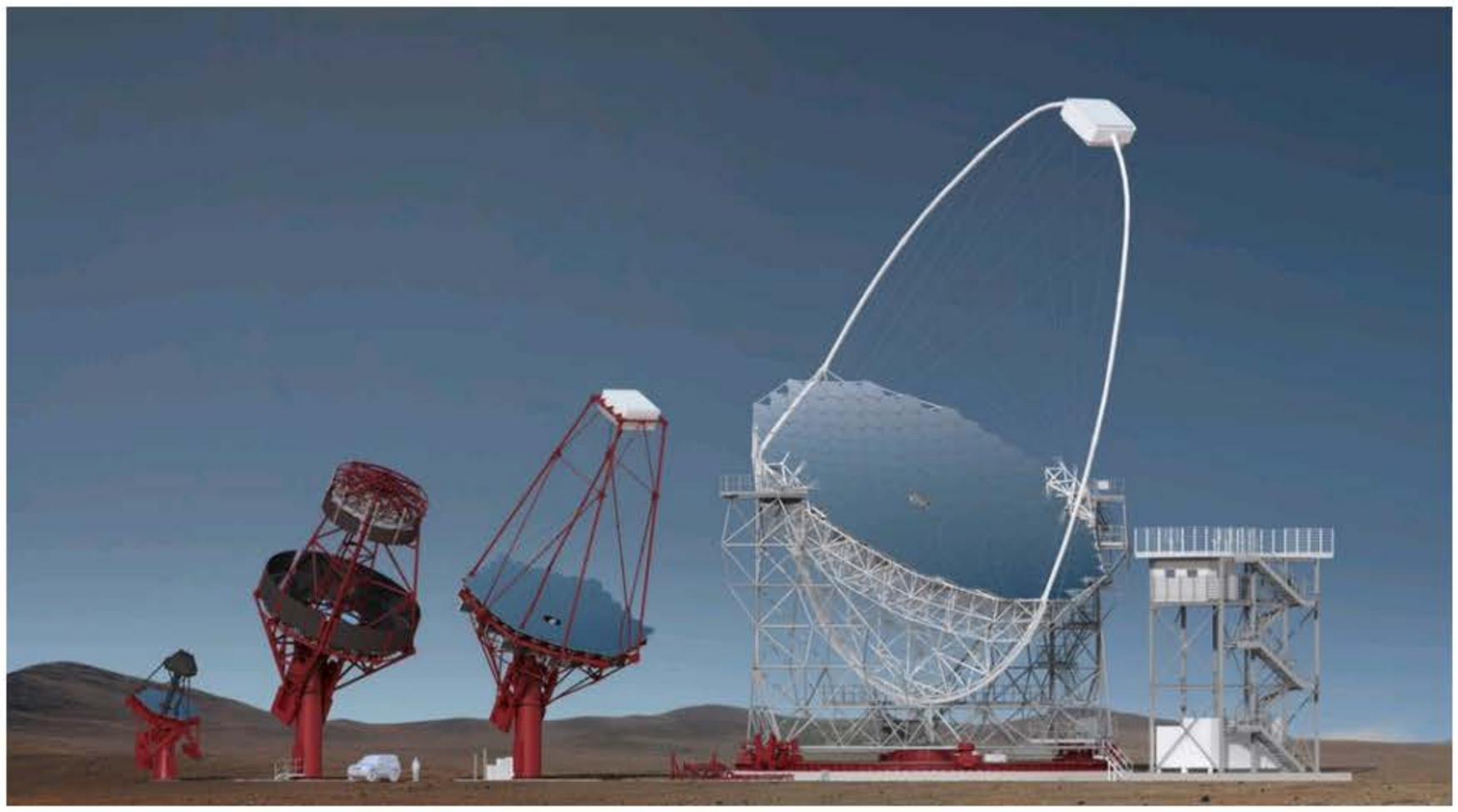

Figure 2.3: A rendered image of the proposed telescopes for CTA providing a comparison of the SST-2m, PSCT, MST and LST telescopes. A notable comparison of the PSCT and MST structures is shown, the impact of using a dual-mirror structure is observed by the difference in mirror diameter [66]

telescope is extended due to the diffraction of light caused by the telescope aperture, the extent of this diffraction is described by the PSF of a telescope. Atmospheric turbulence and mirror aberrations broaden the PSF; telescopes of this kind are therefore diffraction limited and the PSF describes the absolute limit of optical performance and angular resolution. The FoV simply describes the area of sky observable for each telescope.

Figure 2.3 shows a comparison of the three telescope sizes of CTA including both variants of the MST (SCT and MST). As stated previously, the size of each telescope is indicative of the energy range in which each telescope is most sensitive. The intensity of Cherenkov light produced following an EAS is dependent on the energy of the shower progenitor, γ-rays and CRs with higher energy will produce more populated particle cascades and therefore, more intense Cherenkov light pools. Low energy particle cascades result in less intense Cherenkov events, large telescope mirrors are required to collect this and focus it toward the Cherenkov camera. Similarly, the electronics and photosensors for each Cherenkov camera is optimised so that the greatest performance can be achieved

within the specific energy range for each telescope size.

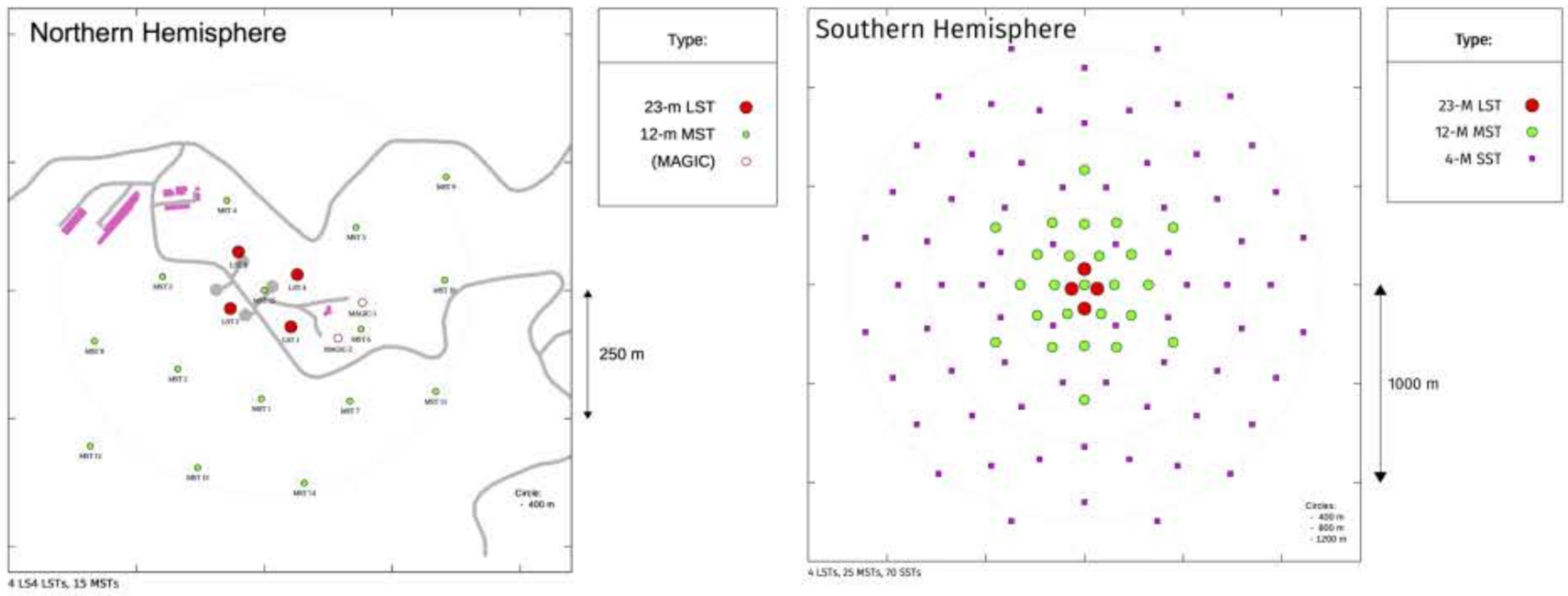

Figure 2.4: Images showing the currently proposed layout of the CTA-North (left) and CTA-South (right) arrays. The layout of each array was chosen by evaluating the simulated performance of varying configurations [67].

CTA will deploy the three telescopes across two array sites: CTA-South in the Atacama Desert of Chile, $10km$ southeast of the European Southern Observatory's (ESO's) Paranal Observatory; and CTA-North at the Observatorio del Roque de los Muchachos on the island of La Palma, home to the existing IACT MAGIC. The layout and composition of the two CTA array sites has been optimised through Monte Carlo simulations to produce the greatest performance possible for the proposed configuration [68]. Figure 2.4 shows the baseline layout for both CTA-North and CTA-South, the composition and layout of these arrays can be used to indicate the expected operation of CTA.

The baseline composition of CTA-South comprises four LSTs, twenty-five MSTs and seventy SSTs spread across an area of $4km^2$. With the use of all three telescope sizes, CTA-South will observe the southern celestial hemisphere across the entire CTA energy range covering the galactic centre and galactic γ-ray sources. As stated previously, the intensity of Cherenkov light produced in a particle shower is proportional to energy of the shower progenitor and as such, the size of the LST mirror is required to observe the lowest energy Cherenkov light events. However, since the flux of low energy γ-rays is relatively high only four telescopes of this kind are required. Conversely, a larger number of SSTs

are required to observe the high energy, high intensity events. The lower frequency of such events provides the necessity for a large number of SSTs covering a vast collection area when compared to the LST and MST.

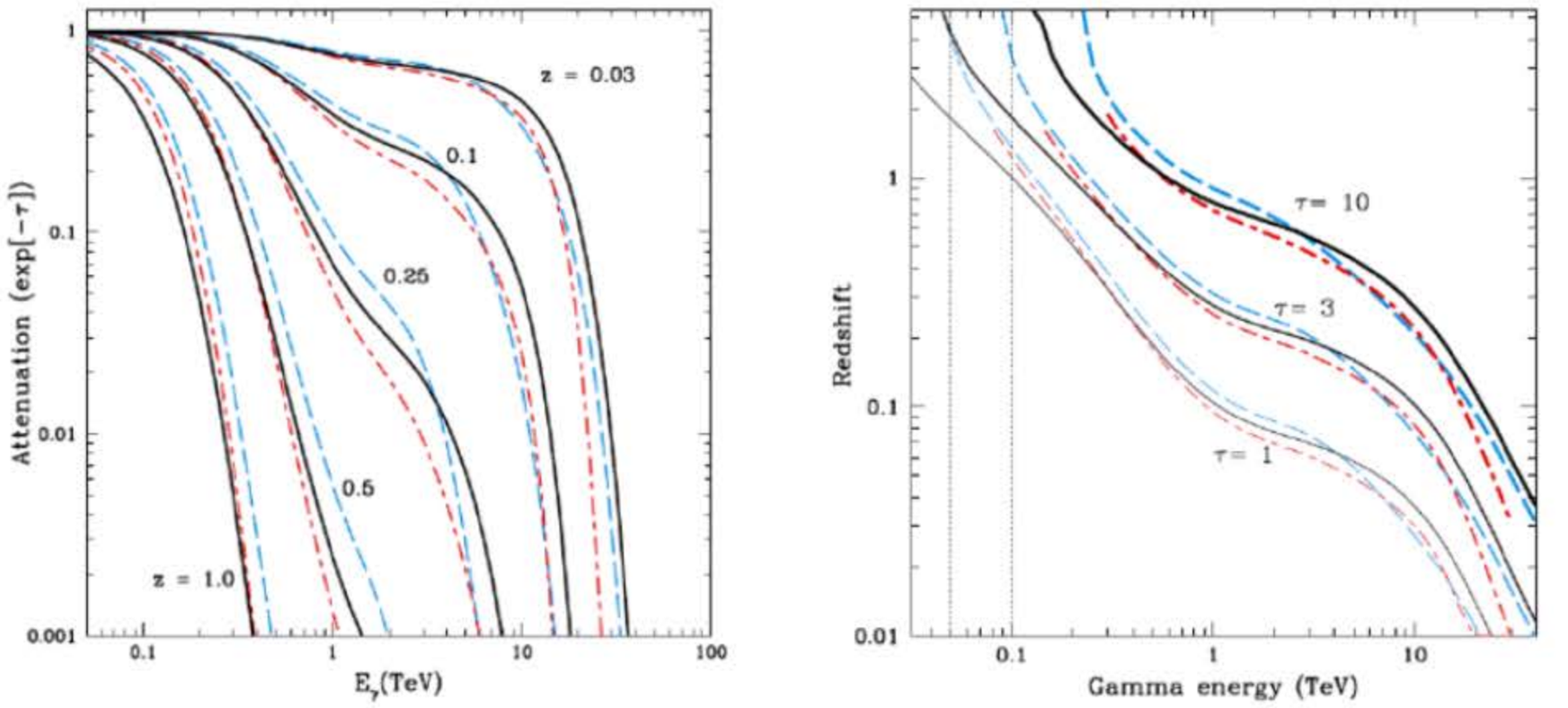

Figure 2.5: Left: The attenuation of gamma-rays at a given photon energy, E_γ, for sources at redshifts of 0.03, 0.1, 0.25, 0.5, and 1.0. The three lines shown in the plot indicate the models used by Primack et al [56]. Right: The gamma-ray attenuation edge produced by the same modules used in the left plot. The curves show the redshift at which the pair-production optical depth reaches the value 1, 3, or 10 as a function of E_γ.

CTA-North will consist of four LSTs, fifteen MSTs, and no SSTs in its baseline configuration. As shown in Figure 2.4, the CTA telescopes will be positioned surrounding the existing MAGIC telescope array. The construction of CTA-North began 9th October 2015, with the inauguration of the first LST telescope (LST-1) on 10th October 2018. In addition to telescope size indicating the observable energy range and target sources, the location of CTA-North and the exclusion of the SST can also be used to illustrate the sources observable to the northern array. The exclusion of the smallest telescope limits the energy range of CTA-North to $20GeV$ - $20TeV$ with the use of LSTs and MSTs alone. The reason for this is the attenuation of VHE γ-rays through photon-photon pair production as γ-rays traverse through background photon fields such as the EBL, which therefore attenuates the γ-ray spectrum when observing extragalactic sources [56]. Figure 2.5 shows the attenuation of γ-rays emitted by sources at varying redshift (z), it can

be seen that the greater the distance to the source, the higher the attenuation of emitted radiation. In addition, it can be seen that the attenuation of γ-rays is greater for increasing photon energies. As CTA-North will observe the northern celestial hemisphere, targeting extragalactic sources, the attenuation of higher energy γ-rays from such sources removes the necessity for the SST.

2.3.1 Small Sized Telescope

Originally, the conceptual design of CTA comprised three unique solutions for the SST shown by Figure 2.6. The use of three SST designs for CTA was adopted to increase prototyping and implementation effort across multiple project teams whilst also responding to the requirements imposed on the funding received by the project teams [65]. The three solutions for the SST implementation are as follows:

- SST-1M, utilising a single mirror Davies-Cotton (DC) layout with a $4m$ diameter segmented reflecting surface, achieving an effective collection area of $6.47m^2$ [69]. The SST-1M Camera utilises a photo-detection plane (PDP) containing 1296 SiPM pixels arranged in 108 modules [70] in conjunction with a novel fully digital readout and trigger system - DigiCam [71]. The design of the DigiCam electronics enables the continuous digitisation of the analogue signal produced by the PDP. This signal is then utilised in the event triggering and readout scheme. The mechanical design of the SST-1M telescope structure necessitates the use of a large Cherenkov camera. As such, the SST-1M Camera is constructed with a hexagonal shape with a diameter (vertex-to-vertex) of $1120mm$ and length $735mm$ and a mass of $\sim 200kg$

CITATION

- SST-2M Astrofisica con Specchi a Tecnologia Replicante Italiana (ASTRI) ~~comprises~~ a dual-mirror Schwarzschild-Couder [72] telescope with primary and secondary mirror diameters of $4.3m$ and $1.8m$ respectively, producing an effective

collection area of $\sim 8m^2$ [73]. The ASTRI Camera utilises a curved focal plane comprising 37 photo detection modules (PDMs). Each PDM contains 64 SiPM pixels, arranged in a 8x8 pixel array, connected to the FEEs and housekeeping field programmable gate array (FPGA) [74]. The main component of the ASTRI Camera FEEs is the EASIROC [75] assembly specific integrated circuit (ASIC), which is designed to interface with SiPM pixels. EASIROC is responsible for the triggering and shaping of the analogue SiPM output. Unlike other FEEs proposed for CTA, EASIROC integrates the analogue signal to produce a single value for the amplitude of this integration. This method is used to reduce the volume of data produced by the Cherenkov camera. The integrated amplitude is then fed through one of two voltage sensitive low noise pre-amplifiers: one high-gain and the other low gain [76]. The use of high and low gain preamplifiers produces a dynamic range of $1 - 2000$ photoelectrons without the need for saturation recovery (See 4.6). The use of a Schwarzschild-Couder layout telescope structure allows for a smaller form factor Cherenkov camera. The mechanical design of the ASTRI Camera follows a truncated-cone shape with dimensions $560mm$ x $500mm$ x $500mm$ and a total mass of $50kg$ [74].

- SST-2M Gamma Cherenkov Telescope (GCT), also utilising a dual-mirror Schwarzschild-Couder telescope structure with primary and secondary mirror diameters of $4m$ and $2m$, producing an effective collection area similar to that of the ASTRI telescope [77]. The camera designed for GCT is the Compact High Energy Camera (CHEC) and currently consists of two prototypes. The first prototype, CHEC-M, comprises 32 camera modules each containing a 64 multi-anode photomultiplier (MAPM) connected to a FEE module via a preamplifier buffer board. The CHEC-M FEEs utilises four TARGET ASICs [78] responsible for the triggering and digitisation of the shaped analogue signal produced by the photosensors. Contrary to the EASIROC ASIC used by the ASTRI camera, the TARGET 5 ASIC used by

CHEC-M samples the analogue photosensor waveform at $1GSample/s$, storing each waveform sample in a deep analogue ring buffer array comprising 16384 samples. Following a successful trigger, the TARGET 5 ASIC digitises a section of the ring buffer with a programmable window width (usually $96ns$). With this implementation, it is possible to readout full waveform events from CHEC-M [79]. The second GCT camera prototype, CHEC-S, utilises similar mechanical design and back-end electronics (BEE) to CHEC-M. However, SiPMs are used instead of MAPMs and an upgrade to the FEE module has been incorporated in the improved camera electronics.

Figure 2.6: A rendered image of the three SST prototype designs. Again, the reduced size of the SST-2M telescopes is clear when compared to the single-mirror SST-1M telescope [64].

Whilst the implementation of three SST designs proved successful in increasing prototyping effort and system development, it does introduce a much higher level of complexity. In early 2018, the CTA Observatory (CTAO) concluded that the optimal solution for CTA would be the simplest and most harmonised solution across all sizes of telescope. As the SSTs represent the greatest source of complexity, it was recognised that the implementation of a single SST design would produce the most optimised system by

removing variations in telescope performance whilst simultaneously reducing maintenance and operational differences across the SST sub-array. It was therefore decided that a single SST design would be implemented in the observatory.

Each project team submitted a detailed telescope design and a large sum of applicable documents in October 2018, describing the proposed telescope and camera sub-systems which would form the in-kind contribution for the SST. The design of the telescope structures for both dual-mirror SSTs allows for the installation of the ASTRI camera and CHEC on either of the SST-2M structures. Following the successful on-telescope campaign of CHEC-S on the ASTRI-Horn telescope at Serra La Nave, Sicily in May 2018 (see Section 5), a joint proposal was submitted comprising the ASTRI telescope structure and CHEC-S. In addition, a second proposal was submitted by the GCT team, again utilising CHEC-S, and a third proposal from SST-1M members. Each proposal included improvements and further development from the base design of the prototypes. An external panel was formed to review the submitted proposals and conduct a number of consultations with the three SST teams in order to determine which of the proposals represented the best solution for the SST. Taking into account the findings and recommendation of the review panel, in addition to funding considerations, the CTAO declared that the SST design should be based on the CHEC/ASTRI proposal. The following section gives a detailed description of the SiPM CHEC prototype (CHEC-S).

2.4 Compact High Energy Camera

The SST of CTA is designed to observe the highest energy γ-ray interactions and, therefore, the highest intensity Cherenkov light events. The high intensity of light produced in such events allows for the use of smaller telescopes. Such events are rare and infrequent which necessitates the use of many high FoV telescopes spread across a large collection area. A key requirement for the SST is that each telescope should be as inexpensive as possible,

allowing for a greater number of SSTs to be built with existing funding, providing a larger collection area. The plate scale of a telescope simply describes the diameter of an image at the focal point of a telescope, which determines the size of detector required to observe an image with a given angular width. In using a dual-mirror Schwarzschild-Couder design telescope, the plate scale is much reduced when compared to a single-mirror DC telescope with identical optical performance [72]. This allows for the use of a compact, lower weight, and cheaper Cherenkov camera [80]. CHEC was designed to fulfill this small plate scale focal plane detector and as such, forms the basis of the SST camera.

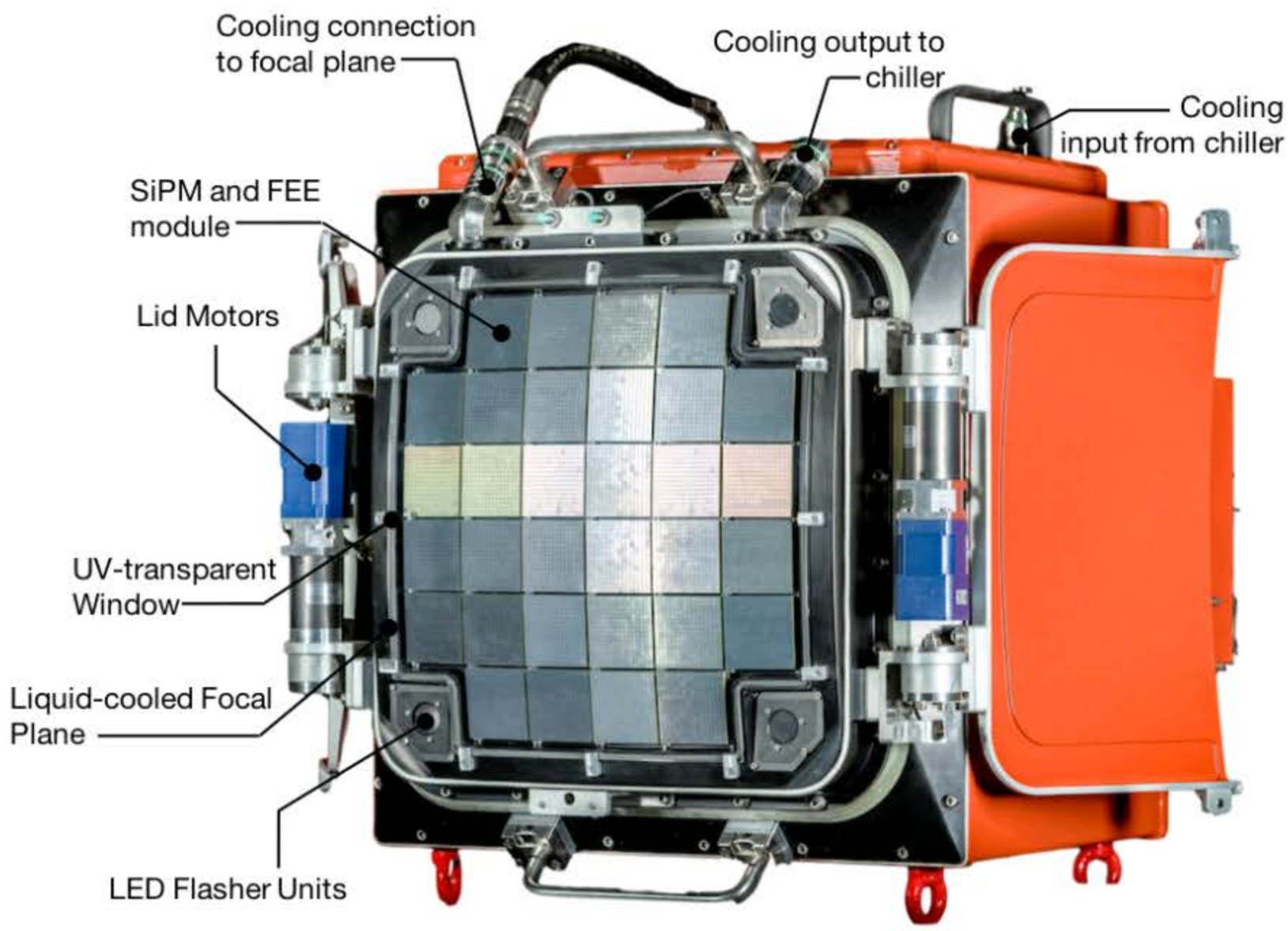

Figure 2.7: An image of the CHEC-S prototype with the key features annotated [29].

The development programme of the CHEC project consisted of the build and characterisation of two prototype Cherenkov cameras: CHEC-M and CHEC-S, utilising differing multi-pixel photosensor arrays. CHEC-M was the first of the two prototypes commissioned utilising MAPM photosensors and TARGET based FEEs [81]. The commissioning of CHEC-M concluded with the inauguration and first light achieved in November

2015 with CHEC-M installed on GCT at the Observatoire de Paris-Meudon [82]. The second prototype, CHEC-S, which utilises SiPM photosensors and incorporates improvements to the FEE chain from the lessons learned with CHEC-M. Figure 2.7 shows CHEC-S annotated with the key features of the Cherenkov imaging camera. The remainder of this chapter will describe the components of CHEC-S, with greater detail given to the photosensor and FEEs as the research covered in this thesis relates heavily to the SiPM and TARGET Module chain.

2.4.1 Mechanical Design

The mechanical design of CHEC-S comprises an internal aluminium rack, for mounting all electronic components, enclosed by an external camera body, focal-plane plate with lid and protective window, thermal exchange unit, network and power inlet panel, and backplane access panel. Figure 2.8 shows an exploded CAD model of CHEC-S with various components annotated.

During operation, the internal camera electronics dissipate a large amount of power as heat within the sealed enclosure. The thermal exchange system is designed to remove heat from within the camera and provide a stable thermal environment for the camera electronics. The thermal exchange unit consists of six fans thermally coupled to a liquid cooled heat sink. The fans, in conjunction with mechanical baffles, are designed to circulate cooled air within the camera enclosure, cooling the electronic components. This is achieved by passing chilled liquid, chilled by a commercially available chilling unit housed in the telescope structure, through the thermal exchange unit. The TARGET-C digitising ASIC represents the single component with the highest temperature dependency, section 4.5 describes the effect of and method for correcting for such temperature dependence. In addition to TARGET-C, SiPM are highly sensitive to temperature and must also be maintained at a stable temperature to maintain optimal performance of all photosensors.

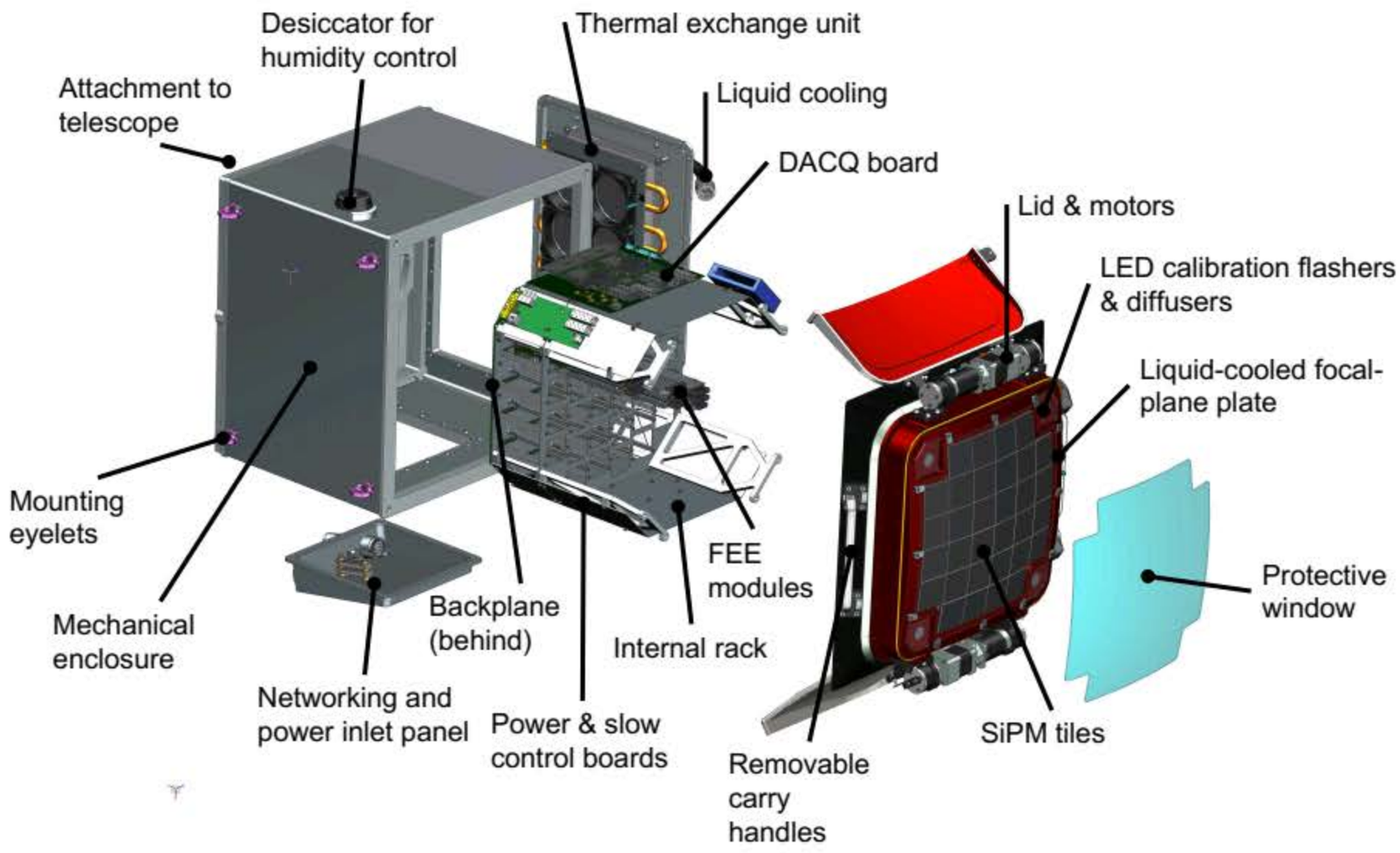

Figure 2.8: An exploded CAD model of CHEC-S with the majority of key elements annotated. Adapted from [83].

In order to cool the SiPM tiles, the chilled liquid from the external chilling unit is passed through the focal-plane plate via channels drilled into the aluminium structure. These channels run directly next to the SiPM tiles and are thermally coupled to copper heat sinks bonded to the SiPM tile printed circuit board (PCB), providing cooling for the SiPMs. A breather desiccator is used to maintain the humidity levels within the camera enclosure as the internal temperature varies.

In addition to facilitating the cooling of the SiPM tiles, the focal-plane plate is responsible for mounting the SiPM tiles and housing the LED flasher units used for on-telescope calibration of the SiPM gain setting. The curvature of the focal-plane is a requirement for all dual-mirror Schwarzschild-Couder telescope cameras in order to maintain focus across the focal-plane and remove aberrations produced by tangential and sagittal astigmatism [72]. Finally, a protective window is used to seal the camera enclosure and protect the SiPMs from dust and moisture, a lid is also used to protect the camera when not in operation.

2.4.2 Photosensors

Current existing IACT arrays almost entirely utilise conventional photomultiplier tubes (PMTs) for the detection of Cherenkov light. PMTs are highly sensitive and provide observations of a single photon to several thousand photons. The photoelectric effect forms the basis for the detection mechanism of a PMT, the general operation of a PMT can be seen in Figure 2.9. The initial Cherenkov photon interacts with the photocathode of the PMT, which releases an electron via the photoelectric effect. This electron is more commonly known as a photoelectron. The focusing electrode is responsible for focusing all photoelectrons into the electron multiplier. A high voltage (HV) is applied across the electrodes, creating an electric field which accelerates the photoelectrons through the electron multiplier, consisting of a number of dynodes. At each stage of the multiplier, electrons are accelerated into the dynodes which produces more electrons through secondary electron emission. As such, the number of electrons is multiplied at each dynode providing a large gain in number of electrons from the initial photoelectron, the gain of the electron multiplier is controlled by the HV applied. Finally, the anode collects all electrons produced in the electron multiplier. The signal produced by each PMT would then be read out through the FEEs of the camera [84].

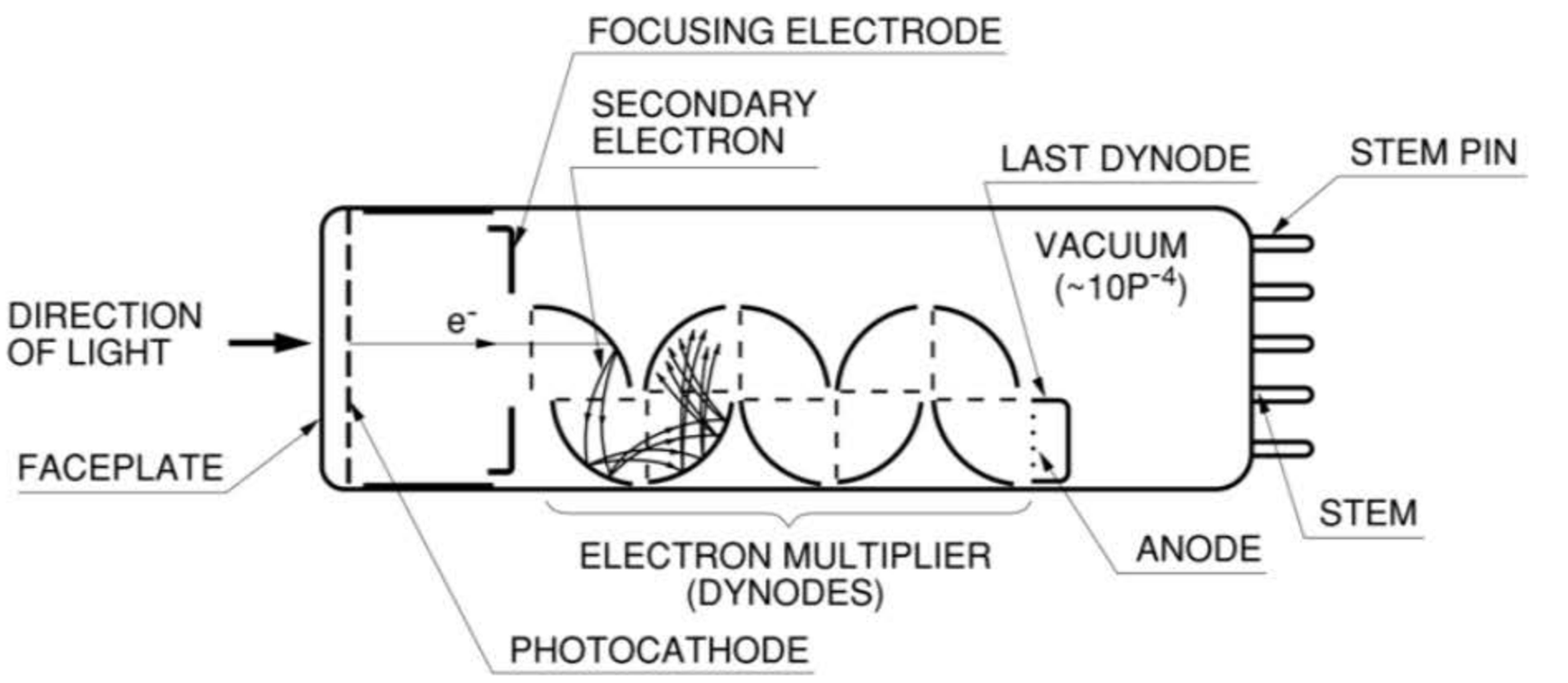

Figure 2.9: A diagram showing the electron multiplication mechanism present in photomultiplier tubes [84].

Although PMTs have been used since the first IACT, they are not without their disadvantages. The HV required to accelerate electrons within the PMT ranges from a few hundred to a few thousand volts per PMT. Providing a stable and high enough voltage incurs an increased cost for infrastructure and greater safety requirements. The plate scale of the SST dictates the size of camera that can be installed on the telescope. As such, standard PMTs cannot be used with the SST as they are too large, instead MAPMs were utilised in the initial, CHEC-M, SST camera prototype. MAPMs consist of many PMTs arranged in a grid matrix as shown by Figure 2.10. The advantage of this photosensor is that they achieve a gain on the order of standard PMTs whilst providing spatial, two-dimensional intensity information when arranged in a pixelated array. Advancements in the development and manufacturing of photosensors has led to a decrease in cost for photosensor technologies that have not previously been used in IACTs. The SiPM has become much more cost-effective in recent years, and forms the photosensor used across all SSTs and the PSCT for the MST.

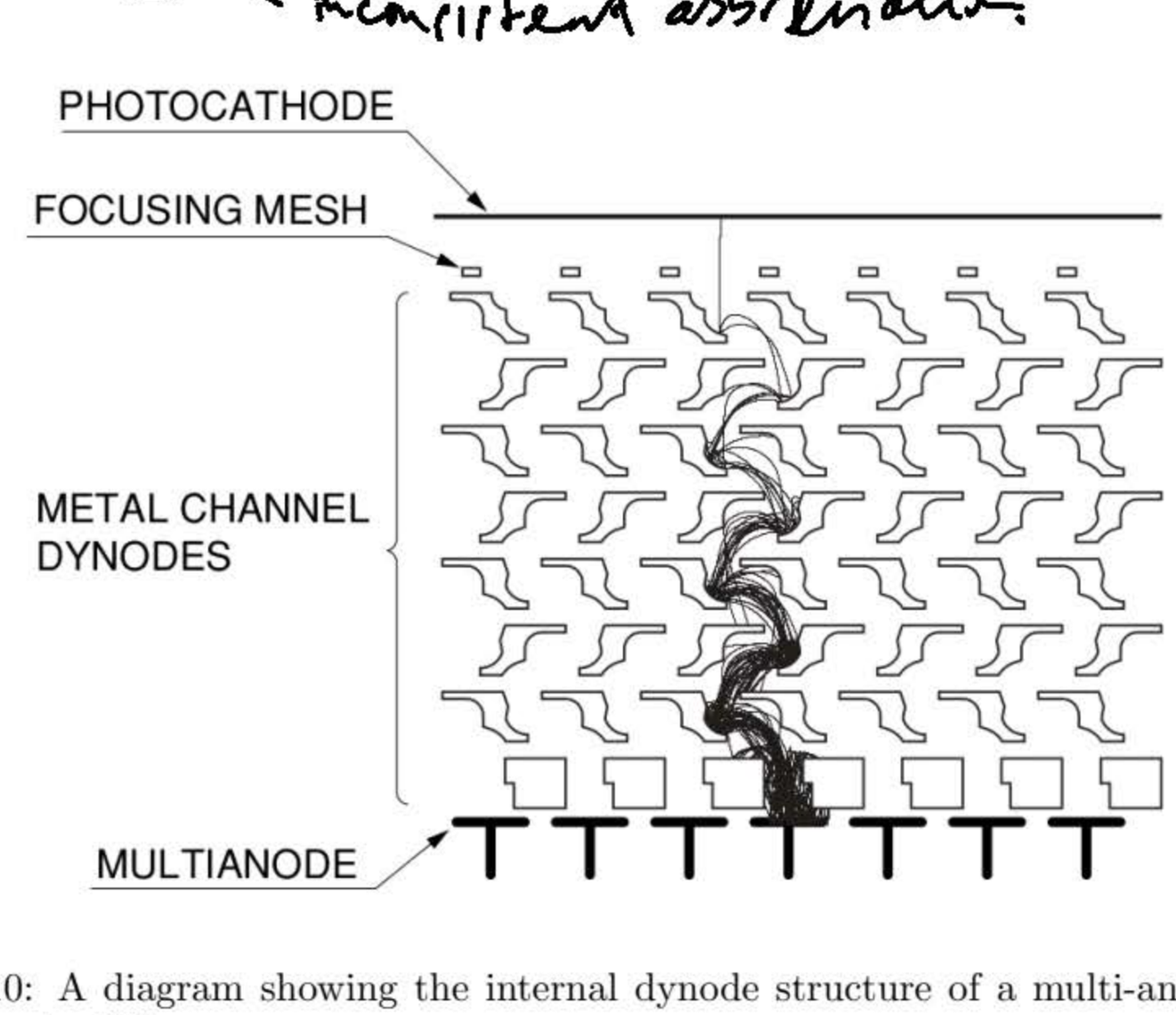

Figure 2.10: A diagram showing the internal dynode structure of a multi-anode photomultiplier tube [84].

2.4.2.1 Silicon Photomultiplier

The SiPM is a solid state semiconducting photosensor by which the fundamental photo-detection mechanism is based on a simple P-N junction (or photodiode). The p-type and n-type materials are created by doping the semiconducting material with impurities, increasing the number of freely moving electrons (for n-type) or holes (for p-type) within the material. When the p-type and n-type materials are joined, a P-N junction is formed. Within this region, a diffusion current forms whereby the freely moving electrons in the n-type material cross the junction and combine with holes present in the p-type material, and freely moving holes in the p-type material cross the junction and combine with free electrons in the n-type material. This diffusion current results in a region surrounding the junction where only immobile positive ions are present in the n-type material and immobile negative ions in the p-type material, this is known as the depletion region. An equilibrium is reached when the electric field produced by the charge difference in the depletion region equals that of the diffusion current. The equilibrium within the depletion region can be disturbed by the introduction of a freely moving electron-hole pair. An electron-hole pair is produced either via thermal excitation (dark count) or by the photoelectric effect when a photon of energy greater than the bandgap of the semiconductor is absorbed. If the photon is absorbed within the depletion region, the excess charge carriers (electron and hole) will be accelerated by the electric field in the direction corresponding to the charge. As such, a free electron produced in the P side of the junction will travel to the N side resulting in a current across the junction. Excess charge carriers produced outside of the depletion region do not result in a current, as there is no electric field in this region to accelerate such ions.

It is possible to further advance the performance of a simple photodiode by increasing the depth of the depletion region either side of the P-N junction. This is achieved by applying a reverse bias voltage across the junction. In doing so, the electric

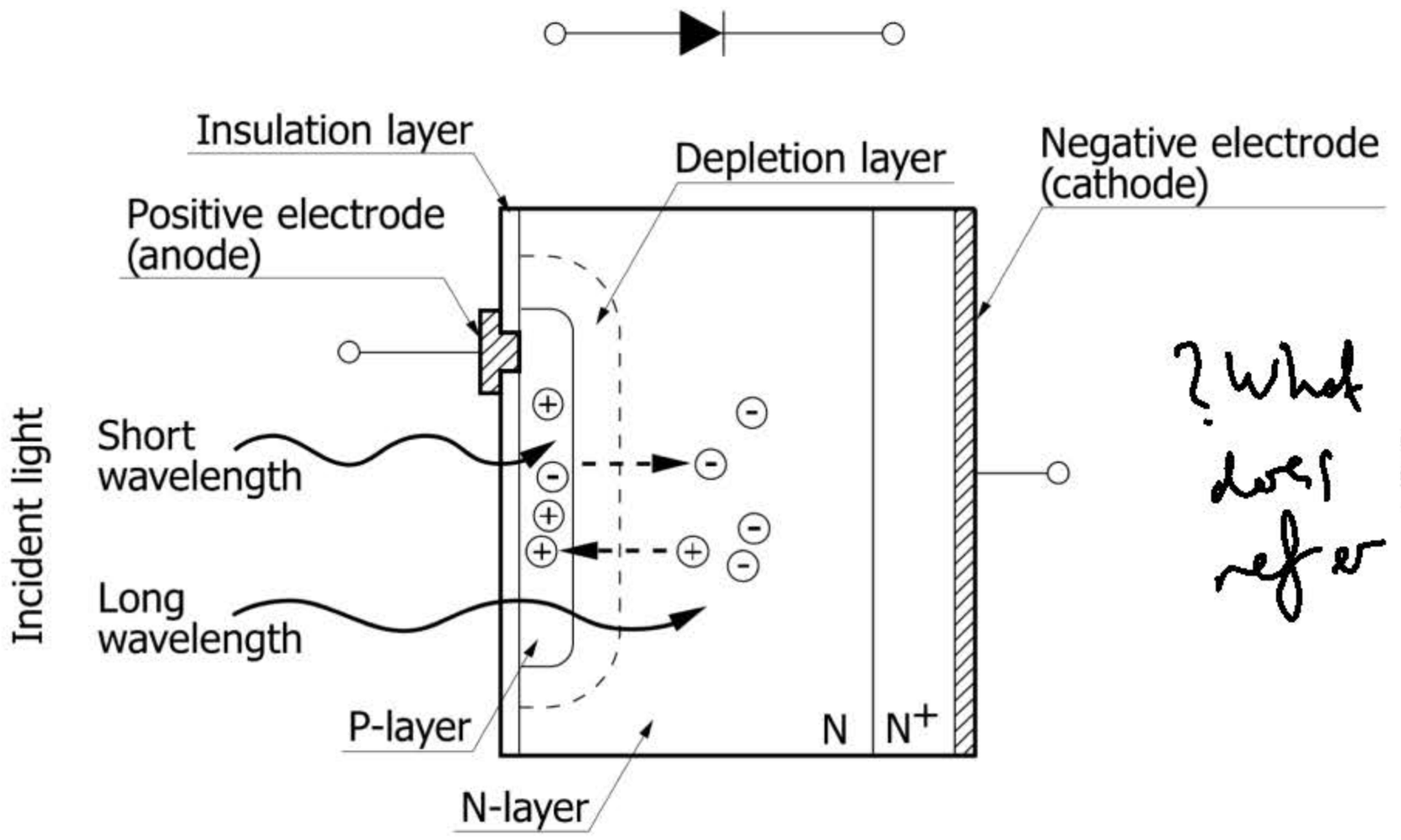

Figure 2.11: A diagram of an avalanche photodiode (APD) annotated with the key features and components used to describe an APD [85].

field is intensified, which causes the freely moving electrons and holes in the N and P material to move further from the junction which therefore extends the depth of the depletion region. The increased depth of the depletion region produces a more sensitive photodiode. As the electric field within the depletion region is increased, any excess charge carriers produced in this region are accelerated to a higher velocity as the charge carriers move towards the electrodes with a greater kinetic energy. If the electric field strength is such that the mean kinetic energy of the charge carrier between collisions is greater than the bandgap energy of the substrate, it is possible to ionise atoms within the lattice through impact ionisation and release another electron-hole pair into the depletion region [85]. Providing the electric field is maintained, the newly created excess charge carriers can consequently produce further electron-hole pairs through impact ionisation. This leads to an avalanche of excess charge carriers through rapid multiplication. Such devices are subsequently known as avalanche photodiodes (APDs) and are used to produce a large gain from the original photoelectric signal. Figure 2.11 shows an example of a typical

APD.

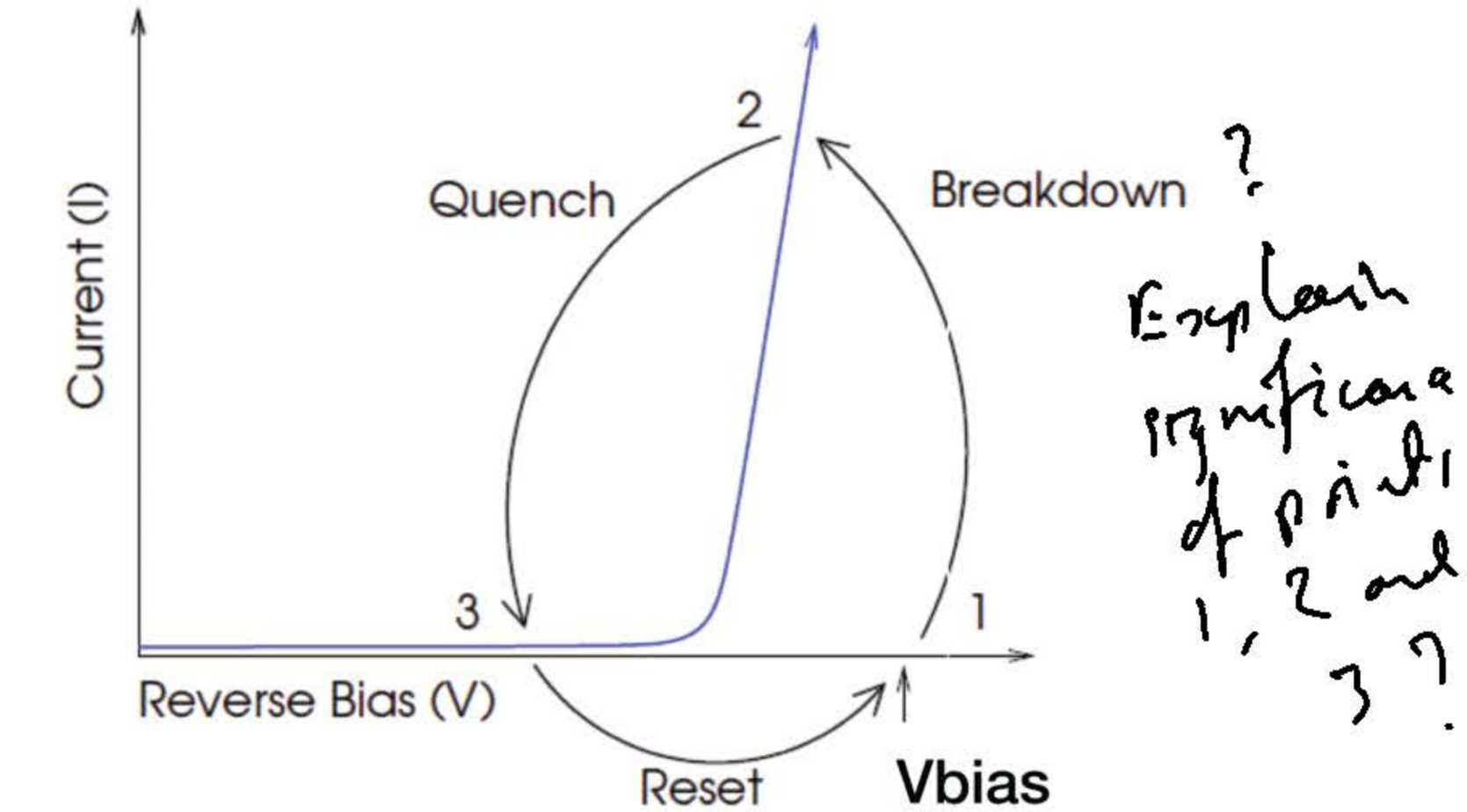

Figure 2.12: Plot showing the breakdown, quench, and reset cycle of a single photon avalanche diode [86].

When a large enough electric field is applied across the APD, a single photoelectron produced in the depletion region will initiate a self-perpetuating ionisation cascade throughout the semiconductor, effectively amplifying the original electron-hole pair into a macroscopic current flow. An APD operating under such conditions is known as a Geiger-mode APD (GAPD) as the ionisation cascade is analogous to the ionisation discharge observed in a Geiger-Müller tube [86]. A resistor placed in series with the GAPD, known as the "quenching" resistor, limits the current drawn by the GAPD during this cascade or breakdown, such that the reverse voltage across the GAPD is lowered. Once the reverse voltage is lower than the breakdown voltage of the GAPD, the avalanche or breakdown is halted and the GAPD must then recharge back to the original reverse bias voltage. Figure 2.12 shows this principle as the current of the GAPD varies with each step in the quenching process. GAPDs operated in this way are known as single photon avalanche diodes (SPADs) which act as a photon-triggered switch providing a binary on or off state

[86]. The signal produced by a SPAD during breakdown is independent of the number of photon interactions within the depletion region.

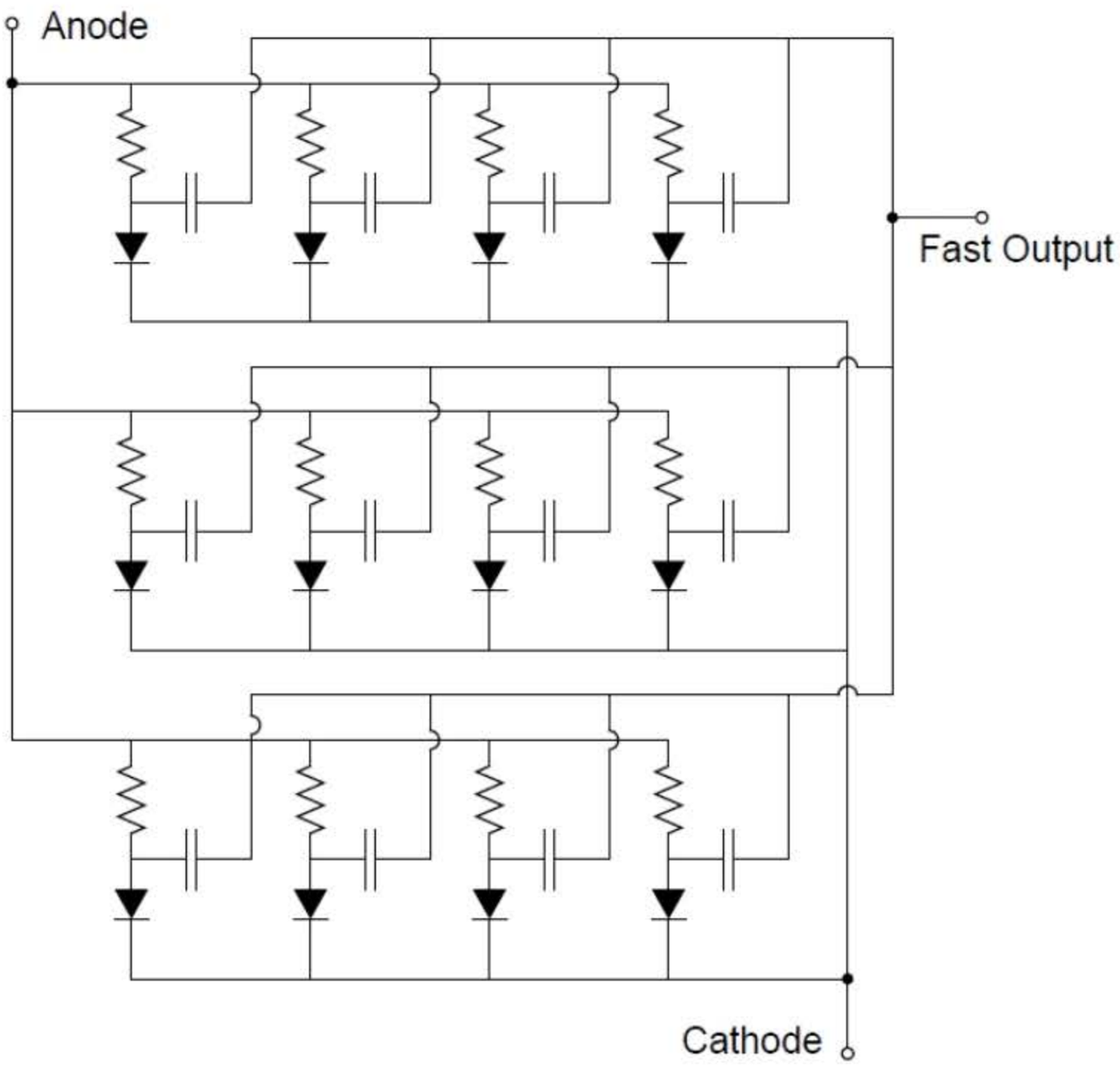

Figure 2.13: The circuit diagram of a silicon photomultiplier pixel, comprising an array of Geiger-mode avalanche photodiodes connected in parallel [86]. Each avalance photodiode here represents a silicon photomultiplier microcell.

~~The final progression from the original PN junction is that of the SiPM~~. A SiPM comprises a densely packed array of SPADs, each with its own quenching resistor, connected in parallel to a common readout bus. The number of SPADs (or microcells) in the array ranges from 100 up to 10,000 ~~SPADs~~ per mm^2. Figure 2.13 shows a simplified circuit diagram for a SiPM. When operated at a reverse bias voltage greater than the breakdown voltage of the SiPM, the output of each fired microcell is summed and ~~readout~~ via the common bus. The number of microcells that fired corresponds to the amplitude of the voltage produced, which can be used to determine the intensity of photons for this single event at a given reverse bias voltage.

The SiPM tiles utilised by CHEC-S are the Hamamatsu S126421616PA-50 packaged as an array of 64, 6 x 6 mm SiPM camera pixels. Each SiPM camera pixel consists of four connected 3 x 3 mm SiPM pixels in a 2 x 2 array. I use SiPM camera pixel here to highlight that the signal readout by the FEEs is that produced by the 6 x 6 mm SiPM. In addition to this, four SiPM camera pixels are grouped in a 2 x 2 array to form what is known as a super pixel for triggering (see 2.4.3) and the application of the biasing high voltage. 32 SiPM tiles comprise the CHEC-S focal plane. The following describes a number of key parameters required to understand the operation of the SiPM:

Gain

The gain, G, of a SiPM simply describes the amount of charge produced for a single photoelectron detected by a microcell and can be determined by the following expression:

$$G = \frac{C\Delta V}{e}, \tag{2.1}$$

where C is the capacitance of the microcell, ΔV the SiPM overvoltage ($\Delta V = V_{bias} - V_{Breakdown}$), and e the electron charge.

The quantised, binary nature of a SiPM produces an output pulse that is proportional to the number of fired microcells [86], N_f, and contains a total charge, Q_T, where $Q_T = N_f \times G \times e$. The gain of a SiPM is often given in units of either *charge/photoelectron* or *voltage/photoelectron*.

Photon Detection Efficiency

The photon detection efficiency (PDE) of a SiPM is a measure of the sensitivity of the photosensor to photons at a given wavelength. The PDE is dependent on overvoltage and is given by the product of the SiPM's quantum efficiency, avalanche initiation probability, and fill factor.

Dark Noise

Dark noise describes the signal noise produced by dark counts. As described previously, a dark count is the name given to an excess charge carrier produced in the depletion region of a photodiode via thermal excitation. The measure of dark count frequency is a parameter often used to describe the performance of a SiPM and is proportional to both overvoltage and temperature [86].

Optical Crosstalk

The optical crosstalk of a SiPM represents an additional noise component. During the avalanche breakdown of a microcell, excess charge carriers with sufficient energy are able to produce secondary photons. These photons are able to travel to adjacent microcells and initiate an additional breakdown which in turn may produce further optical photons. The presence of a secondary photon, and secondary avalanche, produces an excess amount of charge in the SiPM signal which would result in the overestimation of initial photon intensity [86]. Optical crosstalk gives a measure of the probability that a single avalanching microcell will initiate an avalanche in a second microcell.

Afterpulsing

Afterpulsing is the term used to describe a microcell avalanche that was initiated by an excess charge carrier that was temporarily trapped in a defect within the silicon substrate. Afterpulsing therefore occurs after the initial microcell avalanche which produces another source of noise.

Excess Noise Factor

The excess noise factor (ENF) of a SiPM describes the variation of a photosensor to a single photoelectron. The expression combines the statistical fluctuations that arise from optical crosstalk and afterpulsing.

2.4.3 Front End Electronics

In the CHEC-S camera, each

Each of the SiPM tiles is connected to the FEEs which are responsible for the shaping, triggering, sampling, and digitisation of the analogue signal produced by the photosensors. The data digitised by the FEEs is readout via the DACQ boards as described previously. Figure 2.14 shows a SiPM connected to the FEE chain, which consists of a preamplifier buffer board, directly connected to the photosensor, and a TARGET module connected via flexible ribbon cables. These flexible ribbon cables allow the SiPM tiles to be mounted on the curved circular plane whilst the TARGET module is mounted in the internal rack.

to the buffer board

flexible

rectilinearly

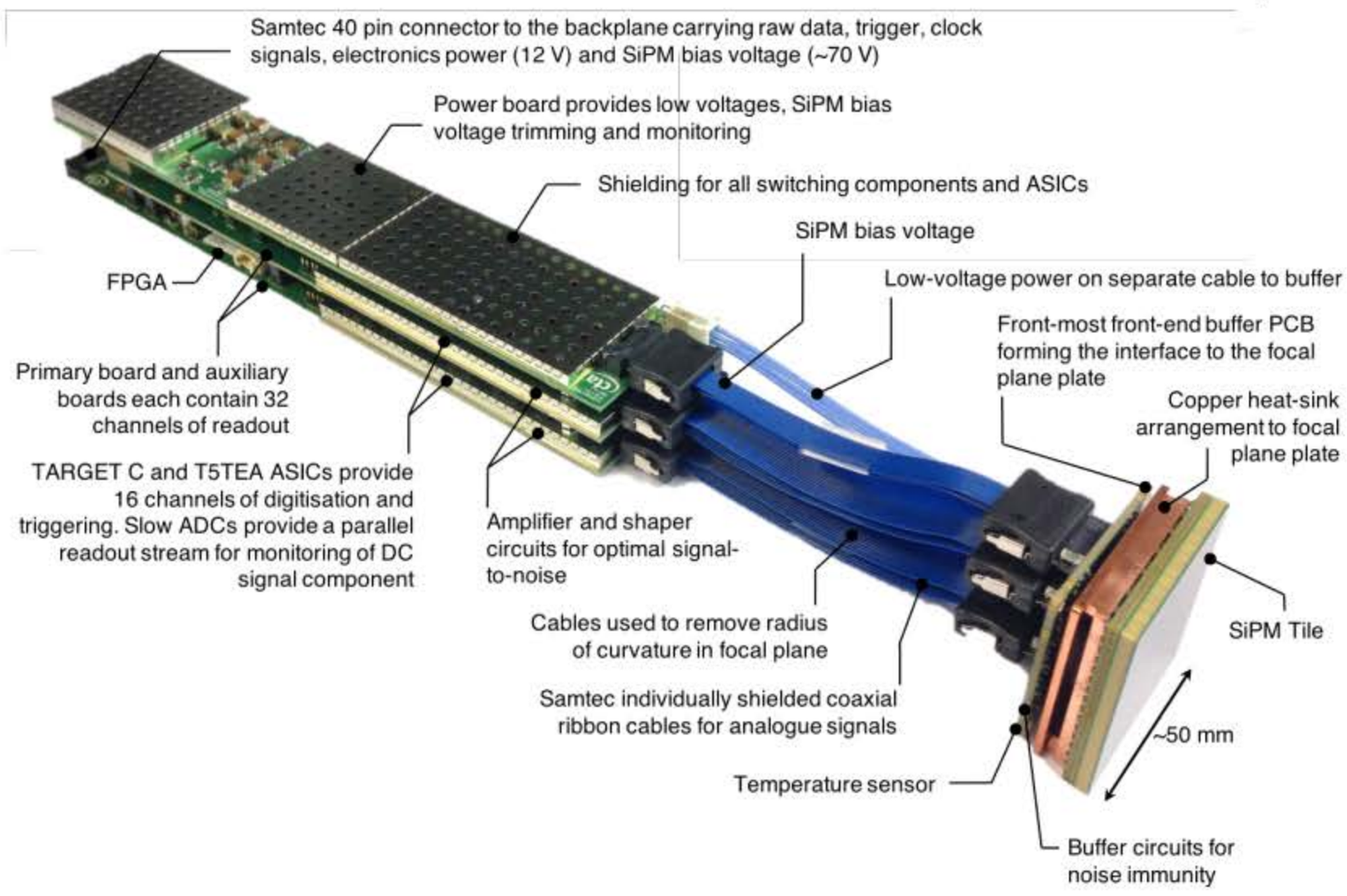

Figure 2.14: An image of the CHEC-S silicon photomultiplier and front end electronics chain, with they key components annotated [87].

The first stage of analogue signal processing is given by the preamplifier buffer board. This preamplifier circuit provides noise immunity to maintain signal integrity of the SiPM output [87]. The analogue signal is then sent to the TARGET module via the shield ribbon cables.

? what do you mean by "noise immunity"? Does the pre-amp amplify?

The second, and main, component of the FEE chain is the TARGET module. It

is given this name as the design of the FEE module is based on the TARGET (TeV Array Readout with GSample/s sampling and Event Triggering) ASICs that perform the event triggering and signal digitisation. The TARGET ASIC was specifically developed for use in IACTs providing triggering and digitisation of Cherenkov events. The first TARGET ASIC iteration (TARGET-1 [78]) was developed from the Buffered Large Analog Bandwidth (BLAB1) ASIC designed for applications in radio neutrino detectors [88]. Since then, the TARGET ASIC has undergone a number of development stages, producing various ASIC iterations. The trigger and sampling ASIC used by CHEC-M was TARGET-5 [89], representing the first TARGET ASIC utilised by an IACT. During the commissioning of CHEC-M, increased dead time and noise produced by the sampling of TARGET-5 impacted the performance of the FEEs [81]. TARGET-7 was developed with the aim that these noise sources would be removed [90], however the change in performance was minimal and the noise effects still present. Despite this, TARGET-7 is utilised by the FEEs of the SCT prototype MST. In CHEC-S, the components of TARGET-7 were separated into two individual ASICs: T5TEA for event triggering and TARGET-C for digitisation. Each of the 32 TARGET modules within CHEC-S contain four T5TEA and four TARGET-C ASICs.

Figure 2.15 shows the functional block diagram of the CHEC-S electronics and communications, highlighting the key components of each electronic stage. The following describes a number of key components within the TARGET module:

Slow Signal Monitoring

The signal input into the TARGET is split into two shaping and digitising chains: the slow and fast chains. The slow signal chain consists of a large time constant integrating circuit and digitiser. The integrator provides a measure of the DC light-level observed by the SiPM as the short timescale, low frequency Cherenkov events are removed by integrating the photosensor output over a large period of time [83]. As such is is possible to track the

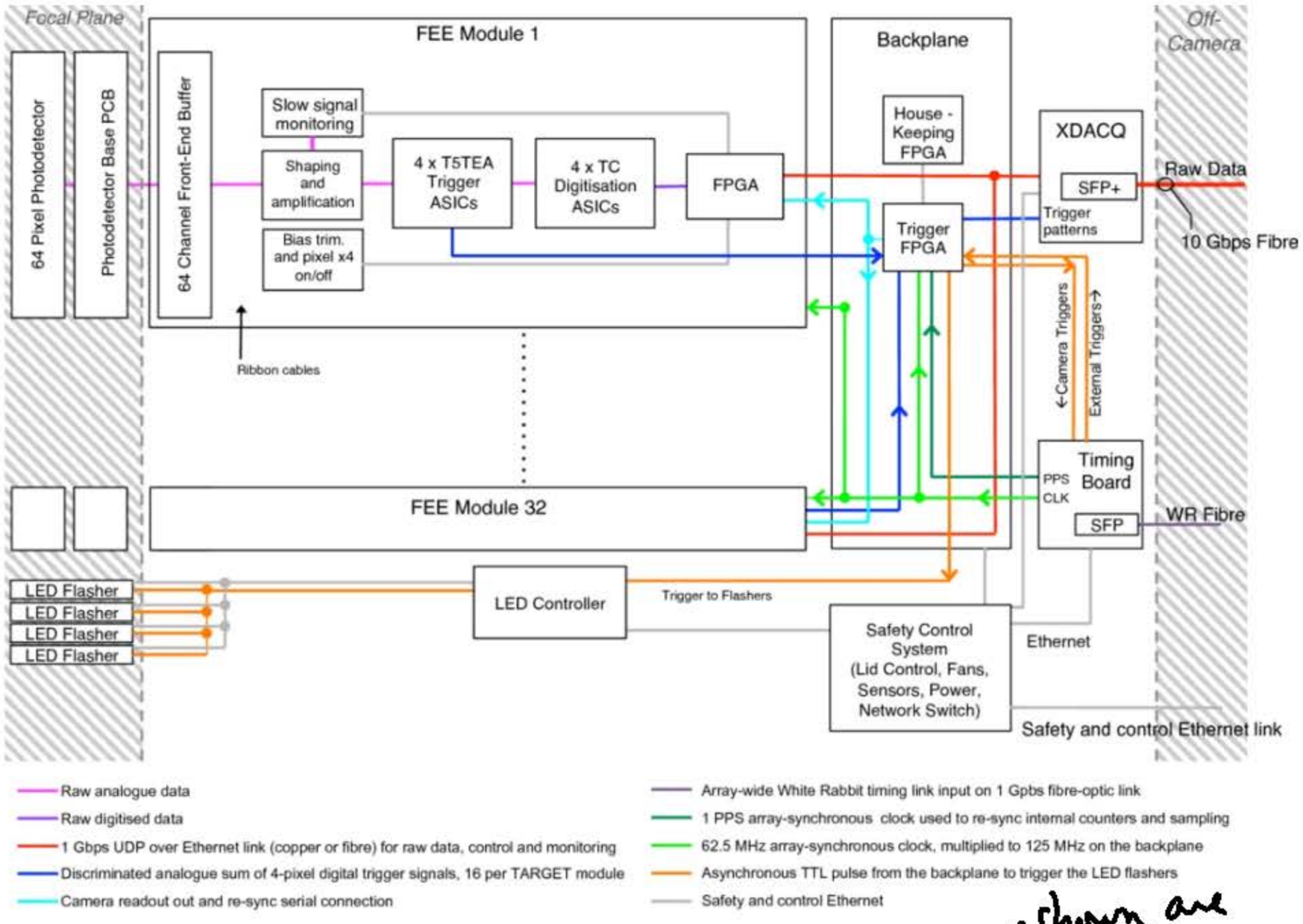

Figure 2.15: A functional block diagram of the CHEC-S electronics, the communication lines between each component, the raw data readout path, the trigger architecture, and distribution of the synchronising clock [83].

position of stars on the focal plane using the per-pixel slow signal, which provides a method for telescope pointing using an online pointing algorithm during telescope operations.

Shaping Electronics

The fast signal chain for each SiPM pixel is routed into the shaping electronics at the front of the TARGET module. The purpose of the shaping electronics is to ensure that the resulting analogue pulses are the optimal shape for triggering whilst maintaining a good pulse shape for offline data analysis. Simulations conducted during the development of CHEC-S found that the optimal pulse shape for triggering has a full width half maximum (FWHM) of 5 to 10 ns and a 10-90% risetime of 2 to 6 ns. The width of the pulse shape has a large effect on the triggering performance of the Cherenkov camera (see 2.4.3). In short, if the width of the pulse is too narrow, the probability of forming coincident trigger

signals with neighbouring pixels is reduced. If the pulse width is too large, it is possible to form coincident trigger signals with NSB photons and dark counts [81]. The pulse shape produced by a SiPM is governed by the rate at which the photosensor discharges and recharges. For CHEC-S SiPMs, the pulse shape has a long fall time which must be reduced to generate the optimal pulse shape, this is achieved via a pole-zero shaping circuit.

In addition to the pulse shaping circuit, CHEC utilises an AC (alternating current) coupling circuit to remove the DC (direct current) component of the SiPM signal which contains both AC and DC components. The AC component of the SiPM signal corresponds to the very fast, short timescale pulses produced in Cherenkov events. The DC component corresponds to the static light level observed by the Cherenkov camera, this is generally produced by the NSB background and any light pollution surrounding the telescope. By removing the DC component, the baseline of the waveform is maintained at 0mV regardless of the NSB rate. Since the AC coupling is simply an RC circuit (a circuit using resistor and capacitor components), the AC coupling performance is governed by the time-constant of the RC circuit. In rapidly varying light conditions, the rate at which the AC coupling circuit adapts to the new light level corresponds to the time constant, the baseline during this period follows an exponential decay or growth depending on whether the light level has increased or decreased. An example of this AC coupling RC decay mechanism can be seen in Figure 5.13, which shows the observation of such effect during the CHEC-ASTRI on-telescope campaign in May 2019.

Trigger ASIC

Following the shaping and AC coupling circuits, the analogue signal passes to the T5TEA trigger ASIC. At this point, the signals from four SiPM pixels are combined to produce one trigger signal for a single trigger superpixel (SP). The triggering of IACTs utilise a two-level trigger criteria during Cherenkov light observations [43]. The first-level (L1)

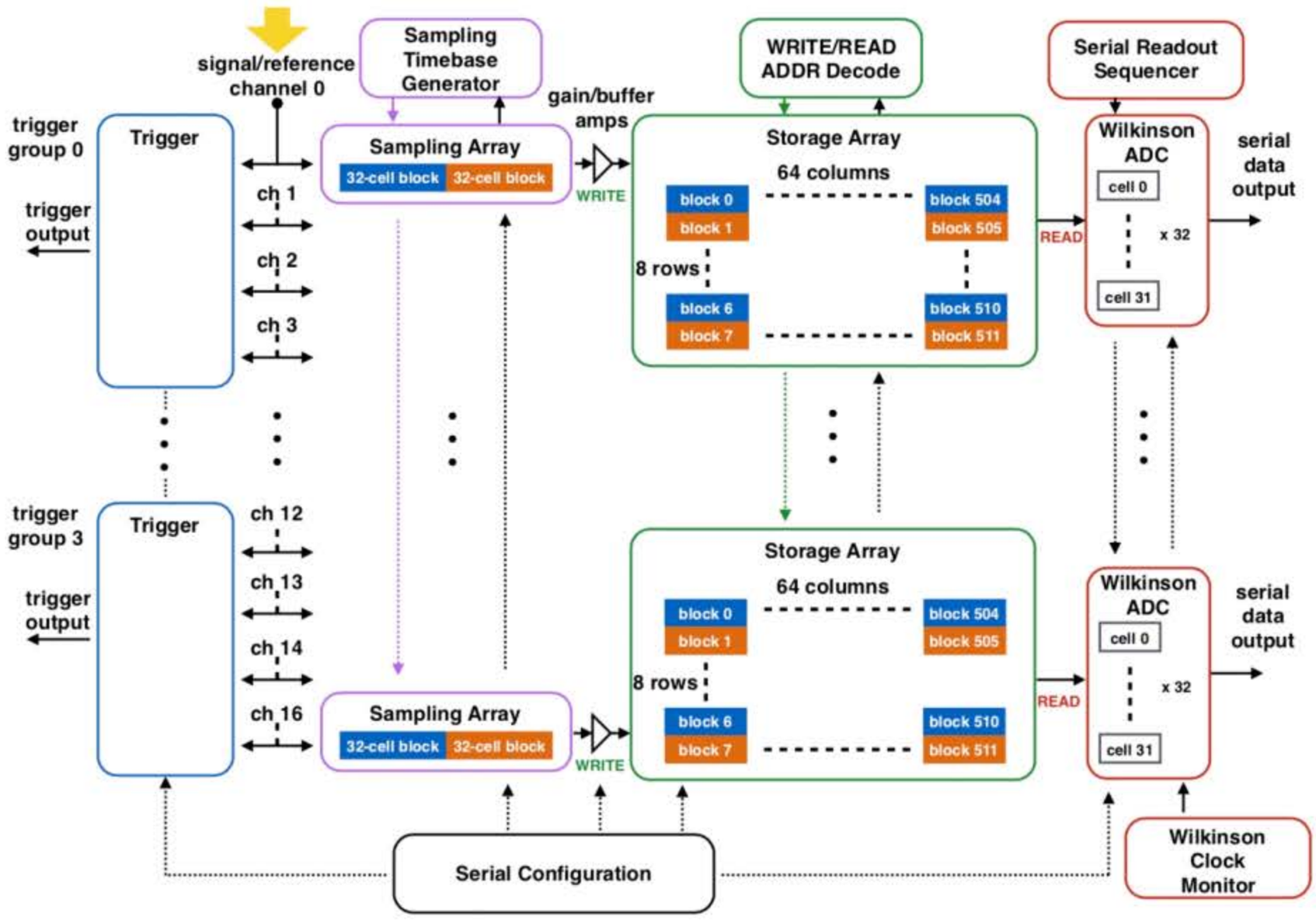

Figure 2.16: The functional block diagram of the TARGET-7 trigger and digitising ASIC. The block diagram is analogous to the combined architecture of the T5TEA trigger ASIC and the TARGET-C digitising ASIC [90].

trigger logic is evaluated by the four T5TEA trigger ASICs on each TARGET module. The L1 criterion states that the analogue sum of four pixels in a trigger SP must be greater than a configurable threshold level set within the camera operating software. Within the T5TEA ASIC, a comparator is used to compare the amplitude of the analogue sum to the threshold level. Following a successful L1 trigger, a trigger signal is sent to the trigger FPGA present on the backplane, containing a timestamp and the SP identification for all SPs ~~surpassing the L1 trigger~~ triggering at L1.

The backplane trigger FPGA determines whether the second-level (L2) trigger criterion is met. The L2 trigger logic states that ~~two~~ or ~~more~~ nearest neighbour trigger SPs must have produced an L1 trigger in a given programmable coincidence window. Following a successful L2 trigger, the backplane trigger FPGA issues a readout request

and the data responsible for producing the trigger is digitised by the TARGET-C digitising ASIC. The L2 trigger logic mitigates false camera triggers caused by NSB photons, providing the L1 trigger threshold is set accordingly (see 5). As described before, if the FWHM of the shaped analogue pulse is too narrow, it will become difficult to produce an L2 trigger unless the coincidence window is increased.

Disgitising ASIC

The TARGET-C digitising ASIC is responsible for the sampling, storage, and digitisation of the shaped analogue signal. Figure 2.16 shows the functional block diagram of the TARGET-7 ASIC. The trigger and digitising components of TARGET-7 were separated in order to produce the T5TEA and TARGET-C ASICs. This can be seen on Figure 2.16 whereby the block diagram to the left of the *signal/reference* line (indicated by the yellow arrow) constitutes the T5TEA ASIC and everything to the right shows the functionality of TARGET-C. It can be seen that TARGET-C comprises a sampling array, storage array and Wilkinson analogue-to-digital converter (ADC).

The sampling array consists of two blocks, where each block is a switched capacitor array (SCA) [91] containing 32 switched capacitors (hereafter known as sampling cells). The sampling array is operated in "ping-pong" mode, which means that whilst one block is sampling the shaped analogue signal, the other block is buffered to the storage array [92]. As such, it is possible to continuously sample the analogue signal, resulting in a deadtime free operation.

The storage array contains 512 blocks, each with 32 storage cells per channel, resulting in a 16,384 cell storage array which guarantees a large buffer depth of $\sim 16\mu s$. As the shaped output of the SiPM is continuously sampled, the storage array is continuously being overwritten by new data in a deep ring buffer.

Following a successful L2 trigger, a readout request is sent from the backplane

trigger FPGA to all TARGET modules. The readout request contains information describing the look-back time and the number of blocks to be digitised. The look-back time is used to determine which segment of the deep analogue ring buffer is to be digitised, and the number of blocks describes the width of this segment which can be configured by the camera operating to increase or reduce the size of the digitised waveform. The first cell to be digitised, given by look-back time, is read by the Wilkinson ADC. A capacitor within the ADC is charged such that the charge is equal to the charge of the first cell. This comparison is conducted using a comparator. The charged capacitor is then discharged at a constant rate. Simultaneously, high-frequency pulses from the Wilkinson clock are counted in a count register. This continues until the capacitor is fully charged and the pulse counting ends. The number of pulse counts in the register is proportional to the charge of the capacitor, which therefore corresponds to the amount of charge in the first storage cell. The number of counts in the register, known as ADC counts, is then read out of the camera via DACQ board. This process is repeated sequentially until all storage cells required by the event are digitised.

Once the digitised waveform has been read out of the camera, it must be calibrated. The calibration process is further described in chapter 4, but simply a conversion of ADC counts to input voltage is measured by injecting electronic signals of a known amplitude into the TARGET module. In doing so, a lookup table containing this conversion for each storage cell per channel is created, which is known as the transfer function (TF). The TF can be applied to digitised data in order to calibrate the ADC counts into a real-world voltage value. In addition to this, each sampling cell (physical capacitor) has a unique residual charge that is always present. The amplitude of this charge varies cell-to-cell and is temperature dependent. This residual pedestal must also be removed during the calibration, such pedestal calibration is described further in section 4.3. As such, the depth of the analogue ring buffer for CHEC-S was reduced from 16,384 cells, to 4,096 cells. This reduces the amount of calibration data required whilst maintaining a

deep enough storage array.

2.4.4 Back End Electronics

The BEE consists of two components: a backplane and data-aquisition (DACQ) board installed on the internal rack of CHEC-S, as shown by Figure 2.8. The role of each component is as follows:

- Backplane: Houses the connection to each TARGET module, providing power, synchronising clock, and triggering via the on-board trigger FPGA (TFPGA). The TARGET module communication and data transfer is also routed through the backplane to the DACQ board.

- DACQ Board: Provides the connection between the camera server PC and the TARGET modules for communication and the transfer of digitised data from each of the 32 TARGET modules. This is achieved in CHEC-S with the use of two 10 Gbps fibre-optic links, ensuring communications and transfer of raw data during operation is possible. All communications with the TARGET modules use a custom format over UDP (user datagram protocol).

In addition to the BEE, there are a number of auxiliary components including the power and slow control boards, LED flasher, and the network switch. The power and slow control boards are responsible for providing each electronic component with the required power and the overall control of the camera by the camera operator and state machine. The LED flasher boards provide the power and timing for each of the LED calibration flasher units housed in each corner of the focal-plane plate. Finally, the network switch enables the communications between the power and slow control board, LED flasher board, backplane, and DACQ board.

Chapter 3

CHEC-S Assembly and Verification

Contents

3.1 Introduction

Section 2.4 describes the design and structure of two small-sized Cherenkov imaging prototype cameras, CHEC-M and CHEC-S, utilising both multi-anode photomultiplier tubes (MAPM) and silicon photomultipliers (SiPM). The initial focus of my doctoral research began with the physical assembly and verification of CHEC-S, the SiPM based Cherenkov camera. The assembly and initial verification of CHEC-S was completed at the University of Leicester. CHEC-S was then shipped to ~~SST-Camera members at~~ the Max-Planck-Institut für Kernphysik (MPIK) in Heidelberg, Germany and installed within a dark room for further verification and characterisation. This Chapter discusses the initial build, component integration and preliminary verification of CHEC-S electronics. A description of more in-depth investigations with a focus on the characterisation and performance of CHEC-S conducted at MPIK during testing campaigns is also given. In addition to the verification of CHEC-S, further evaluation and characterisation of the front-end electronics (FEE) chain was conducted at the University of Leicester. I will discuss a number of investigations conducted with a single TARGET module and SiPM chain. Whilst the investigations described here ~~form a small conclusion on their own, together~~, they can be used to ~~portray~~ a more complete verification of CHEC-S. The results shown here are my own unless indicated otherwise. The inclusion of results obtained by others is done so for completeness and where necessary to provide conclusions to joint investigations.

3.2 CHEC-S Assembly

At the time of my joining the CHEC team, the design and construction of CHEC-S components had been finalised and delivered to the University of Leicester. The following describes the tasks completed during the initial build and integration of CHEC-S mechanical and electronic components. In addition to this, a discussion for the assembly of FEE

Modules is given. The basis of the FEE module is the TARGET (TeV Array Readout with GSample/s sampling and Event Triggering) application specific integrating circuit (ASIC). From here, the FEE module is known as the TARGET module.

3.2.1 Mechanical Build of CHEC-S

As stated previously, the design of both mechanical and electronic components within CHEC-S had been completed following the verification of the MAPM prototype CHEC-M. Following the manufacture of each constituent part, the assembly of CHEC-S began.

The design and structure of CHEC-S can be separated into two parts. Firstly the camera enclosure structure which includes the outer body; focal plane assembly housing the SiPM tile mounting plate; window and doors; power and network connection panel; and the thermal control enclosure. Secondly, the internal component rack. This internal rack houses all networking; safety control and back-end electronics (BEEs) on the outside of the structure. This rack is then connected to the focal plane plate. The TARGET Modules can then be inserted through the focal plane assembly and connected to the backplane via slotted channels and retaining screws.

Initially, the assembly began with the integration of electronic component printed circuit boards (PCBs) to the internal rack and focal plane plate assembly. Figure 3.1 shows the internal component rack and focal plane plate mounted to a support structure used for mounting and diagnostics. Figure 3.1(a) shows the focal plane thermal break and internal component rack below, showing the TARGET Module mounting channels. Figure 3.1(b) shows the populated internal electronic component rack. The completed focal plane assembly can also be seen here with the doors and thermal control plate connected to the thermal break. At this point, the electronic components were connected to power and network communications for initial verification. In addition to this, the thermal control enclosure can be seen resting against the support structure, this must be connected to

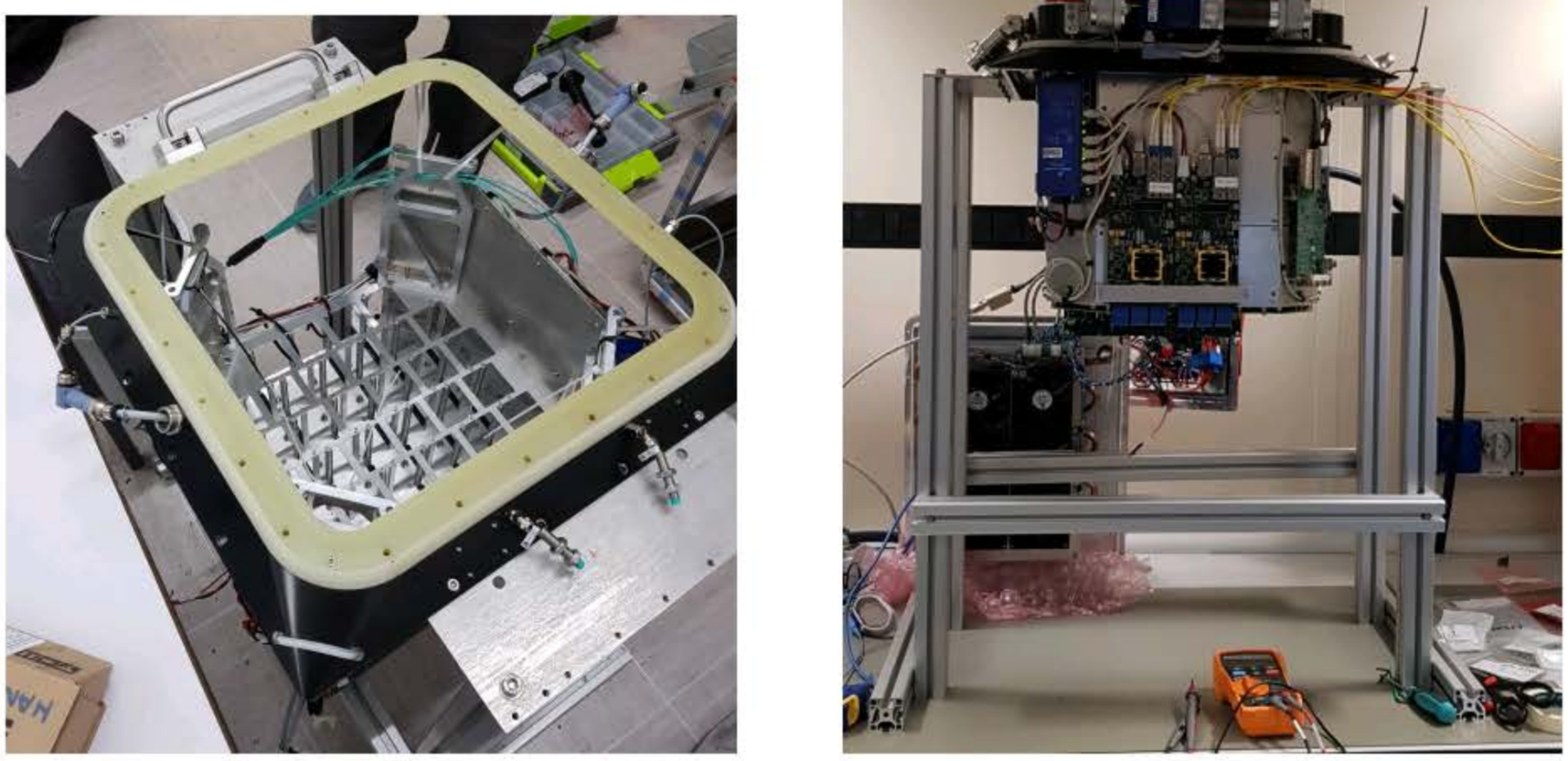

(a) (b)

Figure 3.1: Images of the CHEC-S assembly process. (a) Shows the internal component rack attached to the focal plane thermal break plate before the integration of CHEC-S electronic PCBs. The focal plane thermal break plate is installed on an aluminium mounting rack providing better access during this mounting process. (b) Image showing all back-end electronics installed on the internal component rack including the power and network connections. This can be seen by the fibre optic cables (yellow) connected to the data acquisition boards. In addition to this, the focal plane assembly and doors were also connected. Following this integration, all power and network connections were verified, including the operation of the doors and thermal control fans pictured at the base of the mounting structure.

bypass safe control measures. (?)

Following the integration of the BEE PCBs, it was possible to perform initial testing and verification of each component and the network interface with the use of LABVIEW control software [93] and digital multimeters ~~and network interface evaluation~~. With each PCB powered and enabled via the LABVIEW software, checks were performed to ensure the response of each component was as expected.

After the initial verification of the BEEs, the internal component rack and focal plane assembly was installed within the camera external enclosure. Figure 3.2 shows the

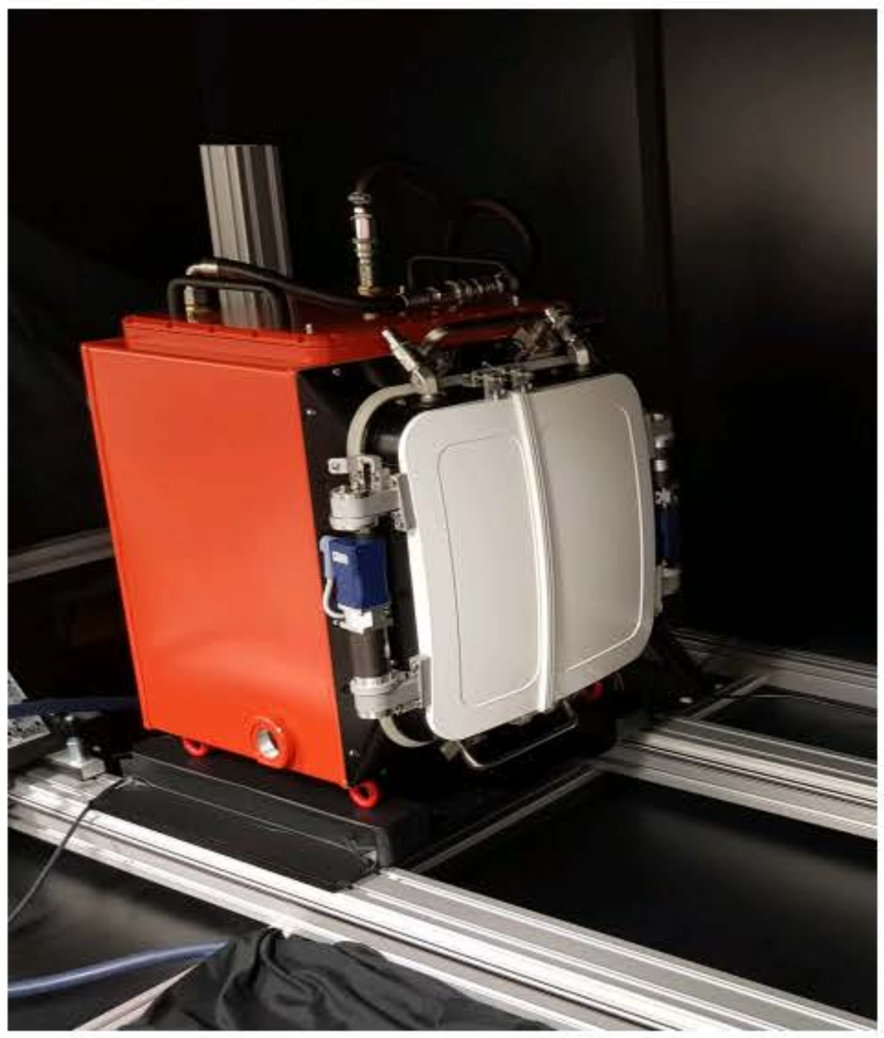

Figure 3.2: This image shows a completed CHEC-S installed in the dark box at the University of Leicester. The dark box is used to provide a dark environment for the verification of CHEC-S with pulsed laser. Upon delivery to MPIK, CHEC-S was installed in a similar setup for continued verification. In addition to this, the liquid coolant pipes can be seen connected to thermal control enclosure at the top of CHEC-S. The thermal control system was first verified in the setup shown.

completed CHEC-S installed within a darkbox at the University of Leicester. With this setup, the liquid cooling and motor controlled doors were evaluated. Finally, the camera was populated with all 32 TARGET Modules and preamplifier buffer boards. CHEC-S and all SiPM tiles were then shipped to MPIK for further characterisation of the Cherenkov camera electronics.

3.2.2 TARGET Module Assembly

The University of Leicester is the lead institute concerning the design, assembly and verification of the TARGET based FEEs for both CHEC-M and CHEC-S. Section 2.4 describes the design and layout of the CHEC-S TARGET Modules, consisting of three

constituent PCB boards. The power board providing power to the TARGET Module; high voltage supply and trimming for the SiPM tile; power for the primary and auxiliary boards containing the analogue shaping circuits, TARGET trigger and digitising ASICs, and a single field programmable gate array (FPGA) installed on the primary board. Figure 3.3 shows the three constituents of multiple TARGET Modules undergoing visible inspection before assembly.

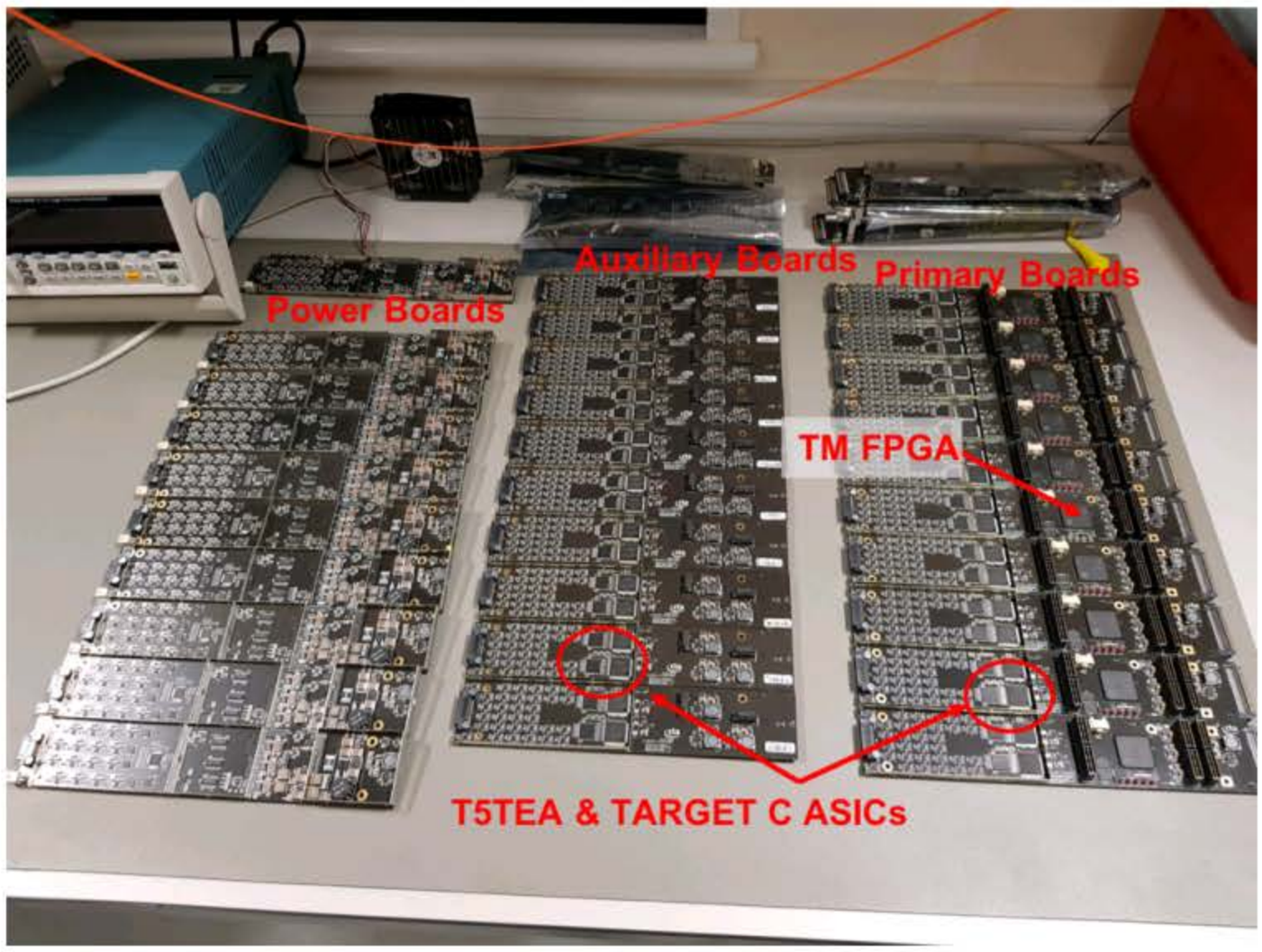

Figure 3.3: Image of the three PCBs of which the TARGET Module is comprised undergoing visual inspection. Highlighted are the three constituent boards, the power board, auxiliary board and primary board. Also highlighted are the trigger and digitising ASICs (T5TEA and TARGET-C respectively) and the TARGET module FPGA aboard the primary board.

During laboratory testing of a fully populated CHEC-S, a large spread in the operating temperature of each TARGET Module was observed across the camera. The highest operating temperatures was observed in TARGET Modules furthest from the thermal control enclosure and cooling fans. In addition to this, TARGET Modules at the side of the camera operated at higher temperatures due to poor airflow and components obstructing the flow of cooling air. The impact of this non-uniform spread in operating temperatures is discussed further in Section 4.5. During routine disassembly

and inspection of CHEC-S it was found that the heatsink of the FPGA of TARGET Modules operating at the highest temperatures had slipped and no longer covered the FPGA as shown by Figure 3.4(a). The cause of this slip was concluded to be due to a phase change material between the heatsink and thermal compound that was not rated for temperatures greater than $\sim 30°$. After this discovery, with my recommendation the FPGA present on all TARGET Modules are now staked with silicone glue during assembly (Figure 3.4(b)) as replacing all heatsinks would be less cost and time efficient and ultimately unnecessary.

(a)

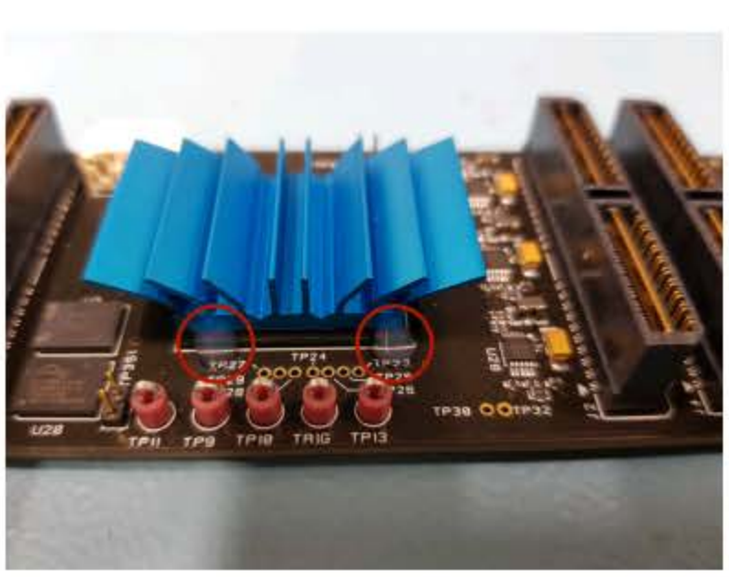

(b)

Figure 3.4: Images of the TARGET module FPGA following high temperatures observed during laboratory testing of CHEC-S. (a) Shows the heat-sink of the FPGA displaced from its nominal position. This slippage was caused by a phase change material that was not rated for such temperatures. (b) Following the observation of displaced heat-sinks, all TARGET module FPGAs are staked with silicone adhesive during the assembly of TARGET modules. This adhesive ensures the heat-sink of the FPGA cannot slip.

Finally, the primary, auxiliary and power boards are assembled into the TARGET Module. Each TARGET Module undergoes functionality testing to verify the operation of the shaping circuitry, T5TEA trigger ASIC, and the TARGET-C digitising ASIC.

It was my responsibility to conduct the functionality testing and produce a performance report containing performance plots of each TARGET module. TARGET Modules that pass this final testing are now inserted into CHEC-S or are used for FEE characterisation via a single TARGET Module laboratory setup.

3.3 CHEC-S Lab Verification

As described in Section 2.2.1, each camera and telescope contribution to the Cherenkov Telescope Array (CTA) must meet specific requirements to be accepted, these include performance, reliability, sustainability, ease of operation and maintenance, and cost. These requirements are necessary to ensure the science goals of CTA [47] can be achieved throughout the lifetime of the telescope array. For CHEC-S, the specific requirements are evaluated through the verification and characterisation of the camera electronics and the performance of CHEC-S under certain environments and stimuli. Such verification can be accomplished through the use of laboratory testing and Monte Carlo simulations. The evaluation of CHEC-S performance with the use of Monte Carlo simulations requires an accurate and representative model describing the camera parameters and performance. Again, such parameters are obtained through the laboratory characterisation of CHEC-S and it's constituents. Presented here is a description of initial investigations towards the verification of CHEC-S conducted during visits to MPIK.

3.3.1 Calibration of the Optical Environment

An accurate characterisation of a Cherenkov imaging camera can be obtained through observations and the analysis of data taken in a controlled dark environment and with the use of injected optical light sources. For CHEC-S, this was performed with the use of a large dark room, a ultraviolet (UV) pulsed laser and a white LED for the simulation of

night sky background (NSB). In order to obtain accurate observations and conclusions of the CHEC-S performance, the input intensity at each pixel produced by the UV pulsed laser must be characterised so that the impact of all parts of the system including CHEC-S electronic components can be determined. The variation in pixel illumination intensity is due to both the uniformity of the UV pulsed laser and variation in pixel positioning.

In addition, certain investigations concerning the SiPM and FEE response require a uniform and homogeneous input in addition to the uniform gain matching of photonsensors described further in Section 2.4.2 again, this also requires a well characterised illumination profile. The illumination profile of the UV pulsed laser was measured using a single SensL reference SiPM and a robot arm allowing for the probing of intensity at each pixel position in the X-Y plane. At each pixel position, the measured illumination intensity was compared to the intensity at the centre the camera focal plane position. By calibrating the laser illumination profile in this manner, a correction factor was produced which describes a multiplicative coefficient that can be applied to the measured waveform of each pixel, producing an absolute uniform and homogeneous intensity providing each SiPM pixel was precisely gain matched. Figure 3.5(b) indicates the correction factor describing the illumination profile of the UV pulsed laser measured at the location of the camera focal plane. The result of not applying this correction would be a non-uniform response measured across all SiPM pixels, it must therefore be applied when a homogeneous illumination profile is required.

As discussed in Section 2.4, CHEC-S comprises a curved focal plane housing the SiPM tiles. The curvature of this focal plane gives rise to a variation in pixel position in the X, Y, and Z axes. Since CHEC-S is designed for use with a dual-mirror Schwarzchild-Couder based telescope, a curved focal plane is required to mitigate tangential and sagittal astigmatism [72]. Whilst the correction for laser beam uniformity corrects for the optical output of the UV laser, it does not account for the disparity in intensity due to the variation of pixel positions in the $Z - axis$, and hence distance from the UV laser. Since

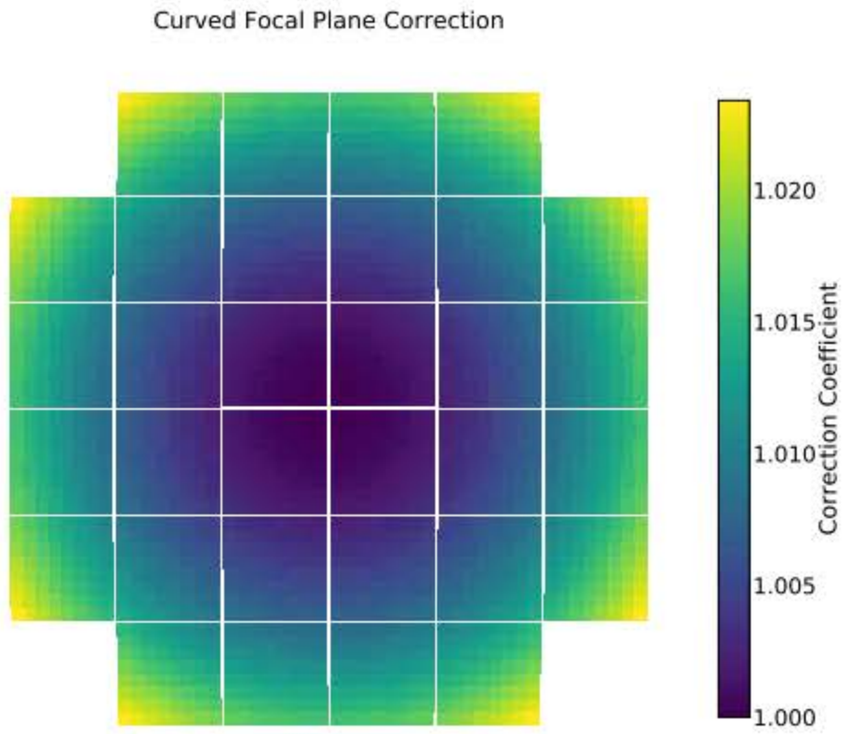

(a)

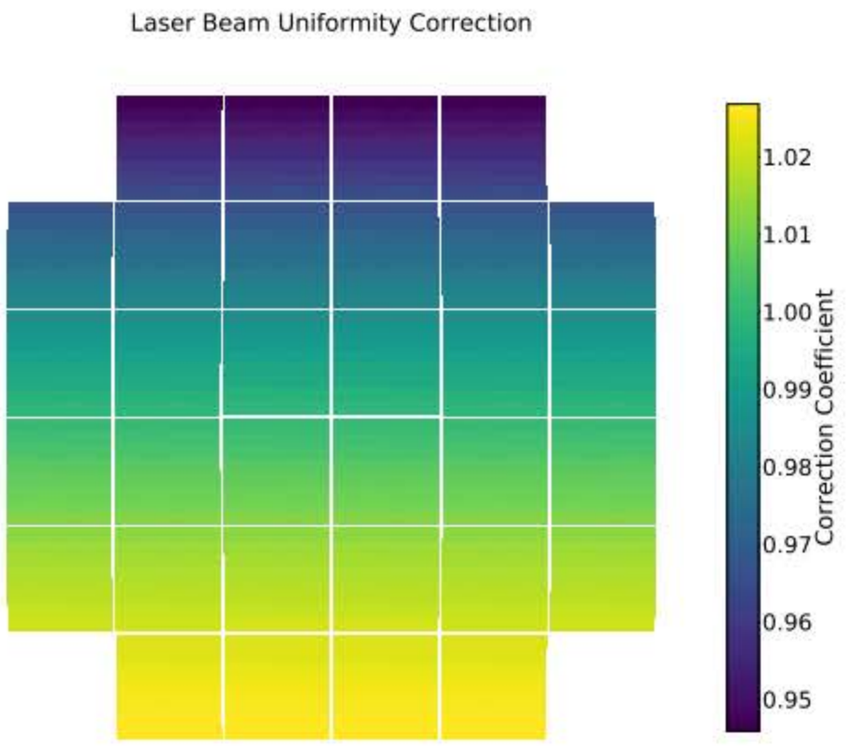

(b)

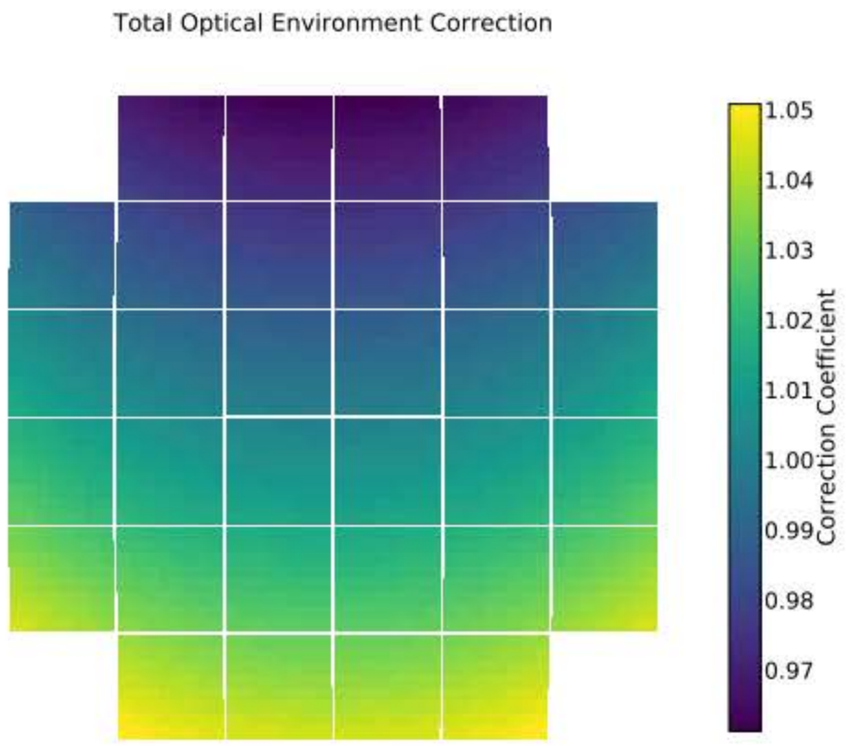

(c)

Figure 3.5: Camera images showing the required correction coefficients describing the optical environment within the dark chamber at MPIK. (a) The correction coefficient per pixel for the correction of CHEC-S geometry and the curved focal plane. SiPM pixels at the centre of the focal plane are closer to the pulsed UV laser and hence require no correction. (b) The correction coefficient describing the correction required for the laser beam non-uniformity. This correction was measured in a flat plane at the position of the CHEC-S focal plane. (c) The total correction coefficient, describing the combined correction factors of (a) and (b). By applying this correction factor, the input intensity at each pixel position should be uniform across the focal plane, variations that remain are due to non-uniformity in the gain matching of SiPM pixels and effects of the electronics for each channel.

the output of the laser results in a flat wavefront at the centre of the camera focal plane following the laser beam uniformity correction, pixels located further from the centre of the optical axis will be at a distance further from the output of the UV laser. As light

intensity follows the inverse square law ($Intensity \propto \frac{1}{distance^2}$), the intensity observed by pixels towards the edge of the camera focal plane will be less than that observed at the centre.

Figure 3.5(a) represents the correction factor required to mitigate the variation in intensity at each pixel due to the curved focal plane. I determined this correction factor by considering the varying distance of each pixel from the laser source. I measured distance from the laser to the centre of the CHEC-S focal plane in the darkroom laboratory ~~wise~~. I then obtained the variation in optical path length using the 3-dimensional pixel positions produced by the CAD design of the camera. Finally, by comparing the variation in optical path length for all pixels, I was able to calculate the difference in laser light intensity compared to pixels at the centre of the camera, resulting in the correction factor. Figure 3.5(c) shows the correction factor required to correct for intensity variation for both laser beam non-uniformity and intensity disparities due to the curvature of the CHEC-S focal plane. This correction factor was to be applied when a uniform input intensity was necessary for laboratory investigations.

3.3.2 Trigger Verification

Section 2.4.3 describes the trigger regime utilised by imaging atmospheric Cherenkov telescopes (IACTs) [43]. As described, IACTs utilise a two-level trigger criteria during Cherenkov light observations in order to mitigate the effect of NSB by reducing the frequency of NSB induced triggers. Firstly, for CHEC-S, the analogue sum of four pixels in a 2x2 square (known as Super Pixel, SP) must be greater than a configurable threshold level set within the camera operating software. This first level criteria is evaluated by the four T5TEA trigger ASICs present on each TARGET Module. Following a successful level-one (L1) trigger, a trigger signal is sent to the trigger FPGA present on the backplane, containing a timestamp and the SP identification for all SPs surpassing the L1 trigger.

The level-two (L2) trigger states that two or more nearest neighbour SPs must have produced L1 triggers within a given coincidence window. The nearest neighbour criterion extends to all nearest SPs, including neighbouring SPs on adjacent SiPM tiles. Figure 3.6(a) highlights the possible nearest neighbour trigger combinations for a single SP at the centre of a SiPM tile, SPs at the edge of the camera focal plane have fewer possible neighbours. Following a successful L2 trigger, a readout request is issued by the backplane trigger FPGA to all TARGET modules. The L2 trigger logic reduces the probability of NSB photons forming a camera trigger and hence reduces the volume of data requiring storage and analysis. Characterisation of the L1 trigger was completed by members of the CHEC team at MPIK. During a visit, I performed an investigation ~~for the verification of~~ to verify the L2 trigger logic, including the SP trigger mapping and an evaluation of the nearest neighbour trigger logic.

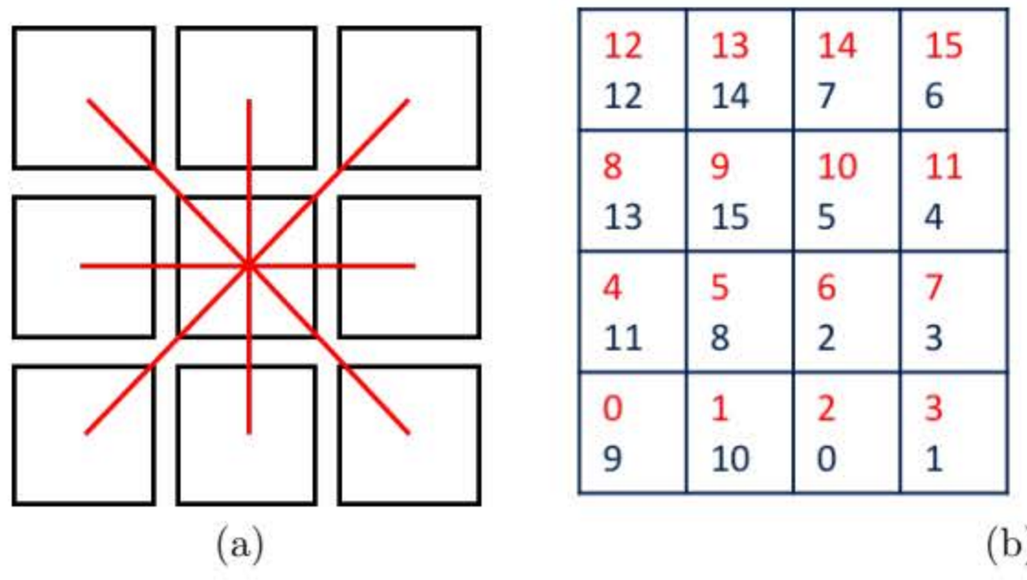

(a) (b)

Figure 3.6: (a) Indicates the number of nearest neighbours per CHEC-S trigger super pixel. The super pixel represents the four pixels combined for the level-one triggering of CHEC-S. The level-two trigger logic states that two nearest neighbour super pixels must produce a trigger signal within a specified coincidence window. This image shows eight nearest neighbour super pixels surrounding a central super pixel and represents the neighbouring pixels that can produce a level-two trigger. (b) Represents the super pixel mapping per CHEC-S SiPM tile. The disparity shown here is to indicate the expected and measured mapping of the super pixels. Following this determination the mapping was updated to match that of the SiPM bias voltage setting mapping (black).

Chapter 5 discusses the observations and performance of CHEC-S and the ASTRI-Horn telescope structure during an on-telescope observing campaign. Throughout this campaign, a number of sources with varying starfields were observed. As the SiPMs

utilised by CHEC-S are sensitive to UV and visible light, the light emitted by bright stars produces a response in pixels covered by such stars. It is possible for large, bright stars to cover multiple pixels, inducing an increased charge observed by each pixel. Pixels containing bright stars can surpass the L1 trigger criterion in the absence of Cherenkov light reducing the trigger efficiency. For such cases, it is possible to mask pixels containing bright stars, removing such pixels from the L2 trigger logic, reducing incorrect camera triggers. I ensured that the correct mapping of SP masks was verified by evaluating the trigger signal produced by various trigger combinations. During this test, all combinations of SP pairs from a single TARGET Module were enabled and the trigger output determined. Figure 3.6(b) shows the possible mapping of SPs: the black SP index shows the expected SP mapping matching that of the mapping for setting SiPM bias voltage per high voltage group; and red the mapping of SPs for the previous prototype camera, CHEC-M. By evaluating the presence or absence of a trigger signal for a given SP pair combination it was determined that the current SP mapping matched that of the CHEC-M mapping. This mapping was then changed to match that of the SiPM bias voltage setting for simplicity.

Following the evaluation of the SP trigger mapping, the nearest neighbour trigger logic could be verified. Figure 3.7 shows the 1910 possible nearest neighbour combinations for each SP within CHEC-S, indicated by the adjoining line from each SP. Again, to verify each of the nearest neighbour combinations, the HV and trigger mask of two SPs was enabled and the trigger logic tested, this was repeated for all valid combinations. Figure 3.8(a) shows the expected output of the nearest neighbour trigger logic verification. The colour scale indicates the number of nearest neighbour combinations resulting in an L2 camera trigger per SP. The measured L2 trigger performance of CHEC-S can be seen in Figure 3.8(b), shown here is a large discrepancy from the expected result. *Wbias* is a configurable parameter set within the TARGET module configuration which describes the length of the output trigger signal of the T5TEA ASIC following a successful L1 trigger. The length of the L1 trigger signal (*Wbias*) was increased and the nearest neighbour logic

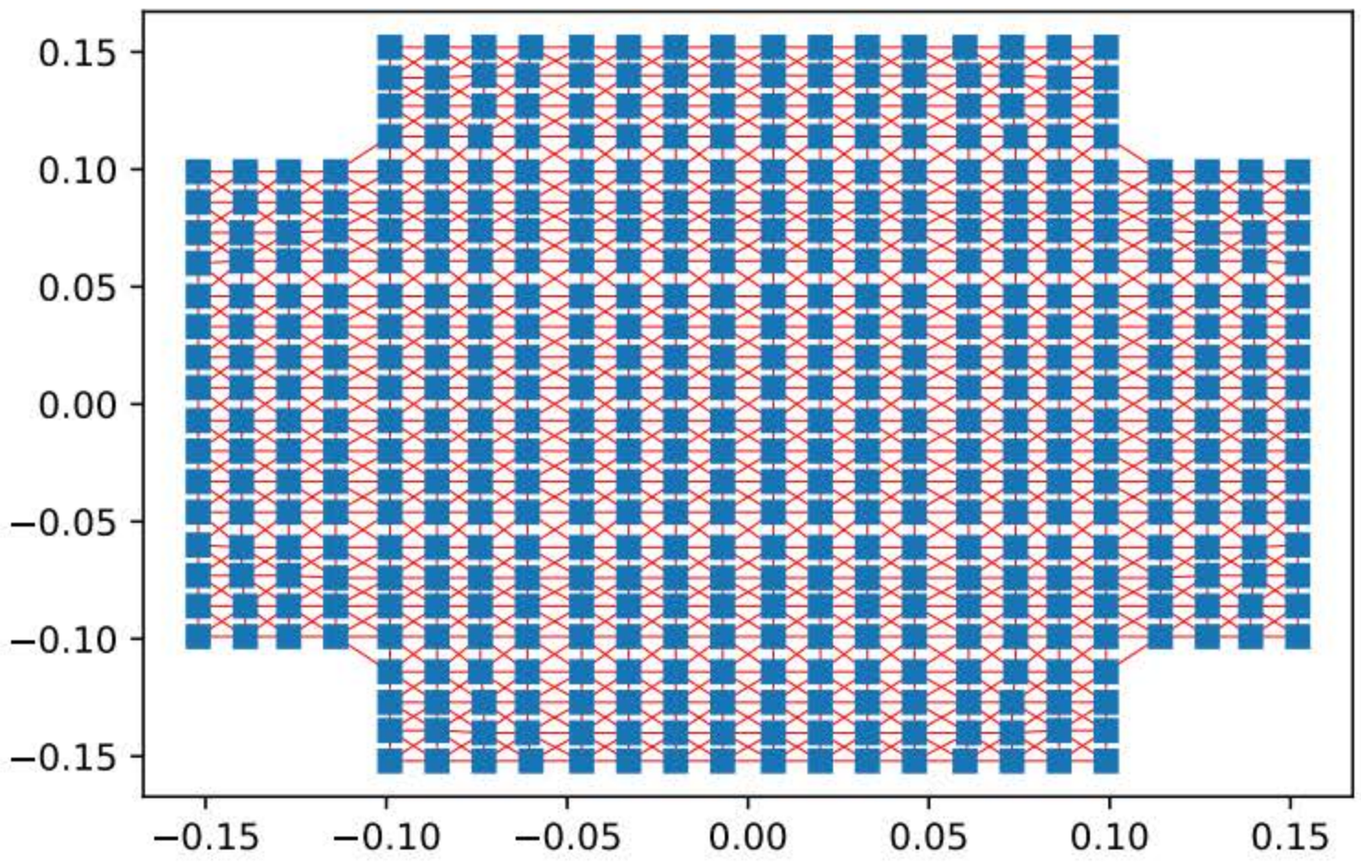

Figure 3.7: Plot showing all nearest neighbour combinations for all super pixels of CHEC-S. The red lines shown here connect super pixels (blue) indicating nearest neighbour combinations. This was used to determine the number possible nearest neighbour combinations (1910) in addition to the nearest neighbour combinations to super pixels of neighbouring TARGET modules.

test repeated resulting in the number of successful nearest neighbour combinations shown in Figure 3.8(c). By increasing the *Wbias*, it is possible to accommodate for the skew between channels. SPs with 0 nearest neighbours indicate a SP that formed no valid triggers with any neighbouring SPs, The large number of non-triggering SPs on the left of the focal plane were produced by a disconnected TARGET Module and expected. It was later determined that the remainder of non-triggering SPs were caused by a SiPM high voltage stability issue. Following the resolution of the SiPM HV stability, the trigger performance was further evaluated to investigate trigger rate and efficiency [94].

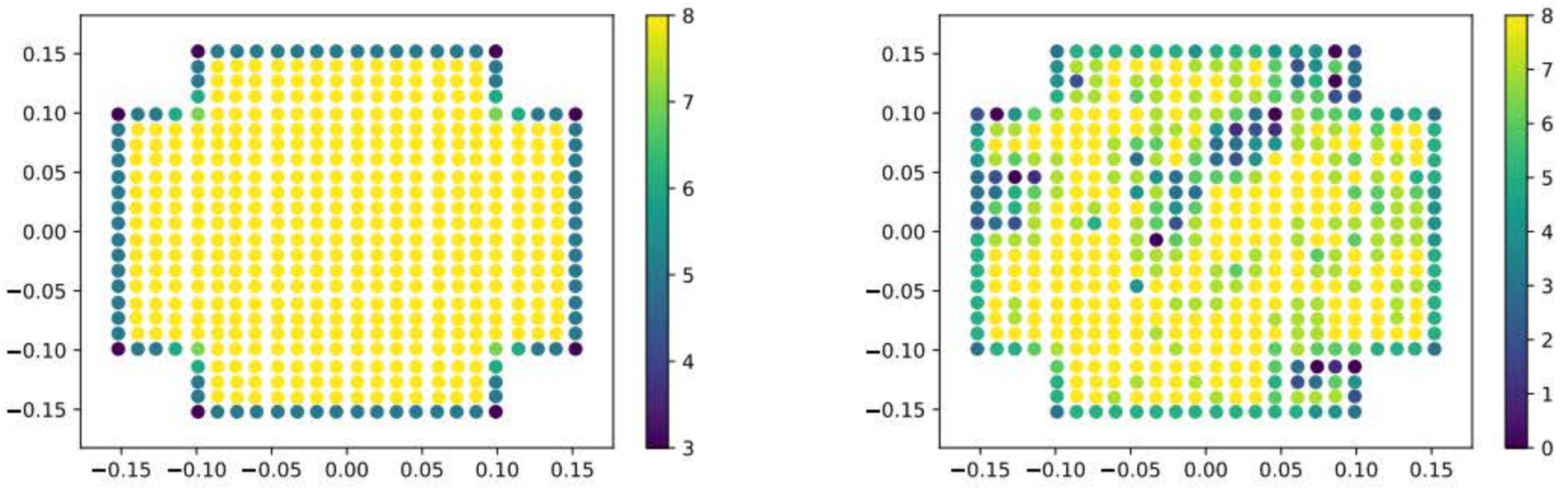

(a)

(b)

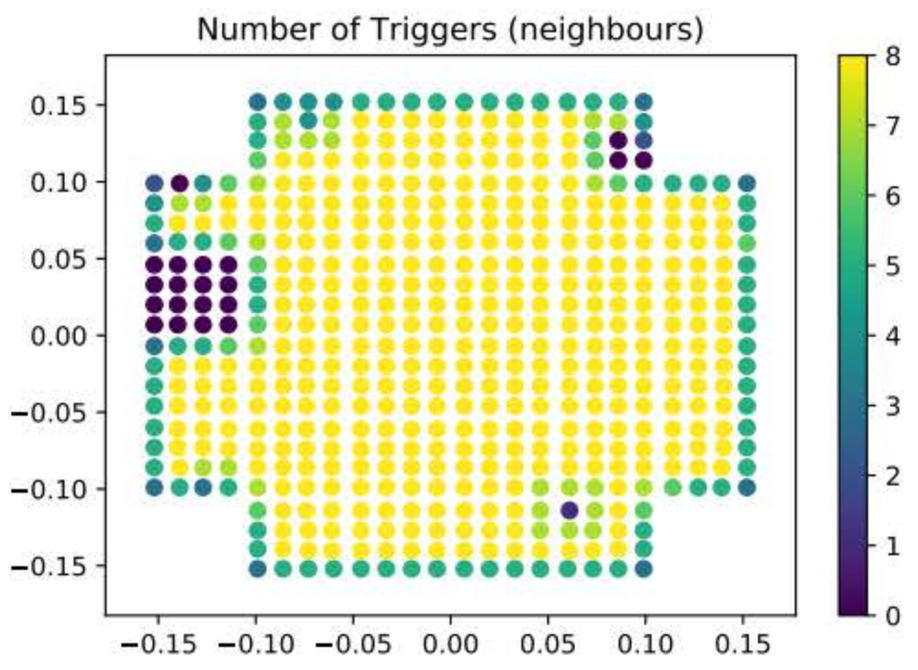

(c)

Figure 3.8: Camera images describing the nearest neighbours and level-two trigger logic following verification of each individual nearest neighbour combination. (a) Shows the ideal output following verification of the level-two trigger with all super pixels producing triggers with all possible combinations. (b) Shows the number of confirmed nearest neighbour combinations following verification. It can be seen that there is a large number of super pixels with reduced trigger efficiency, some of which producing zero triggers. (c) The measured number of combinations per super pixel following the increase in the width of the level-one trigger signal (*Wbias*). During this repeat a TARGET module was removed for diagnostics, indicated by the large number of zero triggers to the left of the camera image. The remaining inefficient super pixels were ~~again removed following~~ corrected by the resolution of a SiPM high voltage stability issue.

3.4 Single TARGET Module Lab Verification

In addition to the full camera investigations conducted at MPIK, numerous test facilities across CHEC member institutions were utilised in the further investigations of camera

component electronics and subsystems. The University of Leicester was responsible for the development and verification of the FEEs including the SiPM tile, preamplifier buffer board and TARGET Module. Investigations conducted at the University of Leicester utilised both pulsed laser and electronically injected stimuli to evaluate the response of CHEC-S FEEs and further the verification and characterisation of CHEC-S.

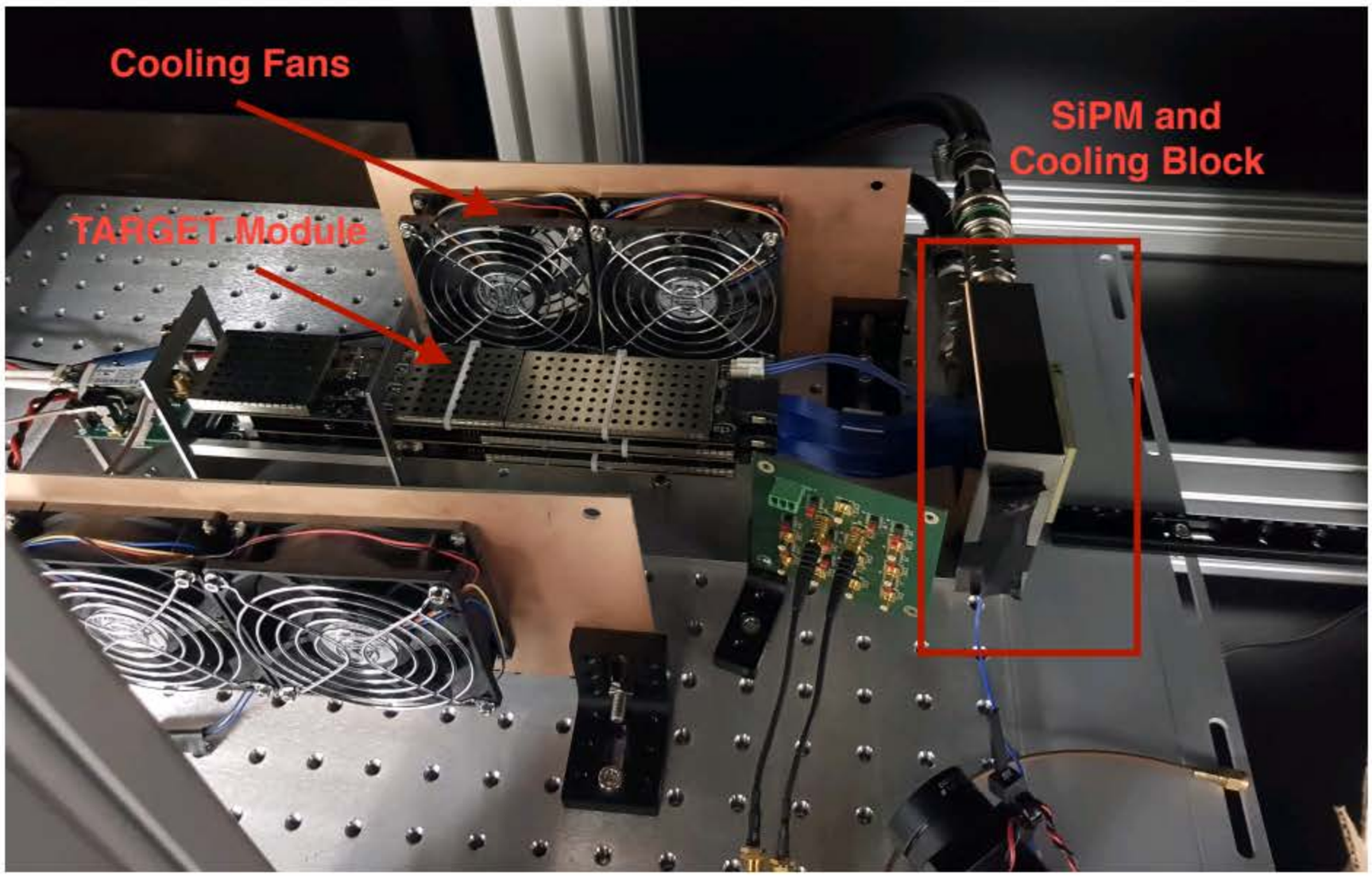

Figure 3.9: Image showing a single CHEC-S TARGET module installed in the dark box at the University of Leicester for verification with pulsed laser light. The TARGET module is connected to the preamplifier buffer board and SiPM tile via the blue Samtec cables identical to the connection within CHEC-S. A readout boad is connected to the *back* of the TARGET module, in place of the CHEC-S backplane and is used to control and readout data from the TARGET module. As shown, the SiPM tile is installed on an aluminium cooling block using the same liquid cooling approach as CHEC-S. This maintains a temperature of $\sim 16°C$ during investigations. In addition to this, cooling fans are used to reduce and stabilise the temperature of the TARGET module.

Figure 3.9 shows a single TARGET Module and SiPM chain installed on an optical bench for verification under laser stimulation. The highlighted cooling fans and

liquid cooling block are used to replicate the thermal control present within CHEC-S and to ensure a stable thermal environment for photosensor and electronics, both of which are sensitive to thermal dependencies. The use of such setup is for the verification of both the CHEC-S SiPM and FEE using a pulsed laser. It is possible to modify the setup presented here with the use of an arbitrary waveform generator and signal splitter board to inject electronic pulses directly into the TARGET Module or preamplifier buffer board. The electronically generated input pulses represent the output of the SiPM in the absence of SiPM related noise such as: optical crosstalk (OCT); dark counts; and afterpulsing. Such electronically generated inputs are used for the verification of the preamplifier buffer board and TARGET module electronics. In addition to this, electronically injected pulses are used in the production of calibration data (Section 4.4).

3.4.1 Splitter Board Variation

The CHEC-S splitter board is designed to split a single analogue input source into many outputs whilst maintaining the shape of the original pulse. The output is then injected into the various channels of the preamplifier buffer board, or directly into the input of the TARGET module, simulating the output of the SiPM or preamplifier. The analogue signal subsequently propagates through the TARGET module, including the fast shaping electronics and digitising ASIC, where it is subject to identical influences as the SiPM output is. The use of the splitter board ~~is therefore necessary, as it is possible~~ to characterise and verify the performance of the preamplifier buffer board and TARGET Module without the introduction of SiPM effects within the digitised signal.

As described in Section 2.4.3, the digitised waveform encompasses the performance of the CHEC-S FEE chain, including that of the SiPM, preamplifier buffer board, shaping electronics, and TARGET-C digitising ASIC. In order to interpret the affect of each component in the FEE chain, an input signal can be injected at multiple locations

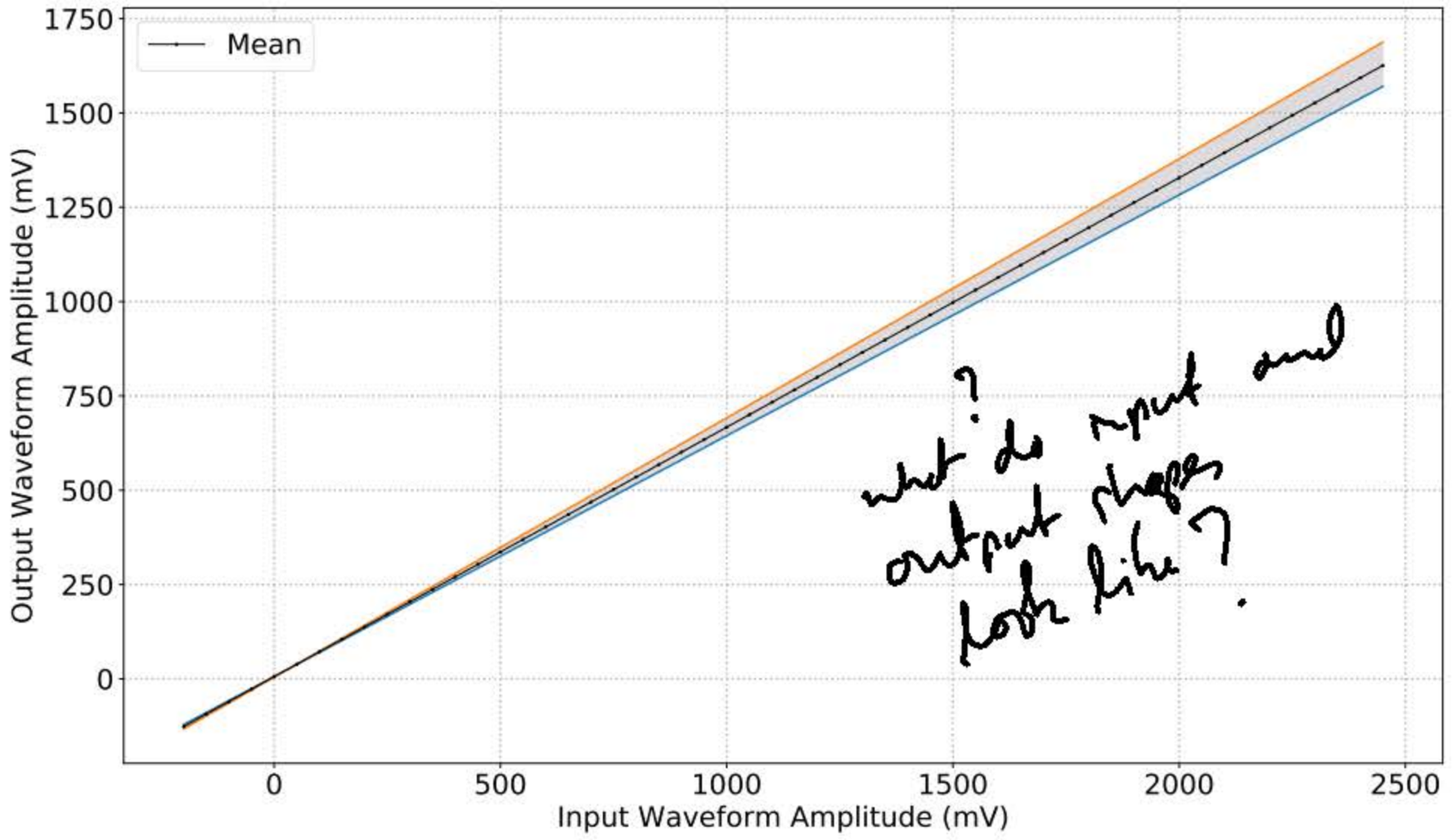

Figure 3.10: Variation in the measured output of the CHEC-S splitter board at varying input amplitudes. Shown here is the waveform peak amplitude at the output of the CHEC-S splitter board averaged across all 16 channels. The spread in amplitude across all channels is indicated by the grey shaded region between the highest and lowest measured output. The variation in setting and measured waveform peak amplitude in addition to the non-uniform response across all channels indicates the need for characterisation since multiple splitter boards are used at numerous SST Camera institutes for the verification of the front end electronics.

along the chain. Removing components of the FEE chain, by injecting electronic pulses after such components, the performance of the remaining chain constituents can be evaluated. Again, to understand the affect of each component on the digitised waveform, the exact shape of the input signal needs to be known. Much like the illumination profile described previously, it is necessary that the CHEC-S splitter board is characterised and the input to each channel in the FEE chain is well understood.

Figure 3.10 shows the amplitude of the analogue waveform at the output of the CHEC-S splitter board at varying input amplitudes. Shown here is the spread in measured peak amplitude across all channels indicated by the shaded region in addition

to the average waveform peak amplitude. This output corresponds to the input signal injected into either the preamplifier buffer board or TARGET Module. It can be seen that there is a disparity in the set peak amplitude of the input waveform and the measured amplitude of the output waveform indicating a signal loss as the input signal is split into multiple outputs. Whilst this is not ideal, the linear response at varying input amplitudes is as expected and can be corrected for providing the output amplitude is characterised similarly to the correction applied for the illumination profile described previously. In addition to this, and more importantly, there is a relatively large spread in the amplitude measured across all channels. As stated before, the ~~use of the~~ CHEC-S splitter board is (used to provide an input source for multiple channel verification. The characterisation and verification of the preamplifier buffer board and TARGET Module components rely on knowledge of the input source for each channel.

? what is the reason for the spread in outputs?

? How much spread is there for one channel?

Previous investigations utilising the CHEC-S splitter board had underestimated the losses present in the splitter board. The losses to the electronic signal results in an output signal with a reduced amplitude compared to the expected output amplitude. I have shown this by the disparity of the amplitude in the input and output waveform shown by Figure 3.10. Clearly, underestimating the amplitude of the electronic signal at the output of the CHEC-S splitter board, and hence input of the preamplifier buffer board or TARGET Module, has a profound impact on the verification approach for (the CHEC-S FEEs). The verification of CHEC-S requires knowledge of the input signal as the performance of the electronic components is determined by comparing the digitised waveform output to that of the input waveform and deducing the impact of each component within the FEEs. Section 4 discusses the calibration of the TARGET-C digitising ASIC resulting in a transfer function (TF) describing the conversion of analogue-to-digital converter (ADC) counts to voltage. The voltage described by the TF relates directly to the input voltage of the electronic signal used to produce such calibration data. The accuracy of the calibration data is therefore reliant on knowledge of the injected signal amplitude from the the CHEC-

verbose!

S splitter board. By underestimating the amplitude of the input signal, the TF, and hence calibrated data, is inaccurate. In addition to this, the verification of CHEC-S FEE and the production of TARGET Module calibration data is conducted at multiple institutions, each utilising the CHEC-S splitter board. I found that the variation induced by the splitter board is much higher than previously thought and as such recommended that all institutes must characterise the CHEC-S splitter board to ensure the characterisation, verification and calibration performed at each institute are subject to accurate input amplitudes. Without accounting for the variation in splitter board outputs, the results obtained at various institutes are incomparable.

3.4.2 SiPM Angular Response

Section 2.3.1 describes the various telescope structures utilised by CTA, with a discussion on the mechanical and optical design of the Small Sized Telescope (SST). The dual-mirror Schwarzschild-Couder design of the SST produces an optical path such that the reflected Cherenkov photons impinge on the CHEC-S focal plane, and thus SiPMs, at incident angles in the range of 30° - 60° [95]. It is therefore important that the performance of CHEC-S SiPMs is evaluated at varying incident angles.

The angular dependence of the CHEC-S SiPM tile was measured using a similar setup to that shown in Figure 3.9 with a diffuse pulsed laser attached to a rotating optical rail. The optical path length was fixed and the rail allowed to rotate about the SiPM tile between -20° and +80°. The laser was positioned such that it was incident at the centre of the SiPM tile. All pixels in the vertical axis at the centre of the SiPM tile were evaluated as the optical path length for pixels either side of the central column vary as the angle of incidence is varied resulting in varying intensities across the SiPM tile. Lambert's cosine law [96] describes the variation in photon flux impinging an illuminated area as a function of the incident angle. It can be used to determine the intensity observed at the surface of

the SiPM tile as a function of the angle of incidence as follows:

$$I_\theta = \frac{I_0}{cos(\theta)} \tag{3.1}$$

where I_0 is the intensity observed with the laser positioned at the normal to the SiPM tile. Here $\frac{1}{cos(\theta)}$ describes the correction factor for the variation in intensity as the laser beam spreads across the tile due to the angle of incidence (θ). This correction coefficient must be applied to the digitised waveform to account for the spread in illuminated area as the pulsed laser rotates about the SiPM tile.

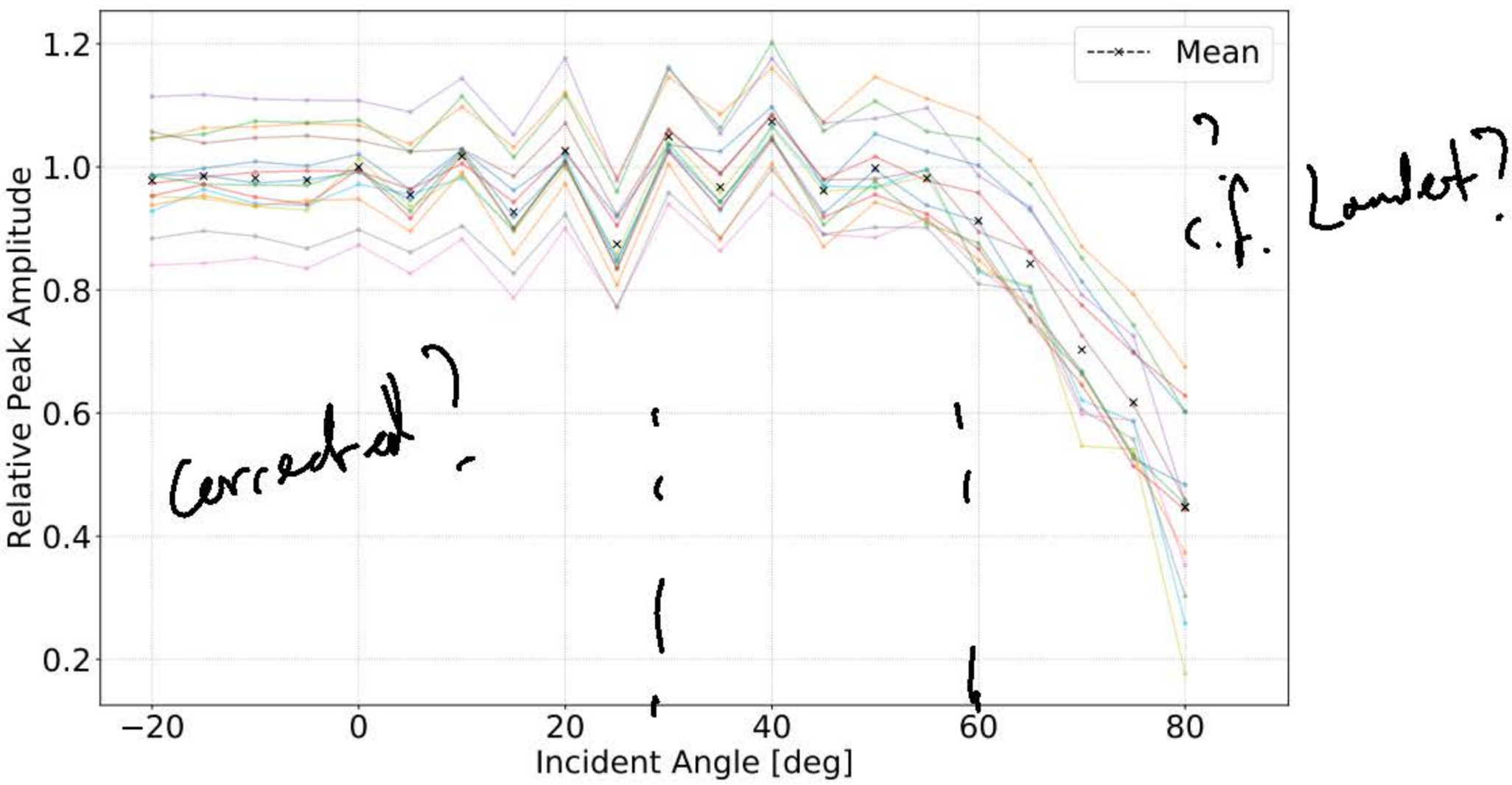

Figure 3.11: Angular dependence of the CHEC-S SiPM tile. Shown here is the measured waveform peak amplitude of pixels in the central column of the CHEC-S SiPM tile, relative to the average peak amplitude measured with an incident angle of 0°, as a fixed intensity pulsed laser is rotated about the centre of the tile. Observations of Cherenkov light on-telescope produces a wavefront which interacts with the CHEC-S focal plane at incident angles ranging from 30° to 60°, the performance here shows that the CHEC-S SiPM tile is well suited for such applications.

At each incident angle the amplitude of the digitised waveform was measured

and the correction coefficient applied as per Equation 3.1. Figure 3.11 shows the resulting angular dependence of the CHEC-S SiPM. The range in incident angle here was used to show the performance of the SiPM at all necessary angles surpassing that of the expected angle of incidence for Cherenkov events observed on-telescope. In addition to this, the range -20° to 0° is included to show a symmetrical response in both positive and negative incident angles, any disparity in the positive and negative incident angles would suggest a misaligned optical setup.

Figure 3.11 shows the measured peak amplitude at each incident angle relative to that of the average measured waveform amplitude with the pulsed laser positioned normal to the SiPM tile. The angular dependence of each pixel from the central column of the SiPM tile is included to indicate the spread in relative peak amplitude as well as the uniform response of each pixel to the varying incident angle. It can be seen that the angular dependence of the SiPM is relatively low as the measured peak amplitude produces a flat response until dropping to 95% at $\sim 58°$. The response shown here indicates that the SiPM utilised by CHEC-S surpasses the required performance for use with a dual-mirror Schwarzchild-Couder telescope.

check actual angular range !

Chapter 4

Calibration of the TARGET-C digitising ASIC

Contents

4.1 Introduction

The CHEC-S front-end electronics (FEE) utilise the TeV Array Readout with GSample/s Sampling and Event Trigger (TARGET) application specific integrated circuit (ASIC) [78]. Each CHEC-S front-end module (TARGET module, TM) houses eight TARGET ASICs of two types: T5TEA for event triggering and TARGET-C for signal sampling and digitisation. Each ASIC requires the application of multiple calibration steps in order to produce meaningful, accurate results from the raw signal outputted by the silicon photomultiplier (SiPM). A main focus of my doctoral research concerns the calibration of the TARGET-C digitising ASIC, covering the production of data to be used in the calibration, the generation of calibration files, and the methods of using calibration data to correct for various effects within the raw data, including the correction of temperature dependence and saturation effects.

At the time of my joining the CHEC project, the method for digitiser calibration had been investigated at great length in both the CHEC-M [81] and CHEC-S [97] prototypes. A calibration pipeline had also been created for the application of the calibration data to the raw digitised data. A large contribution of my research was to improve upon the calibration method and investigate the possibility of using different methods for generating calibration data from the raw input data. Whilst only a small focus of my research (Section 3.3.2), a comprehensive study and characterisation of T5TEA has been completed by other members of the CHEC team [94].

In this chapter I will describe both the previous and current methods of calibrating the TARGET-C ASIC. I will then discuss the implementation of this calibration method and the performance gained in adopting this new approach. Finally, I will outline the method of and performance gained by correcting for the temperature and saturation effects of TARGET-C.

4.2 TARGET-C Digitising ASIC

The T5TEA and TARGET C ASICs are based on the TARGET 7 ASIC, utilised on the CHEC-M prototype [90]. Figure 4.2 shows the functional block diagram of TARGET 7, the architecture in this diagram is identical to the combined structure of both T5TEA and TARGET C. TARGET C is being represented by the three blocks to the right of the trigger block, which represents the T5TEA ASIC. It can be seen that each TARGET C ASIC consists of a sampling array, storage array and a Wilkinson ADC [98] for 16 input channels. The sampling array comprises two blocks of switched capacitor arrays (SCAs) [91] containing 32 cells (physical capacitors). These blocks are operated in "ping-pong" mode, whereby the output of the SiPM is sampled by one block as the other block is buffered to the storage array. The storage array also consists of SCAs, specifically 512 blocks containing 32 cells per block. The output of the SiPM is continuously sampled and stored by the TARGET-C ASIC in a 16384 sample deep analogue buffer, of which only 4096 samples are used for CHEC-S [92]. Following a successful trigger signal (see Section 2.4.3) a portion of the deep analogue ring buffer corresponding to the readout window sample size and trigger delay time is digitised by the Wilkinson ADC. The output of the Wilkinson ADC is a digitised value per sample corresponding to the counts of the Wilkinson ADC ramp register, hereafter referred to as ADC counts.

As the shaped analogue signal propagates through the sampling and storage arrays of the digitising ASIC, passing from one switched capacitor to another, a non-linearity is induced. This non-linearity is produced by the charging and discharging of the switched capacitors and is observed in the digitised signal. The non-linear response of TARGET-C is most obvious when comparing multiple input voltages, for example: if two input signals with an amplitude of 1V and 500mV respectively are injected into the TARGET-C digitising ASIC, the resulting amplitude of the digitised waveform of the 1V input signal would not be twice that of the 500mV input signal. A transfer function (TF)

describes the conversion of input voltage to ADC counts of the digitising ASIC covering the dynamic range and is used to correct for the non-linear response of the TARGET-C ASIC. Since each cell in the deep analogue ring buffer corresponds to a unique switch capacitor, a TF must be produced for every cell of each of the 64 channels present on a TM. An example of the TF for the first cell of each 64 pixels is shown in Figure 4.1, also present is the saturation effect observed at higher input amplitudes (discussed further in Section 4.6.1). For CHEC-S, the cell by cell TFs are stored in a lookup table as a calibration file to be applied to the digitised data as a conversion of ADC counts to voltage, thus removing the non-linear response of the TARGET-C ASIC.

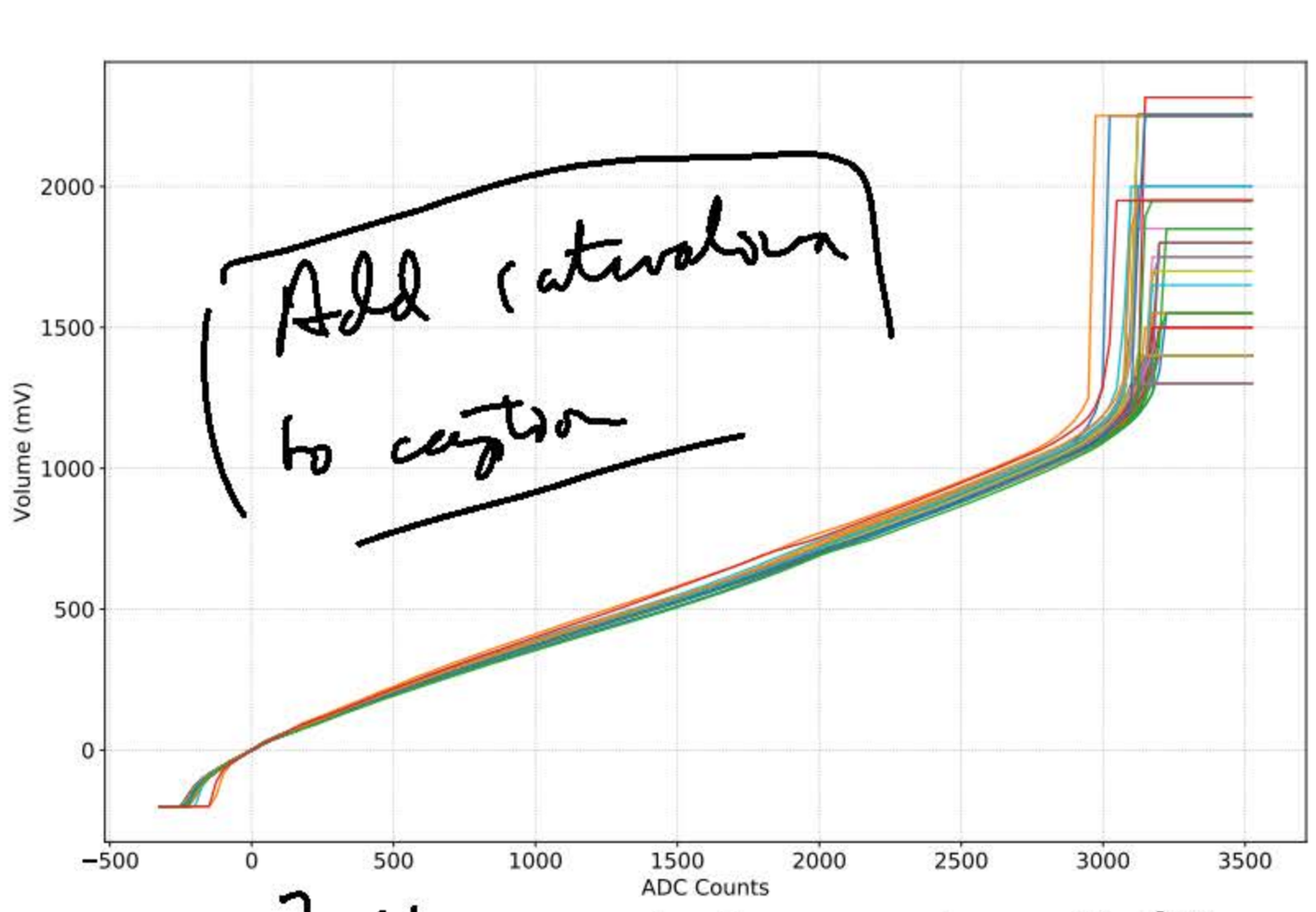

Figure 4.1: An example of the Transfer Function calibration dataset. This plot highlights the conversion of ADC counts to voltage for the first sampling cell of a CHEC-S TM containing 64 channels. This Transfer Function is necessary for the calibration of non-linearity induced in the digitisation of electronic signals.

The methods used to generate calibration files for the calibration of TARGET-C are described here, initially covering the previously developed methods before discussing the improvements made to these calibration approaches, of which the latter represents the

authors research.

The application and processing of the calibration data described here, was performed using the CHEC-S specific software, CHECLabPy [99]. The new methods that I propose for generating calibration data and for evaluating the performance of such methods was completed using my own standalone python scripts.

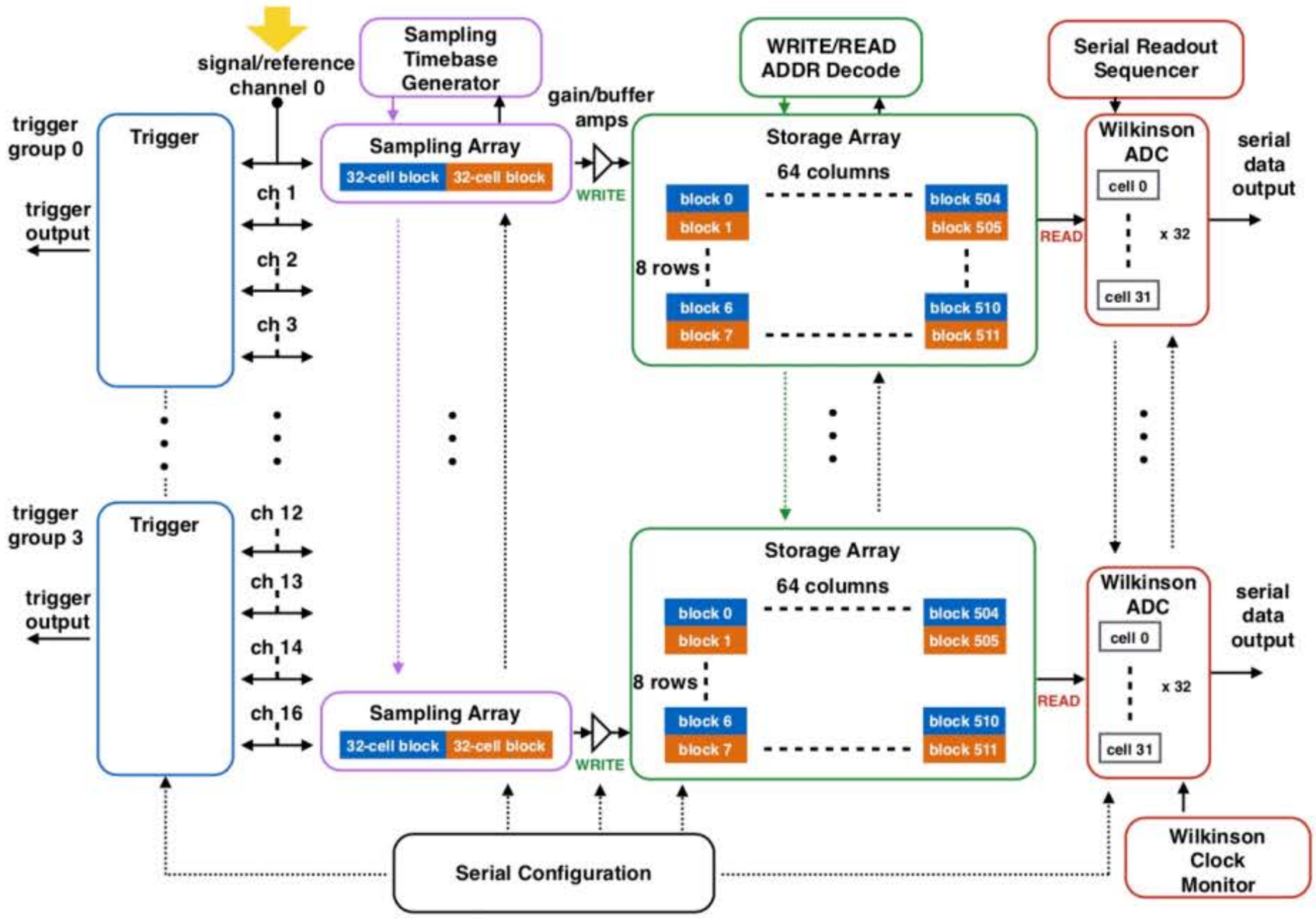

Figure 4.2: Functional block diagram representing the architecture of TARGET 7. This architecture is identical to the combined layout of T5TEA and TARGET C. T5TEA is represented by the trigger blocks to the left of the *signal/reference* (yellow arrow). The remaining block diagram represents the TARGET C digitising ASIC [90]. Here the propagation of the CHEC-S analogue signal can followed through the sampling array, storage array, and Wilkinson ADC.

4.3 Pedestal Calibration

As each of the 4096 storage cells comprises a unique switched capacitor, there is an apparent feed-through error produced by the residual charge of each capacitor [100]. Since

each sample in the CHEC-S digitised waveform corresponds to a specific storage cell, and hence switched capacitor, each sample contains a residual pedestal value which must be removed with a pedestal subtraction to produce a uniform and accurate response. Figure 4.3 shows an example of a digitised waveform before and after pedestal subtraction. The cell-to-cell variation of the pedestal value is very large in the raw R0 data, the impact of residual charge impacts the performance CHEC-S at low amplitude inputs. As described previously, each storage cell is arranged in a physical block of storage capacitors, grouped in blocks of 32 cells. Since adjacent blocks are not entirely decoupled from one another, the stored charge of one block may effect the charge stored in neighbouring blocks. It is because of this that the amplitude of the pedestal value depends on both the position of the storage cell within the digitised waveform and the signal charge of the storage capacitor. This is observed as the large drops in the R0 data of Figure 4.3.

A pedestal calibration file consists of a lookup table containing the pedestal values to be removed from each storage cell of the TM. The pedestal data is produced in calibration data runs where the high voltage of the silicon photomultiplier (SiPM) is disabled, removing any charge produced by dark counts. The camera is then set to trigger either internally or externally so that the digitised data contains only the pedestal values of the ASIC storage cells. A large enough dataset is required so that a reasonable average of each storage cell residual charge can be measured. The pedestal value of each storage cell is also dependent on the temperature of the ASIC itself. A new pedestal calibration dataset is produced before each observation run to ensure the temperature induced residual is removed.

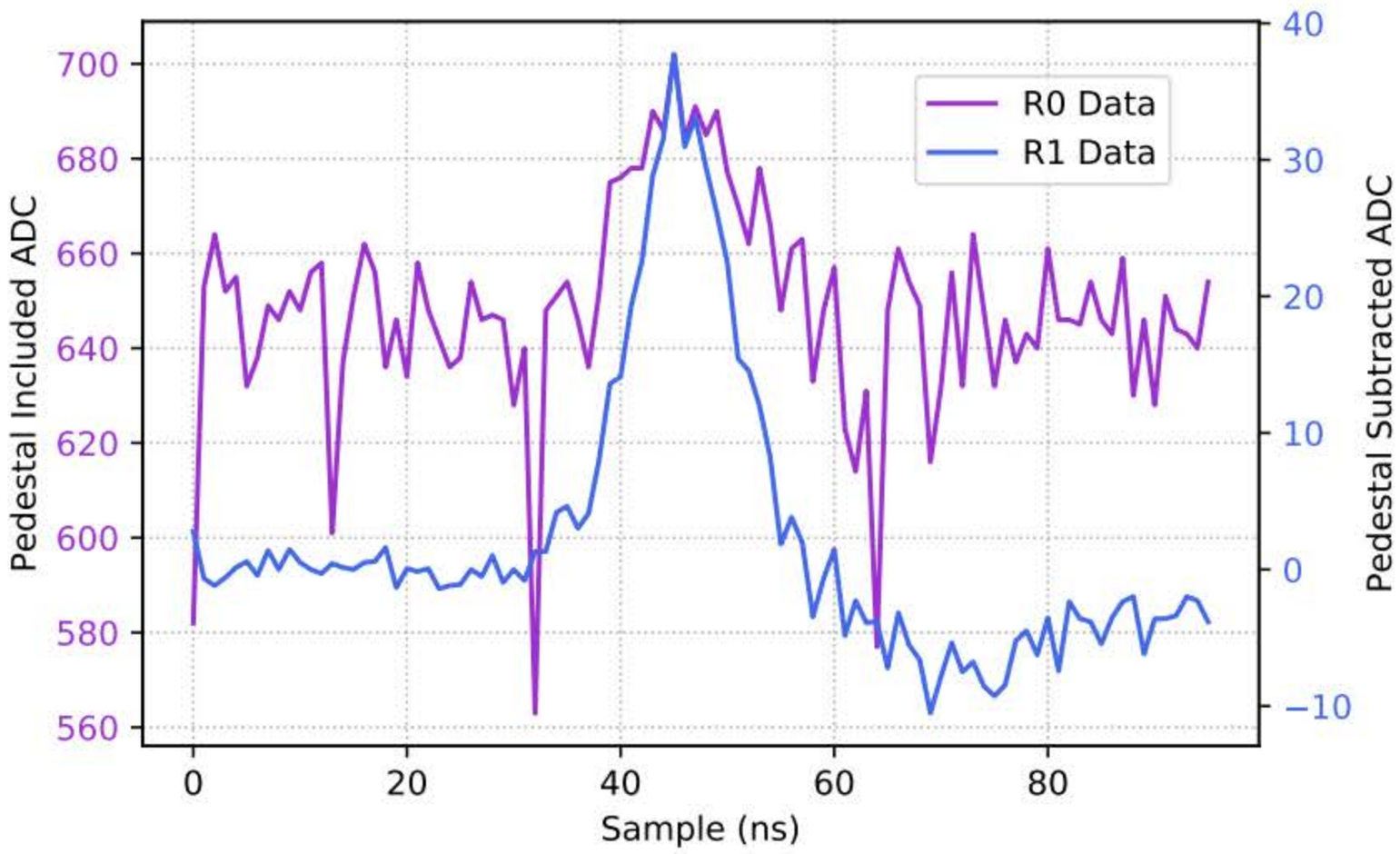

Figure 4.3: CHEC-S digitised waveform containing a 20 mV pulse before and after pedestal subtraction. The R0 data corresponds to the raw non-calibrated waveform and the R1 data to the pedestal subtracted waveform. The pedestal charge present can be indicated by the difference in the y-axis of the two waveforms.

4.4 Transfer Function

The TF describes the conversion of digitised ADC counts to voltage and is used to remove the non-linearity introduced as the analogue signal propagates though the TARGET-C digitising ASIC. Since each sampling cell has its own non-linear response, the calibration file contains a conversion of ADC counts to voltage for each of the 4096 cells. To generate a TF calibration file, an electronic input pulse, resembling the output of the SiPM, is injected into the FEEs and digitised by the TARGET-C ASIC. The sample at the peak of the digitised waveform, in units of ADC counts, is then stored as a rolling average in the TF look-up table for the specific cell at the peak of the waveform as this compares directly to the amplitude of the input pulse. This process is repeated at varying input amplitudes covering the dynamic range of the TARGET-C so that the resulting look-up table can be used to convert all ADC values to their corresponding voltages. In the process of creating a TF calibration dataset, a TFInput, TFInputPCHIP and TF arrays

is produced. The TFInput array simply contains the conversion of ADC to voltage at the measured input voltages. The TFInputPCHIP array contains an interpolated version of the initial TFInput array. This interpolation is produced using a Piece-wise Cubic Hermetic Interpolation (PCHIP) [101]. The TF array is the final output of the generating process, it is a transpose of the TFInputPCHIP array so that it is possible to perform the conversion. This final array is saved as a FITS file, much like the pedestal calibration file. Again, an example of the resulting TF is shown in Figure 4.1.

4.4.1 Legacy Transfer Function Generation

Following the development of CHEC-M and CHEC-S, the calibration of the FEE is well understood and has been investigated at great length throughout the development of the each prototype. It is important to point out that there are two distinct processes in calibrating the TARGET-C ASIC. Firstly, an electronic signal must be injected into the TARGET-C ASIC, this is either with a DC input signal or by AC signal injected into the TM. Secondly, and only for AC input signals, an algorithm is required to determine the peak position of the digitised signal. This peak position is then used to describe the conversion of ADC counts to voltage (i.e. the TF).

The DC transfer function method was developed for CHEC-M for the calibration of the TARGET-5 ASIC. With this method, a constant DC voltage is produced by external digital-to-analogue converters (DAC) and inputted directly into the TARGET-5 ASIC at a known voltage, this voltage is then measured and digitised by the ASIC. The DC voltage is varied so that the entire dynamic range of the digitising ASIC can be probed. The outcome of this is a relation between input voltage and digitised ADC counts which is used to produce the DC Transfer Function. Since a constant input voltage is applied, the data taking process is relatively quick as each sampling cell in the array buffer is calibrated simultaneously, as opposed to the AC method. Section 2.4 shows the improvements and

lessons learned when progressing from CHEC-M to CHEC-S. One improvement made to the FEE for CHEC-S was the introduction of the two TARGET ASICs: T5TEA & TARGET-C. This improvement helped reduce a large amount of digitiser noise, however, in making this improvement the external digital-to-analogue (DAC) chips were removed. With the external DACs removed, it is not possible to repeat this DC TF approach for CHEC-S calibration (see 4.4.3 for the proposed DC TF of CHEC-S).

As the name suggests, the AC TF method uses an AC voltage as the input signal into the digitiser. A common method for calibrating digitising ASICs uses a sinusoidal wave of known amplitudes inputted into the digitiser [78]. Upon investigation of this method for CHEC, an AC saturation effect was found when using high frequency, high amplitude sinusoidal pulses [89]. It was found that the cause of this saturation was the inability of the buffer amplifiers to slew at a high enough rate for the high frequency and amplitude of the sinusoidal input signal. To mitigate these saturation effects, an input pulse matching the output shape of the CHEC-S SiPM tile is input into the shaping electronics of the TM using an arbitrary function generator. By using an input pulse of the same shape as the output of the CHEC-S SiPM, these saturation effects are removed. The amplitude of the input signal corresponds to the value to be used in the lookup of ADC counts to voltage conversion. The following section describes the previous method for extracting this pulse peak ADC value using a double Landau fitting regime.

4.4.1.1 Double Landau Fitting Approach

In order to determine the digitised sample at the peak of the input signal, each digitised waveform must be fitted with a representative expression. Members of the SST team at the Erlangen Centre for Astroparticle Physics (ECAP) concluded that the expression that best describes the output of the CHEC-S SiPM, and therefore electronically injected signal, is that of a double Landau function.

The method previous method for the production of an AC calibration file was to fit the digitised waveform with the double Landau function. The sample position at the maximum of the Landau function corresponds to the sampling cell of the digitised waveform to be input into the TF lookup table [102]. Since there is a negative undershoot in the output of a CHEC-S SiPM, the double Landau fitting algorithm can also be used to calibrate negative amplitudes. In this case, the sample position of the minimum of the Landau function is used for the TF lookup table. It is also possible to inject negative pulses into the TM and fit again with the double Landau expression.

The sampling rate of the TARGET-C ASIC is set to $1\ Gsample/s$, providing a sampling resolution of $1ns$. Due to the shape of the input pulse, it is possible for the absolute peak position of the input signal to fall between two adjacent sampling cells, resulting in a signal peak that is not described by the digitised waveform. In these instances the sensitivity of the sampling cell either side of the peak can impact the transfer function. For this scenario, the sampling cell that lies closest to the peak of the double Landau fit is chosen for the input to the TF lookup table.

Figure 4.4 shows an event where the fitted waveform indicates the peak of the input signal is not at the maximum of the digitised waveform. If a less complex extraction method was used (i.e. $scipy.signal.find\_peaks$) the ADC value inputted into the transfer function lookup table would be the sampling cell with the greatest ADC value, which in this instance would be the incorrect sample. The fitting of each channel per event with a double Landau function requires a large amount of computing power and time (Jason Watson and I wrote a Python script to emulate this method of fitting every channel and every event. Taking 7+ days to generate an AC TF of one TM with 58 input amplitudes). To reduce computing time, a hybrid method was developed [102] whereby a single channel is fitted per event and the sample peak position for each other channel is calculated by considering the signal transit time between adjacent channels.

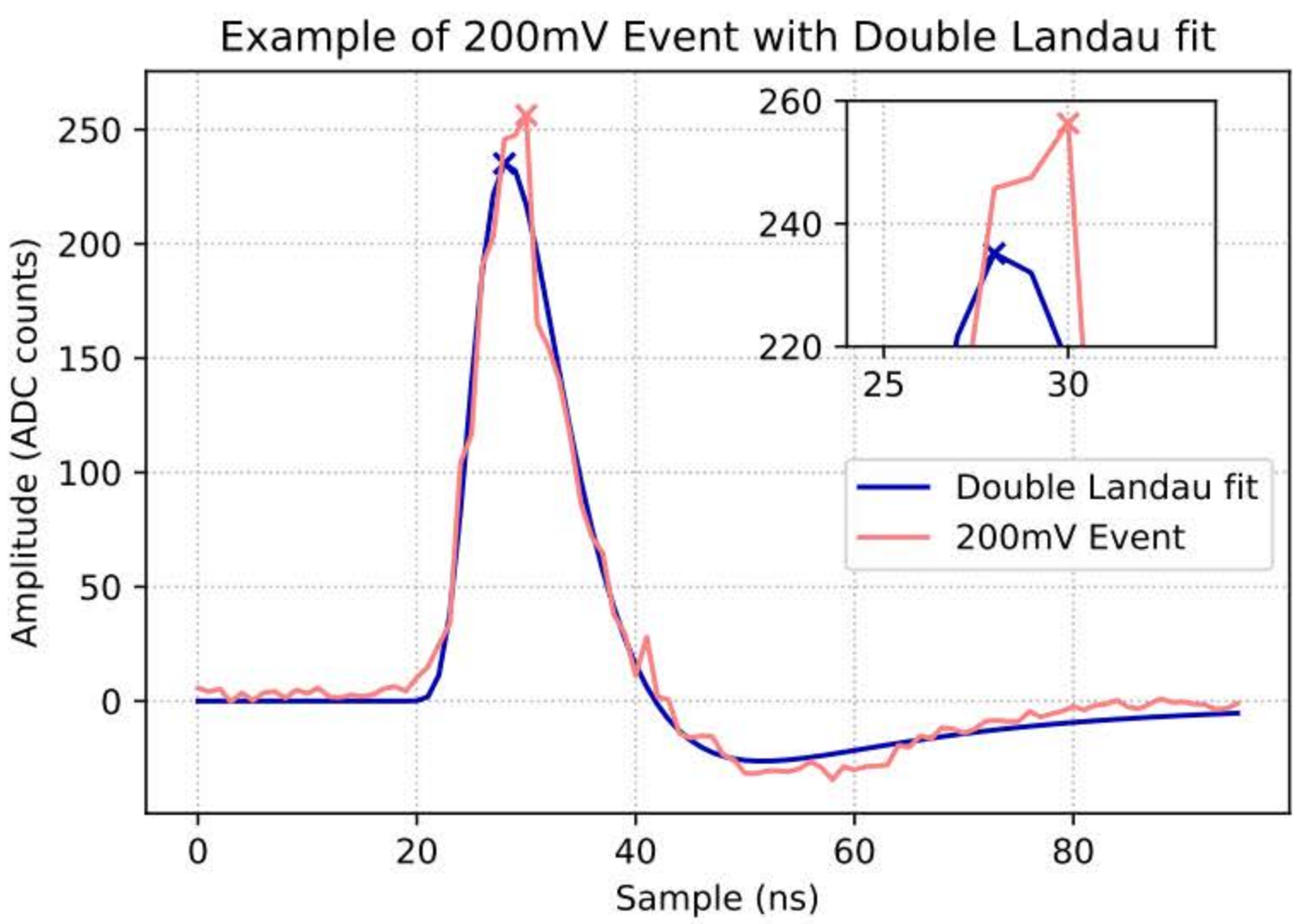

Figure 4.4: CHEC-S waveform containing a 200 mV pulse with the double Landau fitted waveform included. It can be seen that the double Landau fit is not a good representation of this event as the output does not fit the original waveform completely. With this fit, the peak of the waveform is underestimated by the output of the double Landau fit since the digitised sample corresponding to the peak of the double Landau expression is less than the peak of the well defined digitised waveform.

Using a double Landau function to extract the peak position when generating an AC transfer function lookup dataset is by far the most accurate of all previously investigated methods, however, it is not entirely flawless. The double Landau fitting algorithm can only be used when the digitised waveform follows the general shape of this function. At low input amplitudes the electronic noise of the TM begins to dominate the input signal making this fitting method inaccurate. Likewise, at high input amplitudes, the waveform begins to saturate producing a waveform that no longer follows a double Landau distribution. In addition to this, events which produce an inaccurate fit using the double Landau distribution will impact the accuracy of the TF produced.

In both cases, at low and high amplitudes, the waveform peak sample position of the closest working input amplitude is used. The justification for this approach is that the spread in peak position due to input amplitude is relatively small at similar input

amplitudes. In addition to this, the non-linearity of the sampling cells at these amplitudes is overshadowed either by electronic noise or by saturation effects.

The following subsections in this chapter describe the investigations for improving the generation of AC transfer functions. The improvements to be made are both in computing time and power required, and the accuracy of the peak extraction method when compared to the double Landau fitting method. An account for ongoing investigations into a DC TF for CHEC-S is also given, although this does not represent the work concluded in my research, it is included here for completeness.

4.4.2 Current Transfer Function Investigation

Described previously was the legacy method for the calibration of TARGET-C, the digitising ASIC for CHEC-S, using a double Landau expression to determine the peak position of the digitised waveform. What follows is the investigation conducted to improve the generation of the transfer function resulting in a new calibration approach.

4.4.2.1 Cross Correlation

Cross correlation is simply the measure of similarity between two signals as a function of the displacement of one signal to the other. It is a common signal processing technique used to highlight the presence of a specific signal within another signal where the presence of such signal may be overshadowed by noise [103]. For two complex functions, $f(t)$ and $g(t)$, the cross correlation $(f \star g)$ can be described mathematically as:

$$f \star g = \int_{-\infty}^{\infty} \bar{f}(\tau)(g(\tau + t)d\tau \tag{4.1}$$

where $\bar{f}(\tau)$ is the complex conjugate of $f(t)$ and τ is the displacement in time between the

two functions. When using discrete functions that are real valued, such as the CHEC-S digitised waveforms, Eq. 4.1 can be simplified to:

$$[f \star g](n) = \sum_{m=0}^{N} f[m]g[m+n] \tag{4.2}$$

where N is the total number of samples in the waveform and n the sample displacement from sample m.

As Eq. 4.2 shows, it is possible to use cross correlation to compare a digitised waveform ($f[m]$) in this case) with a reference waveform ($g[m+n]$) to determine the sample at which the two waveforms most closely match. To understand this graphically; the reference waveform ($g[m+n]$) traverses the digitised waveform ($f[m]$) in steps equal to the sample size of the waveform resolution. At each step, the two waveforms are multiplied together, the sum of the multiplication following each step results in the cross correlation of the two waveforms at the sample position. This method is outlined in Figure 4.5.

The reference waveform used must represent the expected waveform, following the shaping of the SiPM response, in absence of electronic noise. By correlating a noiseless reference waveform with a digitised waveform, the noise present within the digitised waveform is reduced and any signal correlating to the reference waveform is highlighted. With reference to the TARGET-C transfer function, this cross correlation should reduce any noise rising from sensitivity of sampling cells, as previously mentioned in Section 4.4.1.1. Therefore, the peak in the cross correlation of these two waveforms is the sample at which the two waveforms most closely correlate to one another. And, more importantly, the sample position at the peak of the cross correlation is the sample to be inputted in the TF lookup table.

The reference waveform I use in this cross correlation method is generated from the digitised, pedestal subtracted, event waveforms that are used to create the TF itself

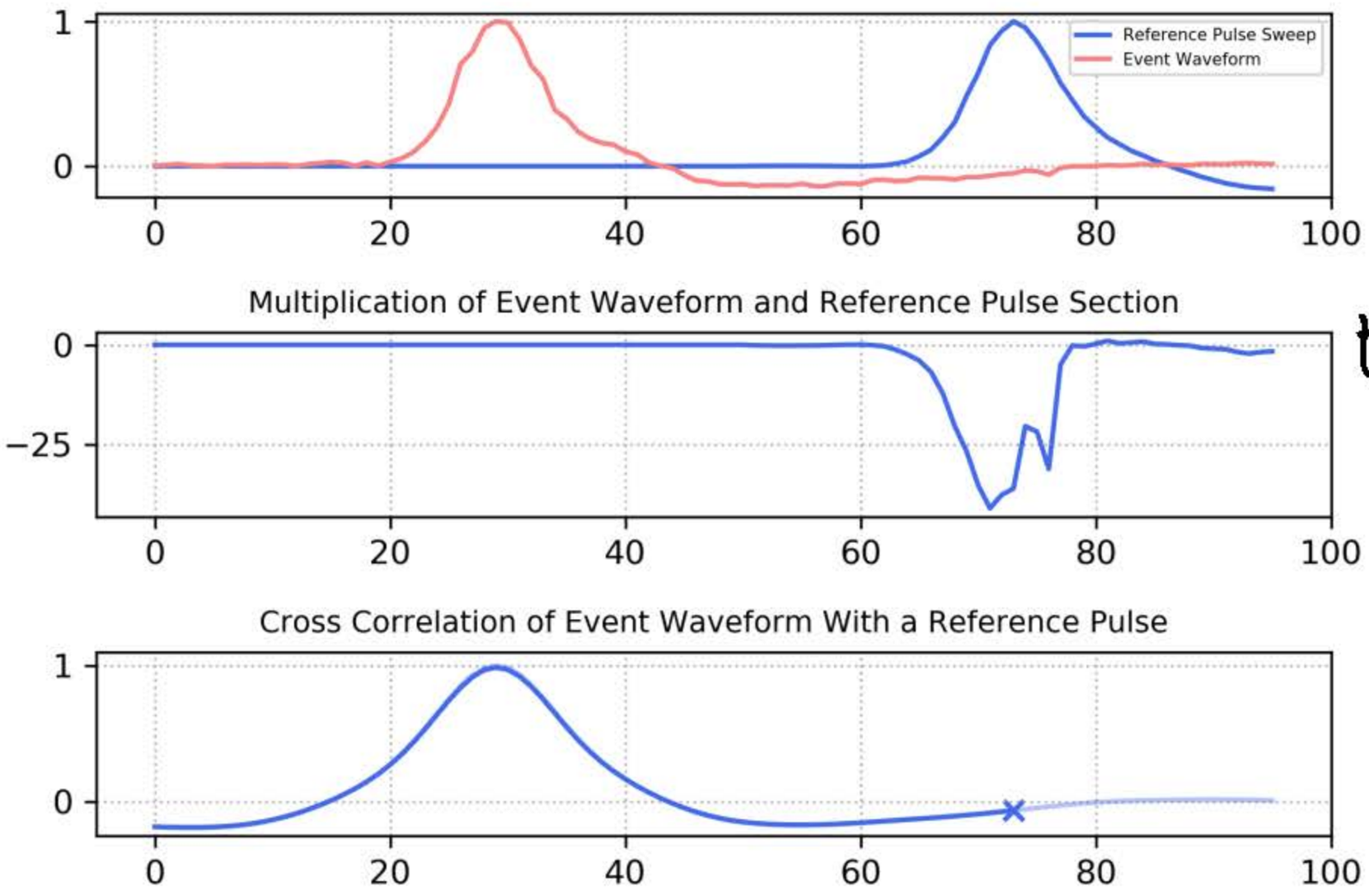

Figure 4.5: An overview of the cross correlation method at a single step in the cross correlation determination. This process is repeated as the reference pulse (Top) sweeps through the event waveform. The multiplication of both the reference and event waveform is shown by the middle plot. Finally the sum of this multiplication is shown by the cross in the bottom plot. As the reference pulse transits the event waveform, the cross correlation (bottom) is populated. The shaded gradient of the bottom plot shows the missing portion of the cross correlation which will be filled following the completion of the cross correlation method

using a function defined in CHECLabPy. Creating a reference waveform from the raw data has two advantages over using an analytical expression such as the double Landau function. Firstly, the shape of the reference pulse corresponds directly to that of the digitised data, ensuring that the two waveforms are nominally identical. Secondly, since the reference waveform is generated from roughly 250,000 digitised waveforms, each occurring at different positions in the sampling buffer, any noise from cell variations, in sensitivity or crosstalk levels, are automatically suppressed. Figure 4.6 shows a comparison of TFInput produced using the three extraction techniques: Simple Peak Finding ($scipy.find\_peaks$), Double Landau Fitting, and cross-correlation. From this you can see that the extraction method used directly effects the generated TF. This variation can be an initial indication

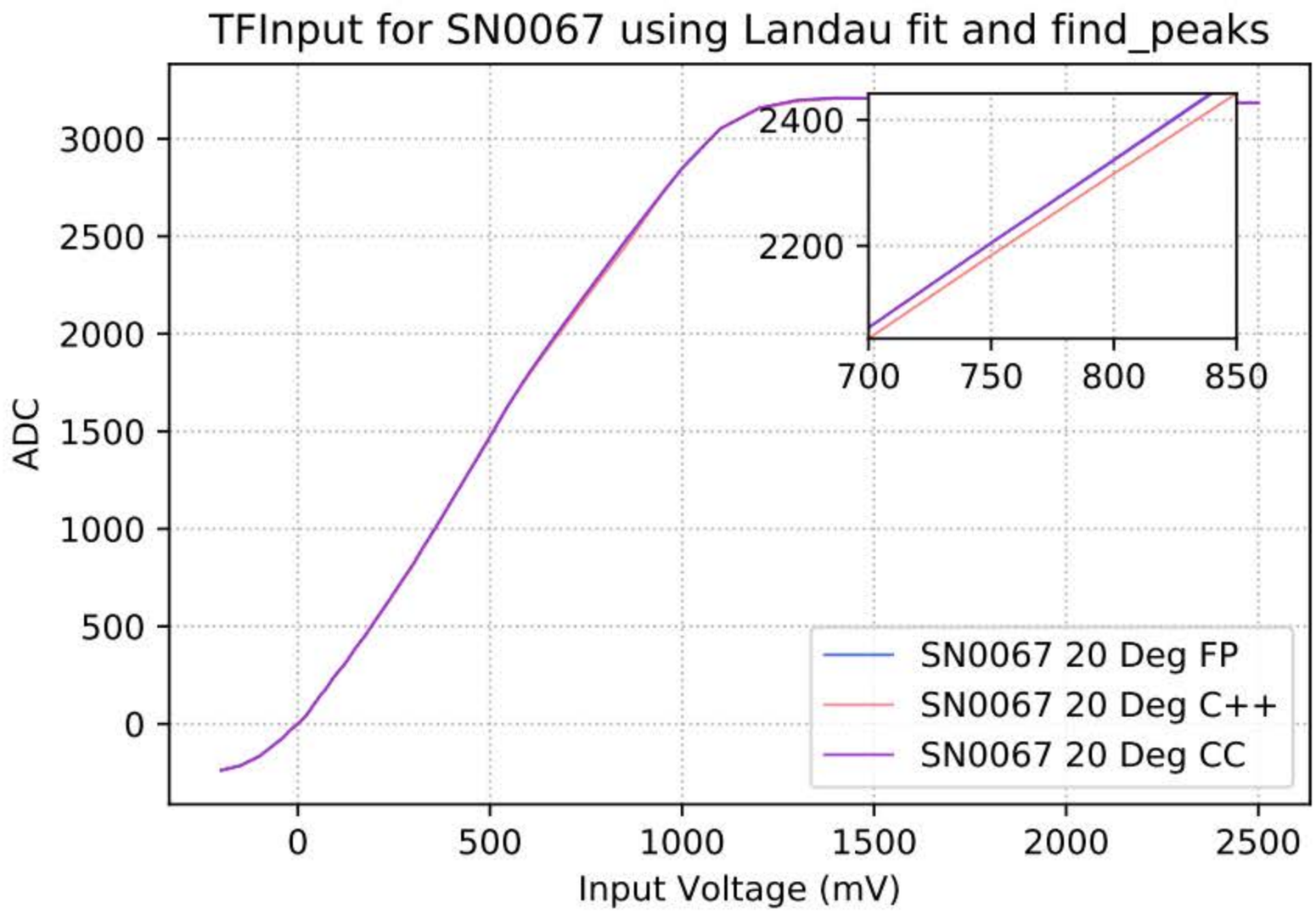

?

Discuss consistency of techniques to outlier shape variation?

Figure 4.6: A comparison of the TFInput produced from the three extraction methods: FP - a simple peak finding algorithm (*scipy.find_peaks*), C++ - the double Landau fitting algorithm, and CC - the cross correlation method. The inset plot indicates region of greatest difference in the TFInput of each peak extraction method.

of the performance of the extraction method. Since the simple peak finding algorithm will always extract the highest amplitude sample, it may overestimate the TF by including the measured signal of sensitive sampling cells. Conversely, the double Landau fitting algorithm may underestimate the peak height of the digitised waveform. The shape of each of the TFInput datasets produced by the three extraction techniques ~~follow a similar shape~~ is similar suggesting the performance of each is reasonably comparable. However, the embedded plot in Figure 4.6 shows the magnitude of the difference between the three techniques.

It is possible to increase the accuracy of the cross correlation method with the use of various signal processing techniques. As described previously, the sampling rate of TARGET-C limits the sample resolution to $1ns$. Since there is jitter in the injected input pulse, it is possible for the peak of the input pulse to fall between two adjacent sampling cells. In these circumstances the peak will not be sampled and the digitised data would

instead describe a flattened peak. It is these events that the cross correlation fails to identify correctly as the extracted peak position is often determined by the more sensitive sampling cell.

It is possible to increase the sample rate of a digitised waveform, and hence increase the sample resolution, by up-sampling [104] and interpolating each waveform. By increasing the sample resolution it is possible for the cross correlation to return a non-integer peak value. This non-integer peak value then represents the peak position of the input pulse. Clearly, it is not possible to use the ADC counts value at this non-integer peak since this is not a *real* digitised value. Instead, the non-integer peak is rounded to the nearest integer, this value is then used as the sampling cell at the maximum of the digitised waveform. Using this method, more sensitive sampling cells around the peak position are suppressed when the correct up-sampling method is applied.

For comparison, a number of different interpolation methods within the Scipy Python library [105] were used to interpolate the event data. These include:

- Nearest - Interpolated point set equal to the nearest real data point
- Zero - Zeroth order spline interpolation, interpolated points set to equal the previous real data point
- Quadratic - Interpolated points generated using a second order spline interpolation
- Cubic - Interpolated points generated using a third order spline interpolation
- PCHIP - Piecewise Cubic Hermetic Interpolation. Third order spline interpolation with dampened overshoot

A single digitised event was used for the initial interpolation investigations. The event chosen was a 200mV waveform of 96 samples, which was chosen specifically because the

peak position in the digitised waveform differs by two samples when compared to the peak given by the double Landau fit (see Figure 4.4).

In the initial investigation, the performance of each interpolation method was determined by the peak position given by the cross correlation and whether it matched that of the double Landau function.

Figure 4.7 shows a comparison of the extracted peak for each of the interpolated cross correlation methods and the previously described double Landau and *scipy.find_peak* algorithms. It can be seen that the quadratic and PCHIP interpolation methods produce the best peak position in the resulting cross correlation. This peak position check was then conducted over a larger number of digitised events to provide further insight into the performance of the quadratic and PCHIP cross correlation methods. Following this, it was observed that the PCHIP method was more accurate than the quadratic interpolation; a TFInput was then generated using the cross correlation with PCHIP interpolation to extract the peak position of each event. The resulting TFInput is compared with that of the double Landau and simple peak finding methods (as shown by Figures 4.8 and 4.9). Again, the TFInput produced in this method shows good general agreement with the TFInput produced using the double Landau function, but there is a discrepancy in both TFInput arrays in the region of 600mV - 900mV; highlighted by Figure 4.9 showing the variation in the two arrays. The TFInput produced using the PCHIP interpolated cross correlation is an improvement upon the simple cross correlation method. In addition to comparative TFInput, the computation time required to generate a TF using the PCHIP cross correlation peak extraction is a vast improvement on the time needed for the double Landau fitting method. A more extensive comparison of the performance of each peak extraction method is given in Section 4.4.2.3 following the description of Continuous Wavelet Transformation (CWT) for the use of peak extraction.

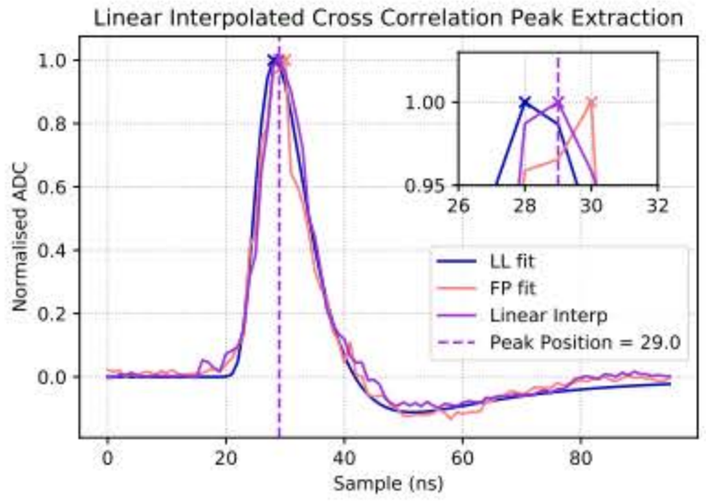

(a)

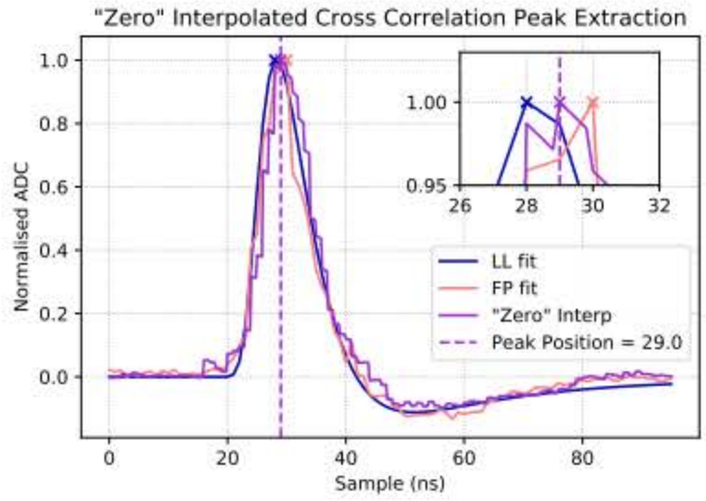

(b)

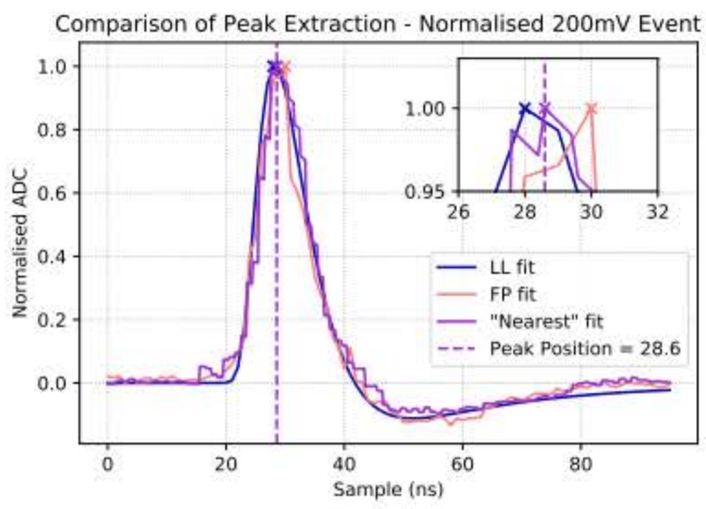

(c)

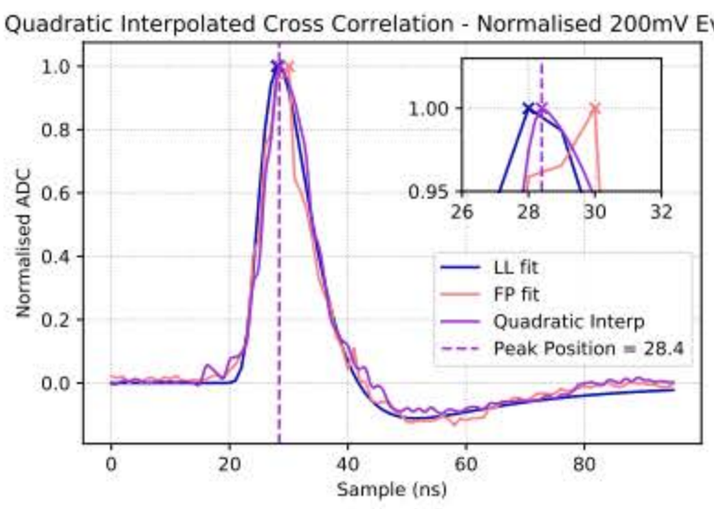

(d)

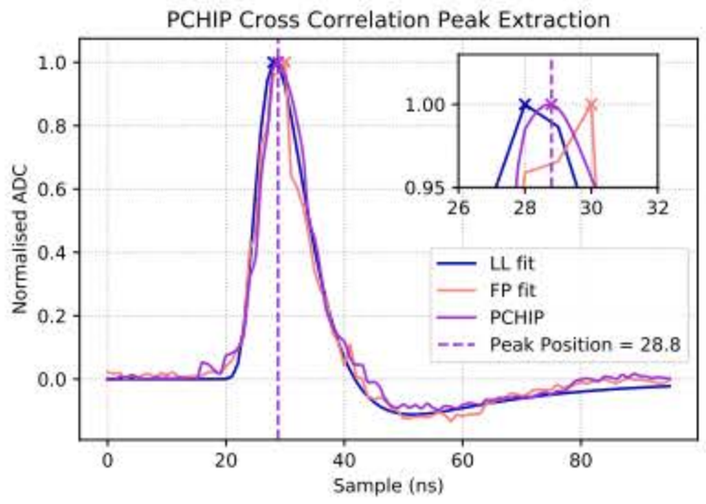

(e)

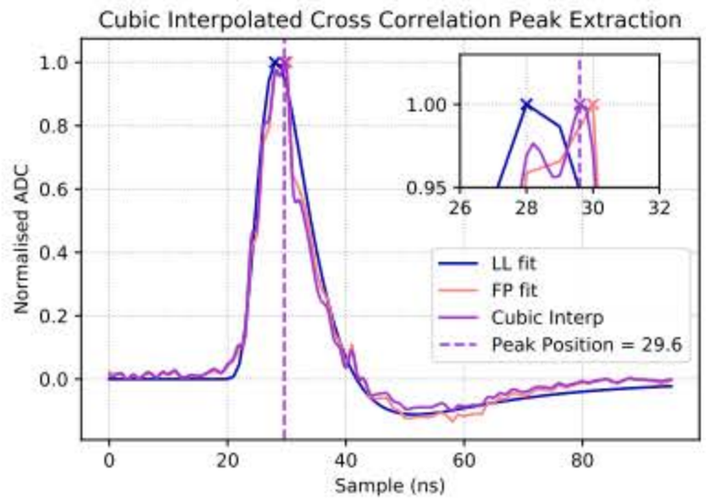

(f)

Figure 4.7: Comparison of the cross correlation peak extraction method of a 200 mV event using various interpolation regimes. The peak position and inset plot can be used to evaluate the peak extraction method.

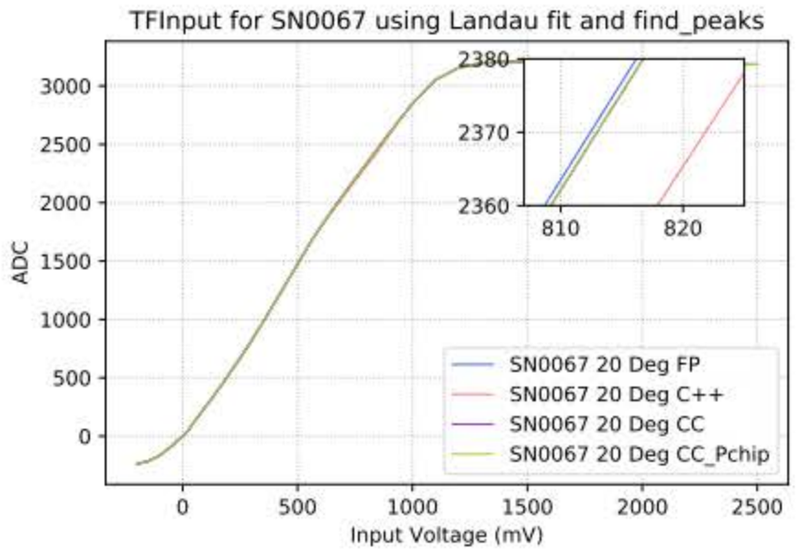

Figure 4.8: The TFInput produced using the simple *find_peaks*, double Landau, cross correlation, and cross correlation with PCHIP peak extraction algorithms. The inset plot again indicates the region of greatest difference between the resulting TFInput arrays.

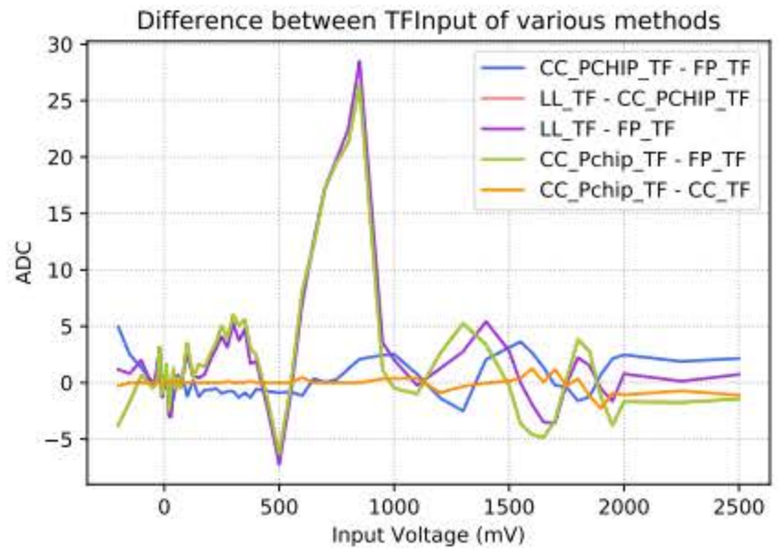

Figure 4.9: The difference between each of the TFInput arrays produced in the testing of the peak extraction method. It can be seen that the double Landau fitting method has the greatest difference between each of the methods.

4.4.2.2 Continuous Wavelet Transformation

Continuous Wavelet Transformation [106] is a technique used in signal processing to identify peaks in signals with low SNR. CWT performs a wavelet transform of a signal with a mother wavelet at numerous wavelet scales to evaluate the original signal and highlight peaks that resemble the scaled mother wavelet. In doing so, it highlights the peaks that resemble the mother wavelet making the peaks more pronounced. The CWT technique is described mathematically by Equation 4.3 [106]:

$$C(a,b) = \int_R s(t)\Psi_{a,b}(t)dt \tag{4.3}$$

$$\Psi_{a,b}(t) = \frac{1}{\sqrt{a}}\Psi(\frac{t-b}{a}) \tag{4.4}$$

where a and b are the scale coefficients (width and height) of the CWT (C), $s(t)$ the signal, $\Psi(t)$ the mother wavelet, and $\Psi_{a,b}(t)$ the scaled and translated daughter wavelet.

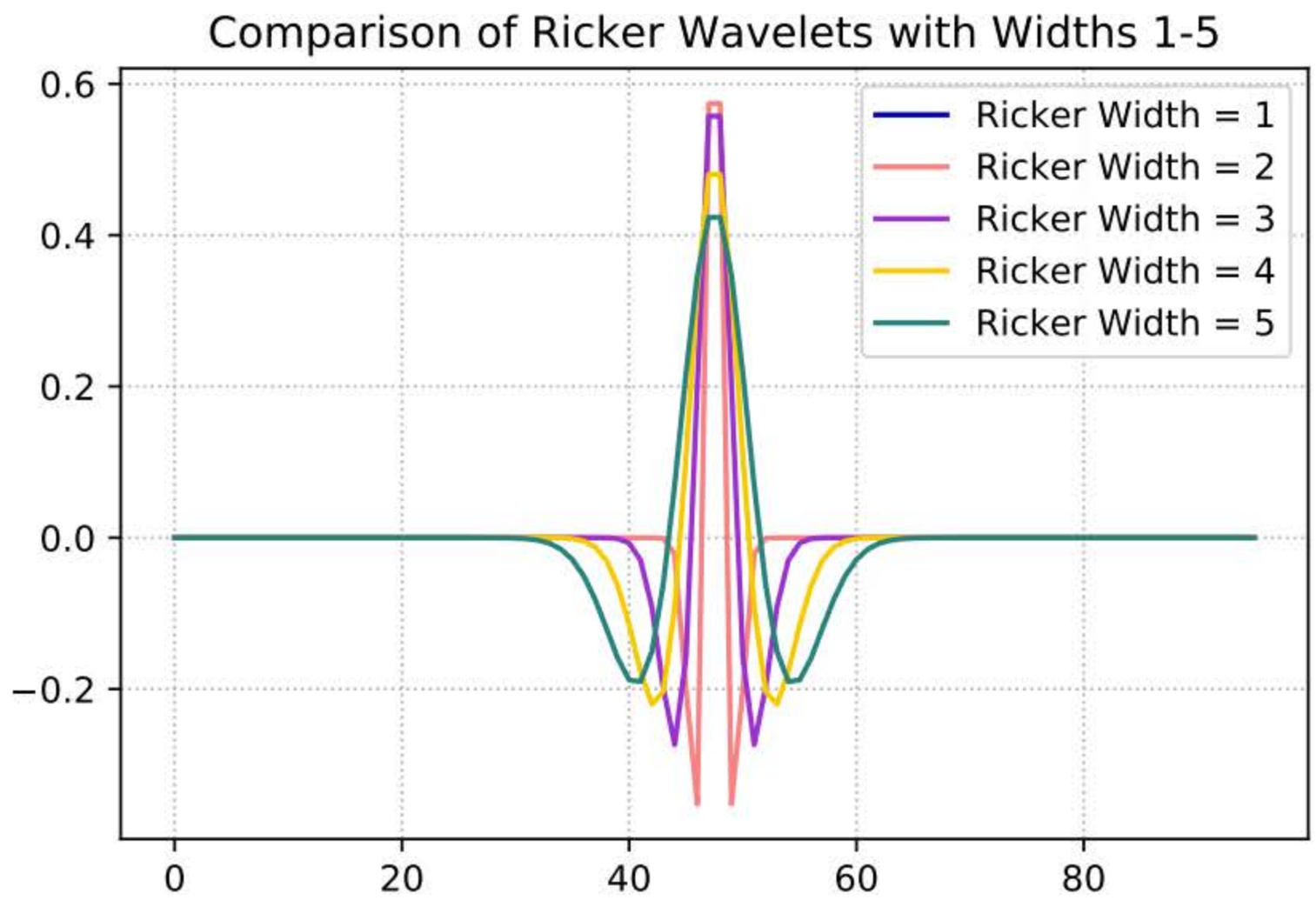

Figure 4.10: An example of the Ricker wavelet at 5 varying width parameters. The integrated area of a Ricker wavelet is normalised, the width of the wavelet therefore impacts the shape of the wavelet.

Similarly to the cross correlation technique, the mother wavelet is correlated with the signal waveform with varying coefficients (a & b). In doing so, the coefficients reflect the matching between the signal and scaled mother wavelet. The output of Equation 4.3 is a 2D matrix containing the wavelet transform of $s(t)$ and $\Psi_{a,b}(t)$. The wavelet with the greatest local maxima represents the wavelet which matches the signal waveform closest. In addition to this, the peak of this wavelet indicates the position which best matches the peak of the wavelet and signal waveform, much like the cross correlation output.

Clearly, the performance of the CWT relies heavily on the chosen mother wavelet. The mother wavelet should therefore approximately represent the shape of the signal waveform. The initial wavelet used in this investigation was the Ricker, or Mexican Hat, Wavelet [107].

Figure 4.10 shows how the variation of the Ricker wavelet with the varying scale

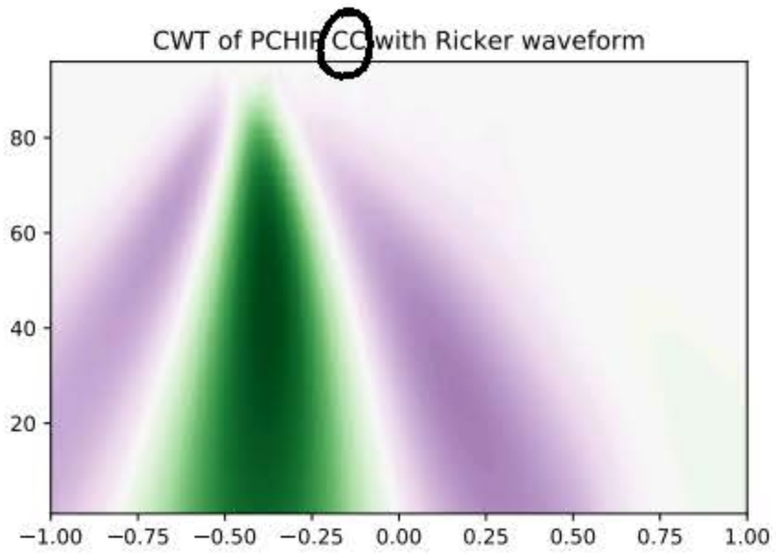

Figure 4.11: The continuous wavelet transformation of the PCHIP cross correlation data. The colours of the 2D plot represent the positive (green) and negative (purple) values of the CWT waveforms. The intensity of the colour denotes the peak in the CWT which corresponds to the maximum wavelet (shown in Figure 4.12)

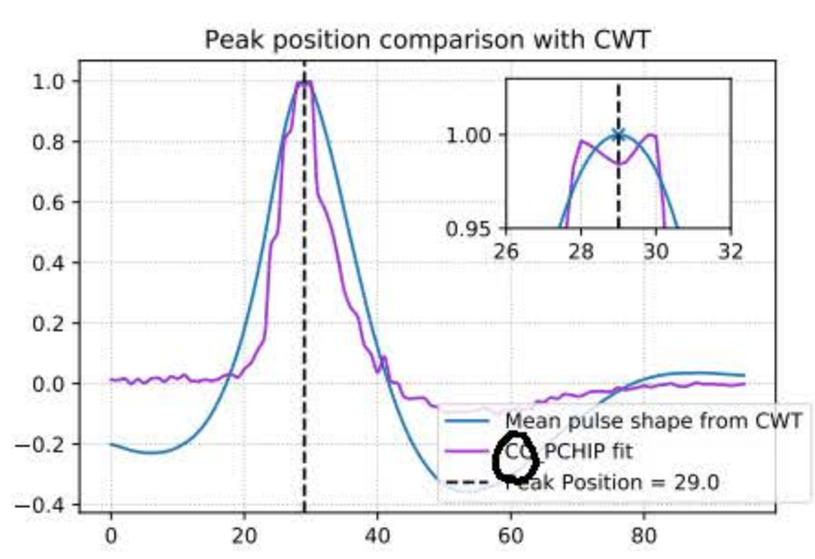

Figure 4.12: An overlay of the cross correlation with PCHIP output waveform and the maximum wavelet of the CWT. The peak of the CWT maximum wavelet corresponds to the peak position determined by this method.

factor applied to it. At each scale, the output of the CWT has a local maximum around the peak in the signal. As the scale increases, the local maximum increases until the scale wavelet best matches the peak width of the signal, the local maximum then decreases as the width of the wavelet surpasses that of the signal. The maximum of all the maxima corresponds to the modified wavelet that best matches the signal pulse. The peak in this wavelet then corresponds to the peak in the signal data. This can be visualised in the 2D space of the output coefficients or as the single 1D wavelet at the maximum as seen by figures 4.11 and 4.12.

The signal used in this investigation is the output of the PCHIP cross correlation (as described in Section 4.4.2.1). The reason this was used for the CWT is that the CC actively smooths the original signal which increases the accuracy of the CWT since the peaks from electronic noise are already suppressed. Figures 4.11 and 4.12 indicate the performance of this CWT approach. Although promising, the *CWT* peak extraction method was found to be less accurate than the use of CC alone, because of this, it was discarded as a possible replacement to the *double Landau* peak extraction technique. In

future, it may be worthwhile to investigate the use of CWT for peak extraction with the use of other mother wavelets which resemble the reference pulse more closely in order to provide more accurate results.

4.4.2.3 Peak Extraction Performance Comparison

As stated previously, the generation of a TF comprises a number of steps. Firstly, electronic pulses, resembling the output of a CHEC-S SiPM, are injected into the TM and digitised by the TARGET-C ASIC at a number of input voltages covering the dynamic range of TARGET-C. Secondly, the peak amplitude of each of the 200,000+ events per input amplitude is determined by a peak extraction technique and inputted into the lookup table producing the TFInput file. Finally, the lookup table is interpolated, extrapolated, and transposed resulting in the final TF file comprising the conversion of ADC counts to voltage for each sampling cell and channel of one TM.

Since the injected pulses match the output of the SiPM, the performance of a TM directly correlates with the performance of the peak extraction method. The better the peak extraction is at identifying the correct peak of the input signal, the more accurate the resulting TF. In order to determine the accuracy of each peak extraction method, the determined peak position of the digitised signal must be compared with the known peak position of the input signal. For electronically injected pulses, the peak position can only be known if it is measured simultaneously with an oscilloscope, introducing a further level of complexity into TF generation. Instead of injecting electronic pulses to determine the performance of each peak extraction regime, a simpler approach was taken.

The performance of each peak extraction technique can be determined by measuring the accuracy of each technique when applied to simulated events, provided the simulated events are comparable to injected events digitised by TARGET-C in the generation of a TF dataset. In order to simulate comparable events, it is necessary to discuss

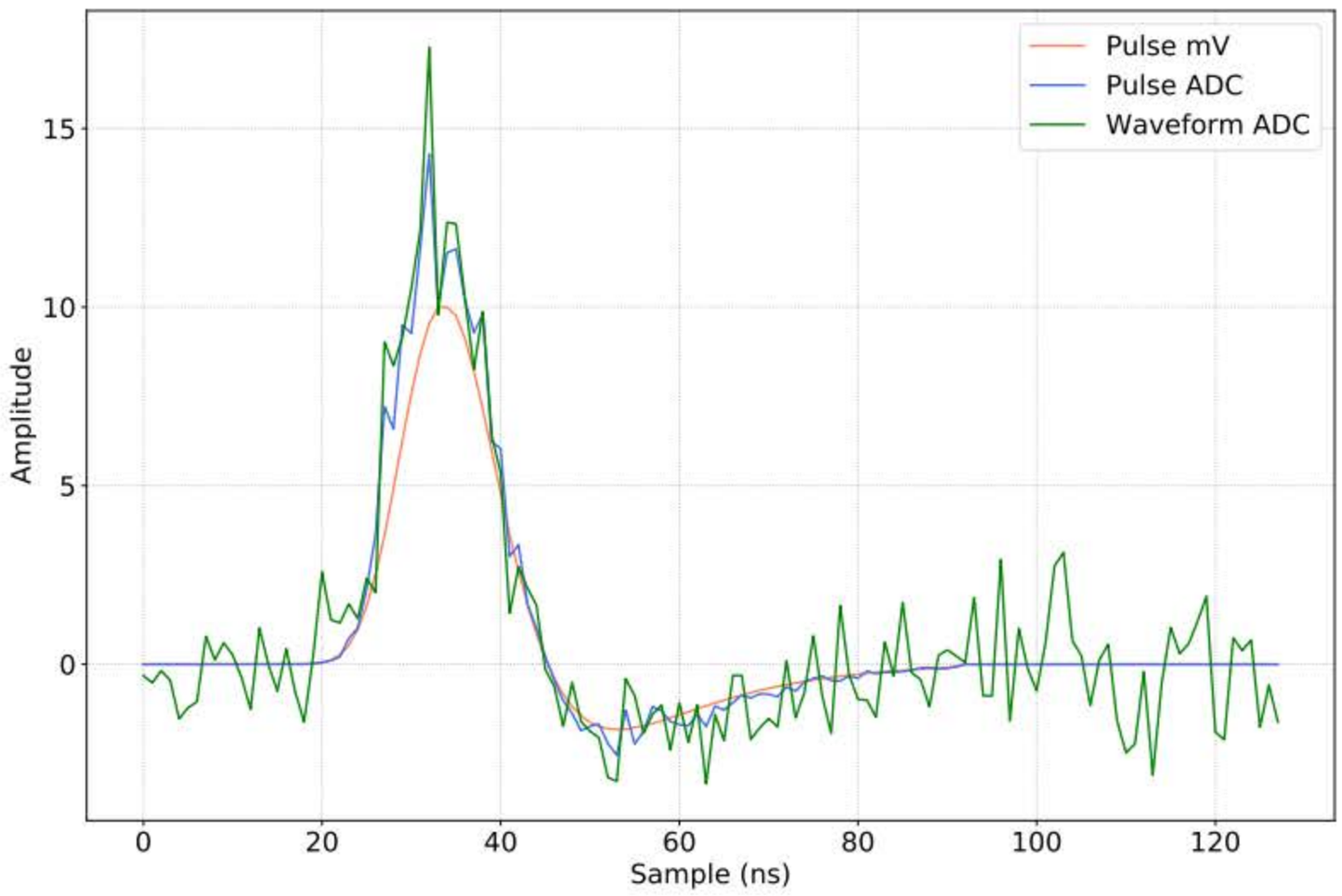

Figure 4.13: An example event of simulated data to be used in the comparison of peak extraction methods. The orange pulse here shows the original reference waveform after the amplitude and peak position has been scaled and shifted. The blue plot shows the subsequent waveform following the reversal of the TF to produce a waveform in terms of ADC counts. Finally, the green waveform shows the simulated event with the additional Gaussian noise representing the noise from pedestal residuals and sensitive sampling cells. Each peak extraction algorithm is then applied to the simulated waveform.

what components must be present in the simulated data to produce meaningful results from the peak extraction comparison when considering the use in TF generation. There are three components of the digitised data used for generating TFs that must be simulated. Firstly, as described before, each cell within TARGET-C has a unique conversion of ADC counts to voltage. Secondly, the peak position of electronically injected signals can be non-integer and vary due to the jitter of the input source, resulting in a peak that is not sampled as the peak position occurs between two sampling cells. Finally, each cell, and therefore switched capacitor, has it's own sensitivity. The effect of this sensitivity is that the digitised peak position can vary compared to the initial injected pulse as cells neighbouring the peak position can produce a higher digitised ADC value than the cell at the peak. The result of these components in a digitised waveform is that the maximum

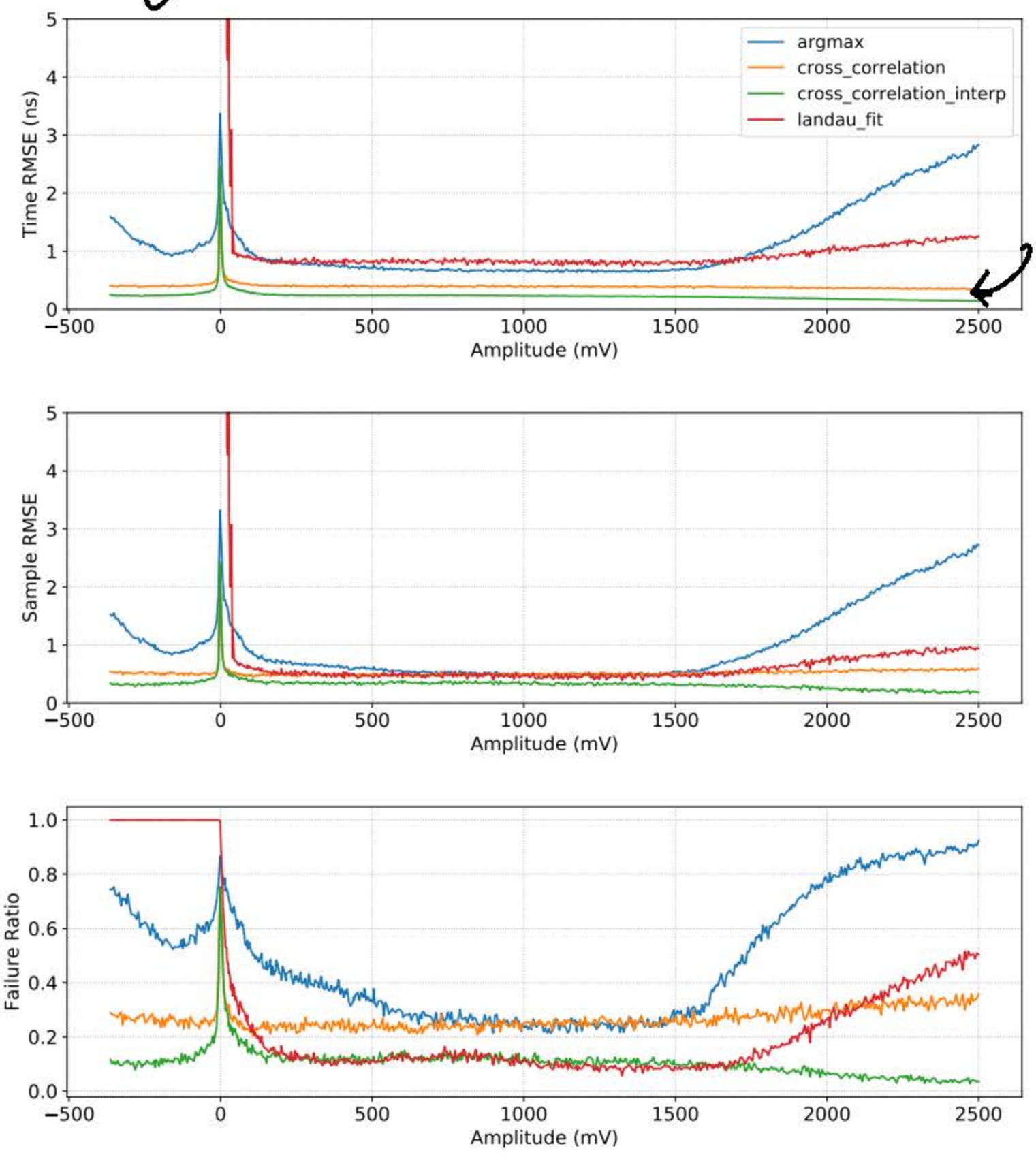

Figure 4.14: An overview of the performance of each peak extraction algorithm when applied to a simulated dataset of various amplitudes and peak positions. The top and upper middle plots show the root-mean-square (RMS) error in both the extracted peak time and sample position of the peak. The lower middle plot shows the failure ratio of each method given by the comparison of the determined peak sample and the sample peak of the initial reference waveform. The bottom plot indicates the execution time for each peak extraction method.

ADC count value of the digitised data could be at a sample position that is not the same as the peak position of the injected pulse. As described in 4.4.1.1, this is mitigated in the legacy TF generation by taking the ADC count value at the peak of the double Landau waveform for the input into the TF lookup table.

The production of simulated events begins with a reference CHEC-S pulse shape taken from a CHEC-S SiPM digitised by a high resolution oscilloscope. Figure 4.13 shows the various stages of producing a single event for the peak extraction comparison. The reference pulse is first scaled and shifted to produce a simulated event with a peak amplitude between $-300mV$ and $2000mV$ and a non-integer peak position between $30ns$ and $40ns$. The cell identification value of the first cell of the waveform (first cell ID, FCI) is randomly chosen and correlates to the first cell, and starting point, of the analogue readout buffer of the TARGET-C storage array. Using the FCI and a suitable TF, the waveform is converted from voltage to ADC counts (shown by the blue plot of Figure 4.13). Finally, random Gaussian noise, with a root-mean-square (RMS) deviation equal to that observed in CHEC-S, is added to represent the variation in sensitivity of storage cells and residual signal following a pedestal subtraction. The resulting waveform is shown by the green plot of Figure 4.13.

Once a simulated event is produced, the peak position and peak amplitude is determined by: simple peak maximum algorithm; cross correlation peak extraction; cross correlation with PCHIP peak extraction; and the double Landau fitting technique. The peak position and peak amplitude are then compared to the known values for the data before the addition of noise to determine the accuracy of each peak extraction method. This process was repeated over a large number of events covering various peak amplitudes and peak positions to ensure the accuracy of this result for varying amplitudes and peak positions.

The outcome of this investigation can be seen in Figure 4.14. The first point

of note is that each peak extraction method fails around $0mV$, clearly at $0mV$ this is expected since there is no peak to be detected. At close to $0mV$, the performance is also decreased for all peak extraction methods as the impact of the additional Gaussian noise is most pronounced in this region. In addition to this, the double Landau algorithm was not optimised for negative pulses, resulting in the 100% failure rate below $0mV$. Figures 4.14a and 4.14b highlight the performance of each peak extraction technique in terms of the determined peak position. Figure 4.14a shows the RMS error in the position of the peak amplitude as determined by each peak extraction algorithm, the non-integer peak value is then rounded to the nearest integer to produce the sampling cell at the peak shown in 4.14b. The amplitude of this cell would be inputted into the TF lookup table in the generation of the TF. The failure ratio is a measure of the ratio of incorrect to correct peak position determined by each for each extraction method as shown by Figure 4.14. Here again the performance of the returned sample by each extraction algorithm can be seen. Finally, the execution time for each peak extraction technique is shown.

From this investigation, with the use of simulated events, it is clear that the performance of the *double Landau* peak extraction method can be surpassed with the use of the *cross correlation with PCHIP* technique. In addition to the improvement in accuracy gained, the time taken to perform each peak extraction is also improved when adopting *cross correlation*. It may also be possible to further reduce the execution time with the optimisation of the *cross correlation with PCHIP* technique. As stated before, the better the performance of the peak extraction technique, the more accurate the resulting TF is. Since the *cross correlation with PCHIP* technique offers an improvement over the *double Landau* fitting method in both time and accuracy, it was decided that CC shall be the basis of the TF generation for the SST camera.

4.4.3 DC Transfer Function

As stated previously in 4.4.1, the DC transfer function is produced using a DC input signal injected into the TARGET-C digitising ASIC. Previously, this was achieved using an external DAC to generate the input signal. However, no such calibrated DAC is present on the CHEC-S TM. To overcome this, it is possible to use an output of the T5TEA trigger ASIC as a DC input into the digitising ASIC. Firstly, the output of the T5TEA is calibrated using external flash ADCs to measure the output voltage at each DAC setting. The DAC setting of the output DC voltage is then varied over the dynamic range of the output whilst the TARGET-C ASIC digitises the DC signal. Since the input to the digitiser is a DC signal, there is no need to determine the peak position. In addition to this, it is possible to calibrate all sampling cells within one digitised waveform simultaneously, as opposed to the single sampling per event of the AC transfer function method. This greatly reduces the number of events required to measure the dynamic range of the DC input and additionally the time needed to generate the DC transfer function from such a dataset.

Whilst the generation of a DC transfer function seems more ideal and less complex than its AC counterpart, it is not without its disadvantages. The dynamic range of the T5TEA output is less than that of the TARGET-C digitising ASIC. When using the DC output of the T5TEA, it is therefore not possible to probe the entirety of the TARGET-C dynamic range, only the low amplitude and linear region can be measured. Therefore, the saturated region of the digitiser cannot be measured, hence, the necessity of the AC transfer function.

Figure 4.15 shows the resulting DC transfer function of 4096 cells from a single channel. It can be seen that the DC TF follows a similar shape to that of the AC TF but ends before the saturation of the digitiser. In addition to this, the variation of transfer function from one sampling cell to another can be seen as well as the non-linearity in the transfer function, again highlighting the need for such calibration.

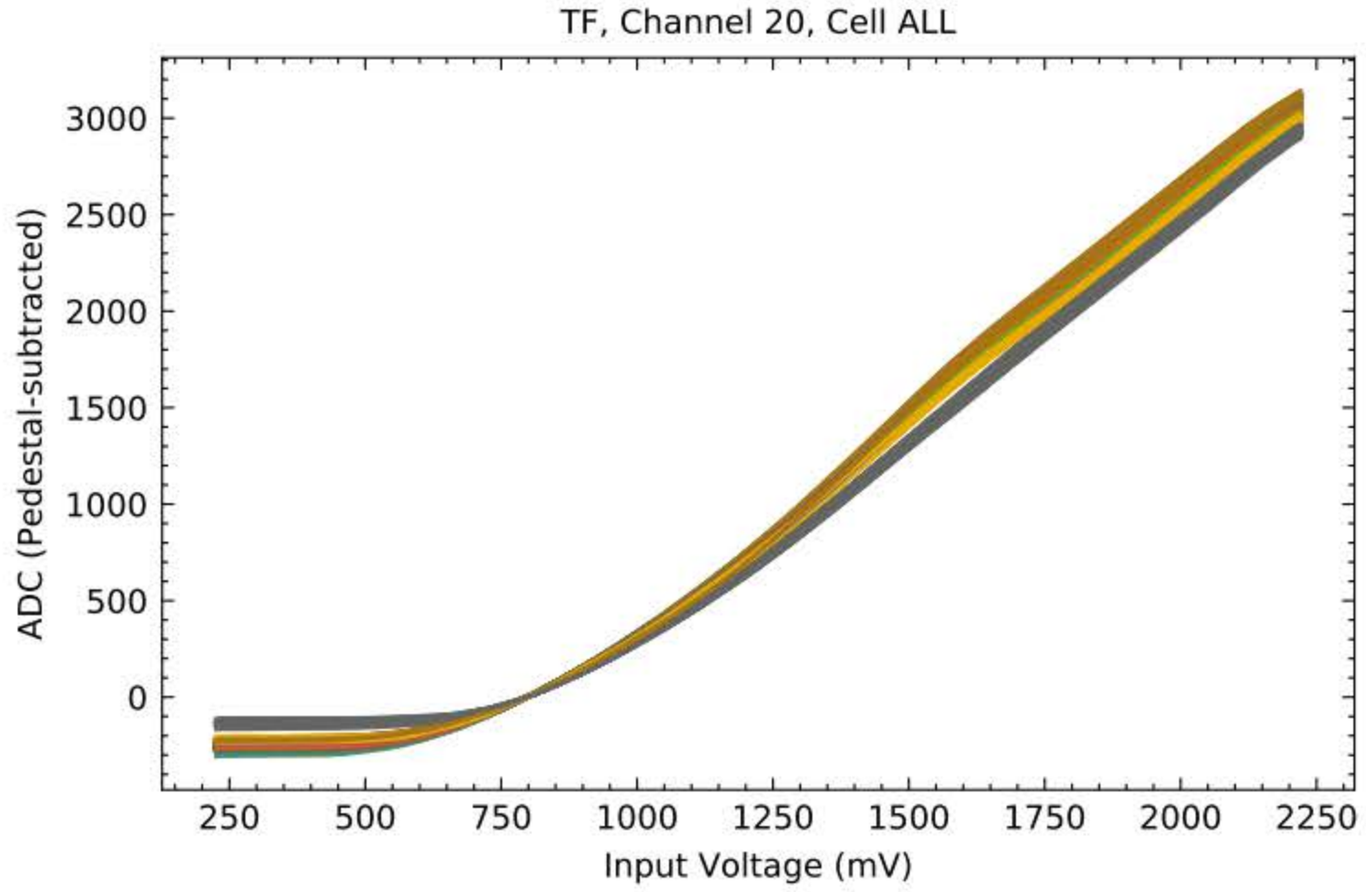

Figure 4.15: The DC transfer function for all cells in one channel. The variation of the transfer function from one cell to another can be seen by the shape of the plot. The dynamic range of the T5TEA output can also be observed as the DC input does not saturate the TARGET-C ASIC.

4.5 Transfer Function Temperature Dependence

The transfer function methods described previously were conducted at various temperatures so the effect of temperature on these TFs, and indeed the TARGET-C ASIC, could be further investigated. For the operation of CHEC-S, each TF was generated at roughly $23°C$. However, the operating temperature of TMs vary from $35°C$ to $45°C$ within CHEC-S, which is clearly vastly different to the temperature at which the TF is generated. It was therefore necessary to determine the effect of applying a TF taken at a temperature different to that of the operating temperature of the TM.

The following subsection describes the temperature dependence of the AC TF and outlines a method that I have developed for recovering and correcting for this. As described previously, the plan for the SST Camera is to create DC TF calibration data in situ with TMs at temperature within the SST Camera. The temperature dependence described here covers the effect of temperature on the AC TF as the generation of such calibrations would be generated per TM within the laboratory.

4.5.1 Variation of Transfer Function with Temperature

The response of both storage and sampling cells of the TARGET-C ASIC vary with temperature. As stated previously, the residual charge of each switched capacitor increases with temperature, this residual is removed with the application of pedestal subtraction, providing the pedestal was taken at the same temperature of the digitised data. In addition to this, the non-linearity of the TARGET-C ASIC varies with temperature. By not accounting for this when digitised data is calibrated, the conversion of ADC counts to voltage is incorrect and the resulting voltage value is inaccurate. Figure 4.16 shows the discrepancies of the resulting TF when the calibration data is taken at varying temperatures, it can be seen that although the shape and extent of the TF remains unchanged, there is an apparent offset between each of the generated TFs. The inset plot of Figure 4.16 highlights the magnitude of this offset, and indeed the effect of temperature on the TF. The amplitude of the variation here is a roughly $40mV$.

Clearly, if a TF is applied to a dataset that was taken at temperature which is different to the temperature at which the TF data was generated, the accuracy of the resulting calibrated dataset is greatly reduced. The returned voltage will not be representative of the true input voltage, reducing the performance of CHEC-S and TARGET-C. Figure 4.17 highlights the effect of applying a TF taken at a temperature that differs to the temperature at which the digitised data is taken. The event data shown here was taken using a single TM within a temperature chamber with the temperature of the TM primary board stabilised to 23°C. An electronically generated pulse resembling the output of a CHEC-S SiPM with an input voltage amplitude of $\sim 900mV$ was injected directly into the TM, producing the digitised waveform observed. Each line shown on this plot represents the calibrated R1 event after a TF taken at a specific temperature is applied to this event. The extent of the temperature dependence on the TF calibration can be seen by the variation observed in the calibrated waveform, here a maximum difference of

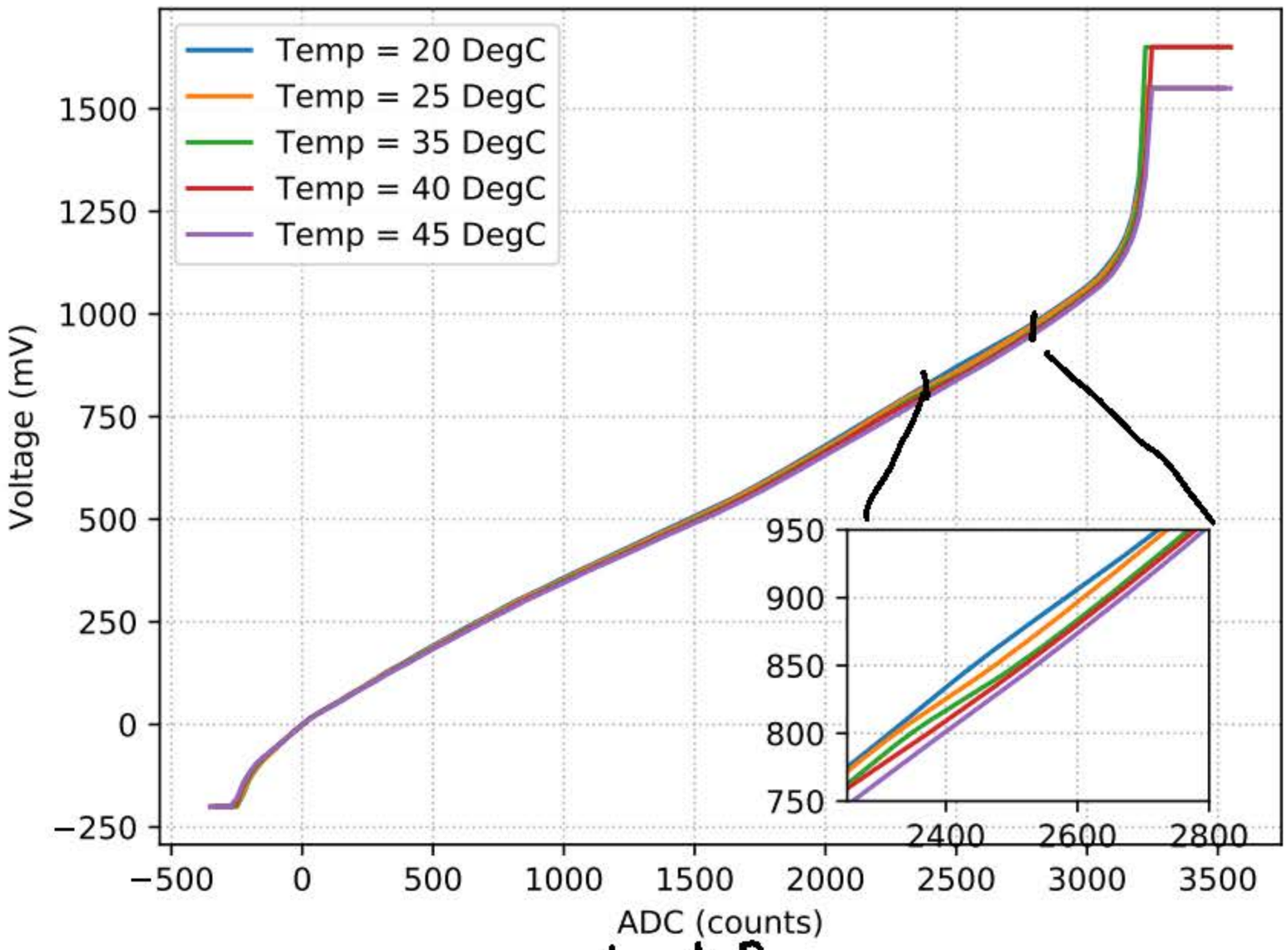

Figure 4.16: Comparison of the TFInput measured at varying ambient temperatures. The plot shows the variation of the resulting TF at different temperatures. The inset plot shows the region of greatest variation of all TFs.

30mV is observed when comparing the resulting event peak height of the waveforms at the extremities of the temperature range. This miscalibration is comparable to the current operation of CHEC-S with TF calibration files applied to data taken at ~20C higher than the temperature of the TF calibration data, which results in an underestimate of the event charge by roughly 7 *photoelectrons* (*p.e.*), assuming a SiPM gain of 4 $mV/p.e.$.

4.5.2 Correcting Temperature Dependence

With TFs generated at multiple temperatures, it is now possible to attempt to correct for the variation seen in calibrated data by the ambient temperature of the TARGET-C ASIC. Initially, it would be beneficial to apply a TF taken at a temperature closest to the temperature at which the uncalibrated data was taken at as this would clearly provide

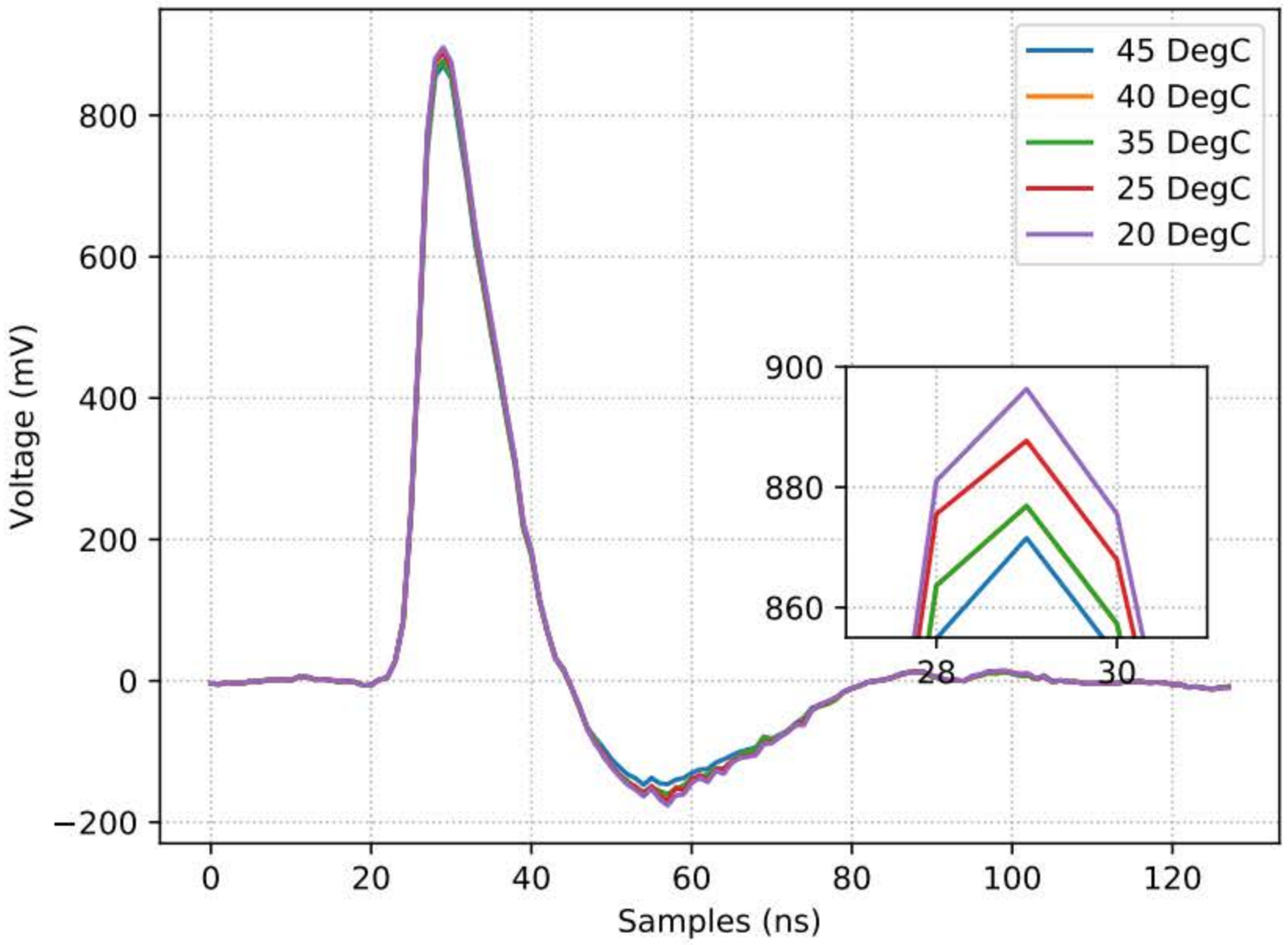

Figure 4.17: The resulting calibrated waveforms following the calibration of a 900 mV pulse with TFs taken at a range of temperatures. The variation in the waveform peak amplitude can be seen by the inset plot. This variation is due only to the variation in TF and hence temperature dependence of the TARGET-C.

a conversion of ADC counts to voltage that most closely relates to the non-linearity of the TARGET-C ASIC at that specific temperature. The closer the temperature of the calibration data is to the temperature of the event data that is to be calibrated, the more accurate the result of the calibration is. It is therefore possible to remove the temperature dependence of the TARGET-C TF by generating calibration datasets at multiple temperatures that cover all possibilities for the operating temperature of each TM. This could be possible providing the thermal environment within CHEC-S (or SST Camera) is measured to ensure the TF datasets cover all possible measurements. However, adopting this approach would require considerable storage space and computing power to analyse and generate all TFs needed for each TM. This, coupled with the large number of SST Cameras that are to be produced, makes this method non ideal.

To overcome the storage implications of measuring a TF at all possible temperatures, other temperature correction approaches have been investigated. The TFs generated at multiple temperatures (shown in Figure 4.16) can be used in two ways to correct for the effect of temperature on the TARGET-C ASIC and TF calibration. Firstly, and most simply, one can apply the TF that was generated from data taken at a temperature that is closest to the temperature of the TM for the dataset that is to be calibrated. This would increase the accuracy of the calibration when compared to the previous approach. However, with TFs taken every $5°C$ it is still possible for the operating temperature of the TM to differ by $\sim 2.5°C$. This is an improvement on the current calibration approach, but again it can be further improved.

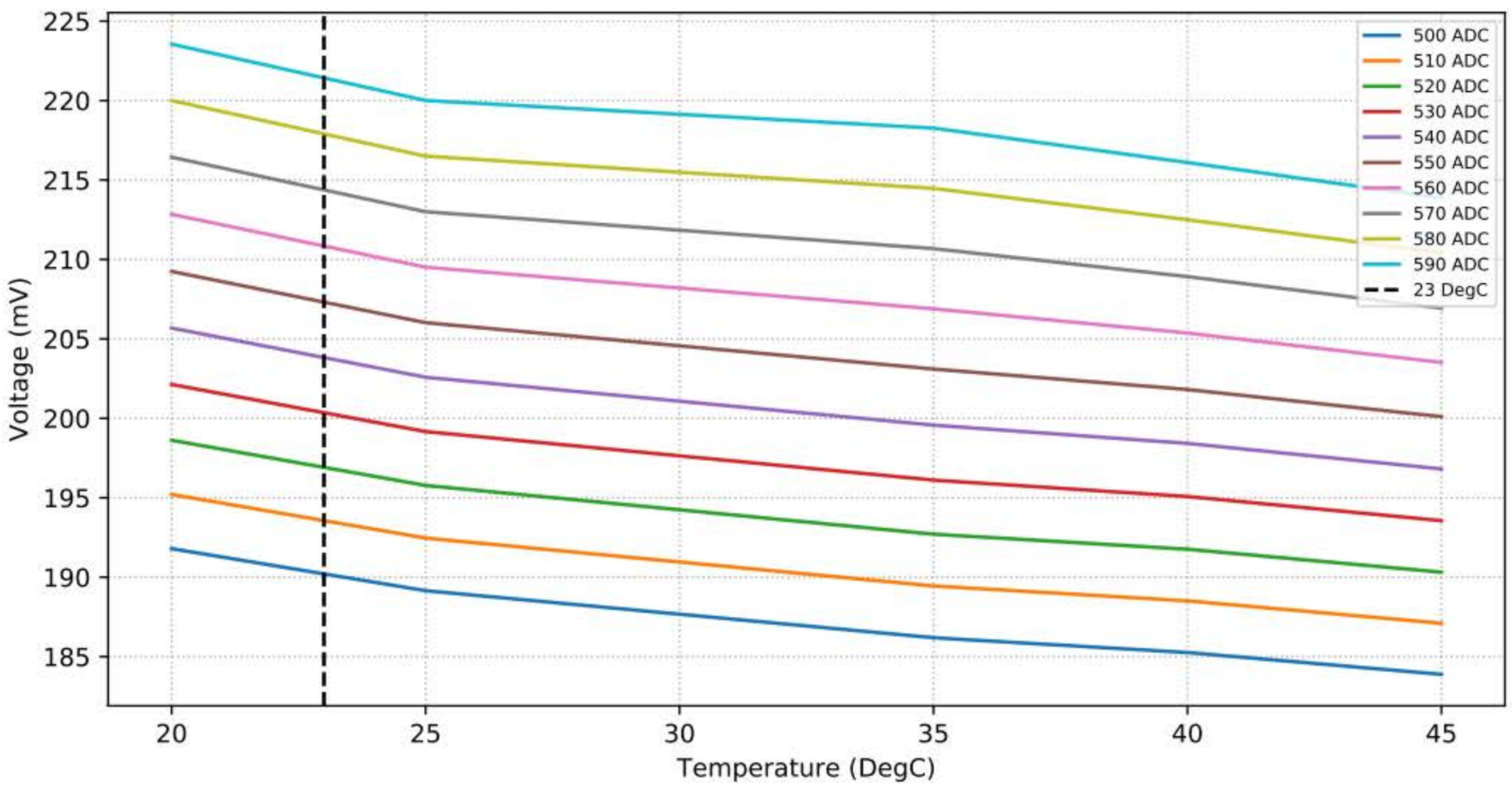

Figure 4.18: The voltage corresponding to each ADC counts value at multiple temperatures. The dotted line here indicates the voltage value to be used in the temperature corrected TF for each ADC value shown. This is completed for all ADC values in the final temperature corrected TF.

The final method for correcting the TF temperature dependence requires the generation of a new temperature corrected TF. This method utilises the five TFs taken at different temperatures to produce a final TF which is specific to a temperature selected

in the generation process by interpolating between each of the TFs. With this method, it is possible to generate a new TF at a temperature that corresponds to the ambient temperature of a TM for a given dataset. Figure 4.18 shows the outline of this method. It can be seen that the variation in voltage across the temperature of the TFs is relatively linear. Because of this it is possible to interpolate between temperatures and return a temperature corrected conversion of ADC counts to voltage. The method shown here was used to produce a TF for the event data shown in Figure 4.17 at $23°C$.

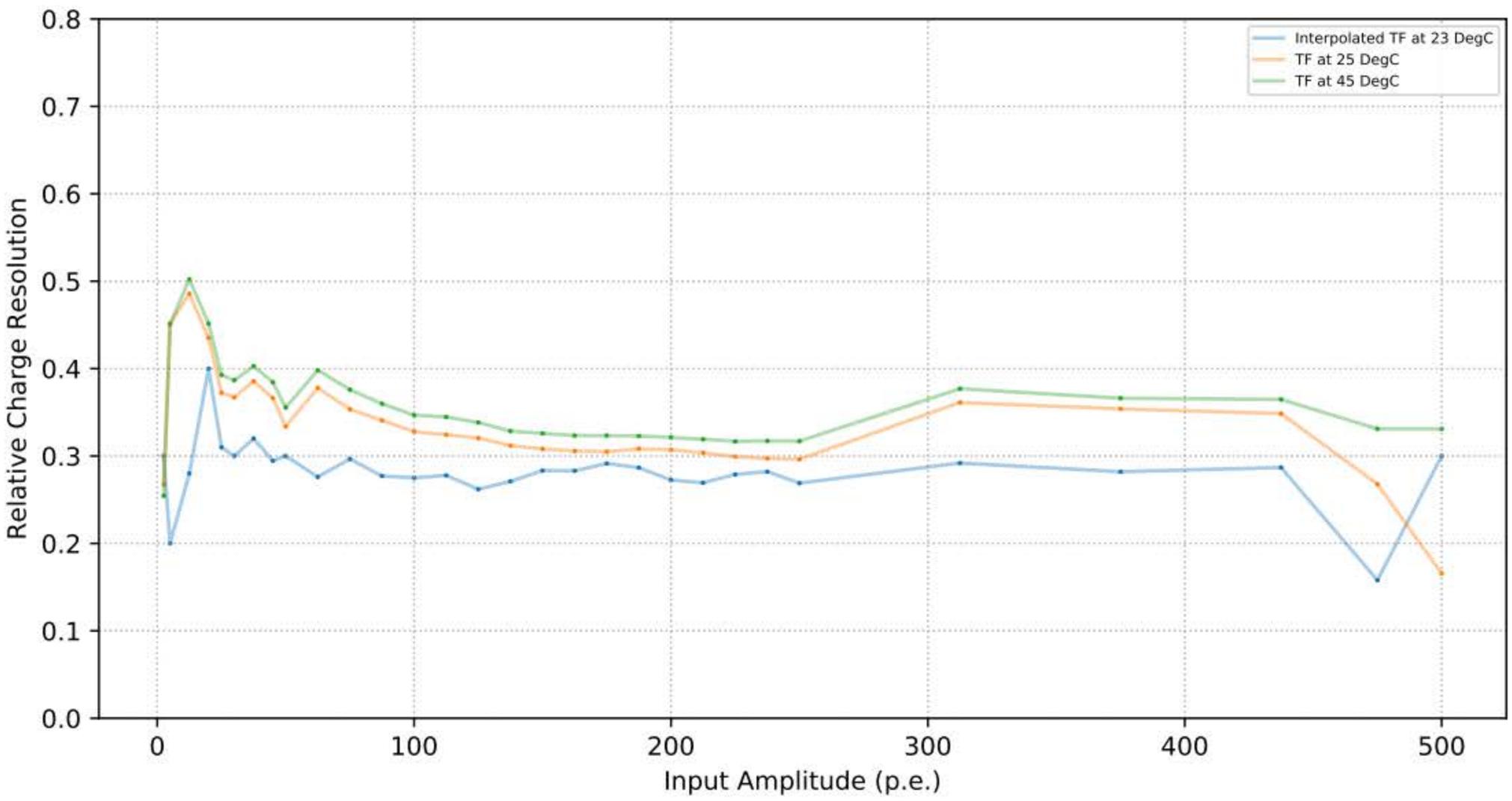

Figure 4.19: Relative charge resolution comparison of a dynamic range dataset taken at 23 $°C$ with three TFs applied. Each of the TFs applied are to represent three application approaches. The TF taken at $45°C$ represents the worst case calibration approach. The TF at $25°C$ represents the application of a TF taken at a temperature closest to operating temperature of the TM. Finally, the TF at $23°C$ represents the temperature corrected TF produced using the interpolated method. The plot shows the charge resolution performance can be improved when a temperature corrected TF is applied.

The performance of the temperature corrected TF can be determined by comparing the resulting charge resolution of the calibrated data. Figure 4.19 shows the charge resolution covering the dynamic range of TARGET-C for a dynamic range dataset taken

at $23°C$ when three different TF calibrations are applied. One TF generated at $45°C$, corresponding to the worst case calibration scenario, with a difference in temperature of $\sim 20°C$, to represent the current calibration of CHEC-S. A second charge resolution with a TF generated at $25°C$ to represent the performance when the TF taken at a temperature closest to that of the uncalibrated dataset is applied. And finally, the resulting charge resolution when a temperature corrected TF is applied.

It is clear that the performance of CHEC-S, ~~indicated by the charge resolution,~~ is improved when the temperature of the TM is considered in the calibration of data ~~digitised by such TM~~. Either by applying a TF taken at a temperature close to that of the TM operating temperature or by correcting for this temperature using a method similar to that shown here. In making no attempt to correct for the operating temperature of a TM, the accuracy of the digitised data is reduced. The impact of temperature on performance is also further compounded when one considers the thermal environment within CHEC-S. As stated previously, the temperature of each TM within CHEC-S varies from $\sim 25°C$ to $\sim 45°C$. Since each TM is operating at a temperature unique to itself, the application of a TF taken at $23°C$ will produce a non-uniform response across the camera. The spread in temperatures across the camera results in a discrepancy of digitised charge (or waveform peak height) when CHEC-S is illuminated (or electronically injected) with a uniform and isotropic input signal. Simply, the charge measured by each TM subjected to a uniform intensity will differ unless the temperature of all TMs is accounted for. In addition to the temperature spread within CHEC-S, there is also a variation in temperature across a TM, observed by differing temperatures of the power supply (PSU) board, primary board, and auxiliary board (see Section 2.4). Clearly again, the temperature of both the primary and auxiliary boards of a TM must be taken into account when applying a calibration dataset in order to produce the most accurate result.

4.6 Saturation Recovery

Section 2.2.1 describes the requirements imposed by the CTA Observatory (CTAO) to ensure the performance of each telescope structure and camera subsystem over the lifetime of the array. Requirement **B-TEL-1010** concerns the charge resolution performance that a Cherenkov imaging camera must meet in order to be accepted as a contribution to the CTA. The specific wording for this requirement is as follows:

Requirement B-TEL-1010

The required fractional charge resolution for Cherenkov signals in each Camera pixel for a specified background level of 0.125 photoelectrons/ns is given in the Figure below. Charge measurements must be possible for 0-1000 photoelectron signals. The average charge resolution should be calculated for the reference Gamma-Ray Spectrum.

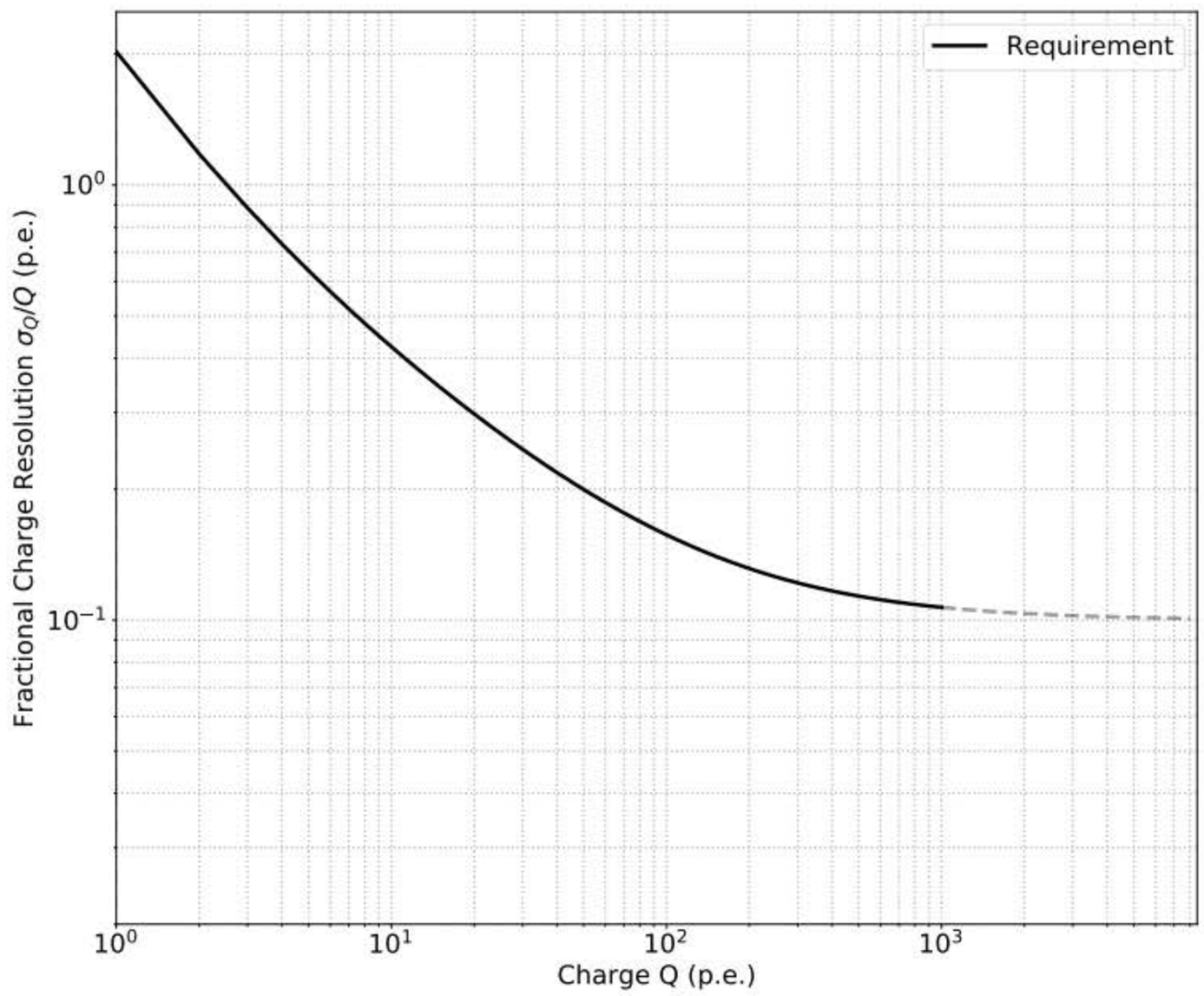

: C

TA Fractional Charge Resolution Requirement.]figureFractional rms charge resolution σ_Q/Q per pixel for different Cherenkov light signal amplitudes, expressed in units of photoelectrons (p.e.). All sources of fluctuations, including Poisson fluctuations in photoelectron number, must be included. The true pixel charge Q is that measured in an ideal detector with the same photon-detection efficiency.

Requirement **B-TEL-1010** describes the fractional charge resolution performance that each camera must meet between 0 - 1000 p.e., however, it is important to note that some sensitivity to increasing input signals must be present between 1000 p.e. and 2000 p.e..

Spaceto lungo

Currently, the CHEC-S FEEs saturate below 1000 p.e. and therefore do not meet the CTAO requirements. This saturation is observed in the TF of the TARGET-C digitising ASIC, and is presented as the plateau of the TF in Figure 4.1 above 1000 mV. The following section describes a method for the correction of the saturated waveform and the performance gained in charge resolution following saturation recovery.

4.6.1 CHEC-S Saturation

The saturation of CHEC-S is now well understood and is observed most clearly in the TF of the TARGET-C ASIC. The dynamic range, and hence limit of charge resolution performance, of this ASIC is determined by the point at which saturation begins. Correcting for this saturation effect is necessary to increase the dynamic range and charge resolution performance of CHEC-S.

The saturation behaviour of CHEC-S when injected with high amplitude input pulses can be seen in the digitised waveforms of Figure 4.20. The saturation shown here occurs following the saturation of two components of the front-end electronics. The first of these is due to the TARGET-C ASIC. The saturation of this ASIC produces a waveform with a flattened peak and shelf feature following this peak. As the input amplitude increases, the peak height is unchanged but the width of the shelf extends within the digitised waveform. At even higher amplitudes, a secondary saturation effect is observed following the saturation of the CHEC-S preamplifier buffer board. Here it can be seen that this saturation produces a non-linear response in the saturation regime at increasing input amplitudes. The behaviour due to the preamplifier buffer board saturation is unpredictable

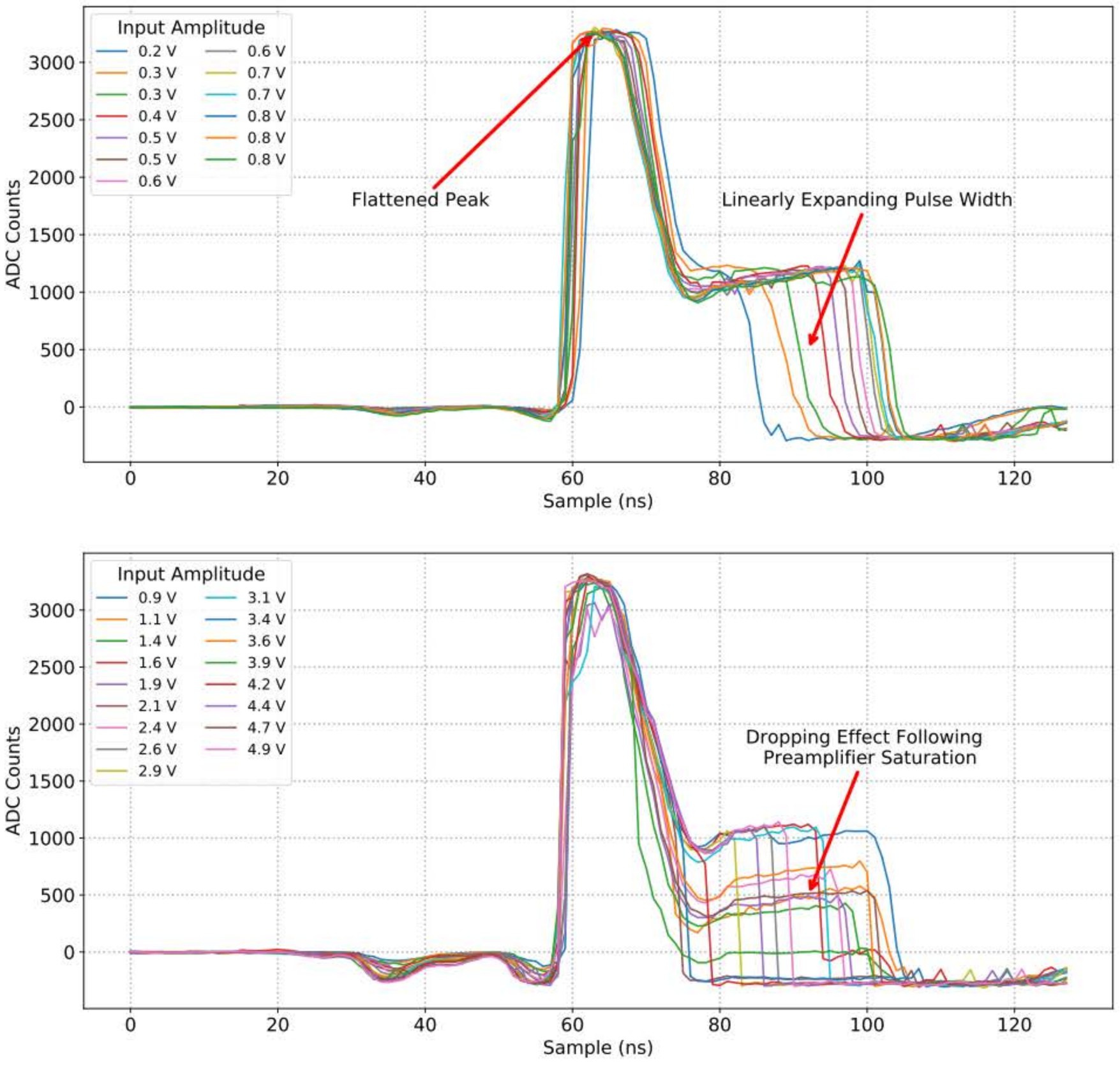

Figure 4.20: The saturation of CHEC-S is highlighted by the above plots. Top: The saturation of the TARGET-C digitising ASIC. The saturation here is identified by a flattened peak height and an expanding shelf. The width of this shelf corresponds to the input amplitude. Bottom: The saturated waveform following the saturation of the preamplifier buffer board. The saturation after this input amplitude can no longer be corrected.

and does not follow an expected pattern. It was found by members of the SST Camera team at ECAP that the saturation of the preamplifier buffer board is caused by insufficient biasing voltage. By increasing the bias voltage of the buffer board, the input amplitude at

which this board saturates is also increased (see Figure 4.22). Operating at an increased preamplifier buffer board bias voltage, therefore, increases the potential for saturation recovery as the saturation of CHEC-S is now more linear as the non-linear saturation behaviour is removed.

4.6.2 Saturation Recovery Method

With the saturation of the preamplifier buffer board somewhat mitigated, the saturation behaviour is now more linear and predictable, providing the opportunity to correct for such saturated events. Again, the aim of saturation recovery is to correct saturated waveforms by producing a correlated waveform charge or peak amplitude corresponding to the input amplitude and representative of the digitised waveform in the absence of saturation effects. The following is a description of the proposed saturation recovery method.

As evident in Figure 4.20, the pulse widths of digitised waveforms within the saturation regime increase linearly as the amplitude of electronically injected pulses increases. It is possible to utilise this behaviour in an attempt to correct these waveforms. By measuring the peak width at a given input amplitude and correlating this width with the input amplitude, a lookup table can be created which describes the conversion of saturated peak width to voltage, this conversion is akin to the method for converting ADC counts to voltage in the calibration of digitised waveforms using the TF and is highlighted in Figure 4.21. The conversion of peak width to voltage at multiple preamplifier buffer board bias voltages is shown in Figure 4.22. This conversion is contained in a lookup table so that it may be applied much like the TF. The input amplitude at which the preamplifier buffer board begins to saturate can be seen as the trend ceases. Again, the effect of the preamplifier buffer board bias voltage is prominent here. In addition, the non-uniform behaviour of the digitised waveform following the preamplifier buffer board saturation is observable in the large standard deviation, represented by the error bars of each plot. The

small error before the preamplifier buffer board saturation also indicates the uniformity of the width measurement before this secondary saturation, again proving the feasibility of this method. Following the creation of the lookup table, it is now used to convert from peak width to voltage. The performance capability of this saturation correction process is given in the following subsection.

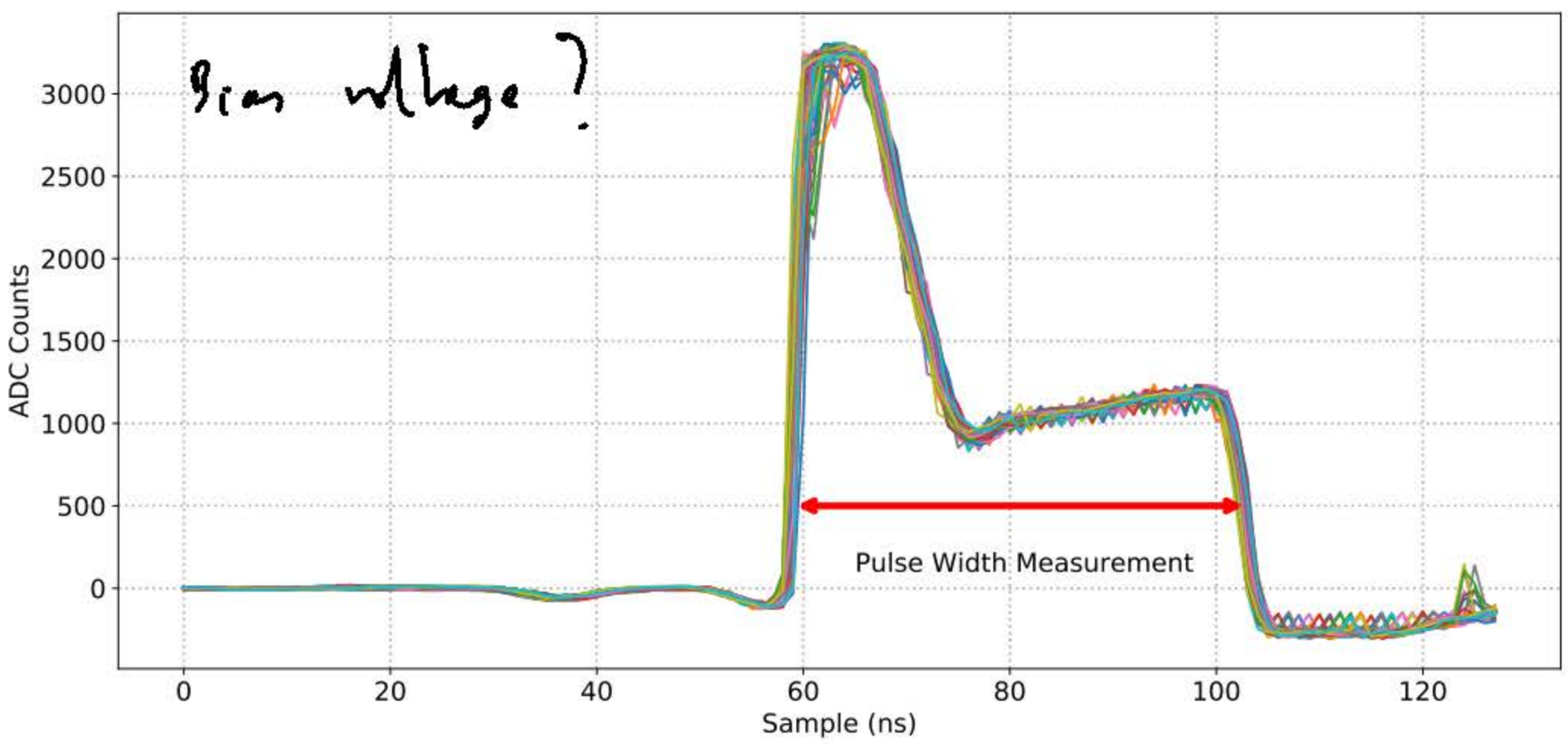

Figure 4.21: An example of the pulse width measurement necessary for the correction of saturated waveforms. The width of the saturated pulse is extracted at $500mV$. This width measurement is inputted into a lookup table for the conversion of pulse width to voltage.

With the width versus input amplitude lookup table now created, it can be used to convert the width of other saturated waveforms to a recovered peak amplitude or p.e. level. Clearly, the application of this lookup table is very simple. Firstly, the width of each saturated waveform is measured at a given amplitude. This width is then converted into voltage corresponding to the peak height of the resulting waveform in the absence of any saturation effects. Finally, the peak amplitude can be converted to a p.e. level using the appropriate SiPM gain conversion. Since the data used in the following performance subsection was measured using an electronically injected pulse, two gain conversions are shown in the later Figures 4.24 and 4.25. The effect of this gain value is discussed and

can provide a recommendation for the gain setting used in the operation of CHEC-S.

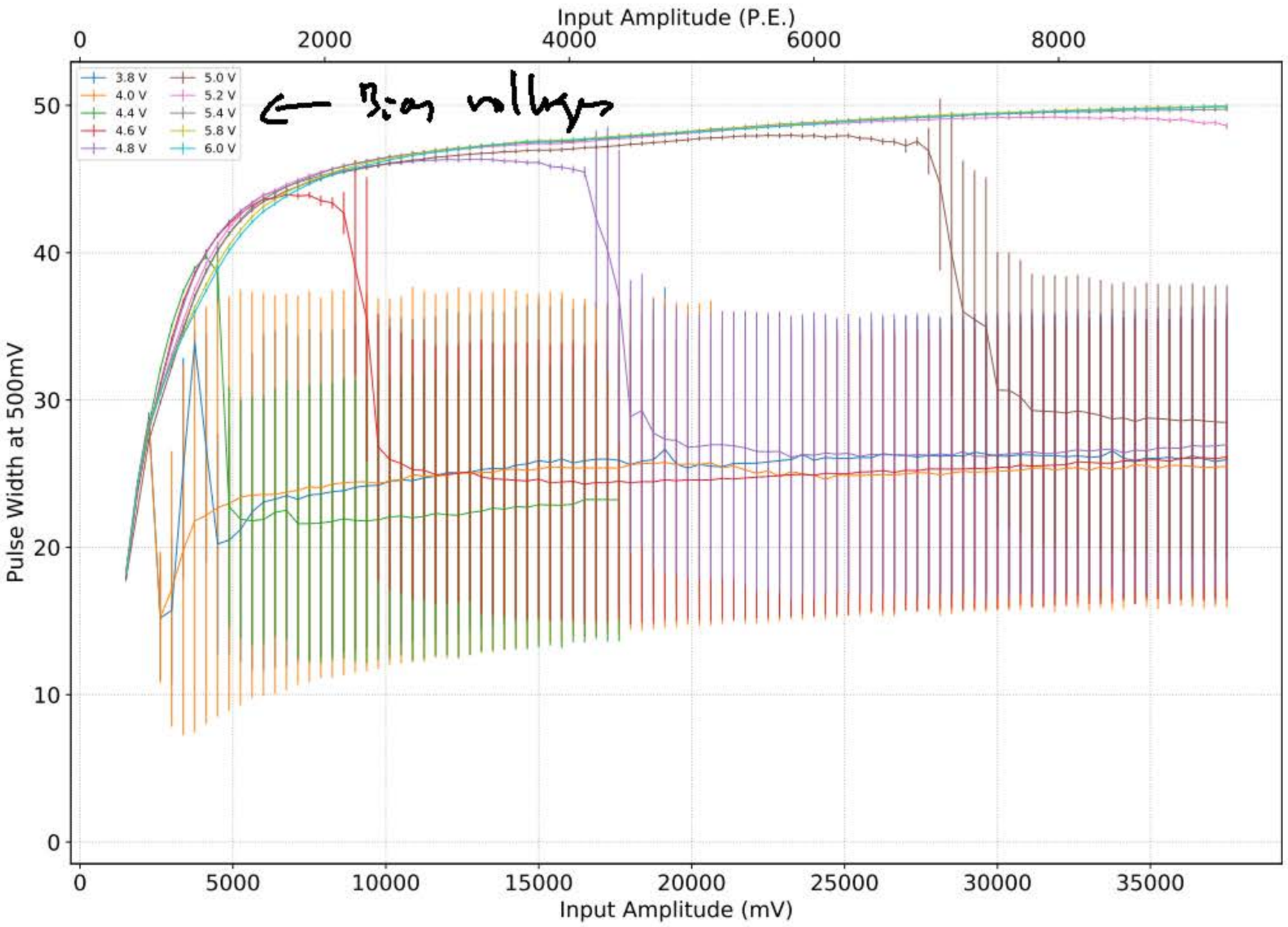

Figure 4.22: The resulting lookup table following the measurement of pulse width at many input amplitudes. Shown here is the lookup table for multiple preamplifier buffer bias voltages. The turning point of each plot indicates the amplitude at which the preamplifier buffer board begins to saturate.

4.6.3 Saturation Recovery Performance

The performance of this saturation recovery and correction is determined by the accuracy of such a method when applied to saturated waveforms. Again the data utilised here was measured using electronically injected pulses, therefore, any effects due to SiPM noise (dark counts, optical crosstalk, CCT, afterpulsing) are not present. The remaining noise and saturation effects are a consequence of the electronic components present in the

preamplifier buffer board of the TM. In addition to this, the input amplitudes stated in the performance plots shown here are indicative of the input amplitude to the TARGET-C ASIC as a conversion is included to account for the various amplification stages in the shaping electronics. The performance highlighted here is, therefore, an indication of the performance possible when applying this saturation recovery algorithm to the TARGET-C digitising ASIC.

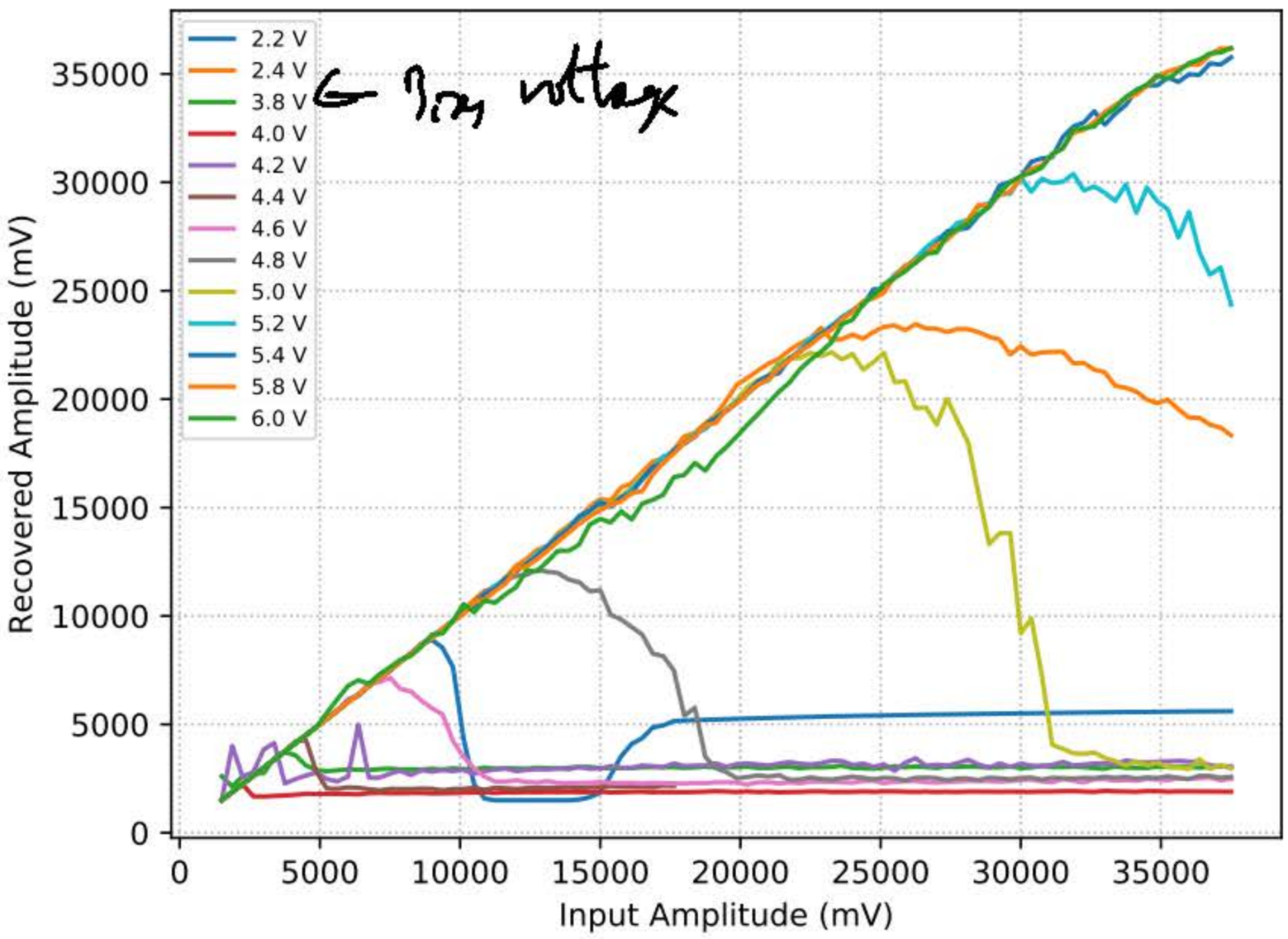

Figure 4.23: A comparison of the recovered amplitude versus input amplitude following the application of the saturation correction lookup table. It can be seen that the performance follows a linear relationship, suggesting that the recovery of saturated waveforms is possible. Again, this relationship fails following the saturation of the preamplifier buffer board.

The initial performance indication of this algorithm concerns the resulting peak amplitude following the application of this correction and the comparison of this peak amplitude to the known injected input amplitude. Figure 4.23 shows the recovered amplitude following the saturation recovery process versus the injected input amplitude at

numerous preamplifier buffer bias voltages. The recovered peak amplitude here shows a relatively linear response before the saturation of the preamplifier buffer board, after this point the recovery process fails, again indicated by the turning point seen in Figure 4.23. After the application of the saturation recovery algorithm, the recovered peak voltage can be converted to p.e. levels by applying a simple mV to p.e. conversion accounting for the gain of the SiPM measured by the TARGET-C digitiser. The SiPM gain values used for this investigation are $2mV/p.e.$ and $4mV/p.e.$, these are representative of the range of gains utilised with CHEC-S SiPMs and provide a baseline for the optimisation of SiPM gain under operation for both CHEC-S and the SST Camera.

As discussed previously, the motivation for this saturation recovery and correction investigation was the CTAO requirement **B-TEL-1010** with the aim to prove the capability of CHEC-S in response to this requirement. Again, the requirement relates specifically to the fractional charge resolution performance of the Cherenkov camera. The fractional charge resolution, σ_Q/Q_T, for a given true charge, Q_T, can be derived from the following equation:

$$\frac{\sigma_Q}{Q_T} = \frac{1}{Q_T}\sqrt{\sigma_M^2 + \sigma_{ENF}Q_T + \sigma_C^2 Q_T^2}, \tag{4.5}$$

where σ_M describes the root mean square deviation of the measured charge to the true charge, σ_{ENF} represents the *Excess Noise Factor* of the CHEC-S SiPM, and σ_C is the error in charge calibration.

As stated in Section 2.4.2, ENF is a mathematical representation for the variation of SiPM response due to a single p.e. and describes the effect of afterpulsing and optical crosstalk (OCT) within the SiPM. For the sake of this investigation, a value of 1.3 was used for the ENF corresponding to a representative value of 30% for CHEC-S OCT. Requirement **B-TEL-1010** is specified at a miscalibration error of 10%, the following

results are presented with a miscalibration of both 10% and 5% in order to highlight the impact of this miscalibration error.

The resulting fractional charge resolution performance at various preamplifier buffer board bias voltages, SiPM gain, and calibration errors are shown in Figures 4.24 - 4.27. One should note that the CTAO charge resolution requirements are defined between $1 - 1000 p.e.$, for completeness, this requirement has been extended to cover the full range of input amplitude and true charge, Q_T. Figures 4.24 and 4.25 show the charge resolution with a miscalibration of 10% applied. It can be seen that the shape of these plots are identical but one should observe the variation in input amplitude. Clearly the impact of a lower SiPM gain setting shifts the charge resolution along the $X-axis$ towards higher amplitudes. This can be seen by comparing the input amplitude at the crossing of the charge resolution and CTAO requirement. Here it can be seen that both SiPM gain settings produce a fractional charge resolution that surpasses the CTAO requirements at a preamplifier buffer board bias voltage of $4.6V$ or higher. The significance of this result is that this would suggest all CHEC-S front-end electronics currently modified for $4.6V$ bias voltage should meet the current CTAO requirements providing the SiPM gain is between $2mV/p.e.$ and $4mV/p.e.$. Figures 4.26 and 4.27 present the fractional charge resolution performance produced with a miscalibration of 5% applied. Here the impact this miscalibration factor has on the charge resolution performance can be observed most clearly. Providing the miscalibration of CHEC-S at high intensities is less than 10%, the fractional charge resolution performance passes the CTA requirement.

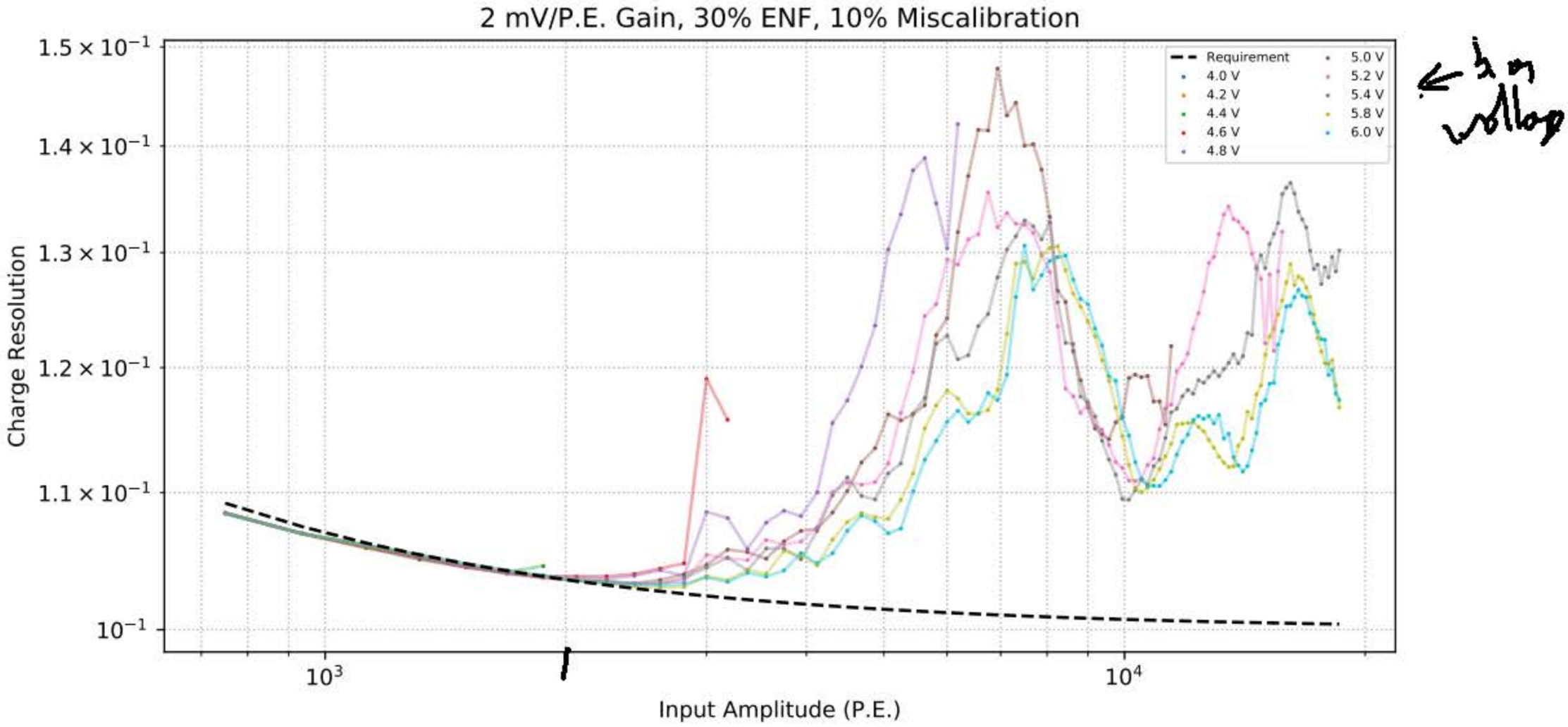

Figure 4.24: Resulting fractional charge resolution performance following the application of a saturation recovery method with a SiPM gain of $2mV/p.e.$ and a miscalibration error of 10%. Also indicated is the CTAO requirement shown by the black dashed line.

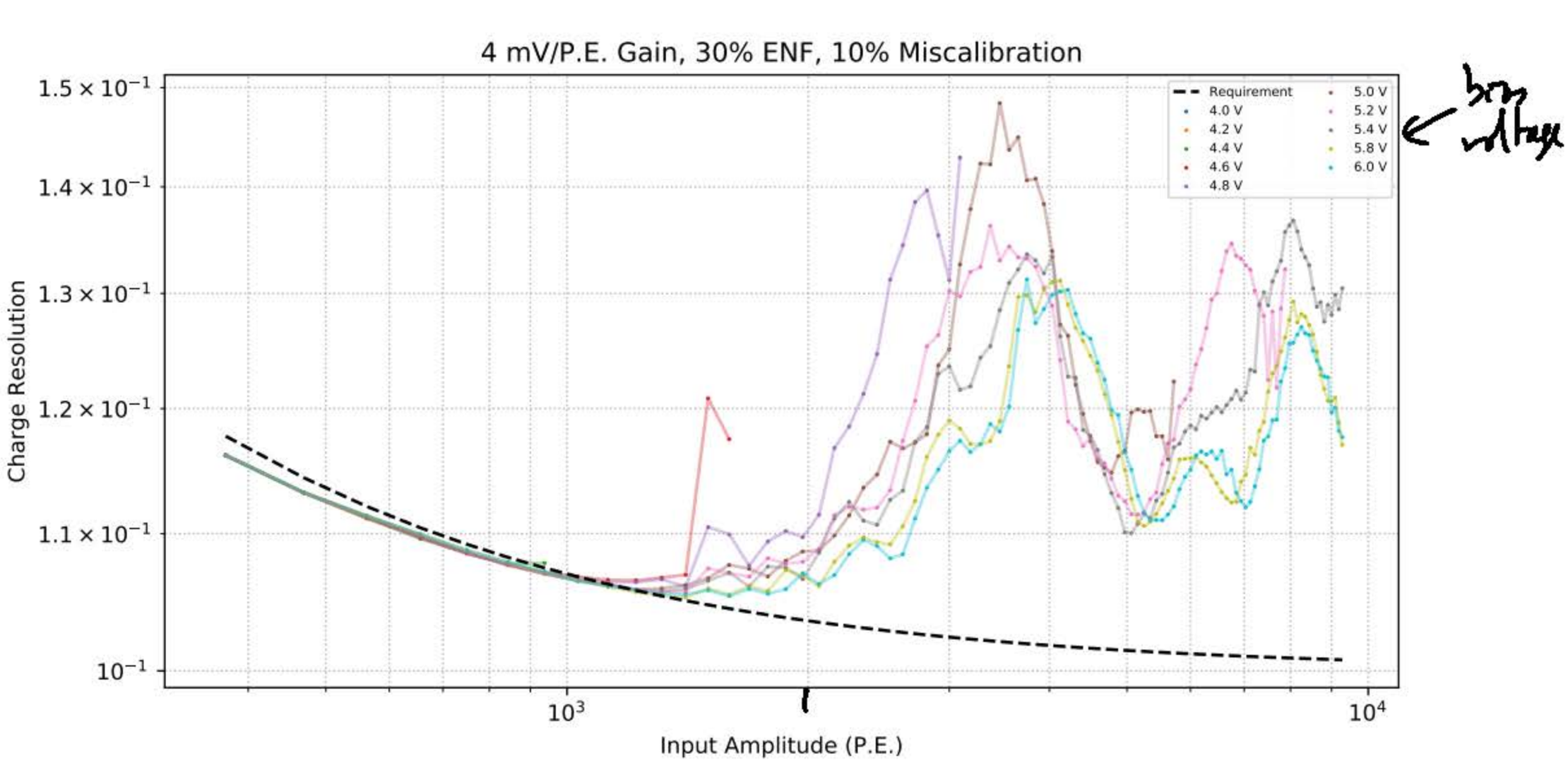

Figure 4.25: Resulting fractional charge resolution performance following the application of a saturation recovery method with a SiPM gain of $4mV/p.e.$ and a miscalibration error of 10%. Also indicated is the CTAO requirement shown by the black dashed line.

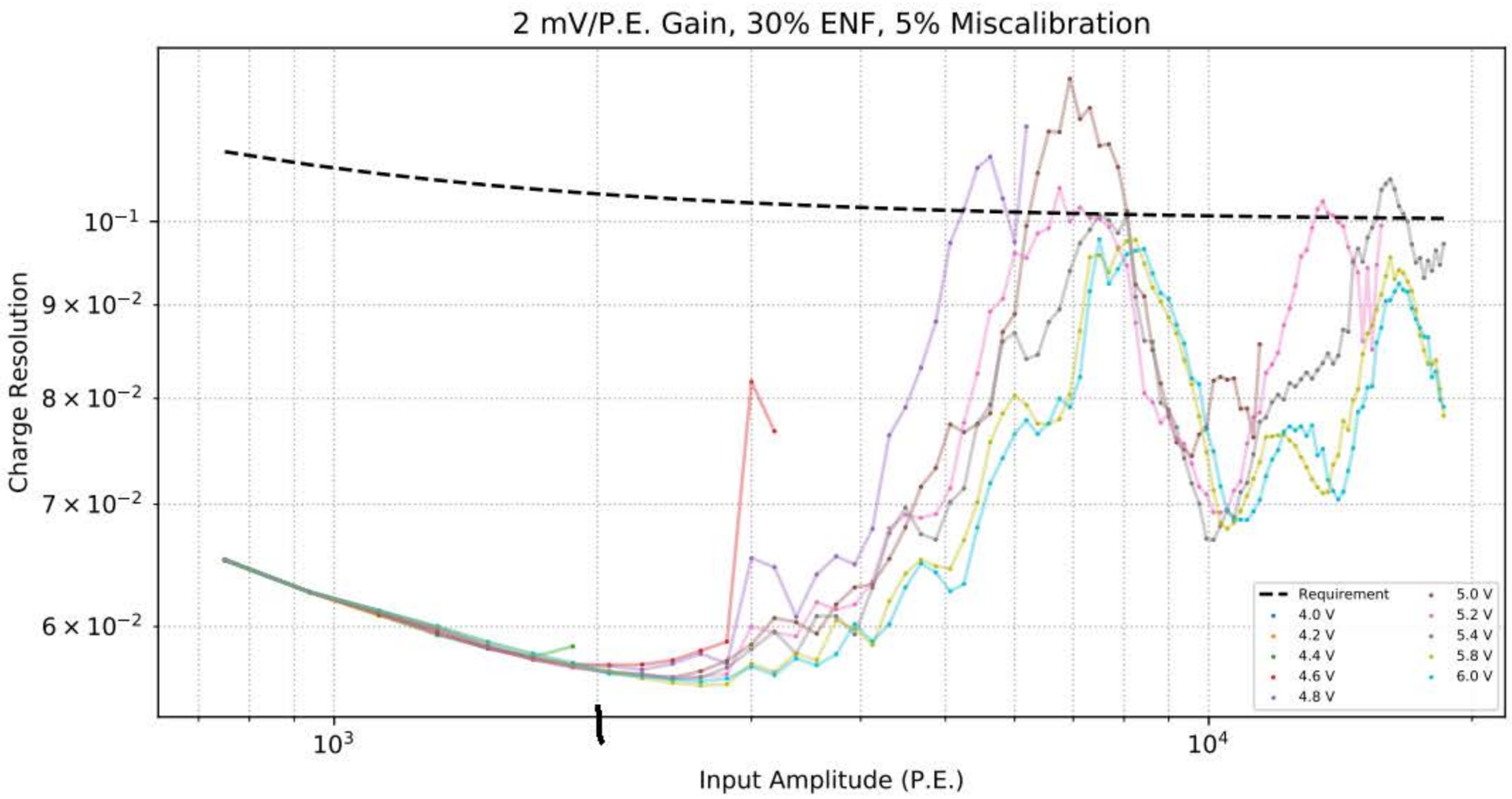

Figure 4.26: Resulting fractional charge resolution performance following the application of a saturation recovery method with a SiPM gain of $2mV/p.e.$ and a miscalibration error of 5%. Also indicated is the CTAO requirement shown by the black dashed line.

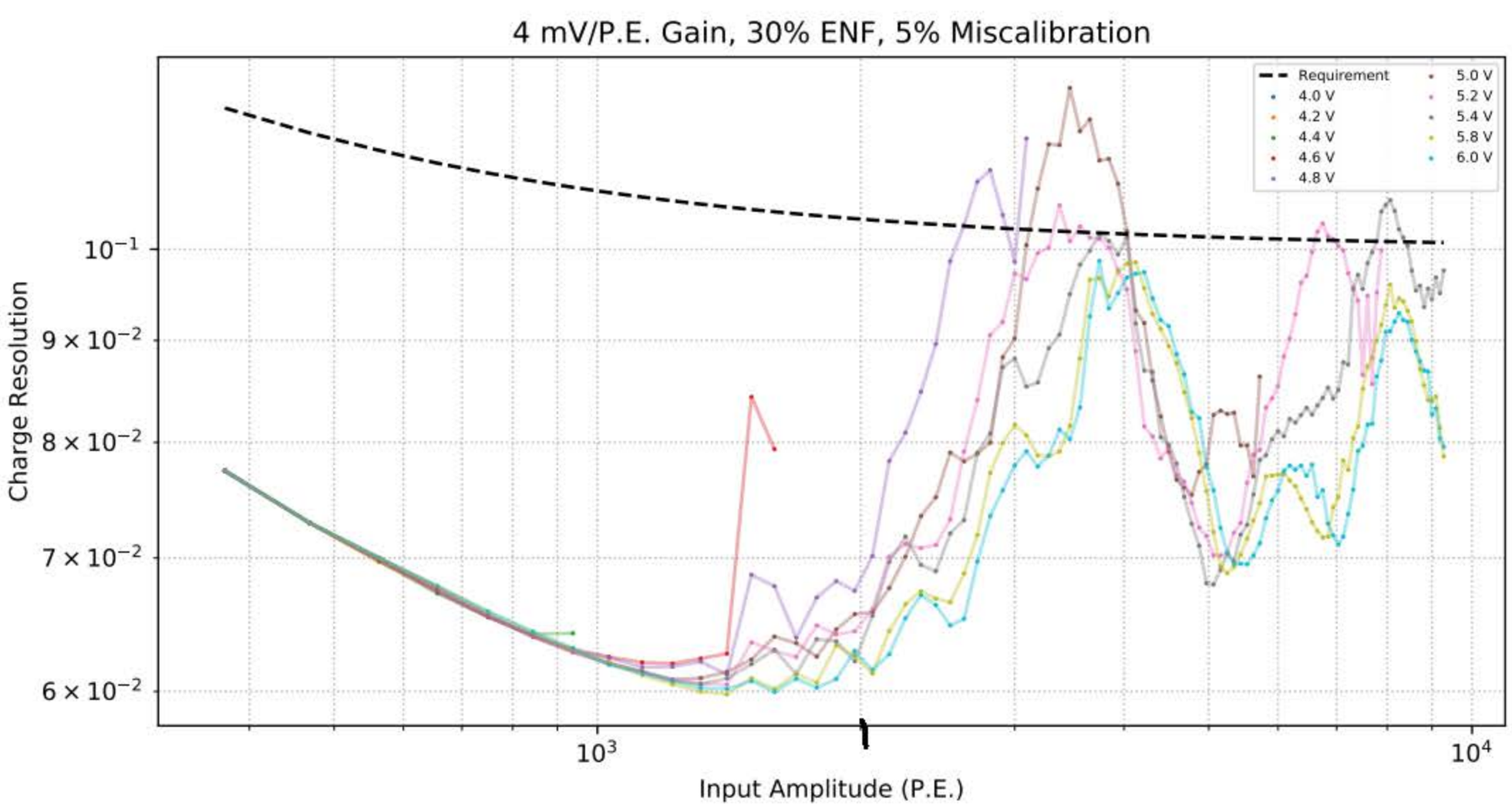

Figure 4.27: Resulting fractional charge resolution performance following the application of a saturation recovery method with a SiPM gain of $4mV/p.e.$ and a miscalibration error of 5%. Also indicated is the CTAO requirement shown by the black dashed line.

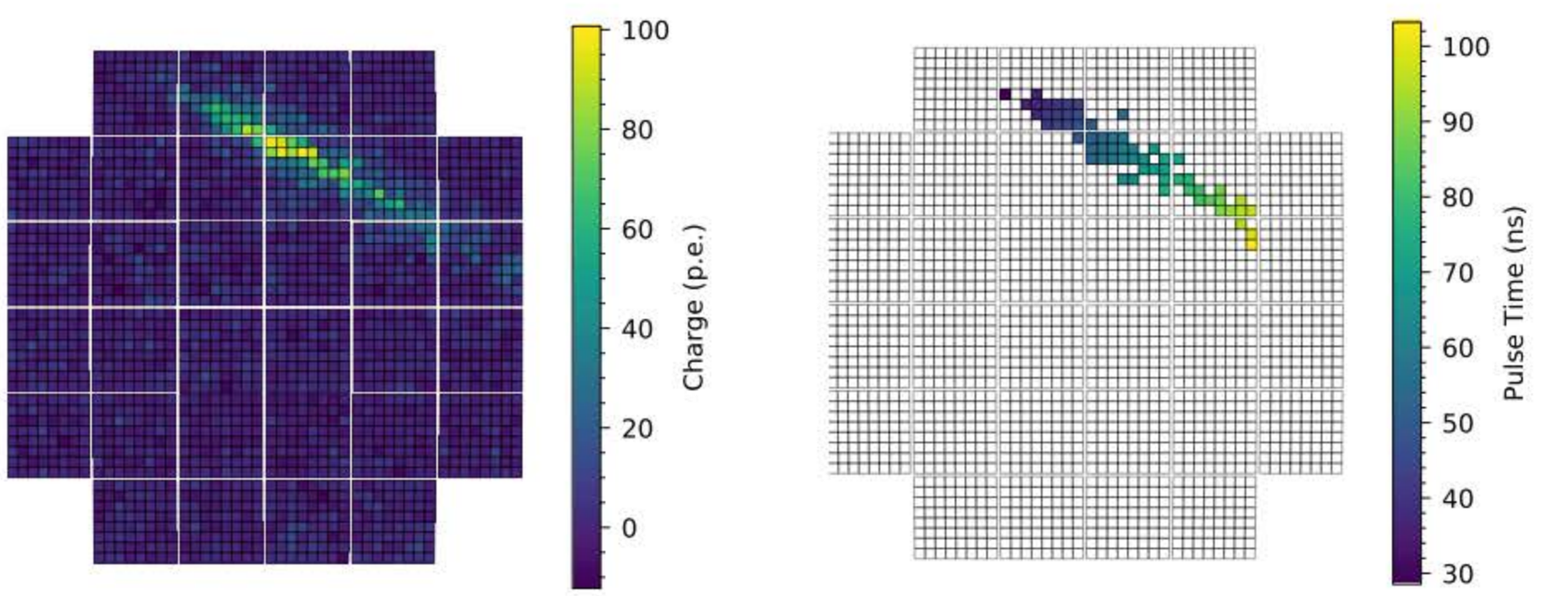

(a) (b)

(c)

Figure 4.28: An example of a long duration Cherenkov event observed during an on-telescope campaign of CHEC-S and the ASTRI-Horn telescope. (a) shows the amplitude of the digitised waveform for each pixel during the Cherenkov event, the track of the Cherenkov light can be seen as it transits the focal plane; (b) highlights the timing of the digitised waveform as the Cherenkov light crosses each pixel; (c) shows the digitised waveforms for a subset of the pixels triggered by the Cherenkov event, again indicating the spread in peak timing for the single digitised event. It can be seen from (b) and (c) that a long duration Cherenkov event can give rise to a variation in peak time of $\sim 50ns$.

4.7 Conclusion

The use of TARGET-C, and all digitising ASICs, require the calibration of the digitised signal in order to produce a meaningful dataset in real-world units, such as voltage for ADCs. Previously, the CHEC-S prototype utilised a double-Landau expression to determine the sampling cell present at the maximum of the electronically injected pulse digitised by TARGET-C. This method was used as it was thought to reduce the impact of sensitive sampling cells on the calibration performance. I have shown in this chapter that this method is not flawless. Figure 4.4 shows an example of the double-Landau expression used in this method. It can be seen that the position of the waveform peak given by the double-Landau expression is incorrect when compared to the digitised waveform. I found that the inconsistency in peak position given by the double-Landau expression is rather common and would lead to an underestimation in the subsequent TF since the amplitude of the sampling cell given by this method is lower than that at the peak of the digitised data. In addition to this, the double-Landau expression is rather slow. To combat this, only the first channel of each ASIC is calibrated in this way. The peak position of all subsequent channels is produced by evaluating the variation in signal transit time in neighbouring channels which is determined by the physical differences in track length for each channel. This method is somewhat valid, as the differences should be minimal, but is also less than desirable as it could possibly compound the inaccuracy in peak position if the initial expression is incorrect.

I have presented here my method for the generation of calibration data using the cross-correlation of digitised data with a reference pulse. I have also shown that it is possible to improve the cross-correlation by interpolating between samples of the digitised waveform. I found that the most accurate interpolation method available for this application was the Piecewise Cubic Hermite Interpolating Polynomial method. In order to test this calibration method, I produced a simulated dataset using the method outlined

by Figure 4.13. The various peak finding methods described in this chapter were applied to this simulated data. Figure 4.14 shows the performance of each peak finding method, clearly showing the improvements that can be gained in adopting a new approach for the generation of TF calibration data. It is also important to note that the cross correlation method here has not been optimised for speed, this is an area of improvement for this method and will be further developed in the future before it's use is adopted completely by the CHEC project.

CHEC-S comprises a thermal control unit for the control and regulation of the thermal environment of all internal components within the camera body. Cooling of the internal electronics is not as important as the cooling of SiPM tiles on the focal plane, but it is important to maintain a constant temperature of all electronics during operation. In regards to temperature, there are two existing concerns for CHEC-S calibration. Firstly, due to inevitable flows in the circulation of cool air within CHEC-S, there is a large spread in temperature as seen by each TARGET module. It is possible for this spread to be $\sim 15°C$ during operation. Secondly, there is a large variation in temperature that the TARGET modules are calibrated at in the laboratory ($23°C$) when compared to TARGET module temperatures during operation (up to $\sim 50°C$). The first point here can be mitigated by minimising the spread in temperatures within CHEC-S, however, this is very difficult and impractical due to the compact nature of the Cherenkov imaging camera. It is possible to remove any discrepancies in the digitised signal produced by temperature variation by correcting for the temperature dependence of the TF calibration.

Figure 4.17 shows the impact this temperature dependence can have on a Cherenkov pulse, producing a variation of $\sim 30mV$ simply by applying a TF generated at a temperature that differs to the operating temperature of a TARGET module within CHEC-S. I have outlined my method for correcting for this temperature dependence through the use of multiple TFs taken at varying temperatures. With this method, it is possible to select a specific TARGET module operating temperature and interpolate between each of the TF

curves in order to produce a TF that is specific to the given temperature (shown by Figure 4.18). Again, I have shown the performance that can be gained when the temperature dependence of the TARGET-C digitising ASIC is removed in Figure 4.19.

The fractional charge resolution performance presented here indicates that, at an operating SiPM gain of $4mV/p.e.$, CHEC-S is likely to meet the CTAO charge resolution requirements at the specified intensity range of $0 - 1000 p.e.$ In addition to this, this saturation recovery and correction investigation can be used to infer specific requirements for the design and operation of the FEEs of the SST Camera. Firstly, it is recommended that that the preamplifier buffer design is modified so that saturation effects are removed or mitigated in a similar fashion to the improvements made by modifying the bias voltage of CHEC-S preamplifier buffer boards. For the operation of CHEC-S, all preamplifier buffer boards should operate at a bias voltage of at least $4.6mV$. Secondly, a recommendation for the number of samples required in the digitised readout window can be deduced. Figure 4.28 shows the peak timing observed for a long duration Cherenkov event as the Cherenkov light transits the focal plane of CHEC-S during on-telescope observations (See Chapter 5). It can be seen that there is a gradient in peak timing giving rise to variation in peak position of digitised waveforms for various pixels across the camera with the peak position of pixels furthest from the trigger pixel arriving $\sim 60ns$ after the initial triggered pixel. In addition to this, the width of saturated waveforms reach a maximum pulse width of $\sim 50ns$ as observed in Figure 4.21. Knowing this, one can determine the required number of samples for a digitised waveform to encapsulate the entirety of a saturated Cherenkov event as follows:

$$NSamples = SaturatedWidth + EventTimeGradient + Req.Baseline$$

Req.Baseline represents the required number of samples at the baseline in order to measure the baseline position and noise of the digitised event, ideally this would be an additional $10ns$ either side of the digitised pulse. With each of these parameters accounted

for, a readout window of $\sim 130ns$ is required. The values used for this determination are somewhat conservative, a long duration high intensity Cherenkov light event is also unlikely. It is therefore pragmatic to state that a readout window size of at least $128ns$ is used for on-telescope observations. Finally, a comment for the operating SiPM gain can be given. It can be seen that the performance of this saturation recovery approach improves when the photosensors are operated at a lower gain. However, there is a compromise that must be evaluated since the SiPM gain controls the ability for a single p.e. event to be observed (discussed further in Section 2.4.2). Although, it is possible to recommend that the operating gain of CHEC-S SiPMs should be no greater than $4mV/p.e.$ since the charge resolution performance above this gain will no longer meet requirements.

4.8 Future Work

The development of the CHEC-S prototype has resulted in a well understood calibration technique. It has been shown here that, although the development has progressed, there are still improvements that can be made concerning the calibration of TARGET-C. As the focus of the CHEC team turns to the development of the SST Camera, the production model for the SST of CTA, there are many aspects of the calibration that may change. The calibration procedure should be simplified with the application of the cross correlation method shown here in Section 4.4.2.1. It has also been shown that there are many characterisation steps that must be followed to ensure the TARGET-C TF calibration is capable of calibrating TFs regardless of operational environments. In addition, it has also been shown that the application of a saturation correction regime is necessary for CHEC-S to meet CTAO requirements. As the development and build of the SST Camera incorporates updated ASICs and electronic designs, it is important to note that the effects shown here will require evaluation to ensure the absolute performance of the SST Camera.

Chapter 5

CHEC-S On-Telescope Observations

Contents

5.1 Introduction

Commissioning a photon-counting Cherenkov imaging camera, such as CHEC-S, requires continuous calibration and testing. Within controlled laboratory conditions, the majority of parameters and aspects of the camera can be tested under repeatable conditions ensuring identical environments for day-to-day testing, producing accurate, comparable results. In undertaking an on-telescope testing campaign, the camera is positioned in a varying and less controllable environment. This coupled with inexperienced camera operators provides the opportunity to further test the performance and procedural operation of CHEC-S as the inexperience and lack of sleep with long night shifts can lead to operational mistakes.

Although not the first on-telescope campaign for the CHEC project (CHEC-M on-telescope campaign took place in November 2015 [77]), the inaugural on-telescope verification of CHEC-S took place in May 2019 at the Serra La Nave Observatory on the slopes of Mt. Etna, Sicily, utilising the INFN Astri-Horn telescope structure [108]. Not only did this site provide the opportunity to verify CHEC-S under varying weather and thermal conditions, it also provided the important opportunity to prove the compatibility of CHEC-S with the ASTRI-Horn telescope structure. As mentioned in 2.3.1, the selected SST system ~~is a telescope system~~ derived from the ASTRI-Horn telescope structure and a CHEC-S based Cherenkov imaging camera. Figure 5.1 shows CHEC-S installed on the ASTRI-Horn telescope. This campaign would become the first proof of concept for an ASTRI-CHEC telescope system.

Located on the slopes of Mt. Etna, Serra La Nave is home to an ever-changing weather system. Ongoing testing during the day and throughout the night gave rise to a temperature range of $+15°C$ to $-5°C$. This coupled with high humidity, rain and, at times, snow, presented the chance to fully test the thermal performance of CHEC-S. In addition to environmental factors, the large city of Catania to the south of Mt. Etna produces a night sky background (NSB) that can impact observations when pointing in

Figure 5.1: Photo of CHEC-S mounted on the ASTRI telescope structure at Serra La Nave Observatory, Sicily.

this direction. Each of these varying parameters enabled further characterisation and verification of CHEC-S.

The primary aim of this on-telescope campaign was to prove the compatibility of CHEC-S and the ASTRI telescope structure in terms of operating procedures and performance. During this campaign, a number of well-studied gamma-ray sources were used for observational targets including: the prominent active galactic nuclei; Markarian-421 and Markarian 501 [109][110]; and the BL Lacertae object, PG 1553+113 [111]. I will outline the operational procedure conducted during observing runs before discussing the use of Hillas analysis for the analysis of Cherenkov event data. In addition to this I will describe an investigation into anomalous high noise events observed during the campaign before highlighting the use of the saturation recovery process covered in Section 4.6 to estimate the intensity of Cherenkov events saturating the FEEs of CHEC-S.

5.2 Trigger Threshold Calibration

Section 2.4.3 describes the two-level trigger criteria that must be met for CHEC-S to form a full camera trigger and event readout. The level-one trigger criterion is evaluated by the T5TEA trigger ASICs within each TARGET module and states that the analogue sum of four SiPM pixels, in a $2x2$ square (Super Pixel, SP), must be greater than a configurable threshold set within the camera software. Following a successful level-one trigger, a trigger signal is sent to the trigger FPGA aboard the Backplane encoding the time at which each SP passed the level-one trigger. The level-two trigger logic is met when two or more nearest neighbour SPs trigger within a configurable coincidence window. Following a successful level-two trigger, a full camera digitisation and readout is initiated by the trigger FPGA. The level-two trigger logic is utilised to reduce the frequency of night sky background (NSB) photon induced camera triggers. Since the NSB environment at Serra La Nave varies largely depending on telescope pointing, the presence of stars within the camera field-of-view (FoV), and cloud coverage, it was necessary to set the trigger threshold level accordingly at the start of each observing run. This was completed by conducting a trigger threshold scan.

A trigger threshold scan evaluates the trigger rate at varying trigger threshold levels. The trigger threshold is varied and the number of level-two, full camera, triggers is measured. The resulting scan conducted at multiple telescope zenith angles can be seen in Figure 5.2. The measured threshold scan consists of two constituent sources contributing to the overall shape of such scan. The high trigger rate observed at lower trigger threshold levels is produced largely by NSB events, with a much smaller frequency of Cherenkov events. This is presented in the threshold scan as an NSB wall preceding the turning point at $\sim 32 mV/SP$ observed in Figure 5.2 [112]. The contributions to the camera trigger rate at trigger threshold levels above this turning point consist largely of Cherenkov events and represent a reduction in the number events triggered solely by NSB.

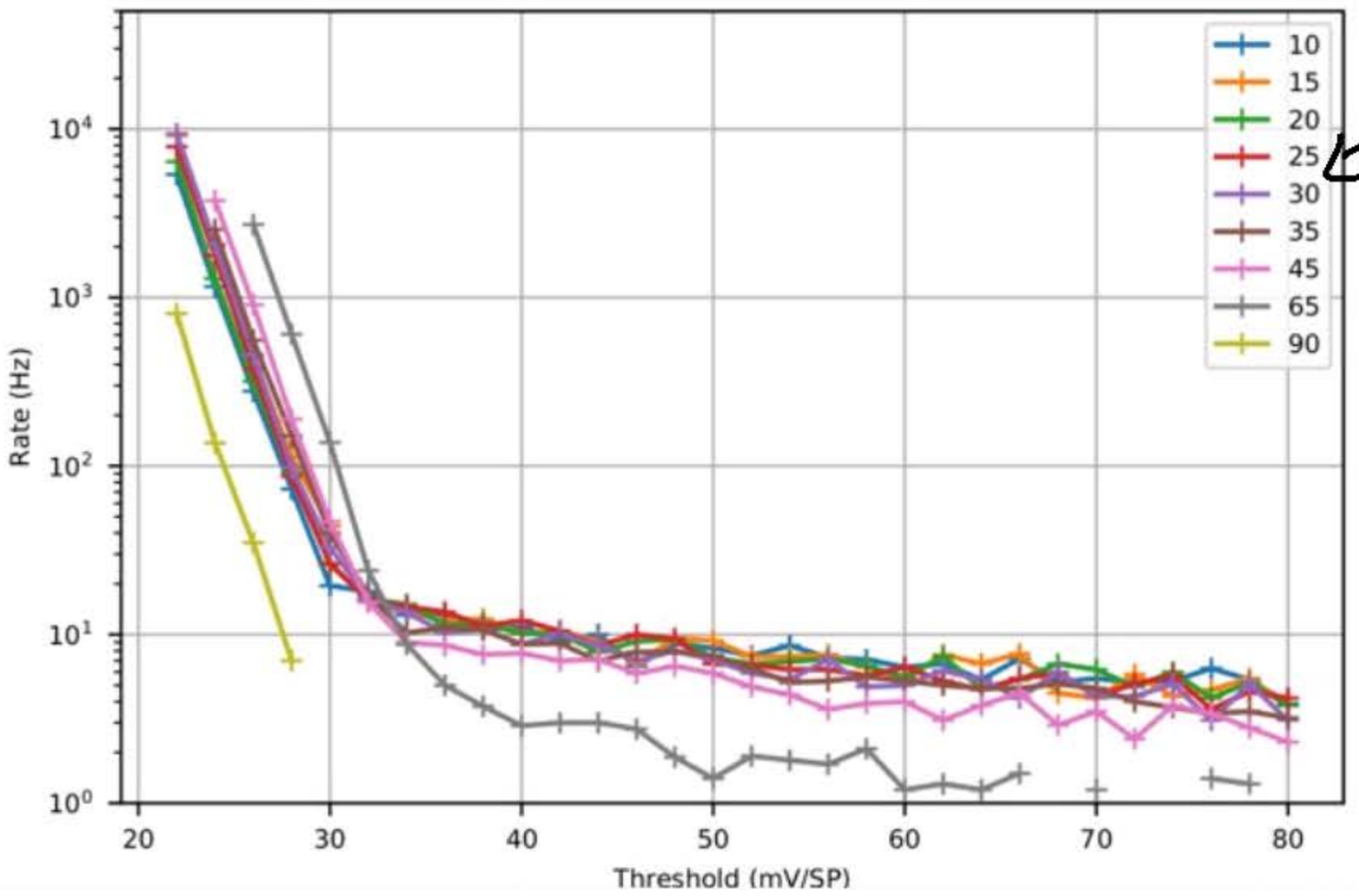

Figure 5.2: An example of a trigger threshold scan conducted at multiple telescope zenith angles. At each angle, the trigger threshold is varied and number of triggers measured. The turning point observed in this plot at $\sim 30 mV/SP$ indicates the threshold at which camera triggers produced by NSB photons is greatly reduced.

photons.

The trigger threshold level of CHEC-S is therefore set to maximise the number of Cherenkov events observed and suppress the number of triggers produced by NSB photons. Since the available data storage at the observatory was limited, the trigger threshold level was set at a level higher than the NSB wall turning point. In setting the trigger threshold level in this manner, one must monitor the camera trigger rate, as a small variation in the NSB illumination level can greatly increase the number of unwanted camera triggers.

5.3 Wobble Observations Technique

The observation of gamma-ray sources by imaging atmospheric Cherenkov telescopes (IACTs) is conducted in one of two modes of operation: On-Off mode or Wobble mode [113]. The On-Off mode of observation positions the gamma-ray source at the centre of the

camera FoV whilst taking Cherenkov data. The advantage of this is such that the source position is well known, providing good telescope pointing performance. However, in order to obtain a good understanding of the source region background, for background subtraction, a further dataset must be taken using a similar sky region that does not contain the original source. Since the background is observed asynchronously to the source, it is possible for environmental and camera conditions (NSB, temperature, etc.) to have changed, thus impacting the reliability and comparability of the background measurements.

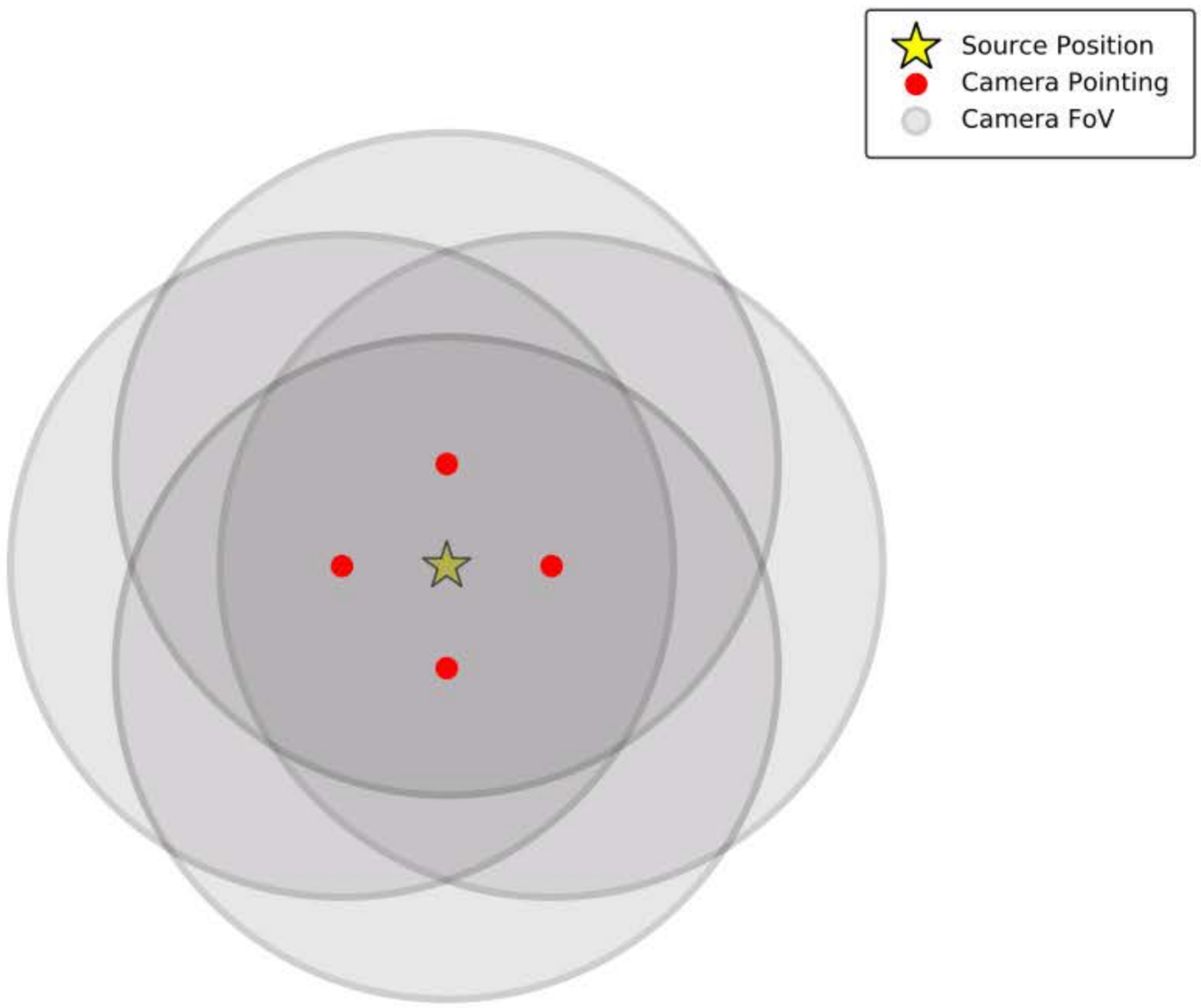

Figure 5.3: An example of the camera field-of-view while operating under the *Wobble* mode. It can be seen that the gamma-ray source is positioned at a constant offset in right ascension or declination from the camera pointing position, allowing for simultaneous observations of the source and background. This is usually repeated at four pointing positions about the target source position.

The Wobble observation mode positions the source at a constant offset in right ascension or declination from the centre of the camera FoV. Consecutive observing runs

are conducted at varying right ascension or declination offsets such that the camera FoV 'wobbles' about the source position [114]. This technique is shown in Figure 5.3. Since the target source is offset from the centre of the FoV, it is possible to use camera data observing the *anti-source* position to measure and obtain a well understood background model. By observing a gamma-ray source and background region simultaneously, the impact of varying environmental and camera conditions is greatly reduced. The validity of such background measurements is also increased as the background region is guaranteed to be comparable to that of the source. In addition to this, inhomogeneities in photosensor and FEE performance are suppressed as the gamma-ray source is observed by multiple SiPM pixels and TARGET modules as opposed to just those at the centre of the focal plane under the On-Off observing mode. The use of this Wobble observing mode is less suited to extended gamma-ray sources (such as EtaCarinae) as it is not always possible to contain the full extent of the source whilst obtaining a background region. For such sources, the On-Off mode is used.

During the on-telescope campaign, CHEC-S was operated in the Wobble observing mode utilising right ascension and declination offsets of $\pm 1.0°$. Figure 5.4 shows an example of Cherenkov events with low α Hillas parameters (See Section 5.4) at each stage in the Wobble mode whilst observing Markarian 501 (Mrk501). The source position is indicated on each camera image, highlighting the varying position at each step in the Wobble mode. Observations of each source continued in this manner throughout the campaign in roughly 20 minute observing runs.

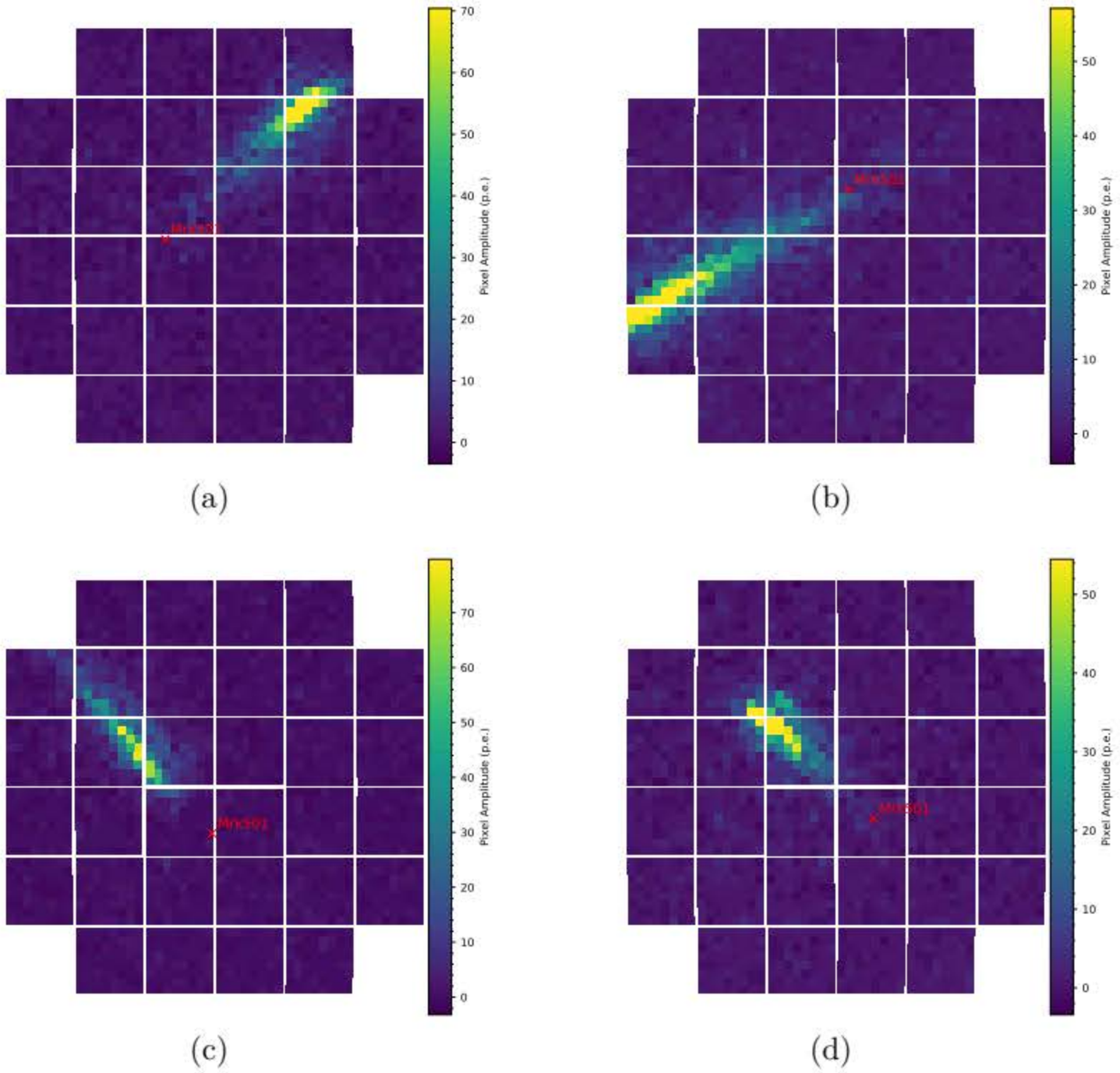

Figure 5.4: Camera images obtained during observations of Mrk501 in four observing runs whilst operating under the *Wobble* mode. The annotated position of Mrk501 indicates the varying position of this source in the camera FoV highlighting this operational mode. In addition to this, it is used to show the direction of the Cherenkov light pointing towards the source, discussed further in 5.4.

5.4 Hillas Analysis

As stated previously, the primary aim of the on-telescope campaign was to further verify the Cherenkov imaging camera, CHEC-S, and validate the use of CHEC-S with the ASTRI-Horn telescope structure. In addition to this, and understandably, it was important to observe Cherenkov shower events produced by extensive air showers (EAS). Following each full camera trigger, the digitised waveform of each channel, and therefore SiPM pixel, is readout and stored for future analysis. Section 2.4.3 describes the data level flow for digitised CHEC-S data. Initially, the raw R0 data is calibrated with the application of

a pedestal and transfer function calibration to the R1 calibrated data level. The R1 data is then extracted to the DL1 data level and stored as a large dataframe containing many extracted parameters such as measured charge per pixel, event timing, sampling cell identification, etc. The DL1 data level describes in full the triggered event and can be used to produce camera images such as those seen in Figure 5.4. However, these shower images require further analysis in order to determine the source direction, energy and particle class of the EAS progenitor. Further analysis of the camera images is conducted through the extraction and application of Hillas parameters. Hillas parameterisation describes the analysis technique utilised by IACTs for the reconstruction of Cherenkov shower events first formulated for the Whipple telescope by A. M. Hillas in 1985 ~~hillas original~~.

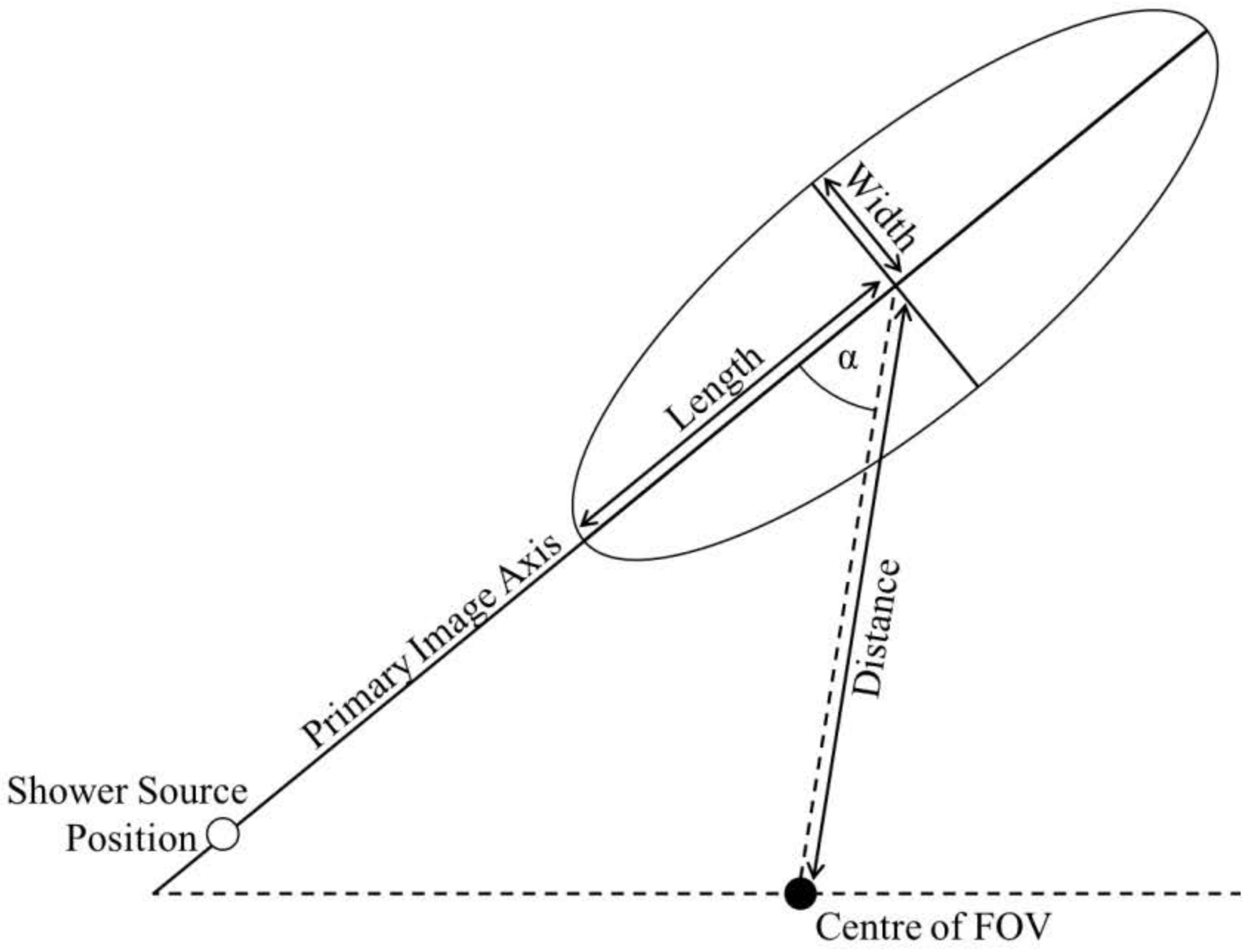

Figure 5.5: Diagram of the Hillas parameters extracted during the analysis of Cherenkov shower events from the ellipse observed in the camera focal plane [29].

5.4.1 Hillas Parameter Extraction

Shower images produced by CHEC-S consist of pixels containing signal both from the Cherenkov shower and the NSB. Each image is processed and cleaned with the application of *tailcuts* to remove photons that do not contain the Cherenkov shower signal. These tailcuts evaluate the charge extracted within each pixel; if the charge of a given pixel is above a configurable threshold, the pixel data is kept. The neighbours of remaining pixels are then evaluated at a lower threshold and again retained if they surpass this threshold. All pixels below such thresholds are discarded. The resulting camera image consists only of pixels containing a signal from the Cherenkov shower in an elliptical shape. By fitting an ellipsis to the cleaned image, the Hillas parameters can be obtained. Figure 5.5 shows an example Hillas ellipse and the corresponding Hillas parameters describing the position and orientation of the primary image axis, and the *Width* and *Length* of the ellipse containing the Cherenkov shower image.

The extracted Hillas parameters, in particular the ellipse *Length*, *Width* and *image size*, can be used to estimate the direction and amplitude of the Cherenkov shower. For a single IACT, this parameterisation results in a degeneracy in the shower position along the primary image axis either side of the image centre of gravity [115]. Whilst it is possible to improve the shower reconstruction of a single IACT using improved analytical methods [116], the performance of such analysis is vastly improved with the introduction of a second Cherenkov telescope. The shower direction is obtained from the intersection of the primary image axes extracted from each IACT. The shower energy can then be estimated from the weighted average of the individual energy reconstruction [117].

In addition to shower reconstruction, Hillas parameters can be used to provide some discrimination between gamma-ray and cosmic-ray initiated EASs [118]. This is conducted by evaluating mainly the *Length*, *Width* and α of shower images. Figure 5.4 shows four shower images with low α distributions, it can therefore be stated with confidence that

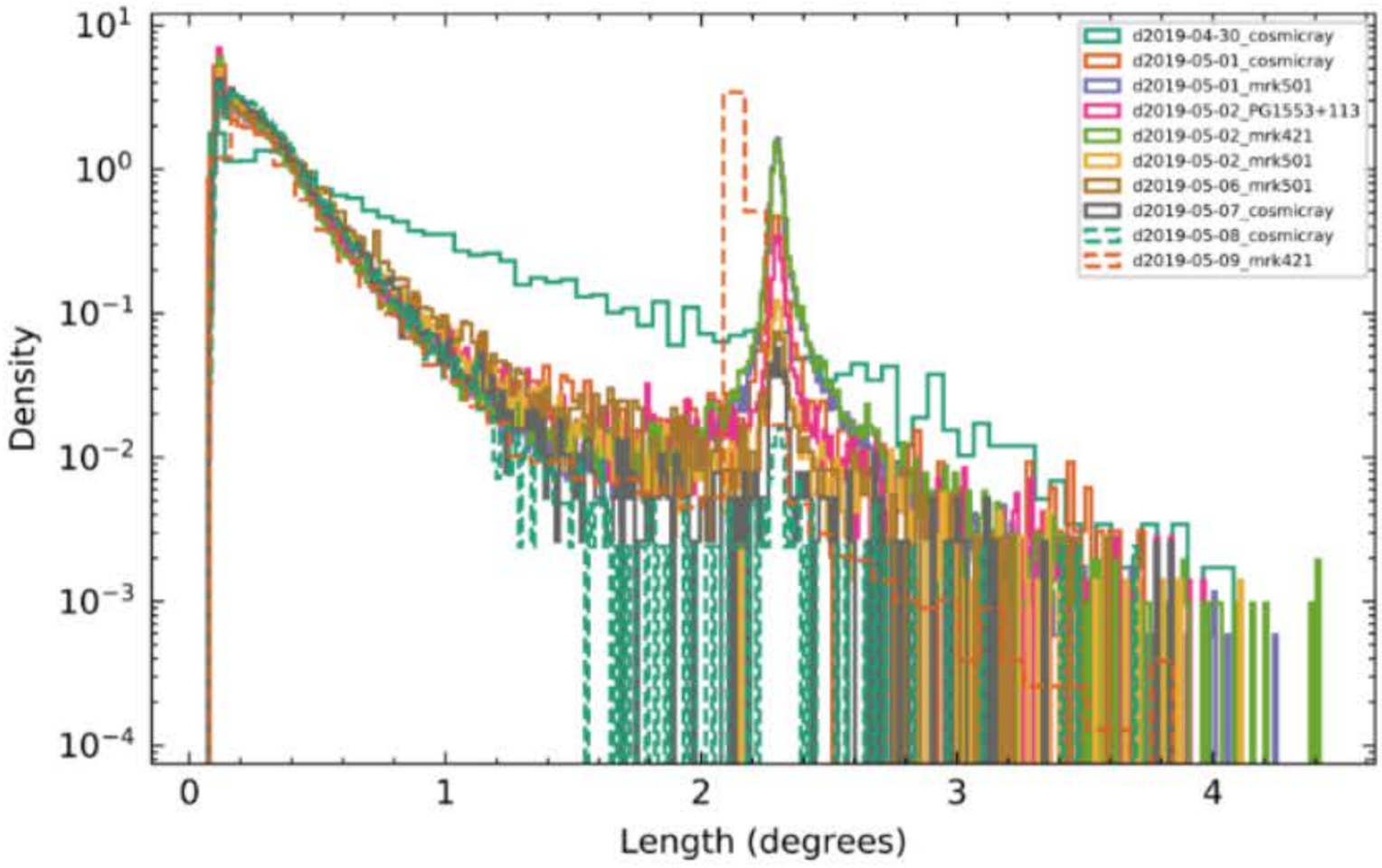

Figure 5.6: The *Length* Hillas parameter obtained during the on-telescope campaign whilst observing each gamma-ray source. The secondary peak between 2° and 3° corresponds to a large number of events producing an unexpected *Length* parameter, an similar peak is also observed in the *Width* parameter. These events were present during observations of each gamma-ray source and is discussed further below.

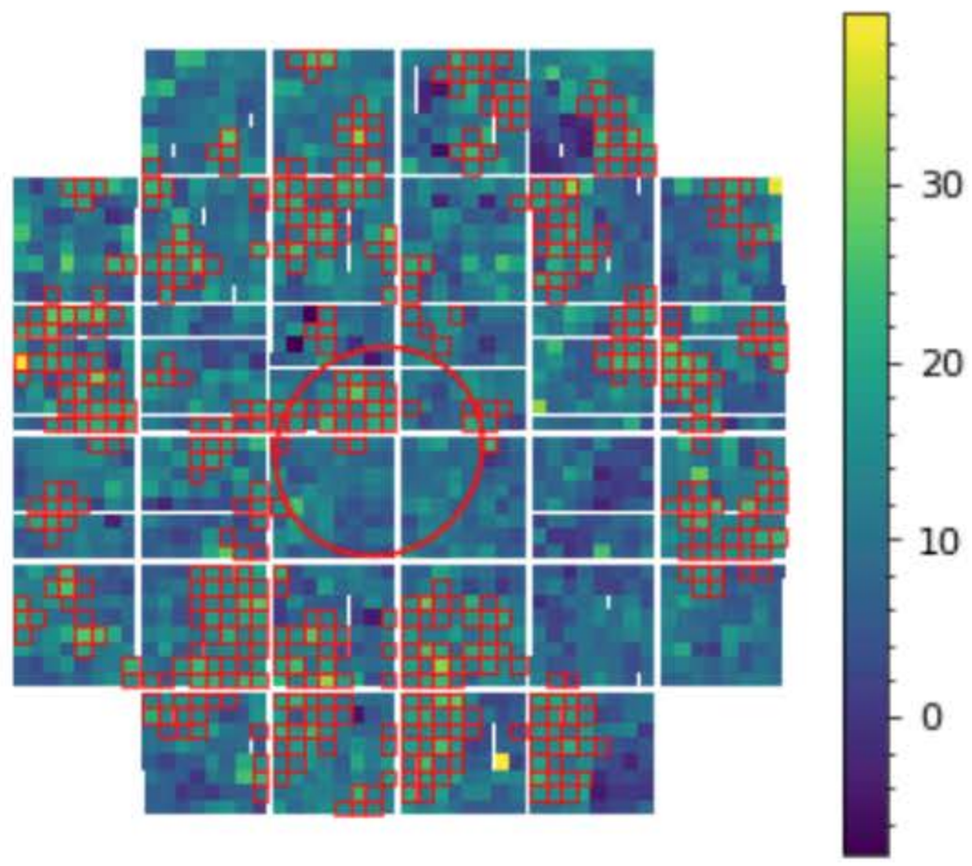

Figure 5.7: An example of the camera image for a triggered event with *Length* and *Width* parameters between 2° and 3, shown by the circular ellipse. The Hillas ellipse here shows the absence of a Cherenkov image, indicating that this event should not be included in the Hillas analysis.

such events were the result of EASs produced by gamma-rays originating from Mrk501. In evaluating the *Length* and *Width* of all events during the on-telescope campaign, it was noted that there was a large number of events that were not as expected. These unexpected events were observed by the peak in Figure 5.6 between 2° and 3°. An almost identical peak in this range was also observed in the *Width* parameter. The resulting Hillas ellipse of such events is therefore almost circular as shown by Figure 5.7. In addition to this, it is clear that there is no Cherenkov shower image present in the digitised data. The following Section describes the investigation into such Hillas events.

5.5 Events with Increased Baseline Noise

Again, a large number of digitised events were found to contain no observable Cherenkov signal during the extraction of Hillas parameters from observing data taken during the on-telescope campaign. Since the frequency of such events seemed independent of the targeted source, as shown by Figure 5.6, it was inferred that the cause of these falsely triggered events must be local to the ASTRI telescope or indeed a product of the CHEC-S electronics. The following describes the investigation conducted to determine the cause of such events.

5.5.1 Identifying Noisy Events

The events responsible for the secondary peak in the *Width* and *Length* Hillas parameters can be characterised by two identifying features. Firstly, each event produces a Hillas ellipse with low eccentricity, resulting in the circular shape of this ellipse and the distribution of Hillas *Lengths* and *Widths*. Whilst it is not impossible for Cherenkov events to produce such ellipses, it is uncommon as it would suggest the EAS was directly along the primary axis of the telescope pointing. This again becomes more unlikely when observ-

ing in the Wobble mode. Secondly, the digitised events show no observable coincidental pulses or peaks within the waveform. Instead, a shift in the baseline of each waveform was observed. Since the baseline has increased, it is possible for these events to produce a level-one trigger providing this baseline shift was above the trigger threshold level. As this was common across all channels and TARGET modules, a large number of neighbouring SPs produced a level-two trigger and full event readout. This again indicates how and why these events surpassed the tailcut cleaning prior to Hillas parameter extraction. Since these events are characterised by an increase in the baseline noise level, they became known as *Noisy Events* and are identified as such for the remainder of this Chapter. What follows is a description of the tasks I have completed in the investigation of *Noisy Events*. For this investigation, all events with *Length* and *Width* Hillas parameters between 2.1° and 2.7° were identified as *Noisy Events*. Although the analysis was conducted on each dataset from the on-telescope campaign, I show only the resulting plots for a number of observing runs. The behaviour highlighted in each plot was common and independent of the targeted source.

5.5.2 Event Timing

As described previously, the CHEC-S Backplane broadcasts a full camera readout following a successful level-two trigger, resulting in the digitisation of stored data from each TARGET module. The Backplane trigger signal contains a *delay time* corresponding to the lookback time required to digitise the correct portion of the analogue ring buffer (further described in Section 2.4.3) within the TARGET-C digitising ASIC. To ensure continuity across all digitising ASICs, each TARGET module is synchronised to a single quad-phase electronic clock within the Backplane. In addition to this, each digitised event is given a 64-bit prefix identification known as a TACK for event identification.

It is possible for all events to be characterised by the phase of the TACK identifier

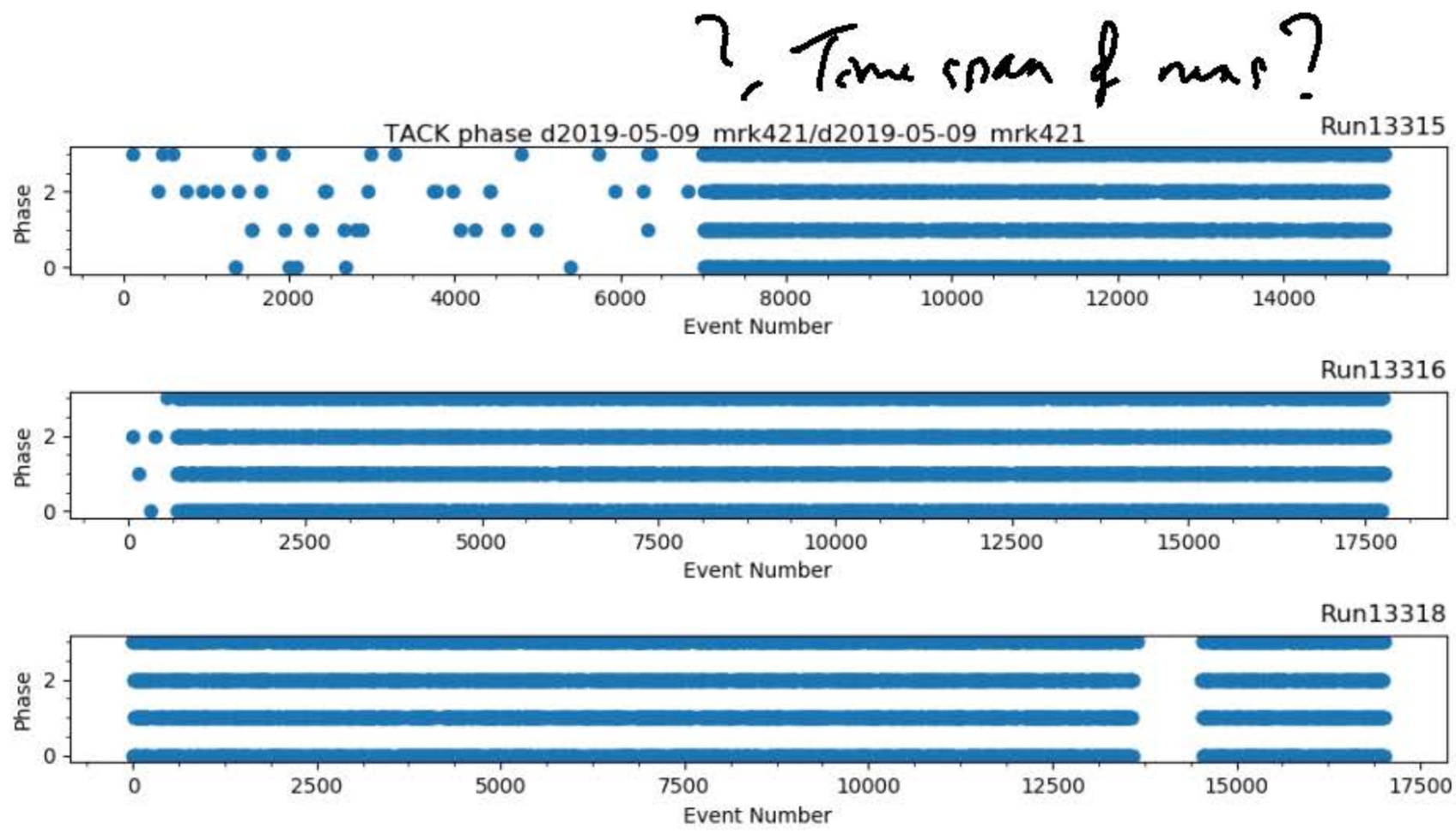

Figure 5.8: The phase of the TACK of each *Noisy Event* observed during three datasets targeting Mrk421. It can be seen that whilst these events occur at both high and lower frequencies, they are indeed independent of the clock phase and are, therefore, unrelated to the synchronising clock of the Backplane.

and therefore phase of the Backplane synchronising clock. Figure 5.8 shows the TACK phase of all *Noisy Events* from three observing runs targeting Mrk421 during the on-telescope campaign. Whilst it can be seen that the occurrence of such events is independent of the TACK phase, it does highlight that these events can occur in either an infrequent or highly frequent mode. This is apparent in *Run13315* and observed by the infrequent occurrence at the beginning of the run and more frequent occurrence for the final half of the run.

The deep analogue ring buffer physically comprises 4096 switched capacitors, each storing the charge of a single waveform sample. As with all electronic circuits, there is the possibility of electronic crosstalk from electronic signals, in the case of the deep analogue ring buffer this may be electronic signals both external and internal to the buffer. I therefore evaluated whether high intensity Cherenkov events could induce a signal elsewhere in the analogue ring buffer, resulting in an increased baseline and the presence of *Noisy Events*. If this was the case, *Noisy Events* would occur at a given time interval following a sufficiently high Cherenkov event.

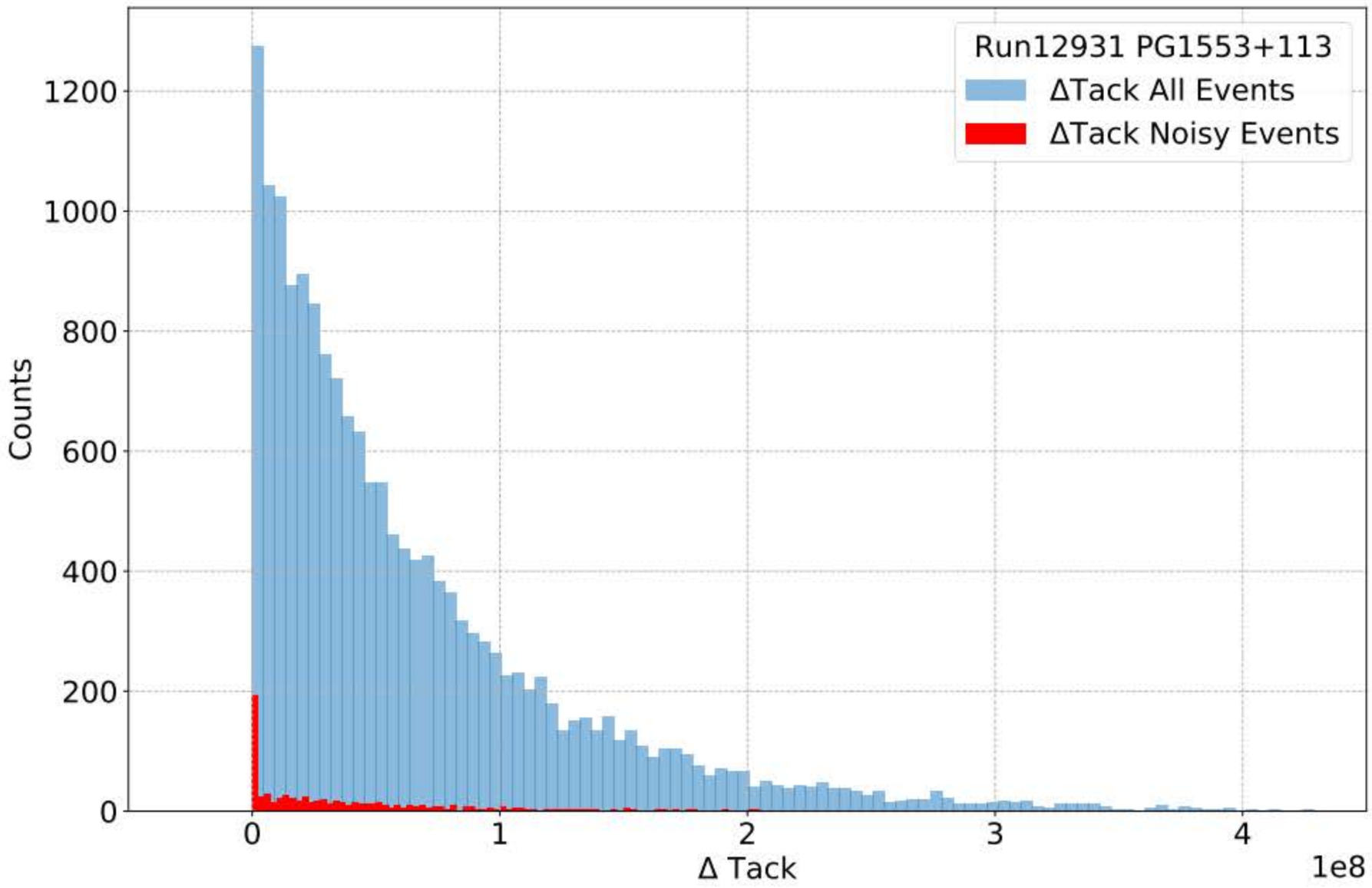

Figure 5.9: A histogram showing the delta-TACK of consecutive events. It can be seen that the delta-TACK of *Noisy Events* follows the expected distribution and is therefore not the cause of such events.

Figure 5.9 shows the delta-TACK between two consecutive events for both all events and *Noisy Events* digitised during *Run12931* observing the gamma-ray source PG1553+113. The delta-TACK describes the difference between the TACK of a given event and that of the previous event. I found that there was no correlation between the occurrence of a *Noisy Event* and the timing of the previous camera trigger event. This does not mean the analogue ring buffer is free of electronic crosstalk, but simply that this is not the cause of such events. In addition, it is interesting to note that no two *Noisy Events* occur consecutively.

5.5.3 Sampling Cell Dependence

As stated previously, the analogue ring buffer consists of 4096 sampling cells. It is possible that inadequately performing sampling cells, common to each TARGET module, could be the cause of *Noisy Events*. Such events would therefore only be present when digitised by *bad* sampling cells. Each digitised event includes metadata containing various parameters corresponding to the state of the TARGET module during the event. One such parameter is the First Cell Identification (FCI) which represents the assigned number of the initial sampling cell at the beginning of a digitised waveform. During usual analysis, the FCI is used to determine the sampling cell responsible for each position in the waveform, for example: the final cell of a $128ns$ waveform is simply $FCI + 128$. This is necessary as the TF and pedestal calibration is unique per sampling cell and is applied on a per cell basis. However, in this case it was used to determine whether *Noisy Events* were dependent on position in the analogue ring buffer.

The position of a sampling cell within the analogue ring buffer can be further categorised by the physical position of the sampling cell within the digitising ASIC. As described in Section 2.4.3, the analogue ring buffer consists of 128 *blocks* of sampling cells, each block containing 32 sampling cells. These blocks are then further arranged within a square structure of columns and rows. It is therefore possible to characterise a single sampling cell by its cell identification (i.e. FCI), block-phase, Row, and Column number. Figure 5.10 shows the identifying values of the first sampling cell for each *Noisy Event* present during observations of PG1553+113. It can be seen again that the presence of such events is independent of the sampling cell position.

Since the occurrence of *Noisy Events* is independent of the position of the sampling cell within the analogue ring buffer and any effects induced by the digitising ASIC itself, it can be said with confidence that the cause of such events must exist prior to the splitting of the digitising and trigger signal. This can be stated since the observed noise

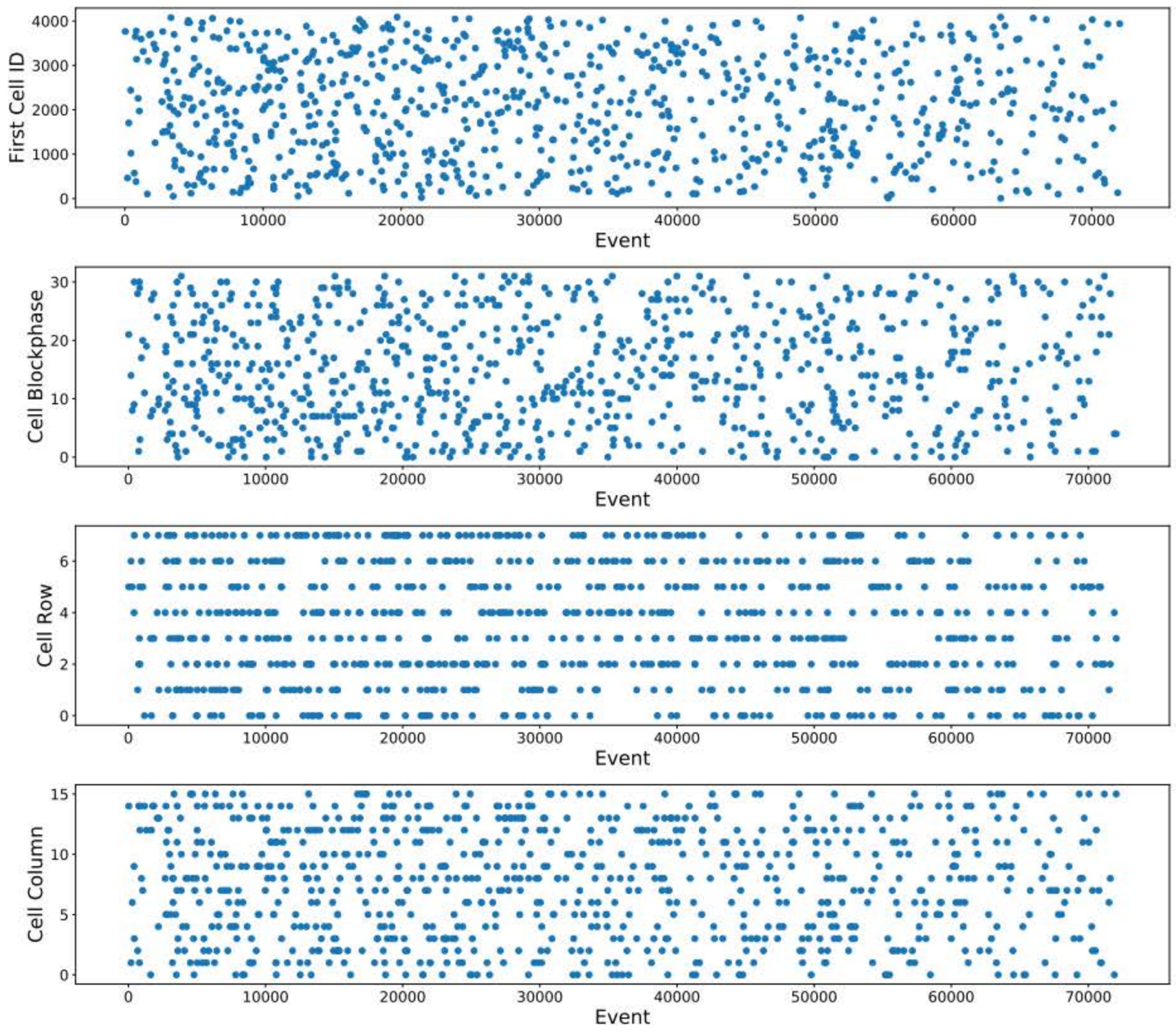

Figure 5.10: The occurrence of *Noisy Events* categorised by the FCI and physical position of the sampling cell at the beginning of the digitised waveform for each event. The cell Blockphase, Row, and Column describe the physical position of the sampling cell within the TARGET-C ASIC. It can be seen that *Noisy Events* are independent of physical position. within the ASIC. of their

must be present before the T5TEA trigger ASIC, if this was not the case a camera trigger would not occur. The noise must then be induced within the TARGET module shaping electronics, preamplifier buffer board, or SiPM. A further understanding of such events can be obtained by comparing the baseline of all observed waveforms.

5.5.4 Comparison of Waveform Baseline

As described previously, the *Noisy Events* present themselves generally as events with an increased baseline level, when compared to the nominal baseline level of Cherenkov events observed on-telescope. It is, therefore, worthwhile to compare the waveform baseline of all digitised events in an attempt to gain further understanding of such events. The *lookback* time utilised by the full camera trigger and readout ensures the that the peak position of the waveform responsible for the event trigger is always placed at the same configurable position within the digitised waveform. This is required to ensure the entirety of the SiPM pulse is contained within the waveform, providing accurate charge extraction of the waveform pulse. For high intensity, long duration (or saturated waveforms) it is possible for the SiPM pulse to be present at a position in the waveform much later than the original trigger peak position (see Figure 4.28). In order to compare variations in the waveform baseline alone, I have therefore evaluated the digitised signal of all events before the trigger peak position using the parameter *baseline_start_mean* extracted during the conversion of digitised data from data level R1 to DL1. This parameter is simply the average of 20 samples at the beginning of the digitised waveform.

Figure 5.11 indicates the *baseline_start_mean* variation during observations of PG1553+113. This dataset is shown as it contains the highest frequency of *Noisy Events*. This analysis was conducted over all observing runs and the resulting performance was found to be comparable. Figure 5.11(a) shows the *baseline_start_mean* averaged over all 2048 pixels per event, this is analogous to the amplitude of the baseline level at the start of the average waveform. It can be seen that in general, the *Noisy Events* exhibit a much higher baseline level. In addition, the spread in this baseline level, indicated by the root-mean-square (RMS) for the 2048 channels of each event, is much higher than that of the standard triggered events indicated by Figure 5.11(b). It is worth noting that there are *Noisy Events* that exhibit nominal baseline levels and regular events that have an increased baseline level,

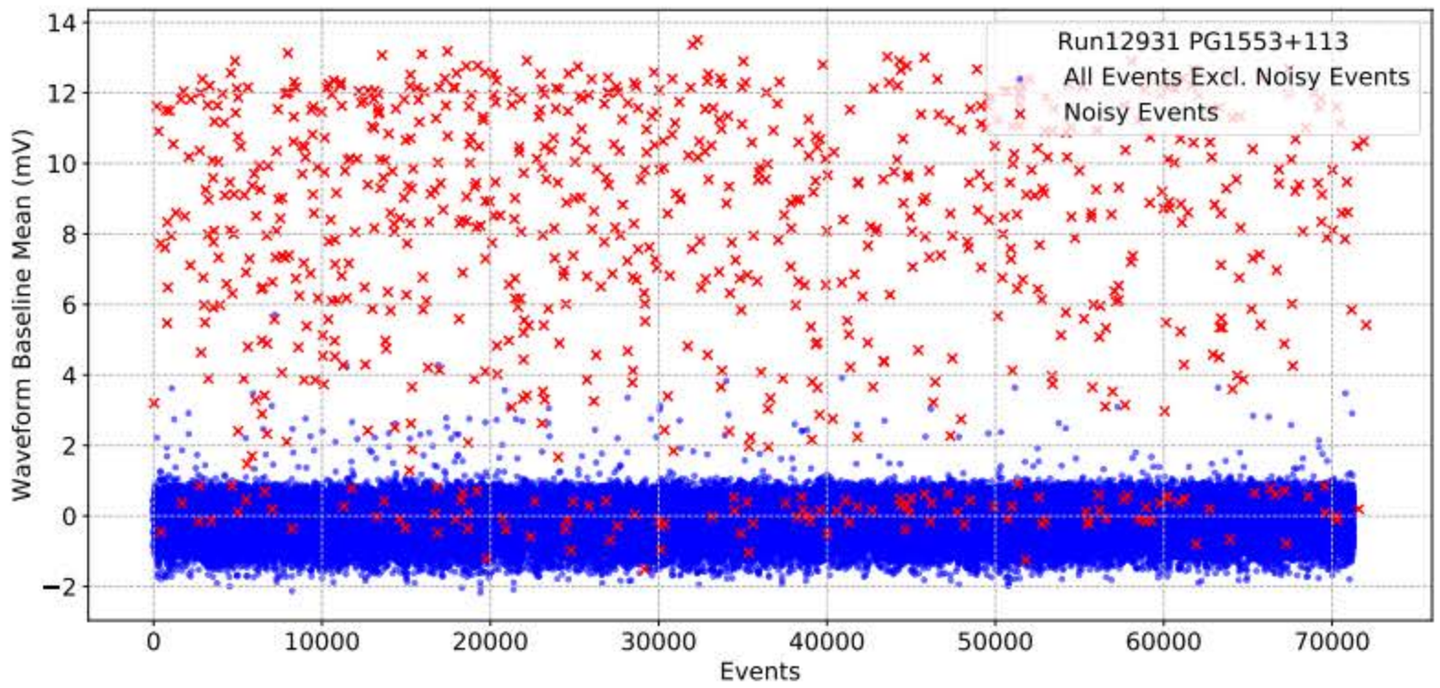

(a)

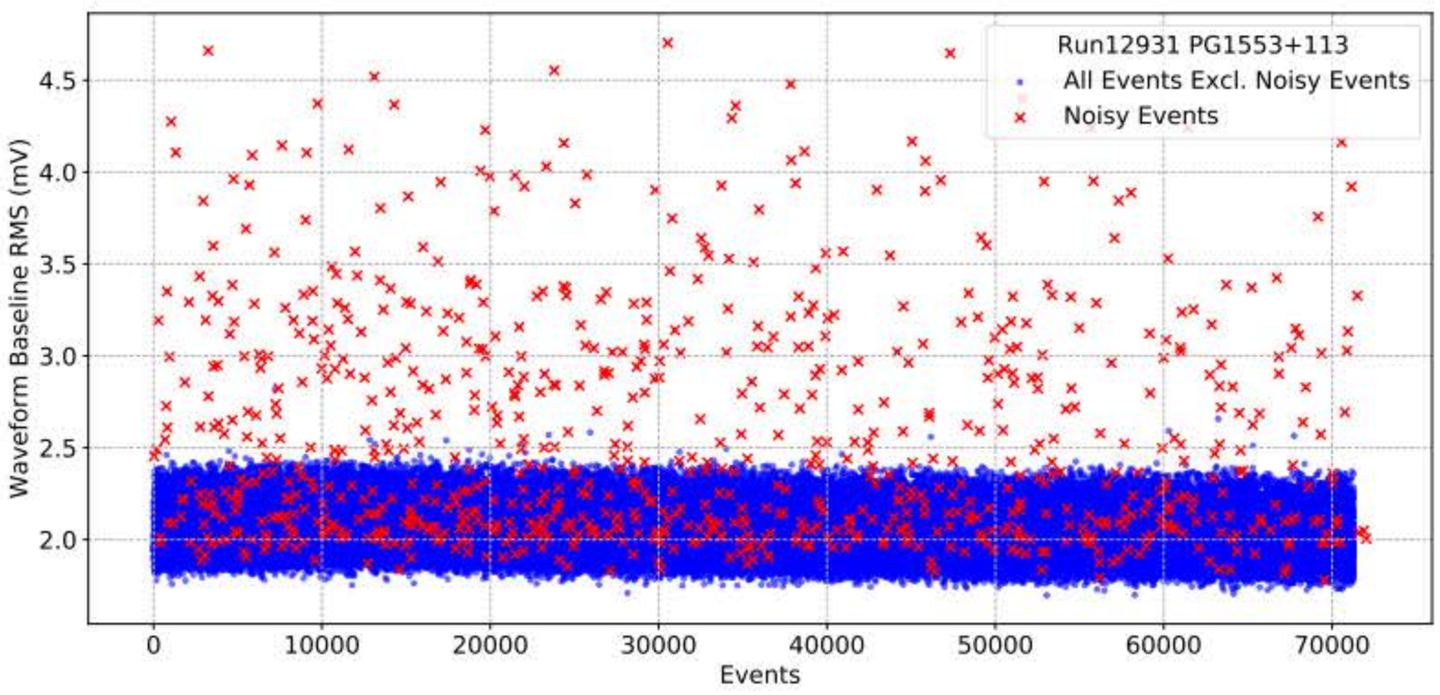

(b)

Figure 5.11: A comparison of the *baseline_start_mean* of all events during observations of PG 1553+113. (a) shows the *baseline_start_mean* averaged over all 2048 channels for a given event. It can be seen that the majority of *Noisy Events* exhibit an increased baseline level when compared to Cherenkov shower events. (b) shows the root-mean-square of the *baseline_start_mean* for the 2048 channels from each event. The plot indicates that *Noisy Events* contain a higher spread in amplitude in addition to the increased baseline level.

although not to the amplitude observed by *Noisy Events*. The cause of this disparity may be due to the inclusion of Cherenkov events in the *Noisy Events*. Nonetheless, it is clear that the majority of *Noisy Events* can be identified by an increased baseline level at the beginning of the digitised waveform.

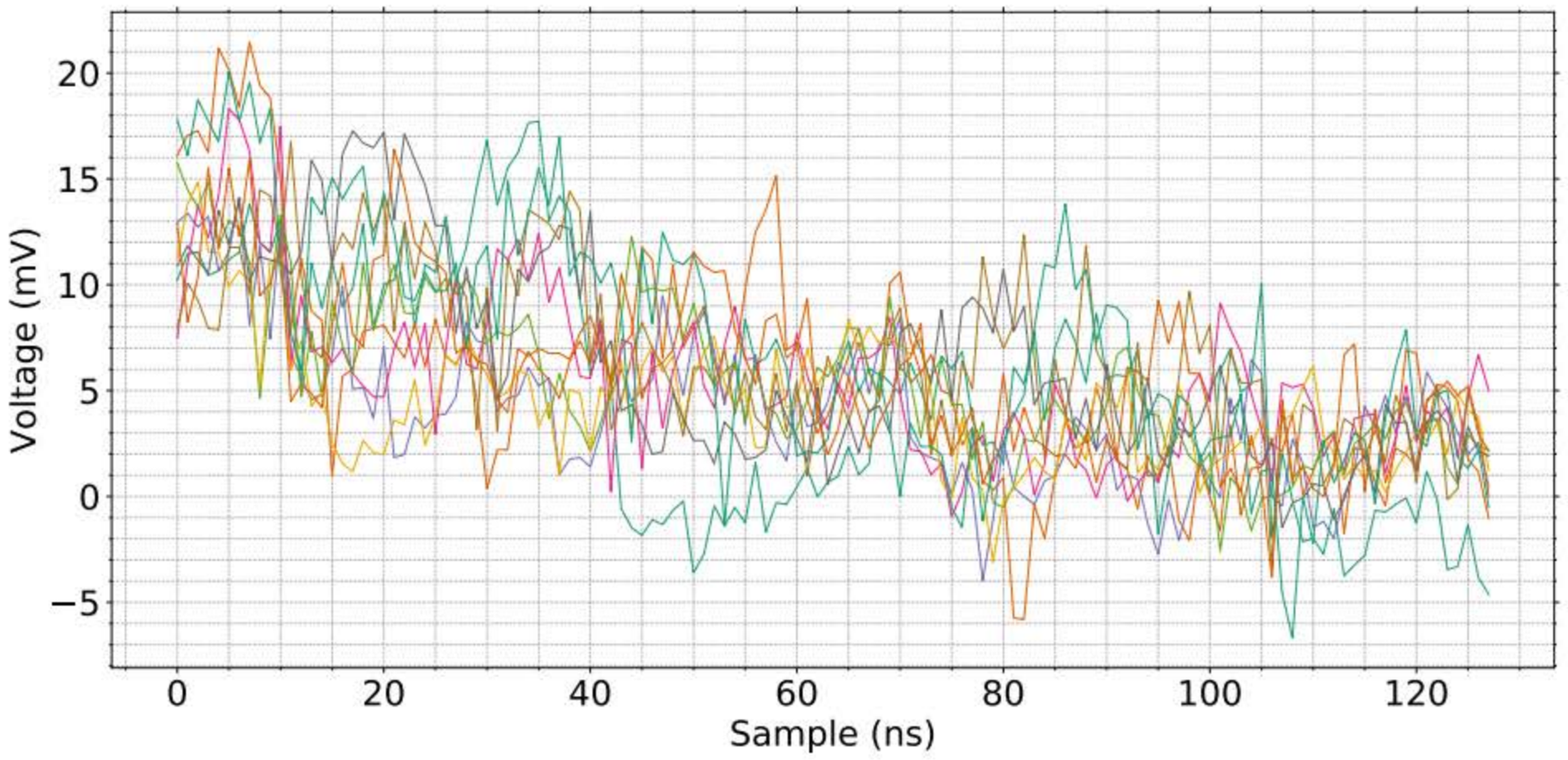

Figure 5.12: An example of the digitised waveforms for 10 pixels during a *Noisy Event*. It can be seen that there is large shift in the baseline level which decreases as the event progresses.

Further insight into the occurrence of *Noisy Events* can be gained by evaluating the digitised waveforms observed during such events. Figure 5.12 shows an example of calibrated waveforms producing a *Noisy Event* whilst observing the source PG1553+113. It can be seen that the relative amplitude of the waveform at each sample position is decreasing, in addition to this, the noise observed within this event is much higher than expected. Section 3.3 describes the shaping electronics integrated in the TARGET module, designed to shape the output of the preamplifier buffer board before the analogue signal is digitised. In addition to this, an alternating current (AC) coupling circuit is present and utilised to remove the direct current (DC) bias present within the analogue signal. The DC bias signal can be thought of as long timescale variations observed by the SiPM. For CHEC-S, this long timescale variation is analogous to the NSB. The AC coupling circuit is therefore used to remove the static NSB level observed on-telescope, acting as a shift in the baseline level, maintaining a baseline position close to 0 mV. A response time is required for the for the AC coupling circuit to take effect and return the baseline to its nominal position following a short timescale increase in NSB. This required response time corresponds to the time constant of the AC coupling circuit. The amplitude of the baseline

level within this response time consequently follows an exponential decay since:

$$V_x = V_0 e^{-\frac{x}{\tau}} \tag{5.1}$$

where V_x is the amplitude at sample position x, V_0 the amplitude at the beginning of the baseline shifted waveform, and τ the RC time constant of the AC coupling circuit.

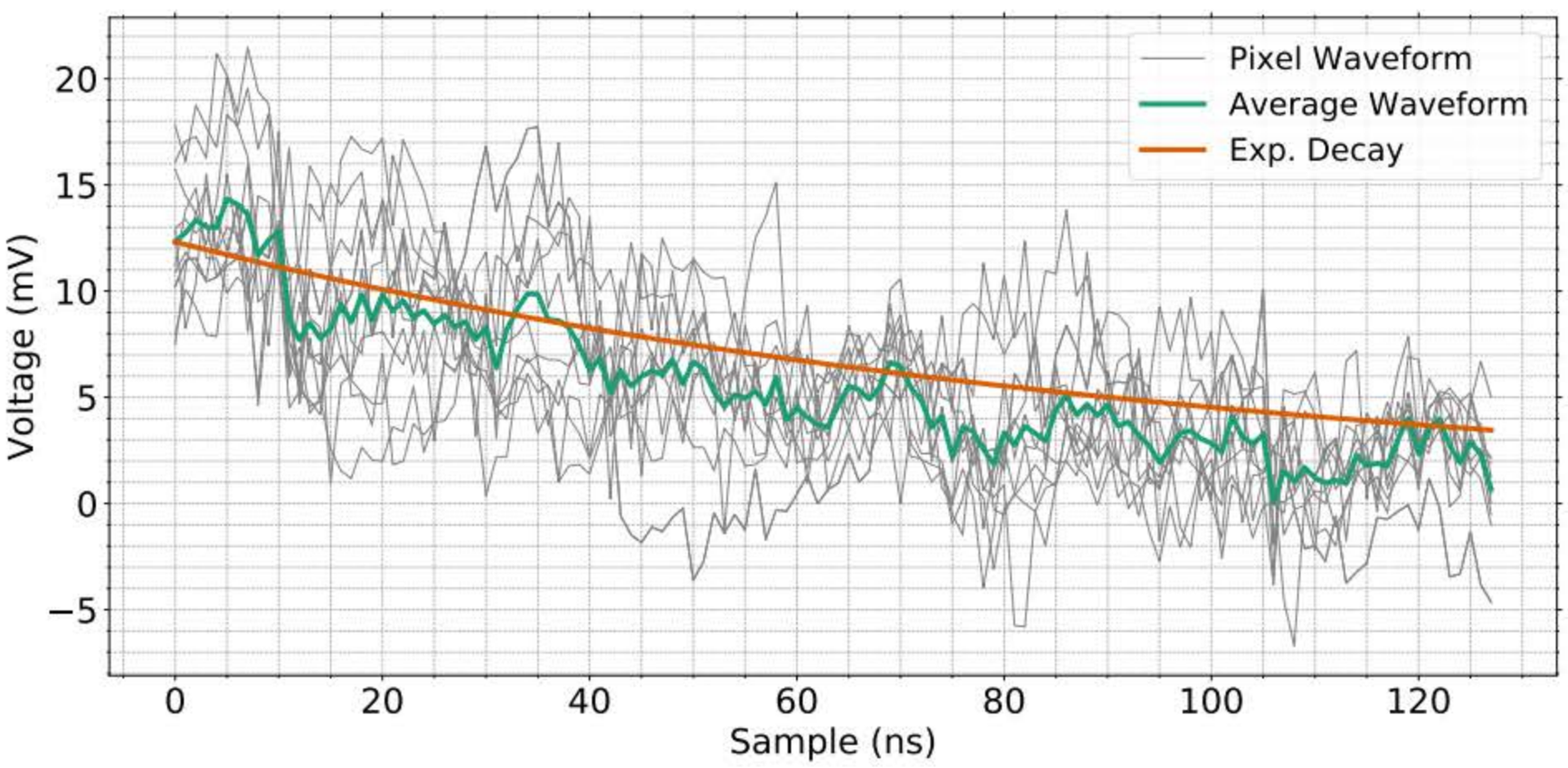

Figure 5.13: An indication of the highlighted exponential decay behaviour produced by the AC coupling circuit following a short timescale increase in NSB illumination. The green line here shows the average of the waveforms shown in Figure 5.12 (also shown in grey). The orange line shows the expected variation in sample amplitude corresponding to the exponential decay of the AC coupling circuit.

Using Equation 5.1, I was able to evaluate the behaviour of the digitised waveforms shown in Figure 5.12 with respect to the expected exponential decay produced by the AC coupling circuit. Figure 5.13 shows the result of applying an exponential decay to the digitised waveforms during a *Noisy Event*. The average of the individual channel waveforms (grey) is shown here (green) and represents the average position of the baseline observed during this event since the stochastic behaviour observed in each individual waveform is effectively removed when averaging across multiple channels. The first value

of the average waveform was then used to provide the initial amplitude (V_0) of the exponential decay, shown in orange. It can be seen that the trend of the average waveform, and hence baseline, is well described by the exponential decay. This would suggest that the event shown here was triggered and captured during the *response time* following a large variation in NSB level at the telescope position before the baseline had returned to the nominal position. I repeated this process for multiple *Noisy Events* and found this conclusion to be common among all events.

Whilst this investigation cannot determine the absolute cause of *Noisy Events*, observed through an unexpected response in the *Length* and *Width* Hillas parameters, it can be used to suggest a credible mechanism for their production. Firstly, a short timescale and large increase in the NSB illumination observed by CHEC-S produces a shift in the baseline signal of each channel. The AC coupling circuit then works to return the shifted baseline to the nominal position within the response time corresponding to the time constant of this circuit. Before the baseline has returned to $\sim 0mV$, the level-two trigger criterion is passed and the full camera is digitised. The resulting digitised event therefore contains no obvious Cherenkov light response, but instead shows an increased baseline amplitude which itself is decreasing at a rate consistent with the exponential decay of the AC coupling circuit.

5.6 Recovery of Saturated Cherenkov Events

Section 2.2.1 describes the requirements that each Cherenkov imaging camera and telescope structure must meet in order to be accepted as an in-kind contribution to the Cherenkov Telescope Array (CTA). Requirement **B-TEL-1010** corresponds to the charge resolution performance that each Cherenkov imaging camera must achieve. I have discussed the limitations of CHEC-S FEEs at high intensities previously in Section 4.6.1, stating that saturated waveforms observed in CHEC-S below 1000 *photoelectron* (p.e.)

would cause CHEC-S to fail the charge resolution requirement. I have also outlined my method for correcting for such saturation and shown the ability of this method to meet the CTA Observatory requirements to an intensity of $1000-2000$ *p.e.* depending on SiPM gain. It is possible to apply this saturation recovery method to high intensity Cherenkov events observed during the on-telescope campaign of CHEC-S in order to obtain an estimation of the intensities observed and to prove the validity of saturation recovery.

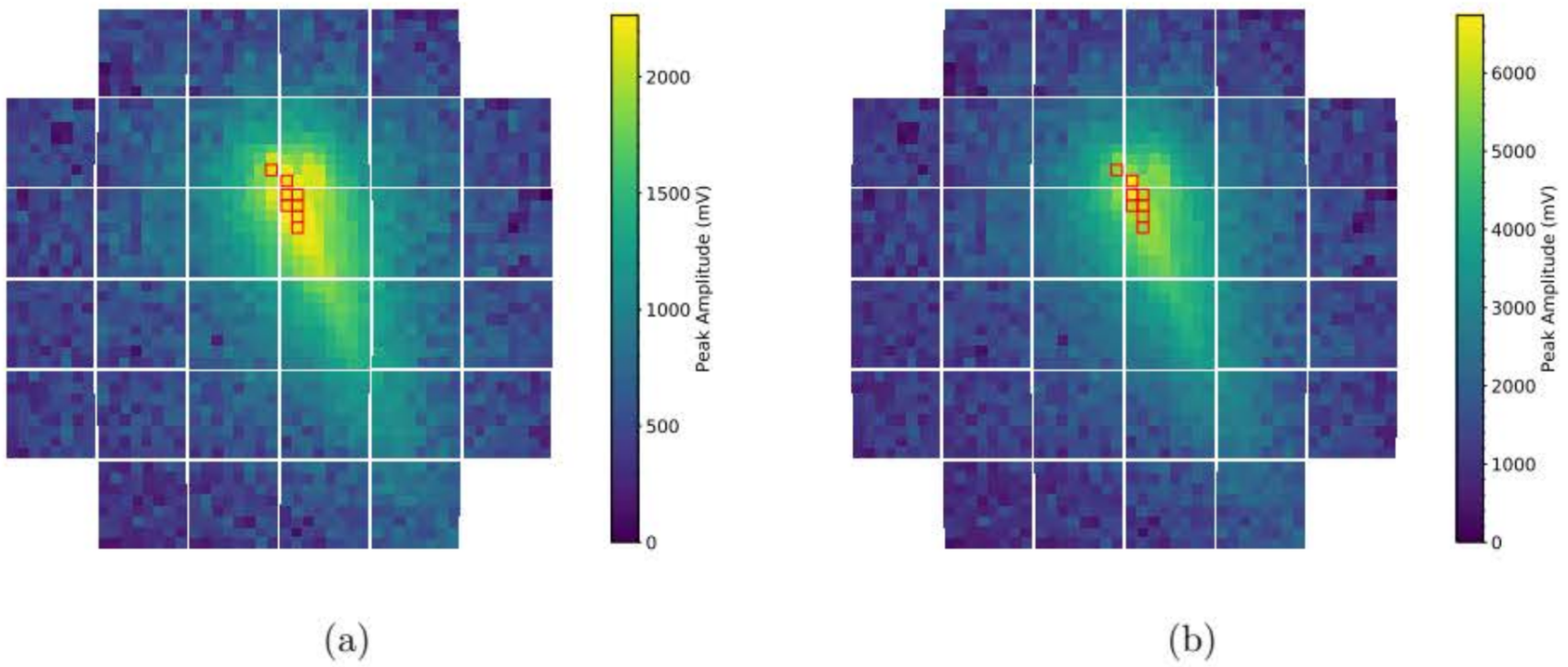

(a) (b)

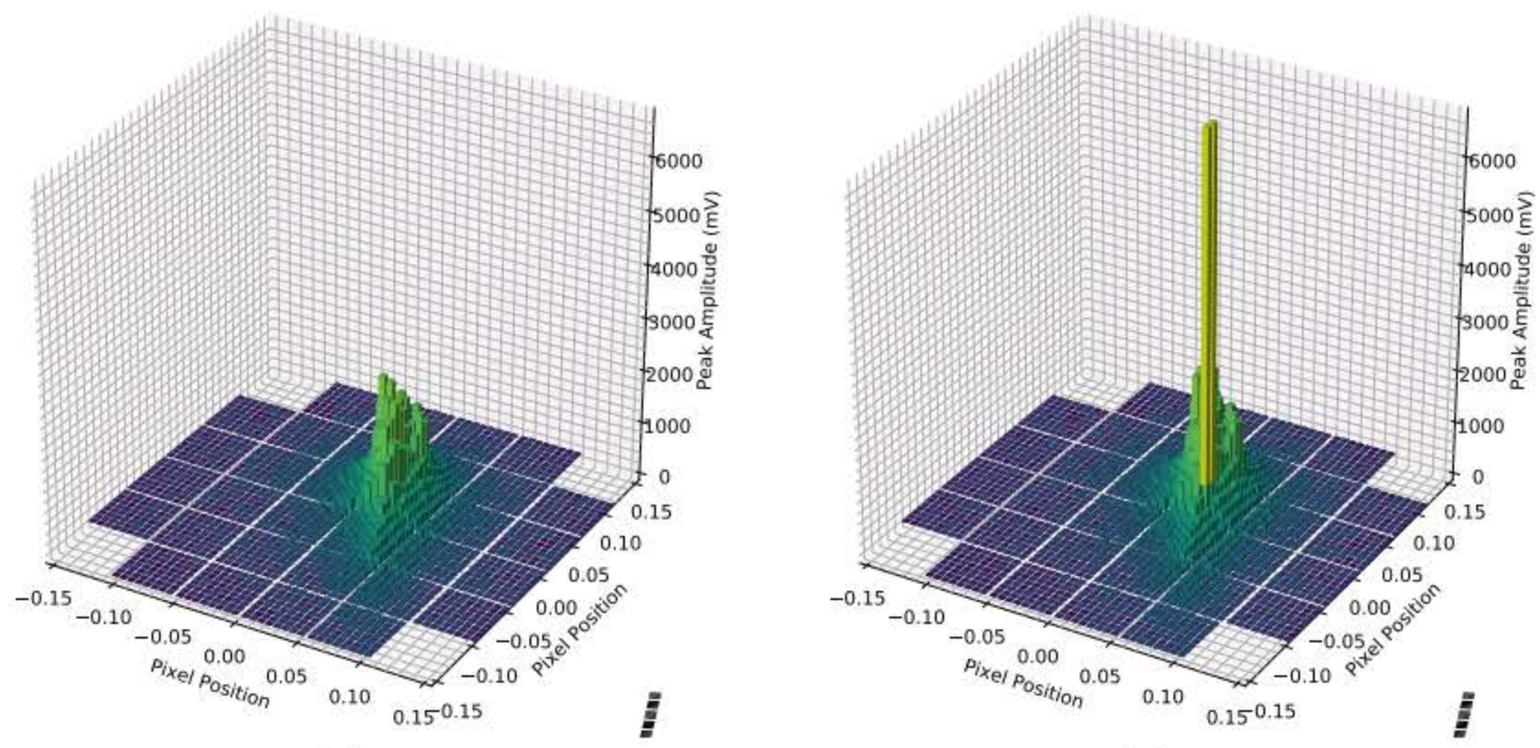

(c) (d)

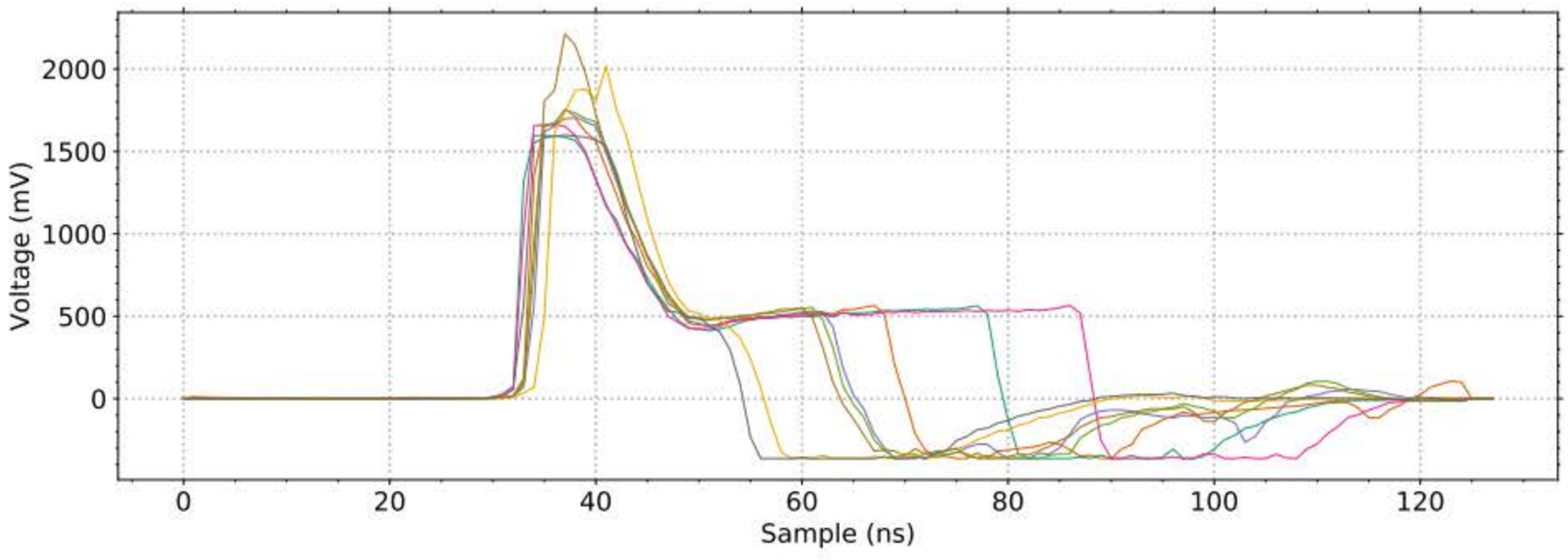

(e)

Figure 5.14

Figure 5.14: An example of a saturated Cherenkov shower image observed on-telescope and the resulting saturation recovery performance. (a) shows the original camera image prior to saturation recovery. The pixels highlighted in red indicate those pixels that have saturated. (b) shows the camera image following the recovery of saturated waveforms. It can be seen that two pixels within the ellipse of the image have a corrected peak amplitude above $6000mV$. (c) shows a 3-dimensional plot of the waveform peak amplitude prior to saturation recovery.(d) shows a 3-dimensional plot of the waveform peak amplitude following the recovery of saturated waveforms. This plot shows the necessity of saturation recovery. (e) shows the saturated waveforms of each highlighted pixel. The varying widths of the saturated waveforms indicates that each pixel has observed varying intensity levels.

The saturation recovery method requires a transfer function that describes the conversion of the width of a saturated waveform to the amplitude of the input that produced the saturated waveform. This conversion was generated for a single TARGET module and is shown in Figure 4.22. It is expected that each TARGET module would require a specific conversion for the accurate recovery of saturated data, similarly to the application of a TARGET-C transfer function calibration. However, since the variation in the width to input amplitude conversion is minimal, it is possible to apply this conversion on high intensity, on-telescope data, providing the resulting corrected peak amplitude serves only as a simple estimation of the Cherenkov light intensity and a proof for the necessity of such procedure.

Figure 5.14 shows an example of a saturated Cherenkov light event whilst observing Mrk501. 5.14(a) shows the camera image of the original data for the event, pixels highlighted by the red annotations indicate the pixels producing a saturated waveform. The waveforms for these pixels are shown in Figure 5.14(e). As described in Section 4.6, the width of a saturated waveform increases linearly with increasing input amplitude. The saturated waveforms here highlight the importance for the recovery of saturated waveforms as each pixel is clearly subjected to varying intensities which may be underestimated if simply the peak amplitude of the waveform is measured. Figure 5.14(b) shows the camera image of the peak amplitude following the application of my saturation recovery method. By comparing the colourbar of each camera image it can be seen that the peak ampli-

tude following this recovery has increased from a saturated $\sim 1600mV$ to a corrected $\sim 6000 mV$ for the highest intensity pixels. The impact of the saturation recovery becomes more apparent when comparing the 3-dimensional camera images shown in Figures 5.14(c) and 5.14(d). With a nominal SiPM gain of $4mV/p.e.$, this corresponds to $400p.e.$ for the original, saturated, wavform, and $1500p.e.$ following the saturation recovery. Again these results are only an estimation but can be used to emphasise the vast improvement in dynamic range that can be gained with the recovery of saturated waveforms.

5.7 Conclusion

The primary aim of the initial CHEC-S on-telescope campaign was to provide further verification of the camera electronics under varying thermal and NSB environments, and allow for the formalisation of operating procedures for on-telescope observations. Whilst the exposure time of each gamma-ray source was insufficient for a source detection, CHEC-S successful observed a large number Cherenkov events, proving the validity of an ASTRI-CHEC based Small Sized Telescope. I have given an explanation for many falsely triggered events containing no Cherenkov light, produced by rapid variation in the NSB environment as indicated by the AC coupling behaviour observed in the baseline of digitised waveforms. Finally, I have demonstrated the necessity of a saturation recovery regime to correct for the saturation of the TARGET-C ASIC when observing high intensity Cherenkov showers.

Chapter 6

Summary

Once completed, the Cherenkov Telescope Array (CTA) will be the most sensitive gamma-ray observatory of its kind. CTA will achieve this accolade by constructing the largest imaging atmospheric Cherenkov telescope array (IACT) to date, with two array locations: CTA-North, on the island of La Palma; and CTA-South, in the Atacama Desert of South America. CTA will construct a total of ~ 100 telescopes spread across the two locations. The observatory will consist of three differing telescope sizes: a Large, Medium, and Small Sized Telescope. The inclusion of three telescope sizes enables CTA to achieve a highly sensitive observatory across the entire energy range of approximately 20GeV to 300TeV.

The accepted telescope design for the Small Sized Telescope (SST) is based on the ASTRI-Horn telescope structure and the CHEC-S Cherenkov imaging camera. This SST design represents a great step forward in the development of IACTs. Most notable is the use of a dual-mirror Schwarzschild-Couder design telescope and the use of silicon photo-multipliers (SiPMs) for photon detection. A significant portion of my doctoral research has been focussed on the characterisation and verification of CHEC-S. This was conducted with the use of both CHEC-S itself and a single front end electronic chain comprising a CHEC-S SiPM tile, preamplifier buffer board, and TARGET module.

In addition to the inclusion of SiPMs, the development of CHEC has lead to the progression of the front end electronics, with the most impactful improvement being that to the TARGET ASICs. The TARGET ASICs found in CHEC-S are the T5TEA trigger ASIC and TARGET-C digitising ASIC. These two ASICs are combined in the previous ASIC iteration, TARGET-7, which is currently utilised by the Medium Sized Telescope prototype: pSCT. TARGET-C comprises a 64 cell sampling array, providing GSample/s sampling; a 4096 cell deep analogue ring buffer storage array; and a Wilkinson analogue-to-digital converter (ADC), which is responsible for the digitisation of the shaped analogue waveform produced by the SiPM. As with all digitising ASICs, TARGET-C requires a calibration scheme to give meaning to the digitised ADC counts produced by the TARGET module.

The calibration of TARGET-C digitised data consists of subtracting the electronic pedestal found in storage cells and correcting for the non-linearities induced during the digitisation process. The Transfer Function describes the conversion of ADC counts to an input voltage and gives true meaning to the CHEC-S digitised data. The key process in the generation of a Transfer Function is the ability to extract the waveform peak position of a calibration dataset. Following from CHEC-M, this was completed using a double Landau fitting regime. I determined that this method was less accurate than previously expected, giving rise to an inaccuracy in the calibration of digitised data. I have proposed a peak extraction method which requires the cross correlation of calibration dataset with an applicable reference waveform. I have shown that the performance of this peak extraction method surpasses that of the double Landau regime and recommend that cross correlation method be adopted for the generation of calibration data.

The dynamic range of TARGET-C is clearly finite and therefore must produce saturated waveforms at a given input intensity. A requirement on the performance of Cherenkov imaging cameras given by CTA states that all cameras must be able to achieve an observable photon intensity. It was shown that the dynamic range of TARGET-C, and

thus CHEC-S, is below this intensity. The saturation of TARGET-C is represented by a flat peaked waveform with a linearly increasing "shelf". The width of this shelf is therefore proportional to the input intensity. I have proposed a saturation recovery method using a lookup table containing the conversion of waveform width to input intensity. Using this method, I have shown that CHEC-S is able to meet the current CTA charge resolution requirements.

The commissioning of CHEC-S concluded with the on-telescope campaign, in which CHEC-S was mounted on the ASTRI-Horn telescope at Serra La Nave, in Sicily, Italy. During this successful campaign, CHEC-S recorded it's first light and proved the validity of a CHEC-ASTRI small sized telescope for CTA.

6.1 Outlook

CHEC-S now forms the basis of the Cherenkov imaging component of the small sized telescope. The future of the project is clearly heading towards the development of a finalised, production camera: the SST Camera. The development of the SST Camera is currently ongoing, and building upon the lessons learned by the characterisation and verification of CHEC-S and previously CHEC-M. The SST Camera will be assembled and verified across Europe, with 13 cameras produced entirely within the UK. The delivery of each SST Camera will include the calibration dataset for each of the TARGET modules used in the front end electronics. These datasets must therefore be produced by each of the institutes responsible for the assembly and delivery of each TARGET module.

I have shown that there is an inherent disparity in the hardware electronics used for the generation of calibration data. This disparity will be present across all institutes, the amplitude and variation of this disparity will be unique to each institute. I recommend that the procedure for generating such datasets requires the complete characterisation of all

components. In doing so, the calibration file (Transfer Function) produced at each institute will be comparable. If a single TARGET module was used to generate a calibration dataset at each institute, the resulting calibration files should be identical.

~~Bibliography~~ References

[1] Académie des sciences (France) and Centre national de la recherche scientifique (France). *Comptes rendus hebdomadaires des séances de l'Académie des sciences*. 1010–1012. publiés avec le concours du Centre national de la recherche scientifique par MM. les secrétaires perpétuels, 1900. URL: https://books.google.co.uk/books?id=W1oDAAAAYAAJ.

[2] Michael F L'Annunziata. *Radioactivity introduction and history*. eng. Oxford: Elsevier, 2007. ISBN: 1-281-11984-9.

[3] N Giglietto. "The contribution by Domenico Pacini to the Cosmic Ray Physics". eng. In: *Nuclear physics. Section B, Proceedings supplement* 212 (2011), pp. 3–12. ISSN: 0920-5632.

[4] Victor Hess. "On the Observations of the Penetrating Radiation during Seven Balloon Flights". eng. In: (2018).

[5] M Walter and A W Wolfendale. "Early history of cosmic particle physics". eng. In: *European physical journal H* 37.3 (2012), pp. 323–358. ISSN: 2102-6459.

[6] Ian Morison. *Introduction to astronomy and cosmology*. eng. Chichester: Wiley, 2008, p. 198. ISBN: 9780470033333.

[7] J. Beringer, J. F. Arguin, R. M. Barnett, et al. "Review of Particle Physics". In: *Phys. Rev. D* 86 (1 2012), p. 309. DOI: 10.1103/PhysRevD.86.010001. URL: https://link.aps.org/doi/10.1103/PhysRevD.86.010001.

[8] A. M. Hillas. "The Origin of Ultra-High-Energy Cosmic Rays". In: *Annual Review of Astronomy and Astrophysics* 22.1 (1984), pp. 425–444. DOI: 10.1146/annurev.aa.22.090184.002233. eprint: https://doi.org/10.1146/annurev.aa.22.090184.002233. URL: https://doi.org/10.1146/annurev.aa.22.090184.002233.

[9] Ali Kheirandish. "Identifying Galactic sources of high-energy neutrinos". eng. In: *Astrophysics and space science* 365.6 (2020). ISSN: 0004-640X.

[10] ENRICO Fermi. "On the Origin of the Cosmic Radiation". eng. In: *Physical review* 75.8 (1949), pp. 1169–1174. ISSN: 0031-899X.

[11] A. R Bell. "The acceleration of cosmic rays in shock fronts – I". eng. In: *Monthly notices of the Royal Astronomical Society* 182.2 (1978), pp. 147–156. ISSN: 0035-8711.

[12] A.R Bell. "Cosmic ray acceleration". eng. In: *Astroparticle physics* 43 (2013), pp. 56–70. ISSN: 0927-6505.

[13] S. G Lucek and A. R Bell. "Non-linear amplification of a magnetic field driven by cosmic ray streaming". eng. In: *Monthly notices of the Royal Astronomical Society* 314.1 (2000), pp. 65–74. ISSN: 0035-8711.

[14] K. M Schure and A. R Bell. "Cosmic ray acceleration in young supernova remnants". eng. In: *Monthly notices of the Royal Astronomical Society* 435.2 (2013), pp. 1174–1185. ISSN: 0035-8711.

[15] Trevor Cecil Weekes. *Very high energy gamma-ray astronomy*. eng. Series in astronomy and astrophysics. Bristol: Institute of Physics, 2003, p. 206. ISBN: 0750306580.

[16] F. A Aharonian. *Very high energy cosmic gamma radiation: a crucial window on the extreme universe*. eng. Singapore: World Scientific Publishing Co. Pte. Ltd, 2004. ISBN: 9810245734.

[17] Matthias Bartelmann. *Theoretical astrophysics: an introduction*. eng. Weinheim: WILEY, 2013, pp. 51,53. ISBN: 3527669787.

[18] O KLEIN and Y NISHINA. "The Scattering of Light by Free Electrons according to Dirac's New Relativistic Dynamics". eng. In: *Nature (London)* 122.3072 (1928), pp. 398–399. ISSN: 0028-0836.

[19] Stefan Ohm and Jim Hinton. "High-energy emission from galaxies: the star-formation/gamma-ray connection". eng. In: *Proceedings of the International Astronomical Union* 7.S284 (2011), pp. 382–388. ISSN: 1743-9213.

[20] H Bethe and W Heitler. "On the stopping of fast particles and on the creation of positive electrons". eng. In: *Proceedings of the Royal Society of London. Series A, Containing papers of a mathematical and physical character* 146.856 (1934), pp. 83–112. ISSN: 0950-1207.

[21] David J. (David Jeffery) Griffiths. *Introduction to elementary particles*. eng. 2nd rev. ed.. Weinheim: Wiley-VCH, 2012. ISBN: 9783527406012.

[22] Stefan Funk. "A new population of very high-energy gamma-ray sources detected with H.E.S.S. in the inner part of the Milky Way". Other thesis. July 2005.

[23] J Matthews. "A Heitler model of extensive air showers". eng. In: *Astroparticle physics* 22.5-6 (2005), pp. 387–397. ISSN: 0927-6505.

[24] Yoichiro Suzuki. "The Super-Kamiokande experiment". eng. In: *The European physical journal. C, Particles and fields* 79.4 (2019), pp. 1–18. ISSN: 1434-6044.

[25] A Achterberg, D.W Atlee, J Baccus, et al. "First year performance of the IceCube neutrino telescope". eng. In: *Astroparticle physics* 26.3 (2006), pp. 155–173. ISSN: 0927-6505.

[26] Fabian Schmidt. *CORSIKA - CORSIKA*. URL: `https://www.iap.kit.edu/corsika/`.

[27] D. Heck, J. Knapp, J. N. Capdevielle, et al. "CORSIKA: A Monte Carlo code to simulate extensive air showers". In: (Feb. 1998).

[28] John Valentine Jelley. *Čerenkov radiation and its applications*. eng. Published for the United Kingdom Atomic Energy Authority by Pergamon P, 1958.

[29] Jason Watson. "Calibration and analysis of the GCT camera for the Cherenkov Telescope Array". English. PhD thesis. 2018. URL: `http://ethos.bl.uk/OrderDetails.do?uin=uk.bl.ethos.780497`.

[30] Heinrich J Volk and Konrad Bernlohr. "Imaging very high energy gamma-ray telescopes". eng. In: *Experimental astronomy* 25.1-3 (2009), pp. 173–191. ISSN: 0922-6435.

[31] I. M. Frank and I. E. Tamm. "Coherent visible radiation of fast electrons passing through matter". In: *Compt. Rend. Acad. Sci. URSS* 14.3 (1937), pp. 109–114. DOI: `10.3367/UFNr.0093.196710o.0388`.

[32] Aurelien Bouvier, Lloyd Gebremedhin, Caitlin Johnson, et al. "Photosensor Characterization for the Cherenkov Telescope Array: Silicon Photomultiplier versus Multi-Anode Photomultiplier Tube". eng. In: 2013.

[33] M Ackermann, W Althouse, B Anderson, et al. "The Large Area Telescope on the Fermi Gamma-Ray Space Telescope Mission". eng. In: *The Astrophysical journal* 697.2 (2009), pp. 1071–1102. ISSN: 0004-637X.

[34] J.A. Hinton and W. Hofmann. "Teraelectronvolt Astronomy". In: *Annual Review of Astronomy and Astrophysics* 47.1 (2009), pp. 523–565. DOI: 10.1146/annurev-astro-082708-101816. eprint: https://doi.org/10.1146/annurev-astro-082708-101816. URL: https://doi.org/10.1146/annurev-astro-082708-101816.

[35] T. C WEEKES, M. F CAWLEY, P. T REYNOLDS, et al. "Observation of TeV gamma rays from the Crab Nebula using the atmospheric Cerenkov imaging technique". eng. In: *The Astrophysical journal* 342.1 (1989), pp. 379–395. ISSN: 0004-637X.

[36] K Bernlöhr, O Carrol, R Cornils, et al. "The optical system of the H.E.S.S. imaging atmospheric Cherenkov telescopes. Part I: layout and components of the system". eng. In: *Astroparticle physics* 20.2 (2003), pp. 111–128. ISSN: 0927-6505.

[37] T.C Weekes, H Badran, S.D Biller, et al. "VERITAS: the Very Energetic Radiation Imaging Telescope Array System". eng. In: *Astroparticle physics* 17.2 (2002), pp. 221–243. ISSN: 0927-6505.

[38] C Baixeras, D Bastieri, C Bigongiari, et al. "Commissioning and first tests of the MAGIC telescope". eng. In: *Nuclear instruments methods in physics re-*

search. Section A, Accelerators, spectrometers, detectors and associated equipment 518.1 (2004), pp. 188–192. ISSN: 0168-9002.

[39] Jamie Holder. "Atmospheric Cherenkov Gamma-ray Telescopes". In: (Oct. 2015). arXiv: 1510.05675 [astro-ph.IM].

[40] A. M. Hillas. *Cerenkov light images of EAS produced by primary gamma.* Tech. rep. M1: N–85-34862. 1985, p. v. URL: http://inis.iaea.org/search/search.aspx?orig_q=RN:19020694.

[41] Jamie Holder. "Atmospheric Cherenkov Gamma-ray Telescopes". eng. In: (2015). ?

[42] A. Mitchell, V. Marandon, R. Parsons, et al. "A Generic Algorithm for IACT Optical Efficiency Calibration using Muons". In: 2015. ?

[43] S. Funk, G. Hermann, J. Hinton, et al. "The trigger system of the H.E.S.S. telescope array". In: *Astroparticle Physics* 22.3-4 (2004), 285–296. ISSN: 0927-6505. DOI: 10.1016/j.astropartphys.2004.08.001. URL: http://dx.doi.org/10.1016/j.astropartphys.2004.08.001.

[44] Alison Mairi Wallace Mitchell. "Optical Efficiency Calibration for Inhomogeneous IACT Arrays and a Detailed Study of the Highly Extended Pulsar Wind Nebula HESS J1825-137". PhD thesis. U. Heidelberg (main), 2016. DOI: 10.11588/heidok.00021768.

[45] A. M. W Mitchell, V Marandon, R. D Parsons, et al. "A Generic Algorithm for IACT Optical Efficiency Calibration using Muons". eng. In: (2015).

[46] M Actis, [Unknown] et al., and S.B Markoff. *Design concepts for the Cherenkov Telescope Array CTA: an advanced facility for ground-based high-energy gamma-ray astronomy.* eng. Dordrecht: The CTA Consortium, 2011.

[47] I Agudo, C Aramo, L Arrabito, et al. *Science with the Cherenkov Telescope Array*. eng. Vol. 240. 2. WORLD SCIENTIFIC, 2017, p. 32. ISBN: 9789813270084.

[48] H. Abdalla, F. Aharonian, F. Ait Benkhali, et al. "Revealing x-ray and gamma ray temporal and spectral similarities in the GRB 190829A afterglow". In: *Science* 372.6546 (2021), 1081–1085. ISSN: 1095-9203. DOI: 10.1126/science.abe8560. URL: http://dx.doi.org/10.1126/science.abe8560.

[49] L. A Antonelli, A Arbet Engels, K Asano, et al. "MAGIC Observations of the Nearby Short Gamma-Ray Burst GRB 160821B". eng. In: *The Astrophysical journal* 908.1 (2021), p. 90. ISSN: 0004-637X.

[50] Ž Bošnjak, A. M Brown, P Cristofari, et al. "Multi-messenger and transient astrophysics with the Cherenkov Telescope Array". eng. In: (2021).

[51] C Boisson, A. M Brown, A Burtovoi, et al. "Probing extreme environments with the Cherenkov Telescope Array". eng. In: (2021).

[52] Avery E BRODERICK, Philip CHANG, and Christoph PFROMMER. "THE COSMOLOGICAL IMPACT OF LUMINOUS TeV BLAZARS. I. IMPLICATIONS OF PLASMA INSTABILITIES FOR THE INTERGALACTIC MAGNETIC FIELD AND EXTRAGALACTIC GAMMA-RAY BACKGROUND". eng. In: *The Astrophysical journal* 752.1 (2012), p. 22. ISSN: 0004-637X.

[53] M. Doro, J. Conrad, D. Emmanoulopoulos, et al. "Dark matter and fundamental physics with the Cherenkov Telescope Array". In: *Astroparticle Physics* 43 (2013). Seeing the High-Energy Universe with the Cherenkov Telescope Array - The Science Explored with the CTA, pp. 189–214. ISSN: 0927-6505. DOI: https://doi.org/10.1016/j.astropartphys.2012.

08.002. URL: https://www.sciencedirect.com/science/article/pii/S092765051200148X.

[54] Joerg Jaeckel and Andreas Ringwald. "The Low-Energy Frontier of Particle Physics". In: *Annual Review of Nuclear and Particle Science* 60.1 (2010), 405–437. ISSN: 1545-4134. DOI: 10.1146/annurev.nucl.012809.104433. URL: http://dx.doi.org/10.1146/annurev.nucl.012809.104433.

[55] Manuel Meyer and Tanja Petrushevska. "Search for Axionlike-Particle-Induced Prompt -Ray Emission from Extragalactic Core-Collapse Supernovae with the Fermi Large Area Telescope". In: *Physical Review Letters* 124.23 (2020). ISSN: 1079-7114. DOI: 10.1103/physrevlett.124.231101. URL: http://dx.doi.org/10.1103/PhysRevLett.124.231101.

[56] Joel R. Primack, Alberto Dominguez, Rudy C. Gilmore, et al. "Extragalactic Background Light and Gamma-Ray Attenuation". In: (2011). DOI: 10.1063/1.3635825. URL: http://dx.doi.org/10.1063/1.3635825.

[57] *CTA Requirements*. https://jama.cta-observatory.org/.. Accessed: 13-Jul-2021.

[58] CTA Consortium. *"Large Sized Telescope." From Chernkov Telescope Array*. URL: https://www.cta-observatory.org/project/technology/lst/.

[59] D Mazin, J Cortina, M Teshima, et al. "Large Size Telescope Report". eng. In: 2016.

[60] Markus Garczarczyk, Stefan Schlenstedt, Louise Oakes, et al. *Status of the Medium-Sized Telescope for the Cherenkov Telescope Array*. 2015. arXiv: 1509.01361 [astro-ph.IM].

[61] G. Pühlhofer, C. Bauer, S. Bernhard, et al. *FlashCam: a fully-digital camera for the medium-sized telescopes of the Cherenkov Telescope Array*. 2015. arXiv: 1509.02434 [astro-ph.IM].

[62] J-F. Glicenstein, O. Abril, J-A. Barrio, et al. *NectarCAM : a camera for the medium size telescopes of the Cherenkov Telescope Array*. 2015. arXiv: 1508.06555 [astro-ph.IM].

[63] W Benbow, A. N Otte, for the pSCT Consortium, et al. "Status of the Schwarzchild-Couder Medium-Sized Telescope for the Cherenkov Telescope Array". eng. In: 2016. ?

[64] CTA Consortium. *"Small Sized Telescope." From Chernkov Telescope Array.* URL: https://www.cta-observatory.org/project/technology/sst/.

[65] Teresa Montaruli, Giovanni Pareschi, and Tim Greenshaw. *The small size telescope projects for the Cherenkov Telescope Array*. 2015. arXiv: 1508.06472 [astro-ph.IM].

[66] Cherenkov Telescope Array. *"Proposed CTA Telescopes"*. URL: https://www.flickr.com/photos/cta_observatory/30329828142/in/album-72157672713462861/.

[67] Cherenkov Telescope Array. *"The technology behind the next generation very-high energy gamma-ray detector"*. URL: https://www.cta-observatory.org/project/technology/.

[68] A. Acharyya, I. Agudo, E.O. Angüner, et al. "Monte Carlo studies for the optimisation of the Cherenkov Telescope Array layout". In: *Astroparticle Physics* 111 (2019), 35–53. ISSN: 0927-6505. DOI: 10.1016/j.astropartphys.2019.04.001. URL: http://dx.doi.org/10.1016/j.astropartphys.2019.04.001.

[69] "The single mirror small sized telescope for the Cherenkov telescope array". In: (2017). DOI: 10.1063/1.4969024. URL: http://dx.doi.org/10.1063/1.4969024.

[70] J.A Aguilar, W Bilnik, J Błocki, et al. "Characterization and commissioning of the SST-1M camera for the Cherenkov Telescope Array". eng. In: *Nuclear instruments methods in physics research. Section A, Accelerators, spectrometers, detectors and associated equipment* 845 (2017), pp. 350–354. ISSN: 0168-9002.

[71] P. Rajda, K. Zietara, W. Bilnik, et al. *DigiCam - Fully Digital Compact Read-out and Trigger Electronics for the SST-1M Telescope proposed for the Cherenkov Telescope Array*. 2015. arXiv: 1508.06082 [astro-ph.IM].

[72] V Vassiliev, S Fegan, and P Brousseau. "Wide field aplanatic two-mirror telescopes for ground-based -ray astronomy". eng. In: *Astroparticle physics* 28.1 (2007), pp. 10–27. ISSN: 0927-6505.

[73] Maria Concetta Maccarone. *ASTRI for the Cherenkov Telescope Array*. 2017. arXiv: 1709.03078 [astro-ph.IM].

[74] V. Caprio, M. Belluso, Giovanni Bonanno, et al. "The ASTRI SST-2M prototype: camera design". In: vol. 8836. Sept. 2013. DOI: 10.1117/12.2025570.

[75] Stéphane Callier, Christophe Dela Taille, Gisèle Martin-Chassard, et al. "EASIROC, an Easy & Versatile ReadOut Device for SiPM". In: *Phys. Procedia* 37 (2012). Ed. by Ted Liu, pp. 1569–1576. DOI: 10.1016/j.phpro.2012.02.486.

[76] Osvaldo Catalano, Salvo Giarrusso, Giovanni La Rosa, et al. *The ASTRI SST-2M Prototype: Camera and Electronics*. 2013. arXiv: 1307.5142 [astro-ph.IM].

[77] A. M Brown, A Abchiche, D Allan, et al. *The GCT camera for the Cherenkov Telescope Array*. eng. 2018.

[78] K. Bechtol, S. Funk, A. Okumura, et al. "TARGET: A multi-channel digitizer chip for very-high-energy gamma-ray telescopes". In: *Astroparticle Physics* 36.1 (2012). ID: $\mathrm{TN}_{e}lsevier_{s}doi_{1}0_{1}016_{ja}stropartphys_{2}012_{0}5_{0}16$, pp. 156–165. DOI: 10.1016/j.astropartphys.2012.05.016.

[79] A. De Franco, R. White, D. Allan, et al. *The first GCT camera for the Cherenkov Telescope Array*. 2015. arXiv: 1509.01480 [astro-ph.IM].

[80] Michael Daniel, R. White, D. Berge, et al. "A Compact High Energy Camera for the Cherenkov Telescope Array". In: July 2013.

[81] J. Zorn, R. White, J. J. Watson, et al. "Characterisation and testing of CHEC-M—A camera prototype for the small-sized telescopes of the Cherenkov telescope array". In: *Nuclear instruments methods in physics research.Section A, Accelerators, spectrometers, detectors and associated equipment* 904 (2018). USDOE; Japan Society for the Promotion of Science (JSPS); AC02-76SF00515; JP17H04838; JP25610040; JP15H02086; JP23244051; ID: $\mathrm{TN}_{c}di_{o}sti_{s}citechconnect_{1}490682$, pp. 44–63. DOI: 10.1016/j.nima.2018.06.078.

[82] "Inauguration and first light of the GCT-M prototype for the Cherenkov telescope array". In: *AIP Conference Proceedings* (2017). ISSN: 0094-243X. DOI: 10.1063/1.4969027. URL: http://dx.doi.org/10.1063/1.4969027.

[83] R White. "CHEC: a Compact High Energy Camera for the Cherenkov Telescope Array". eng. In: *Journal of instrumentation* 12.12 (2017), pp. C12059–C12059. ISSN: 1748-0221.

[84] Hamamatsu. *"Photomultiplier Tubes"*. URL: https://www.hamamatsu.com/resources/pdf/etd/PMT_handbook_v3aE.pdf.

[85] Hamamatsu. *"Multi Pixel Photon-Counter"*. URL: https://www.hamamatsu.com/resources/pdf/ssd/mppc_kapd9005e.pdf.

[86] SensL. *"An Introduction to the Silicon Photomultiplier"*. URL: https://www.sensl.com/downloads/ds/TN%20-%20Intro%20to%20SPM%20Tech.pdf.

[87] Richard White and Harm Schoorlemmer. *A Compact High Energy Camera (CHEC) for the Gamma-ray Cherenkov Telescope of the Cherenkov Telescope Array*. 2017. arXiv: 1709.05799 [astro-ph.IM].

[88] G. Varner, L. Ruckman, and A. Wong. "The first version buffered large analog bandwidth (BLAB1) ASIC for high luminosity collider and extensive radio neutrino detectors". In: *Nuclear Instruments and Methods in Physics Research Section A: Accelerators, Spectrometers, Detectors and Associated Equipment* 591.3 (2008), 534–545. ISSN: 0168-9002. DOI: 10.1016/j.nima.2008.03.095. URL: http://dx.doi.org/10.1016/j.nima.2008.03.095.

[89] A. Albert, S. Funk, H. Katagiri, et al. "TARGET 5: A new multi-channel digitizer with triggering capabilities for gamma-ray atmospheric Cherenkov telescopes.(Report)". In: *Astroparticle Physics* 92 (2017). ID: $\mathrm{TN}_{g}ale_{o}fa521585743$, p. 49. DOI: 10.1016/j.astropartphys.2017.05.003.

[90] L. Tibaldo, J. A. Vandenbroucke, A. M. Albert, et al. "TARGET: toward a solution for the readout electronics of the Cherenkov Telescope Array". In: (2015). ID: $\mathrm{TN}_{c}di_{a}rxiv_{p}rimary_{1}508_{0}6296$.

[91] Mingliang Liu. *Chapter 5 - Switched-Capacitor Data Converters*. ID: $\mathrm{TN}_{c}di_{e}lsevier_{s}ciencedirect_{d}oi$ 2006. DOI: 10.1016/B978-075067907-7/50017-0.

[92] S. Funk, D. Jankowsky, H. Katagiri, et al. *TARGET: A Digitizing And Trigger ASIC For The Cherenkov Telescope Array*. ID: $\mathrm{TN}_{a}rxiv1610.01536$. 2017. DOI: 10.1063/1.4969033.

[93] Rick Bitter, Taqi Mohiuddin, and Matt Nawrocki. *LabVIEW: Advanced programming techniques*. Crc Press, 2006.

[94] Justus Zorn. "Cherenkov Camera and Analysis Development for Highest-Energy Gamma-Ray Astronomy". PhD thesis. 2020.

[95] A Asano, D Berge, G Bonanno, et al. "Evaluation of silicon photomultipliers for dual-mirror Small-Sized Telescopes of Cherenkov Telescope Array". eng. In: (2018).

[96] RCA Corporation. *RCA Electro-optics Handbook*. RCA solid State. RCA/Commercial Engineering, 1974. URL: https://books.google.co.uk/books?id=VNaZAAAAIAAJ.

[97] Jason John Watson and Justus Zorn. "Commissioning and Performance of CHEC-S – a compact high-energy camera for the Cherenkov Telescope Array". In: (2019). ID: TN$_c$*di$_a$rxiv$_p$rimary$_1$*907$_0$9252.

[98] Gerard Fernandez, David Gascon, and Jose de la Rosa M. *Design of a 9-bit 4MS/s wilkinson ADC for SiPM-based imaging detectors*. ID: TN$_c$*di$_s$copus$_p$rimary$_{2s}$*2$_{08}$5015821137 2016. DOI: 10.1109/MWSCAS.2016.7869979.

[99] Jason Watson. *CHECLabPy*. 2019. URL: https://github.com/sstcam/CHECLabPy.

[100] D. MacQuigg. "Residual charge on a switched capacitor [MOS type]". In: *IEEE Journal of Solid-State Circuits* 18.6 (1983). ID: TN$_c$*di$_p$ascal francis$_p$rimary$_9$*714950, pp. 811–813. DOI: 10.1109/JSSC.1983.1052037.

[101] F. N. Fritsch and R. E. Carlson. "Monotone Piecewise Cubic Interpolation". In: *SIAM journal on numerical analysis* 17.2 (1980). ID: TN$_c$*di$_p$roquest$_j$ournals$_9$*23606904, pp. 238–246. DOI: 10.1137/0717021.

[102] David Jankowsky. "Measurement of the Cosmic Ray Proton Spectrum with H.E.S.S. and Characterization of the Target C and T5TEA Asics". PhD thesis.

[103] Eric W. Weisstein. *"Cross-Correlation." From MathWorld–A Wolfram Web Resource.* URL: http://mathworld.wolfram.com/Cross-Correlation.html.

[104] George J. Miao. *Signal processing in digital communications.* Includes bibliographical references and index.; ID: 44UOLE$_A$*LMA*5113696902000274 6. Boston, MA: Artech House, 2007, pp. 94–110. ISBN: 1-58053-668-9.

[105] P. Virtanen, R. Gommers, T. E. Oliphant, et al. "SciPy 1.0: fundamental algorithms for scientific computing in Python: 24 February 2020 : An amendment to this paper has been published and can be accessed via a link at the top of the paper". In: *Nature Methods* 17.3 (2020). ID: TN$_h$*al*$_s$*oai*$_H$*AL*$_h$*al*$_0$2520043*v*1, pp. 261–272. DOI: 10.1038/s41592-019-0686-2.

[106] Pan Du, Warren A. Kibbe, and Simon M. Lin. "Improved peak detection in mass spectrum by incorporating continuous wavelet transform-based pattern matching". In: *Bioinformatics (Oxford, England)* 22.17 (2006). ID: TN$_m$*edline*16820428, p. 2059. DOI: 10.1093/bioinformatics/btl355.

[107] Norman Ricker. "WAVELET FUNCTIONS AND THEIR POLYNOMIALS". In: *Geophysics* 9.3 (1944). ID: TN$_c$*rossref*10.1190/1.1445082, pp. 314–323. DOI: 10.1190/1.1445082.

[108] Maria Concetta Maccarone. "ASTRI for the Cherenkov Telescope Array". eng. In: (2017).

[109] M Chantell, M. A Lawrence, M. F Cawley, et al. "Detection of TeV photons from the active galaxy Markarian 421". eng. In: *Nature (London)* 358.6386 (1992), pp. 477–478. ISSN: 0028-0836.

[110] J Quinn, C. W Akerlof, S Biller, et al. "Detection of Gamma Rays with E ¿ 300 GeV from Markarian 501". eng. In: *The Astrophysical journal* 456.2 (1996), p. L83. ISSN: 1538-4357.

[111] F Aharonian, A. G Akhperjanian, A. R Bazer-Bachi, et al. "Evidence for VHE -ray emission from the distant BL Lac PG1553+113". eng. In: *Astronomy and astrophysics (Berlin)* 448.2 (2006), pp. L19–L23. ISSN: 0004-6361.

[112] Simon Sailer. "The FlashCam camera for CTA: trigger verification and fluorescence light detection capabilities". English. PhD thesis. 2020. URL: `https://www.imprs-hd.mpg.de/424678/thesis_Sailer.pdf`.

[113] Thomas Bretz, D. Dorner, B. Riegel, et al. "Comparison of On-Off and Wobble mode observations for MAGIC". In: *B. Sripathi Acharya, Sunil Gupta, Ajai Iyer, P. Jagadeesan, Atul Jain, S. Karthikeyan, Samuel Morris, Suresh C. Tonwar: ICRC 2005, 311-314 (2006)* (Jan. 2005).

[114] Gary Finnegan and for the VERITAS Collaboration. "Orbit Mode observation Technique Developed for VERITAS". eng. In: (2011).

[115] Mathieu de Naurois. "Analysis methods for Atmospheric Cerenkov Telescopes". eng. In: (2006).

[116] R.W Lessard, J.H Buckley, V Connaughton, et al. "A new analysis method for reconstructing the arrival direction of TeV gamma rays using a single imaging atmospheric Cherenkov telescope". eng. In: *Astroparticle physics* 15.1 (2001), pp. 1–18. ISSN: 0927-6505.

[117] HEGRA Collaboration and A. Daum et al. "First Results on the Performance of the HEGRA IACT Array". eng. In: (1997).

[118] David J Fegan. "/hadron separation at TeV energies". In: *Journal of Physics G: Nuclear and Particle Physics* 23.9 (1997), pp. 1013–1060. DOI: 10.1088/0954-3899/23/9/004. URL: https://doi.org/10.1088/0954-3899/23/9/004.